Oxygen kinetics and charge doping for high critical current YBCO films

Alexander Stangl

Oxygen kinetics and charge doping for high critical current YBCO films

A dissertation submitted for the degree of
DOCTOR OF PHILOSOPHY IN PHYSICS
by

Alexander Stangl

Supervisors:
Prof. Teresa Puig Molina
Dra. Anna Palau Masoliver

Superconducting Materials and Large Scale Nanostructures
Institut de Ciència de Materials de Barcelona (ICMAB-CSIC)

Tutor: Prof. Àlvar Sànchez Moreno
Doctorat en Física
Departament de Física - Facultat de Ciències
Universitat Autònoma de Barcelona

February 2019

ICMAB
INSTITUT DE CIÈNCIA DE MATERIALS DE BARCELONA
EXCELENCIA SEVERO OCHOA
CSIC
CONSEJO SUPERIOR DE INVESTIGACIONES CIENTÍFICAS

UAB
Universitat Autònoma de Barcelona
Facultat de Ciències
Departament de Física

Memòria que porta per títol **"Oxygen kinetics and charge doping for high critical current YBCO films"** i presentada per aspirar al Grau de Doctor en Física per **Alexander Stangl**

Autor:
Dipl.-Ing. Alexander Stangl, BSc.

amb el vist i plau de: **Prof. Teresa Puig Molina**, Professora d'investigació del Institut de Ciències de Materials de Barcelona (ICMAB-CSIC); **Dra. Anna Palau Masoliver**, Científica Titular del Institut de Ciències de Materials de Barcelona (ICMAB-CSIC) i **Prof. Àlvar Sànchez Moreno**, catedràtic del Departament de Física de la Universitat Autònoma de Barcelona (UAB).
I per a que així consti, signen el present certificat.

Directora:	*Directora:*	*Tutor:*
Prof. Teresa Puig Molina	Dra. Anna Palau Masoliver	Prof. Àlvar Sànchez Moreno

Bellaterra, 19 de febrer de 2019

Abstract

High temperature superconductors, especially cuprates, in the form of coated conductors have the potential to be part of the next technological revolution due to unchallenged, extraordinary superconducting properties. Oxygen plays an essential role in these cuprate high-temperature superconductors, where superconductivity is governed by hole doping.

In this thesis we have intensively studied all oxygen involved processes, from the initial incorporation of oxygen into the $YBa_2Cu_3O_{7-\delta}$ structure and related mechanism, up to the influence of oxygen doping on the superconducting properties. A deep understanding of each particular step is not only interesting from an academic point of view, but also necessary in the optimisation and improvement for any commercial production line.

Using *in situ* electrical conductivity relaxation and *in situ* X-ray diffraction measurements we have analysed oxygen exchange kinetics in YBCO thin films. A broad variety of samples and microstructures, obtained by different growth methods, cation substitution, nanocomposites, variations in thickness and substrate, have been studied. Our studies reveal different influences of macroscopic and microscopic strain on activation energies for oxygen exchange. In this work silver was found to be an excellent catalytic agent for oxygen incorporation, by providing a catalytic alternative reaction path, which enabled faster oxygenation kinetics and lower oxygenation temperatures. Further, we have successfully identified the rate determining step (RDS) of oxygen exchange kinetics in silver coated YBCO thin films, which we have found to be the recombination of oxygen ions with surface vacancies.

The thorough use of electrical *in situ* measurements in combination with ex situ analysis techniques as XRD, STEM, SEM, electrical resistivity, Hall and magnetisation measurements enabled us to study the effects of thermal treatment parameters on the surface chemistry and bulk microstructure of YBCO thin films. On one hand, we have identified the formation of stacking faults already during low temperature annealings. On the other hand, a deactivation of surface exchange kinetics was found for non-silver coated films, resulting in significantly slower oxygen incorporation with increasing annealing time.

Surface coating dependent degeneration rates point towards a modification of the RDS upon silver coating of YBCO thin films.

We have not only studied the incorporation of oxygen in great detail, but also its effect on the doping state of the cuprate material. The influence of oxygen partial pressure, oxygenation temperature and oxygenation time on the charge carrier density and normal/superconducting physical properties was intensively studied. We have prepared highly overdoped YBCO thin films grown by PLD with record-high critical current densities reaching 90 MA/cm^2 at 5 K and self-field, reaching a third of the depairing current density. The doping state was analysed by the use of temperature dependent resistivity, Hall and mobility measurements, as well as XRD and critical temperature measurements. By using a two band model for the electrical transport of electrons and holes, we have obtained a temperature independent charge carrier density. We have demonstrated a linear correlation between the charge carrier density and the critical current densities in the overdoped state, thus evidencing the powerfulness of these studies for the enhancement of superconducting properties of YBCO thin films.

Acknowledgements

First of all, I would like to thank the head of the SUMAN group and my supervisor Prof. Teresa Puig for giving me the chance to join her group, for her constant support and encouraging supervision, especially in the last months of this work, and her catching excitement about science in general and superconductivity in particular. I would also like to thank Dr. Anna Palau for her supervision and our discussions on the manuscript.

I'm very thankful to Prof. Harald W. Weber, who not only had paved my way into the field of superconductivity many years ago, but also continued his mentoring in our frequent meetings in Barcelona.

I would like to thank Dr. Pablo Cayado for all his help and patience at the beginning of my PhD and the introduction to *Nona* and the secrets of YBCO oxygenations. It is a big pleasure to express my very special appreciation to Dr. Juan Carlos Gonzalez for the many roles he took on during this PhD. I would like to acknowledge scientific input and fruitful discussions with Prof. Xavier Obradors and Dr. Susagna Ricart.

I'm grateful for our successful collaboration with Dr. José Santiso and Dr. Jessica Padilla from ICN2 regarding the *in situ* X-ray analysis. We could not have achieved as good results without the constant, professional assistance of the scientific and technical services of ICMAB, first and foremost Mariona de Palau and Joshua Bailo from the SUMAN group, Dr. Bernat Bozzo of the low temperatures and magnetometry service, Anna Crespi, Joan Esquius and Javier Campos from the X-ray diffraction lab, Raul Solanas from the Thin Films Laboratory and Luigi Morrone from the Nanoquim Platform. Thanks to Dr. Bernat Mundet for the TEM analysis and Dr. Ziliang Li for the many samples he provided to our studies. I highly appreciate the help from Xavi Sintas in the automatisation of the measurement set-up.

I very much acknowledge Dr. Mar Tristany, Patricia Alvarez and ICMAB administration personnel for the guidance through the necessary bureaucracy and for keeping things running in the background. Furthermore I would like to thank Dr. Sebastian Reparaz (ICN2), Dr. Emigdio Chávez (ICN2), Dr. Bernhard Dorling (ICMAB) and José Piers Jurado (ICMAB) for their help and assistance with Seebeck measurements.

This PhD experience would not have been the same without my colleagues and dear friends Júlia Jareño and Dr. Laia Soler from day 0 here at ICMAB. Thanks for all your help on the *chemical stuff*, to prevent me from burning down the lab, all our discussions and your support and love! Tack vare Dr. Stephan Steinhauer for your scientific advices and friendship. Prof. Michael Eisterer, you deserve your spot here for your kind and special way (Ich war's nicht!).

To my colleagues here at ICMAB, a big thank you for all your help, advices, discussions, good moments, excursions and beers after work: Bohores, Ferran, Juri, Coco, Marta, Anna, Max, Pedro, Flavio, Alejandro, Artur, Joffre and all current and past members of the SUMAN group and the office 234.

The presented work was conducted at the Institut de Ciència de Materials de Barcelona (ICMAB-CSIC). We acknowledge financial support from Spanish Ministry of Economy and Competitiveness through the "Severo Ochoa" Programme for Centres of Excellence in R&D (SEV-2015-0496), COACHSUPENERGY project (MAT2014-51778-C2-1-R, co-financed by the European Regional Development Fund). We also thank support from the European Union for EUROTAPES project (FP7-NMP-Large-2011-280432) and from the Catalan Government with 2017-SGR-1519.

I have really enjoyed my last four years here in Barcelona. The following lines are dedicated to all the people, who made this time such a great experience. Thank you for your friendship, support, trust and love!

DesGraciades you have eternised the Kingdoms of Gràcia. Tordera will be unforgettable and an indelible part of my life. Júlia, thanks for Escaló, Calella,..., our late night talks at our corners in the north and especially your craziiiness. Laia, you marked a turning point - without you I'd still only dance waltz. Thanks for our trips to Putxet and Barceloneta, Pizza Circus and magenta. Juanca, thanks for your commmedy, wisdom and songs and especially your open (balcony) door. I'm grateful for your incredible massages to my back and to my soul, Ana.
Silvia, for all our spontaneous beers. David, for sharing the passion for Käsespätzle. Vish, for your kind and helpful nature. Paula, for opening Tordera to us. Sergio, por empujar a hablar. Thomas, for pushing to run. Thanks!

To my families in Lesseps and Sant Salvador, Clara, Moli, Garoe, Thibaud, Javi & Anna, Ralf, Vitto, Théo and Mar. El guapo, thanks for the crêpes in the morning and your friendship throughout the day. Merci beaucoup i moltes gràcies a Maud, Nuria and Natalia for not cleaning: Sant Salvador 56/3 rocks and Montse lives forever!

Adriá, Magalí, Fran i tots els Nens del Vendrell, Charlotte, Ana, Jan, Patricia, Benni & Laura, Jone, Christian, Helena, Dolores thanks for all the good times we had here. *Let's jam* to Sònia, Leo, Anna, Anh-Van, Noelia and all the Lindy hoppers. Ski forofos, la muntanya crida! Cheers to Antonio, Fransesc, Toni & the ICMAB football team!

Als Calçots i Calçotades, al Vermut i papa bravas! Al Carmel i la Miranda, Al Putxet i la Virreina. A les festes majors i corre-focs, a la Costa Brava i secrets llocs. Al Miquel i senyor Tano, Sant Joan i caga tió. A la llegenda de Sant Jordi,

i Gràcia, el meu barri. A la Patum i Patufet, als Castellers i pa amb tomàquet. V.C.

To my dear friends in Vienna, allen voran Johnny, Stephan, Kathi, Paul, Bene, Christl, Sigrid, Stephan, Hanno, Carmen & co.: thanks for your long and lasting friendships, your visits and uncountable special moments! Ein Hoch auf die Spritzbärigkeit! Nils, now it's your turn to finish your Doctor my friend! To Marius and Adrian and our amazing reunions.

Maragda, you have brought so many things into my life. Without you I would not be where I am today and now I'm here without you. Thanks for the unique time we had, for all the *souvenirs*, for sharing all parts of your life with me, for making this place my home, for teaching me so much, for your art and for your big heart. This all will remain.

And finally I would like to express my deep gratitude and love to my family. Thank you for always being there for me. Danke! Für euer Vertrauen und eure Unterstützung. Pia, Valeria, & co, für die viel zu seltenen aber wunderbaren Momente mit euch. Rita, dass du Teil meiner Familie bist. Oma, Opa, danke für eure immer offene Tür, offenen Ohren und Herzen. Opa und Oma, ihr fehlt aber bleibt unvergessen! Philipp, Danke für deine vielen Besuche, deine Weisheit und deine liebenswerte Art. Danke, dass ich mich immer auf dich verlassen kann Papa.
Mama, weil ich immer dort zuhause sein werde wo du bist. Weil du immer für mich da bist. Weil ich es ohne dich nicht hier her geschafft hätte. Danke!

Contents

"Las mariposas son el polvo mágico de la vida"

La noia del ferro

Chapter 1

Introduction

The discovery of superconductivity more than one century ago immediately awakened high expectations on ultra high magnetic fields, believed to be out of any technological reach, and dissipation free transport of electric power. The realisation of these dreams, however, was hold back for many years due to fundamental superconducting and material specific limitations.

The development of low temperature superconducting wires in the second half of the 20^{th} century, made from NbTi and Nb_3Sn, paved the way to first superconducting magnets, pushing the limits of magnetic applications and still being a key technology nowadays for scientific (NMR, high energy physics) and medical (MRI) purposes.

A new era of superconducting research and development was heralded by the discovery of high temperature superconductivity three decades ago, also known as the *Woodstock of Physics*. For the first time the fascinating state of superconductivity was observed at temperatures above the boiling point of liquid nitrogen, a cheap and superabundant coolant, creating vast expectations on a technological revolution. This early stage enthusiasm was soon replaced by the challenging reality of obtaining brittle ceramic, superconducting materials in the desired form of wires and tapes.

A first generation of HTS wires, based on a powder-in-tube process (BSCCO tapes), advanced wire technology but did not yield exceptional advantages. However, the outstanding superconducting performance of the REBCO (RE=Rare earth elements) material class attracted the attention of many researches world wide and resulted in the development of so-called coated conductors (CC). This 2^{nd} generation (2G) of HTS tapes requires the epitaxial deposition of REBCO on a metallic substrate over long lengths - a never seen challenge in material science, research and development.

Major improvements have been made within recent years to tackle the most critical issues, as the uniform textured deposition of nano-structures in kilometres length (a desired correlation over twelve orders of magnitude!), a

drastic increase of the homogeneity of the thin films and its thickness, a nano-engineered pinning landscape via the introduction of artificial pinning sites and mainly a lowering of the production costs (€/kA/m) by the development of different deposition techniques (CSD, MOCVD, PLD).

The advent and commercialisation of high temperature superconducting materials can have a major impact on our modern urban societies. Current and near-future progress in the production of CCs has the possibility to boost moonshot projects as the next fusion reactors beyond ITER, dissipation-free transmission of electricity in a superconducting grid of renewable energy systems, light and highly efficient engines for electrical aviation and new transportation technologies as levitating trains. As we are on the abyss of loosing the fight against climate change the potential of superconducting technology is indispensable.

Superconductivity in YBCO is governed by hole doping into the CuO_2-planes via the oxidation of the crystal. This so-called oxygenation process is the last fabrication step in the production of YBCO and the main subject of this thesis. A high oxygen content in the YBCO layer is a prerequisite for its exceptional and unrivalled superconducting properties, such as the highest achievable critical current densities and upper critical fields. The optimisation of the oxygenation process requires a fundamental understanding of the oxygen incorporation mechanisms into the structure, comprising surface exchange kinetics and bulk diffusion. Other than stoichiometric effects of heat treatments on the microstructure and the chemical composition of the surface, as the formation of microstructural defects, or surface cation segregation, must be understood as well to enable the production of high quality coated conductors with homogeneous properties over long lengths (>1 km). A thorough understanding of the oxygenation process opens the door to reach the overdoped state of the YBCO phase diagram. This phase is very promising to allow further enhancement of the superconducting properties of YBCO close to the limits of the depairing current, where the fundamental state of charge pairing is destroyed.

In summary, this thesis is organised as follows:

- Chapter 2 introduces the fundamental concepts of superconductivity and physical chemistry of oxygen exchange kinetics in oxide materials.
- Chapter 3 describes experimental methodologies, comprising sample production and preparation techniques and measurement methods used throughout the thesis to characterise normal state and superconducting properties of the derived samples.

- Chapter 4 shows the results on our study of oxygen exchange in pristine and silver coated YBCO, elucidating the rate determining step of silver coated YBCO thin films and the influence of different microstructures and strain on the oxidation mechanism.
- Chapter 5 concentrates on the stability of YBCO under both oxidation and reduction conditions, modifications of the microstructure during thermal annealings and long term chemical stability of the surface.
- Chapter 6 summarizes our efforts on reaching the overdoped state of the YBCO phase diagram by means of different oxygen treatments and analyses the doping dependence of superconducting properties.

Chapter 2

Fundamental Concepts

2.1 Superconductivity

Superconductivity (SC) is a low temperature phase with extraordinary electrical and magnetic properties. The superconducting state was first discovered by the Dutch physicist Heike Kamerlingh Onnes in 1911 in highly pure mercury [1]. Below a certain material dependent temperature, the critical temperature T_c, the material loses its electrical resistivity and exhibits perfect diamagnetism, expelling all magnetic field from its interior. The latter is called Meißner-Ochsenfeld effect [2] and is essential to make SC a thermodynamic phase. The superconducting state is confined by a critical temperature, a critical current density and a critical external magnetic field. Upon exceeding any of these parameters superconductivity is destroyed.

Superconductivity arises due to a lower Gibbs free energy G of the SC state as compared to the normal state (NS). The energy difference in zero field is the so called condensation energy and defines the thermodynamic critical field $\mu_0 H_c$:

$$E_c(T) = G_{SC}(0,T) - G_{NS}(0,T) = -\frac{\mu_0 H_c^2(T)}{2} V, \tag{2.1}$$

with the vacuum permeability μ_0 and the volume V of the superconductor. As we will see later E_c is of essential importance for the transportation of dissipation free currents. The origin of this phase transition can be explained within the BCS theory, postulated by Bardeen, Cooper and Schrieffer in 1957 [3] for low-temperature superconductors. The energy of the system is lowered by the pairing of free electrons of opposite spin and wave vector, a so-called Cooper pair, which is subject to a weak attractive interaction with the lattice (electron-phonon interaction). Due to the pairing mechanism former fermionic particles can condensate into a bosonic-like, degenerated ground state, forming a macroscopic, phase coherent quantum state. As a result of

the condensation, a superconducting gap Δ opens in the energy spectrum of the superconductor.

Normal resistivity is caused by scattering of electrons into higher energy states by impurities in the lattice. Due to the SC gap no free states are available in the range of the scattering energy around the Fermi surface, effectively suppressing any electrical resistance. The thermodynamic limit for resistance free current flow is the so called depairing current, whereupon the kinetic energy of the charge carriers exceeds the binding energy of the Cooper pairs 2Δ. However, dissipation free current transport in real superconducting materials is limited already before by the motion of magnetic flux lines, as will be discussed in section 2.1.3.

2.1.1 Superconductors in external magnetic fields

In the superconducting state, external magnetic field is expelled from its interior by the circulation of shielding currents at the surface of the SC. Within the magnetic penetration depth λ the applied field drops exponentially to zero. On the other hand local variations of the Cooper pair density (or rather the so-called order parameter ψ) are limited by the coherence length ξ. Both physical quantities, λ and ξ, are material dependent and were introduced within the phenomenological Ginzburg-Landau theory in 1950 [4].

Superconductors can be classified by the ratio of these two parameters, the Ginzburg-Landau parameter κ, into type-I and type-II superconductors via:

$$\kappa = \frac{\lambda}{\xi} \begin{cases} \kappa < 1/\sqrt{2}\text{: type-I SC} \\ \kappa > 1/\sqrt{2}\text{: type-II SC} \end{cases} \tag{2.2}$$

which determines the behaviour of the SC in an external magnetic field. This can be understood by looking at the surface energy σ_{ns} at the interphase of the superconducting and normal phase. Near the interface the condensation energy and the exclusion energy E_b, required to expel the magnetic field from the interior of the SC, are competing. Depending on λ and ξ the energy difference $\Delta E = E_b + E_c \propto \sigma_{ns}$ is either positive or negative.

The magnetic penetration into a superconductor is shown in Fig. 2.1. In type-I superconductors, where the coherence length is much larger than the magnetic penetration depth, E_b rapidly increases to its maximum value, while E_c builds up over a broader region, as schematically shown in Fig. 2.1(c). Thus, the surface energy σ_{ns} is positive and the system tends to minimise this boundary as it requires energy to generate a S-N interphase. The SC remains in the Meißner-state until the external magnetic field exceeds the critical field

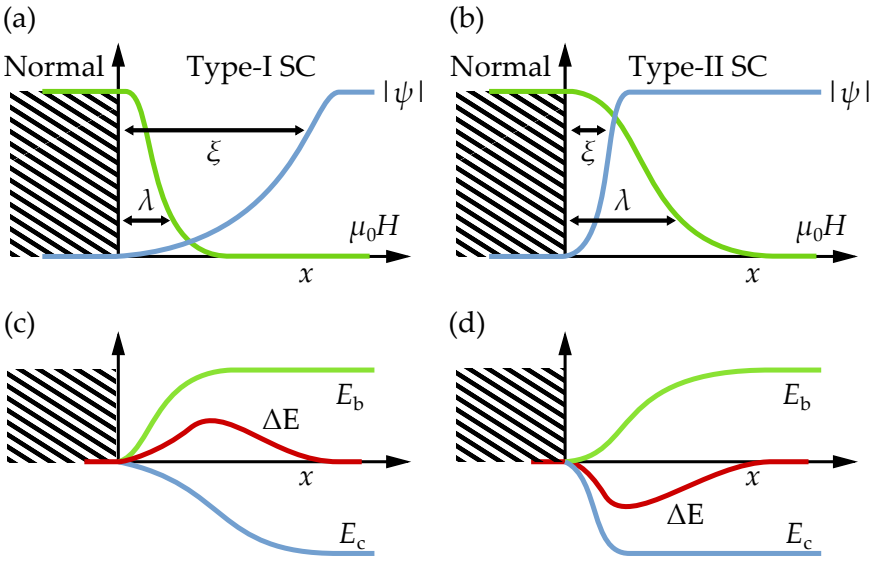

FIGURE 2.1: Schematic representation of the magnetic penetration depth λ and the superconducting coherence length ξ at the interphase of a normal region and (a) a type-I and (b) a type-II superconductor and corresponding variations of the energy landscape in (c) and (d), respectively, with the exclusion energy E_b and the negative condensation energy E_c.

H_c, whereupon superconductivity vanishes. Most superconducting elements are of type-I.

Type-II superconductors are in the Meißner-state, showing perfect diamagnetism only below a rather small magnetic field, the so-called lower critical field $\mu_0 H_{c1}$. Above $\mu_0 H_{c1}$ it becomes energetically preferential for the system to let quantised magnetic flux vortices penetrate the superconducting specimen. This can be understood by much shorter coherence lengths of type-II superconductors. Therefore the condensation energy reaches its full value in close proximity to the boundary and σ_{ns} becomes negative (see Fig. 2.1(b) and (d)). The gain of σ_{ns} overcompensates the loss of condensation energy due to the normal core of the vortex, making it energetically more stable. This phase is called mixed-state or Shubnikov-phase.

Each flux line carries a so-called flux quantum $\phi_0 = h/2e = 2.07 \cdot 10^{-15}\,\mathrm{Tm}^2$, generated by a superconducting current flowing in a plane perpendicular to the field direction. Superconductivity in the mixed-state is preserved until an external field exceeds the upper critical field $\mu_0 H_{c2}$, which can reach very

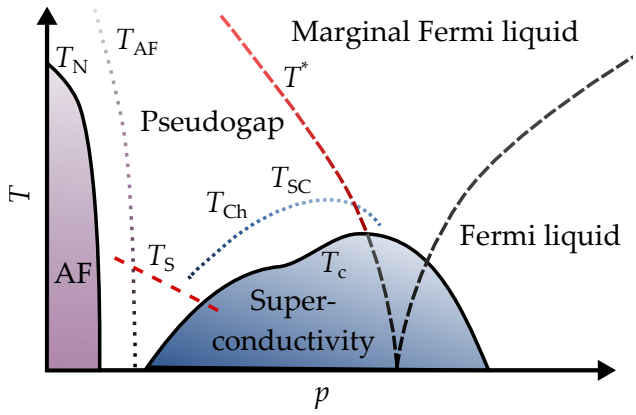

FIGURE 2.2: Schematic T-p phase diagram of the cuprate family with many different phases, as AF-ordering (below T_N), superconductivity (T_c), the pseudogap region (T^*) and the (marginal) Fermi liquid phases. T_{AF}, T_S, T_{Ch}, T_{SC} indicate the onset temperatures of antiferromagnetic, spin, charge and superconducting fluctuations. Adopted from [10].

high fields (>100 T). High $\mu_0 H_{c2}$ fields are a fundamental requirement for large technical applications of superconductors.

2.1.2 High temperature superconductors

The discovery of high temperature superconductivity (HTS) in 1986 by Bednorz and Müller [5] in $Ba_xLa_{5-x}Cu_5O_{5(3-y)}$ marks the advent of the renaissance of superconductivity research. Soon after in 1987, the first compound with a superconducting transition above liquid nitrogen temperature was announced: $YBa_2Cu_3O_{7-\delta}$ with a T_c of 93 K [6]. In the following years HTS was found in many compounds and different material classes, as cuprates with its most promising candidates $Bi_2Sr_2CaCu_2O_8$ (Bi2212) [7] and YBCO and iron-based materials [8].In recent years a major step towards potential room-temperature superconductivity has been made by the discovery of HTS in sulfur hydride systems with $T_c = 203$ K [9]. So far, all known high temperature superconductors are of type-II, where the mixed state mainly governs the $H - T$ phase diagram. The Shubnikov-phase therefore is of extraordinary importance for the technological use of HTS.

While low temperature superconductivity can be sufficiently explained within the framework of BCS theory, there is still no clear conclusion on the mechanism of HTS in its entirety. Cuprate superconductors exhibit a very rich

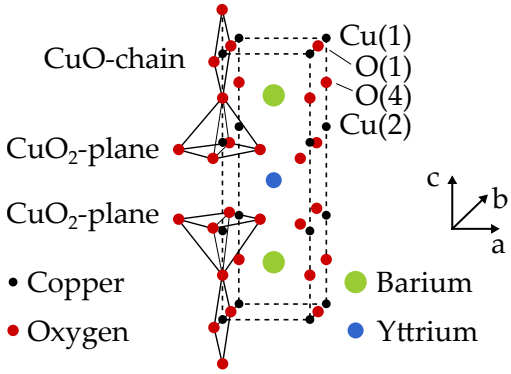

FIGURE 2.3: Orthorhombic structure of $YBa_2Cu_3O_{7-\delta}$ indicating the CuO-chain in *b* direction and the two *CuO2*-planes per unit cell.

and complex phase diagram, as schematically shown in Fig. 2.2. It is widely believed that the understanding of the intricate *normal* state above T_c will provide a clue to the origin of HTS [11, 12], especially the so called pseudogap is of very special concern. Superconductivity in cuprates arises upon charge doping into Mott insulators [13], where strong Coulomb repulsion of electrons leads to an antiferromagnetic insulating state (even though a half filled energy band crosses the Fermi surface, as *e.g.* the Cu d orbitals in cuprates). At low doping a pseudogap opens in the energy spectrum of the charge carriers around the Fermi energy, similar to the superconducting gap, however, at higher temperatures. Above the pseudogap, a marginal Fermi liquid phase evolves with unusual metallic properties (*strange* metal). At very high doping, cuprate superconductors can be described within the Fermi liquid theory. The critical temperature has its maximum at **optimal doping**. At lower doping (**underdoped regime**) T_c decreases with decreasing doping. This might be caused by phase fluctuations of the superconducting order parameter rather than the breaking of the Cooper pairs, due to low carrier densities, *i.e.* see [14]. On the other hand, in the **overdoped regime** T_c decreases with increasing doping possibly due to the decrease of the superconducting gap [15].
There are many different attempts trying to explain HTS, *e.g.* by linking the origin of superconductivity to charge density waves [16], competing order parameters and *d*-density wave order [17, 18] or to spin fluctuations [19]. However, there is no theoretical model yet combining the many various experimental results.

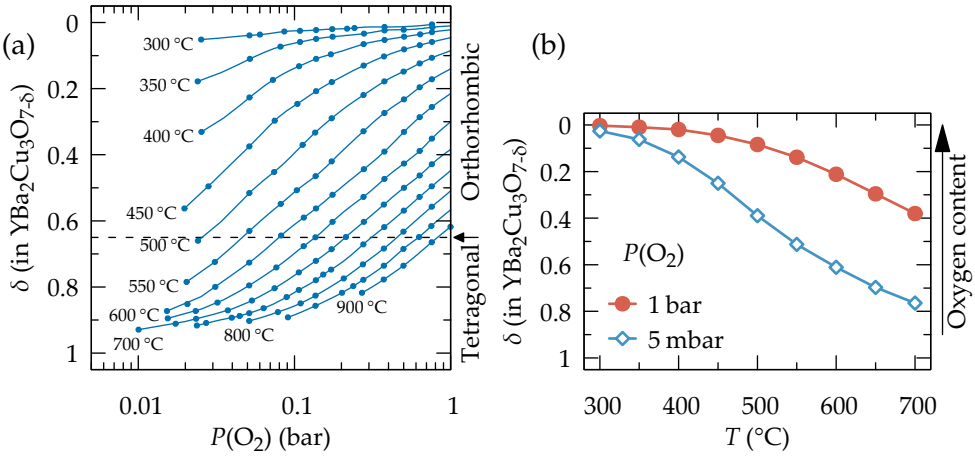

FIGURE 2.4: (a) Oxygen non-stoichiometry *vs.* $P(O_2)$ of $YBa_2Cu_3O_{7-\delta}$ for different temperatures. (b) δ as a function of temperature for the working pressures of 1 bar and 5 mbar. Data reproduced from [21] with permission.

$YBa_2Cu_3O_{7-\delta}$: Crystal structure and oxygen non-stoichiometry

YBCO, as part of the REBCO (RE=rare earth) material family, is one of the most promising materials for the commercial breakthrough of HTS, with its high critical temperature and record high critical current densities up to very high magnetic fields. The YBCO structure consists of an oxygen deficient triple perovskite cell and is shown in Fig. 2.3. The atomic arrangement of perovskites is based on a cubic structure of the formula ABX_3, with positive, metallic cations A and B in the centre and the corners of the cube, respectively. The negative charged, non-metallic anions X are located in the centre of the twelve edges.
The stacking sequence of YBCO *ab*-planes is Y-CuO_2-BaO-CuO-BaO-CuO_2-Y, with two CuO_2-planes and one CuO-chain in *b*-direction. CuO_2-planes are found in all cuprate SC and are thought to be the key for superconductivity in this material class, while the separating spacer layers and especially the CuO-chains are known to serve as charge reservoir. There is a strong covalent bonding between the partly occupied Cu $3d_{x^2-y^2}$ orbital and the O $2p_x$ and O $2p_y$ orbitals and charge transfer between the CuO planes and CuO_2-planes is linked via the apical oxygen between the plane and the chain [20].

The oxygen content of $YBa_2Cu_3O_{7-\delta}$ can vary between 6 and 7. The oxygen deficiency $7-\delta$ corresponds to the oxygen content in the CuO-chains, which are empty at O_6 and fully filled at O_7 [22]. Electron holes are created in the

p orbitals of oxygen. YBCO is subject to a phase transition depending on the oxygen content. If $\delta > 0.65$ the compound exhibits a non-superconducting, tetragonal symmetry. Upon filling oxygen into the chain sites the b-parameter of the unit cell increases, while a gets compressed and the material becomes orthorhombic, showing superconductivity for $\delta < 0.6$. The phase diagram of the oxygen non-stoichiometry as a function of oxygen partial pressure is shown in Fig. 2.4(a). In Fig. 2.4(b) we have extracted the oxygen content as a function of temperature for two different pressures, as they will be used as standard conditions in Chapter 4.

The temperature dependence of the oxygen stoichiometry can be qualitatively understood by thermodynamic considerations. The free enthalpy G of a real crystal consists of the two ideal components, the static bonding and vibrational enthalpy of the perfect crystal, G_{perfect}, and a configurational, entropic component ($G_{\text{cfg}} < 0$) [23]:

$$G = G_{\text{perfect}} + \underbrace{N_{\text{d}} \left(\Delta_{\text{d}} g + k_{\text{B}} T \ln \frac{N_{\text{d}}}{N} \right)}_{G_{\text{cfg}}}, \tag{2.3}$$

with the number of defects N_{d} (*e.g.* vacancies) and the total number of crystals sites N. The term $\Delta_{\text{d}} g$ accounts for changes in the bonding and vibrational contributions due to defects. G_{cfg} enables the existence of point defects at equilibrium at finite temperatures. The equilibrium defect concentration is defined by the temperature dependent minimum of G, which is seen to increase with increasing temperature.

The layered structure of YBCO causes a strong anisotropy of normal-state and superconducting properties and is typically expressed by the anisotropy parameter γ:

$$\gamma = \frac{\xi_{ab}}{\xi_c} = \frac{\lambda_c}{\lambda_{ab}} = \sqrt{\frac{m_c}{m_{ab}}} = \frac{\mu_0 H_{\text{c2}}^{ab}}{\mu_0 H_{\text{c2}}^{c}}, \tag{2.4}$$

with the coherence lengths, London penetration depths, effective electron masses m and critical field H_{c2} in the ab-plane and in c-direction. Typically in YBCO one finds $\gamma = 5 - 7$, thus there are huge differences between the upper critical field H_{c2} for fields applied parallel or perpendicular to the superconducting CuO_2-planes.

Due to a very small coherence length in HTS materials (ξ is of the order of 1 nm) and d-wave superconducting pairing symmetry, high angle grain boundaries strongly decrease superconducting performance [24, 25]. Therefore, epitaxial growth is a prerequisite for any application of cuprate superconductors. Commercial production of YBCO superconducting tapes is based

on the so called coated conductor architecture. The superconducting layer is deposited on a metallic substrate with several epitaxial buffer layers on top to match the cell parameters of YBCO [26].

2.1.3 Vortex pinning in YBCO

As we have seen above, type-II SC are characterised by a new phase, the mixed state, where the free energy of the total system in an external field can be lowered by the penetration of quantised magnetic flux (vortices). The vortex has a normal core ($|\psi| = 0$), therefore the system loses the condensation energy related with the volume of the core. In a perfect, defect-free SC the vortices are driven by an applied current due to a Lorentz-like force $\vec{F}_\mathrm{L}$. The moving normal core of the vortices causes an electric field and therefore energy dissipation in the material.

As any crystal has defects, which are non-superconducting, the system can regain the condensation energy of the vortex core by placing the flux line in the defect, resulting in a force $\vec{F}_\mathrm{P}$ of opposite direction to $\vec{F}_\mathrm{L}$. This effect is called vortex pinning and is essential for bulk current densities.
As long as $|\vec{F}_\mathrm{L}| < |\vec{F}_\mathrm{P}|$, vortices are pinned and DC currents can flow dissipation-free through the superconductor. The critical current density J_c is reached, when the Lorentz force density equals the pinning force density:

$$\vec{f}_\mathrm{L} = \vec{J}_\mathrm{c} \times \vec{B} = -\vec{f}_\mathrm{P}. \tag{2.5}$$

At higher currents, magnetic vortices are getting unpinned, spontaneously flowing through the material. This state is called flux-flow regime with $J_\mathrm{c} = 0$. However, superconductivity is preserved until the applied current reaches the so-called depairing current J_d, where electrons have enough kinetic energy to break the condensation into Cooper pairs (the kinetic energy exceeds the superconducting gap 2Δ). Within the Ginzburg-Landau theory the depairing current J_d can be written as [27]:

$$J_\mathrm{d}^\mathrm{GL} = \phi_0 \frac{1}{2^{3/2}\pi\mu_0\lambda^2(T)\xi(T)}, \tag{2.6}$$

with the temperature and material dependent magnetic penetration depth $\lambda(T) = \lambda(0)/\sqrt{1-t^4}$ and coherence length $\xi(T) = \xi(0)\sqrt{(1+t^2)/(1-t^2)}$, the flux quantum ϕ_0, the vacuum permeability μ_0 and the reduced temperature $t = T/T_\mathrm{c}$.

The maximum pinning effect can be achieved by defects of dimension $\sim 2\xi$ with a similar density as the vortices and a maximum condensation energy. There are many different kinds of defects present in YBCO. One can

sort the various defects by means of their dimensionality. Natural crystal imperfections as oxygen vacancies and interstitial atoms are 0D, while edge and screw dislocations are 1D defects. Twin and grain boundaries are two dimensional pinning sites, while nanophases are 3D volume defects.

Artificially introduced defects, via the embedding of nanoparticles, self-assembled columnar nanorods during growth, or irradiation can significantly improve pinning properties of YBCO.

The layered structure of cuprates leads to an additional, intrinsic pinning contribution, specially for magnetic fields parallel to the CuO_2-planes, due to suppressed superconductivity in between the CuO_2-planes (*d*-wave SC).

At high temperatures flux pinning is weakened by thermal fluctuations within the material. As different defect types are governing the pinning at different temperatures, nano-engineering of HTS material can customize fundamental superconducting properties to the required working conditions, as *e.g.* high fields at low temperature for magnet applications, or high temperatures and low fields for current-carrying technologies.

2.1.4 Bean critical state model

In a reversible, defect-free type-II superconductor in the mixed state, magnetic vortices arrange in a homogeneous hexagonal lattice to minimise repulsive interactions between the flux lines. However, in most type-II SC we find defects, where vortices are pinned, resulting in a hysteresis of the magnetisation process. This remanent magnetisation was first explained within the Bean critical state model, as described in the following [28, 29].

We will assume an infinite cylindrical superconductor with radius r in an axial external magnetic field, a field independent critical current density $J_c(B) = const$ and we will neglect thermally activated movement of vortices. In the Meißner phase, superconductors exhibit perfect diamagnetism, with $\mu_0 H = -\mu_0 M$. However, above H_{c1} magnetic flux lines penetrate the superconductor from the edges, reducing the magnetisation. Due to pinning, a field gradient inside the specimen will build up, as shown schematically in Fig. 2.5(a) for three different fields. This gradient induces locally a current, equivalent to the critical current J_c (critical state). As we assume $J_c = const$, the field decays linearly inside the superconducting material. The penetration depth of vortices is field dependent and at $H = H^*$ the field fully penetrates the sample and the saturation reaches its saturation. Upon further increase of the applied field (as long as $H_a \ll H_{c2}$), the field gradient stays the same (hence the magnetisation), but the vortex density increases.

When the external field is reduced, vortices leave the specimen first at the edge, reversing the gradient as indicated in Fig. 2.5(b). When the external

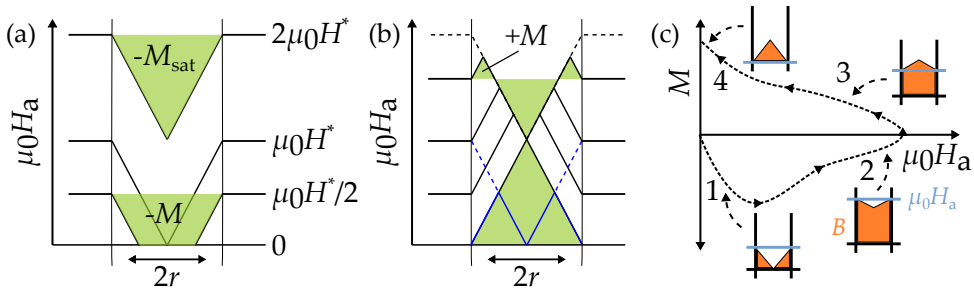

FIGURE 2.5: Bean model to explain remanent magnetisation of type-II superconductors: field distribution above superconducting sample upon (a) increasing and (b) decreasing external field $\mu_0 H_a$. (c) Schematic representation of magnetisation process of real, irreversible type-II SC, with indicated field distributions at certain points in the $M - H$ diagram. Reproduced from [30].

magnetic field is reduced to zero, a magnetisation due to pinning remains within the superconductor. The maximum magnetisation M_{sat} is reached, when the field has initially exceeded $2H^*$.
Figure 2.5(c) shows schematically the magnetisation process of a irreversible superconductor. The trapped field, corresponding to the magnetisation is indicated in orange in the field distribution sketches.
Opposite to the classical magnetisation, where M arises from microscopic currents due to electrons orbiting the atomic nuclei, in a superconductor M is generated by a macroscopic current flowing inside the sample.
The calculation of the J_c for cylindrical specimen is the simplest case. Nevertheless, it can be performed as well for thin film geometries[1]. With the definition relation of the magnetisation M of the full sample in an external magnetic field

$$\mu_0 M = \frac{1}{V} \int B(V) \mathrm{d}V - \mu_0 H \tag{2.7}$$

and Ampère's law with the field $\vec{B}$ in z-direction and the current flowing within the xy-plane

$$\nabla \times \vec{B} = \mu_0 \vec{J}, \tag{2.8}$$

[1] In cuboid shaped samples the actual current density varies with the polar coordinate φ. $J(\varphi)$ varies between $J(\varphi) = J_c$ for $\varphi = 0\,^\circ$ and $J(\varphi) = J_c \cos(45°) \approx 0.7 J_c$ for $\varphi = 45\,^\circ$ along the diagonal.

we can assess the critical current density to

$$J_c = \frac{6M}{d} A_{corr} = \frac{6m}{d^3 t} A_{corr}, \tag{2.9}$$

with d being the side length of the squared sample of thickness t. We have introduced a correction factor A_{corr} accounting for variations in thickness of the sample at the edges and demagnetisation effects. A_{corr} was obtained by calibration with electrical transport measurements.
The Bean model has been extended by several authors (*e.g.* see [31]) to account for the field dependence of the critical current density in real superconductors.

2.2 Reaction chemistry and transport phenomena: general considerations

In many oxides the oxygen content of the material is crucial to physical (e.g. structural, electrical, superconducting) and chemical properties. Understanding the fundamental processes behind the in- and excorporation of oxygen into the material structure is a very important topic in many different branches of physics and materials sciences and of great technological relevance. Many electrochemical devices are based on this process as *e.g.* mixed conducting solid oxide fuel cells (SOFC) cathodes, gas sensing devices, oxygen permeation membranes and memristors based on resistive switching [32, 33]. The central equation of this process, the oxygen reduction reaction (ORR) can be simply written in the Kröger-Vink notation[2] as:

$$\frac{1}{2}O_2 + V_O^{\bullet\bullet} \rightarrow O_O^{\times} + 2h^{\bullet}, \tag{2.10}$$

with the oxygen vacancy $V_O^{\bullet\bullet}$ and the occupied oxygen crystal site $O_O^{\times}$. In contrast to its apparent simplicity, the significance and complexity of the ORR for solid state ionics has started to be understood only in recent years.

The process of oxygen exchange can be divided into several steps and ranges from the adsorption of oxygen molecules on the surface to chemical diffusion into the bulk, which will be discussed in detail below. Stoichiometric changes can be triggered by a change of an external thermodynamic parameter as for example the total pressure P, the oxygen partial pressure $P(O_2)$, the temperature T, or an applied electric field. We will start with an introduction

[2] In the Kröger-Vink notation electric charge is given relative to the specific crystal site, which is indicated by lowered letter. $^{\times}$ indicates neutral charge, $^{\bullet}$ and $'$ correspond to single positively and negatively charged sites.

into basic methods of defect chemistry necessary to describe and understand the ongoing processes, as outlined in [34] and then discuss the specific reactions relevant for the oxygen exchange in YBCO. Very helpful introductions into the field of solid-gas interactions can be found in the standard works of P. Atkins [35], J. Maier [23] and elsewhere [36, 37].

A reversible, heterogeneous reaction can be written as

$$A(x_1) \rightleftharpoons B(x_2), \tag{2.11}$$

describing the conversion from A to B and the simultaneous translation from x_1 to x_2. The reaction affinity is generally given by differences in chemical potentials between A and B, as any system tends to minimise its free energy. The corresponding net reaction rate is defined as the difference between forward and backward reaction rates $\vec{\Re}$ and $\overleftarrow{\Re}$ and we can write the mass action law as:

$$\Re = \vec{\Re} - \overleftarrow{\Re} = \vec{k}[A(x_1)] - \overleftarrow{k}[B(x_2)]. \tag{2.12}$$

Here we have used the definition of the forward/backward reaction rate via the corresponding reaction rate constants $\vec{k}$ and $\overleftarrow{k}$ and reactant and product concentrations $[A]$ and $[B]$. The forward and backward rate constants are thermally activated and can be generally written as:

$$\vec{k}_{\text{in}} = k_0 \exp\left[-\frac{\Delta\vec{G}}{k_{\text{B}}T}\right] \tag{2.13}$$

and

$$\overleftarrow{k}_{\text{out}} = k_0 \exp\left[-\frac{\Delta\overleftarrow{G}}{k_{\text{B}}T}\right], \tag{2.14}$$

where k_0 depends on the oxygen partial pressure and $\vec{G}$ and $\overleftarrow{G}$ are the according energy barriers. In our considerations we neglect any additional driving force coming from non-vanishing internal electric fields.

If our model reaction (2.11) is in equilibrium the net reaction rate $\Re$ vanishes and we can define the equilibrium constant as

$$K_{\text{eq}}(\Re = 0) \equiv \vec{k}/\overleftarrow{k} = \frac{[B]}{[A]}. \tag{2.15}$$

If the modification of a thermodynamic variable (*e.g.* T or $P(\text{O}_2)$) causes only a slight deviation out of equilibrium the reaction rate can be approximated by

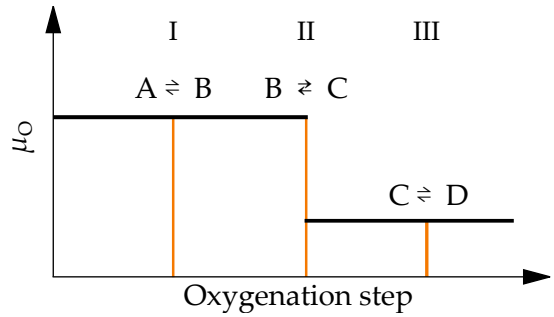

FIGURE 2.6: (a) Schematic representation of a process, where the chemical potential of oxygen μ_O drops only over a single step, thus the rate determining step (step II, RDS) of oxygen exchange. Precedent and subsequent steps (step I & III) are in quasi-equilibrium.

the equilibrium exchange rate $\Re^0$ [38]:

$$\Re^0 = \sqrt{\vec{\Re} \cdot \overleftarrow{\Re}} = \sqrt{\vec{k}\,[\mathrm{A}]_{\mathrm{eq}} \cdot \overleftarrow{k}\,[\mathrm{B}]_{\mathrm{eq}}}. \tag{2.16}$$

A commonly taken assumption is that one single step is limiting the overall exchange rate of oxygen between the ambient and the bulk. This step is generally referred to as the rate determining step (RDS) as schematically shown in Fig. 2.6 for a three step process (I - III), where step II is the RDS. The only significant drop of the chemical potential μ occurs across the RDS, while precedent and subsequent steps are in *quasi*-equilibrium. The first step to enhance the oxygen exchange rate of a material, as desired in many different applications, is the identification of the RDS. In a second step one must find a possible alternative reaction path, as *e.g.* via catalysis.

In the following we contemplate a stoichiometric change initiated by a change in the oxygen atmosphere. We investigate the elementary mechanisms involved in the transformation of the oxygen molecule into a lattice oxygen atom. The discussion will be limited to the exchange of molecules and atoms between the solid and the gas phase and inner-bulk diffusion. The formation and motion of interfaces and structural changes, other than of stoichiometric nature, will be neglected for simplicity. These aspects will be discussed at a later stage in this thesis (Chapter 5).

The presented order follows the reaction scheme outlined in [36], modified for the case that all charges are provided by the formation of holes. The order of the relevant reaction steps might be altered and steps might be combined or further divided [39]. However, in the framework of the performed

	Reaction mechanism		Rate equation
Step 0	$O_2(x_1) \rightleftharpoons O_2(x_2)$	Atmosphere change	
Step 1	$O_2 \rightleftharpoons O_2^- + h^\bullet$	Physi- and chemisorption*	(2.17a)
Step 2	$O_2^- \rightleftharpoons O_2^{2-} + h^\bullet$	Ionisation*	(2.17b)
Step 3	$O_2^{2-} \rightleftharpoons 2O^-$	Dissociation*	(2.17c)
Step 4	$O^-(x_1) \rightleftharpoons O^-(x_2)$	Surface diffusion	(2.17d)
Step 5	$2O^- + 2V_O^{\bullet\bullet} \rightleftharpoons 2O_O^\times + 2h^\bullet$	Incorporation	(2.17e)
Step 6	$O_O^\times(x_1) \rightleftharpoons O_O^\times(x_2)$	Bulk diffusion	(2.17f)

TABLE 2.1: Relevant transport and reaction mechanisms of the process of oxygen incorporation into YBCO. All charges for the oxidation of oxygen are provided by the formation of holes. Steps marked with * are expected to be enhanced upon coating with a catalyst.

analysis we will stick to this structure. Furthermore, YBCO exhibits rather high changes in stoichiometry as a function of the oxygen partial pressure compared to other oxides as for example $SrTiO_{3-x}$. Therefore, defect-defect interactions must be taken into account, while the framework of ideal defect chemistry only treats randomly distributed, non-interacting elementary defects [40]. A coupling of ionised oxygen with neighbouring copper ions is expected. The majority of doped holes are localised in the CuO-chains, while only a fraction is available as free charges in the CuO-planes [40].

All relevant transport and reaction mechanisms are enlisted in Table 2.1 and schematically drawn in Fig. 2.7. **Step 0** describes the change in oxygen partial pressure above the sample. This step depends on the experimental setup (chamber geometry and total gas flow) and can technically be assured to be comparatively fast. In **Step 1** physical and chemical adsorption of oxygen molecules onto the free surface of the specimen are combined. Adsorption mechanisms will be discussed in section 2.2.1, followed by an analysis of the surface coverage Θ in section 2.2.2. **Step 2** is the ionisation of the oxygen molecule by the formation of a hole in the YBCO surface layer, which is followed by **Step 3**, which is the dissociation of O_2^{2-} into charged oxygen ions. The diffusion of oxygen at the surface of the specimen to find an oxygen vacancy is described in **Step 4**. **Step 5** is the recombination of an O ion with a vacancy of the surface layer, accompanied with a charge transfer to reach the bulk oxidation state of $O^{2-} = O_O^\times$. The last step (**step 6**) is the chemical diffusion of oxygen in the bulk, along and across interfaces (*e.g.* grain boundaries)

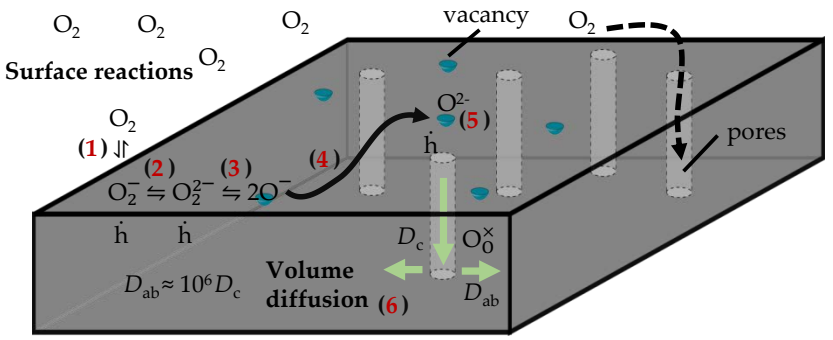

FIGURE 2.7: Schematic representation of the oxygen exchange process in YBCO thin films including surface reactions and bulk diffusion. The relevant steps are (1) chemisorption, (2) ionisation, (3) dissociation (4) surface diffusion, (5) incorporation and (6) bulk diffusion.

as outlined in detail in section 2.2.3. Electrical neutrality within the material is guaranteed by simultaneous diffusion of electrical and ionic defects, as electrons, holes and oxygen vacancies.
The reaction and transport steps 1-5 are mechanisms related to the surface, while step 6 is of purely bulk nature. The steps 1-3, marked with *, might be enhanced by a catalyst [41, 42].

We can write the reaction rate $\Re_i(T)$ for each step ($i = 1, ..., 6$) with the corresponding temperature dependent defect concentrations (in squared brackets) and reaction rate constants $\vec{k}_i(T)$, $\overleftarrow{k}_i(T)$. In the case of YBCO we need to consider oxygen, oxygen vacancy and electron hole concentrations, as they all considerably change with oxygen partial pressure. In the following we will omit the explicit temperature dependence of all quantities. If we assume that the particular step i is the RDS, preceding and succeeding steps are in equilibrium and can be expressed via their equilibrium constants $K_{j\neq i}$ via Eq. (2.15). This assumptions yield the equations 2.17(a-f) for each of the steps being considered the RDS. Additionally we have calculated the pressure dependence of the corresponding equilibrium reaction rate $\Re_i^0$ using Eq. (2.16), as discussed below.

$$\Re_1 = P(O_2)\vec{k}_1 - \frac{1}{K_2K_3K_5}\frac{[O_O^\times]^2[h^\bullet]^4}{[V_O^{\bullet\bullet}]^2}\overleftarrow{k}_1 \tag{2.17a}$$
$$\Re_1^0 \propto P(O_2)^{(1+4n_h+2n_O-2n_V)/2}$$

$$\Re_2 = \frac{K_1}{[h^\bullet]}P(O_2)\vec{k}_2 - \frac{1}{K_3K_5}\frac{[O_O^\times]^2[h^\bullet]^3}{[V_O^{\bullet\bullet}]^2}\overleftarrow{k}_2 \tag{2.17b}$$
$$\Re_2^0 \propto P(O_2)^{(1+2n_h+2n_O-2n_V)/2}$$

$$\Re_3 = \frac{K_1K_2}{[h^\bullet]^2}P(O_2)\vec{k}_3 - \frac{1}{K_5}\frac{[O_O^\times]^2[h^\bullet]^2}{[V_O^{\bullet\bullet}]^2}\overleftarrow{k}_3 \tag{2.17c}$$
$$\Re_3^0 \propto P(O_2)^{(1+2n_O-2n_V)/2}$$

$$\begin{aligned}\Re_4 &= k_4\left([O^-](x_1) - [O^-](x_2)\right)\\ &= k_4\left(\sqrt{\frac{K_1K_2K_3}{[h^\bullet]^2}}(x)\sqrt{P(O_2)} - \frac{[O_O^\times][h^\bullet]}{\sqrt{K_5}[V_O^{\bullet\bullet}]}(x')\right)\end{aligned} \tag{2.17d}$$
$$\Re_4^0 \propto P(O_2)^{(0.5+n_O-n_V)/2}$$

$$\Re_5 = \sqrt{\frac{K_1K_2K_3}{[h^\bullet]^2}}\sqrt{P(O_2)}[V_O^{\bullet\bullet}]\vec{k}_5 - [O_O^\times][h^\bullet]\overleftarrow{k}_5 \tag{2.17e}$$
$$\Re_5^0 \propto P(O_2)^{(0.5+n_V+n_O)/2}$$

$$\Re_6 = k_6\left([O_O^{x1}](x) - [O_O^{x2}](x')\right) \tag{2.17f}$$
$$\Re_6^0 \propto P(O_2)^{(0.5-2n_h+n_V+n_O)/2}$$

For surface diffusion and bulk diffusion processes, activation energy barriers $\vec{G}$ and $\overleftarrow{G}$ are the same (see Eq. (2.13) and (2.14)) and therefore reaction rate constants are equal for forward and backward reaction. Thus, the equilibrium constants become $K_i = 1$ for $i = 4, 6$. Note, that the implicit dependence of $\Re_i$ on the oxygen partial pressure of step 1-5 will enable the analysis of the RDS in section 4.4.

The $P(O_2)$ dependences of the equilibrium reaction rates $\Re_i^0$ are given as a function of the individual defect pressure dependences, where the $P(O_2)$ dependences for YBCO bulk defects are given by: $[O_O^\times] \propto P(O_2)^{n_O}$, $[h^\bullet] \propto P(O_2)^{n_h}$ and $[V_O^{\bullet\bullet}] \propto P(O_2)^{n_V}$ for lattice oxygen, electron hole and oxygen vacancy concentrations. While it is reported that the pressure dependencies of the defect concentrations decrease from $1/2$ at very low oxygen partial pressures to below $1/4$ when approaching 1 bar [43], the different exponents are assumed to be linked via $n_h = n_O = -n_V$ [44, 45].

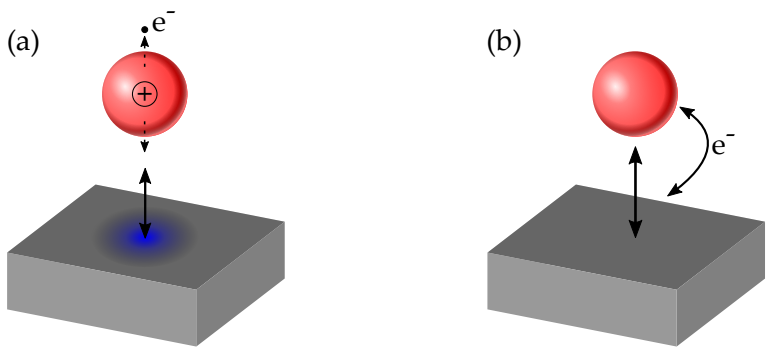

FIGURE 2.8: Schematic draft of two types of surface interaction: (a) physisorption: interaction due to polarization of the molecule and induced image charges on the surface and (b) chemisorption: chemical bondings via charge transfer

2.2.1 Adsorption onto the surface

Two main mechanism of adsorption can be distinguished by their effect on the electronic structure of the gas molecules (see Fig.2.8):

- **Physical adsorption (physisorption):**
  the adsorbate is bonded to the surface via an attractive but weak Van der Waals force ($E_{\text{phys}} = 0.2\,\text{eV/molecule}$). The dipole-dipole interaction is caused by a transient shift of the electron densities of the molecule and the formation of image charges on the surface due to the polarization. In a simple model it can be described with a valence electron e^- hopping in one dimension, normal to the surface, around a positive ion [46]. There is no charge transfer between the adsorbent and the adsorbate.

- **Chemical adsorption (chemisorption):**
  charge transfer and/or new formed hybrid orbitals between the surface and a molecule create strong chemical bonds. Its concept is comparable to covalent or ionic bonding of molecules. The involved enthalpies are usually higher than in the case of physisorption (E_{chem} = several eV/molecule) and equilibrium separations are shorter. The rearrangement of e^--shells can lead to dissociation, which requires two empty nearest-neighbour sites at the surface.

The interaction of a molecule with the solid surface with distance r can be approximated using the Lennard-Jones potential. The Lennard-Jones potential is the superposition of a fast decaying repulsive r^{-12} term (Pauli repulsion) due to the overlap of electron orbitals and a long range attractive van

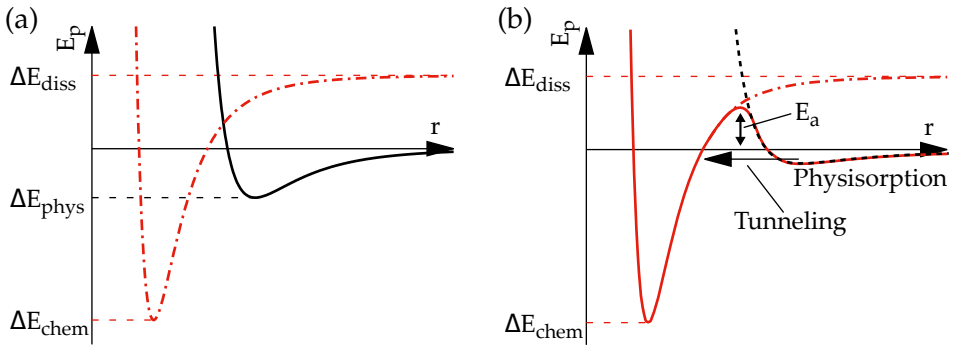

FIGURE 2.9: Potential energy as a function of the distance between the surface and a gas molecule modelled by a Lennard-Jones potential (a) red dashed line for the case of chemisorption, black solid line for physisorption (b) Red solid line shows the case where physisorption (black dashed) is a precursor state for chemisorption (red dashed)

der Waals force proportional to r^{-6}:

$$V(r) = 4\epsilon \left\{ \left(\frac{r_0}{r}\right)^{12} - \left(\frac{r_0}{r}\right)^{6} \right\}, \tag{2.18}$$

with the potential depth ϵ and a characteristic length r_0, which is correlated to the position of the minimum of the potential via $r_{\min} = 2^{1/6} r_0$. Figure 2.9(a) shows typical potential shapes for physisorption (black line) and chemisorption (red, dashed line). In case of dissociative chemisorption the molecule is dissociated into its constituents. The potential is therefore shifted to approach the dissociation enthalpy E_{diss} at large distances. The physisorbed state often serves as a precursor state to a stronger bonded, potentially dissociative chemical adsorbed state (Fig. 2.9(b)). The potential energy barrier E_a between those two states can be referred to the initial increase of the bonding length of the impinging gas molecule before it gets fragmented into its constituents. Depending on the sign of E_a one can distinguish between activated $E_a > 0$ and non-activated $E_a < 0$ chemisorption.

2.2.2 Surface coverage

The surface coverage Θ is defined as the fraction of occupied sites with respect to the total number of adsorption sites available, assuming a complete monolayer. The rate of change of Θ can be expressed with two terms, one related to adsorption and the other to desorption. The surface coverage increases due

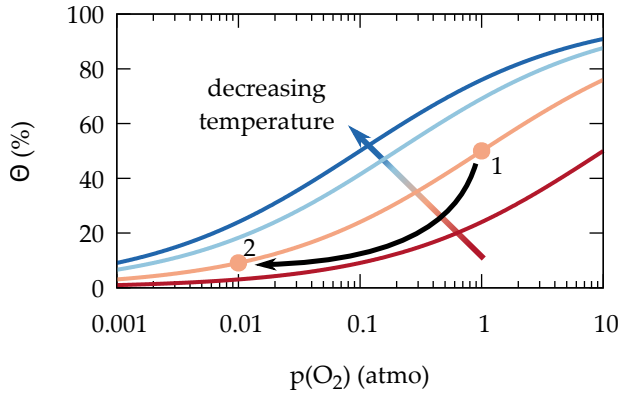

FIGURE 2.10: Langmuirs isotherm surface coverage θ as a function of oxygen partial pressure at different temperatures.

to adsorption with the rate constant $\vec{k}(T)_{\text{ads}}$, proportional to the number of vacant sites and the partial pressure $P(O_2)$. On the other hand desorption decreases the number of occupied sites proportional to the number of adsorbed species and the desorption rate constant $\overleftarrow{k}(T)_{\text{des}}$. The total change reads

$$\frac{d\Theta(T)}{dt} = \vec{k}(T)_{\text{ads}} P(O_2) \Big[1 - \Theta(T)\Big]^x - \overleftarrow{k}(T)_{\text{des}} \Big[\Theta(T)\Big]^x. \tag{2.19}$$

In the case of an exchange process involving single atoms, x in Equation (2.19) is equal unity. For dissociative adsorption of a diatomic molecule the probability for both atoms to find a vacant site is proportional to $[1-\Theta]^2$, thus $x = 2$. Any variation of the net coverage due to chemical oxygen in- and excorporation and resulting stoichiometric changes in the crystal are neglected in this simple model.

For a dynamic equilibrium situation with no net exchange the rate Equation (2.19) transforms to Langmuir isotherms

$$\Theta = \frac{(KP(O_2))^{1/x}}{1 + (KP(O_2))^{1/x}} \tag{2.20}$$

with the equilibrium constant $K = \vec{k}_{\text{ads}}/\overleftarrow{k}_{\text{des}}$. This simple model assumes a constant adsorption energy, independent of the surface coverage. More sophisticated approaches, as the Freundlich and Horikoshi-Temkin isotherms take into account a non-constant binding energy dependence on the coverage [47–49].

Figure 2.10 shows the Langmuir isotherms for different temperatures. The fractional surface coverage Θ increases with decreasing temperature. After a change of partial pressure, e.g. from high to low $P(O_2)$ as indicated with the black arrow, a new equilibrium coverage has to be established. This process is limited by the adsorption and desorption rate constants and might be the RDS.

So far electrostatic effects have not been considered. The $P(O_2)$ dependence of the oxygen surface coverage of charged adsorbates has been profoundly studied by Fleig, Merkle, and Maier [50]. Negative ad-ions cause a positive polarisation within the surface layer leading to a surface potential step χ. This potential step depends on the different ionic surface species, which are present on the oxide surface, as O^-_{ad}, superoxide $O^-_{2,ad}$ and peroxide $O^{2-}_{2,ad}$. The final surface coverage can be calculated if a predominant specie is assumed. If the majority specie is O^-_{ad} and the materials hole concentration is $P(O_2)$ dependent, the surface coverage reads [50]

$$\Theta = K_{O^2_{ad}} \frac{\sqrt{P}}{a_h} \exp\left(-\frac{e\chi_{max}\Theta}{k_B T}\right) \tag{2.21}$$

with the equilibrium constant $K_{O^2_{ad}} = \exp\left[\left(\mu^0_{O_2}/2 - \mu^0_{O^-_{ad}} - \mu^0_h\right)/k_B T\right]$, χ_{max} as the surface potential step at maximum coverage ($\Theta = 1$), and an additional parameter a_h considering changes in the hole concentration and formation of ionic point defects, e.g. oxygen vacancies. Further complication might arise due to the influence of surface step and grain boundary densities on the surface coverage [51, 52].

2.2.3 Bulk diffusion

Bulk diffusion (or generally speaking any diffusion mechanism) is the process of balancing differences in concentrations leading to a homogeneous distribution of matter due to thermal movement of atoms. This process is of purely statistical nature. Differences in concentration c over time and space are linked by Fick's second law, the diffusion equation

$$\frac{\partial c}{\partial t} = \nabla\left(D_{chem}\nabla c\right). \tag{2.22}$$

The empirical diffusion coefficient D_{chem} is directly linked to the mean square displacement of atoms due to Brownian motion [53].

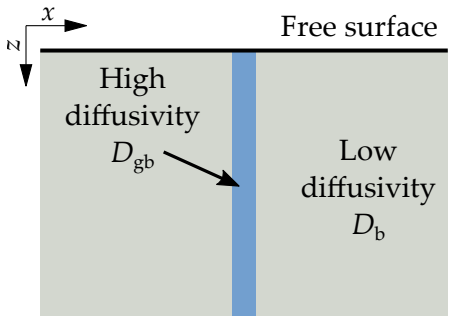

FIGURE 2.11: Fisher model of chemical diffusion in a material with regions of different diffusivity, as *e.g.* grain boundaries.

One distinguishes between different diffusion mechanism, depending on the number and type of particles and crystal sites participating in the process. Most relevant are direct and indirect interstitial and vacancy diffusion mechanism [54]. In the first case an interstitial atom jumps from its position to the closest interstitial site. This process causes only a small and temporary displacement of nearby lattice atoms, making it energetically favourable. It is quasi independent of the crystals defect concentration. The indirect interstitial (interstitialcy) mechanism is based on the replacement of a lattice atom, which becomes the new interstitial. The vacancy mechanism is based on vacant crystal sites diffusing through the crystal by neighbouring atoms jumping into the vacancy.

Grain boundaries are well known regions of high diffusivity and provide fast exchange paths [54]. The Fisher model provides a mathematical description of grain boundary diffusion by considering areas with different chemical diffusion coefficients D_{chem} [55]. This is schematically shown for a single GB in Fig. 2.11, with high grain boundary diffusivity compared to bulk diffusion $D_{\text{gb}} \gg D_{\text{b}}$. Atoms diffuse along grain boundaries in z and leak into the bulk along the x and y direction, enhancing the overall diffusion process [56]. The same approach will be used in section 4.3 to analyse the influence of percolation currents on conductivity relaxation measurements. Additionally grain boundaries were found to have significant influence on the surface exchange rates, providing areas with higher surface exchange coefficients [52, 57].

Theoretical model for the analysis of electrical relaxation measurements

Changes in the oxygen stoichiometry of YBCO are triggered by changing the oxygen partial pressure and therefore the standard chemical potential of oxygen on top of the surface. This will lead to a gradient of the chemical potential within the sample its surface and the YBCO bulk. As the electrical conductivity σ is sensitive to the oxygen content, the relaxation process causes changes in σ, which are experimentally accessible. The transients of the electrical conductivity can be modelled by Fick's second law (Eq. (2.22)).
For a first order chemical reaction one can always write for the rate of change [58, 59]:

$$\Re = \frac{\mathrm{d}c}{\mathrm{d}t} \equiv \frac{\mathrm{d}\partial c}{\mathrm{d}t} = -k\partial c. \tag{2.23}$$

The affinity for this reaction is a deviation from the thermodynamic equilibrium concentration $\partial c = c_\infty - c$, as the process is limited by the chemical reaction rate constant k. This chemical reaction is the source of particles for the diffusion process at the solid-gas interface. Using Fick's first law for the diffusion flux J, we can write the Neumann boundary condition to solve the diffusion equation (2.22) in one dimension as:

$$J = -D_{\mathrm{chem}} \frac{\mathrm{d}c}{\mathrm{d}x}\bigg|_{x=l} = k_{\mathrm{chem}}\partial c, \tag{2.24}$$

with the bulk diffusion coefficient D_{chem}, the film thickness l and the chemical surface exchange constant k_{chem}. The concentration c is a function of time t and position x: $c = c(x,t)$. For simplicity we use $c = [\mathrm{O}_\mathrm{O}^\times]$ for the oxygen concentration in the following. We assume no oxygen exchange at the film-substrate interface and therefore:

$$J = -D_{\mathrm{chem}} \frac{\mathrm{d}c}{\mathrm{d}x}\bigg|_{x=0} = 0, \tag{2.25}$$

which is equivalent to the case of a thin film with a thickness of $2l$ and the same physical boundary conditions at $x = l$ and $x = -l$ [60]. With the boundary conditions (2.24) and (2.25) and an initial homogeneous oxygen concentration c_0, we can solve the diffusion equation (2.22) by the standard technique of Laplace transformation. The exact analytical solution is given by (see p. 60ff in [61]):

$$c(x,t) = c_\infty - (c_0 - c_\infty) \sum_{n=1}^{\infty} \frac{2\delta \cos(\beta_n x/l)}{(\beta_n^2 + \delta^2 + \delta)\cos\beta_n} \mathrm{e}^{-\beta_n^2 Dt/l^2}, \tag{2.26}$$

with β_n being the n'th positive root of the transcendental equation [62]

$$\beta \tan \beta = \delta. \tag{2.27}$$

and

$$\delta = \frac{l k_{\text{chem}}}{D_{\text{chem}}}. \tag{2.28}$$

As electrical measurements do not provide spatial resolution we are only interested in the average oxygen concentration as a function of time, which we obtain by integrating Eq. (2.26) over the film thickness. The averaged time dependent solution reads:

$$\bar{c}(t) = \frac{1}{l}\int_0^l c(x,t)\mathrm{d}x = c_\infty - (c_0 - c_\infty)\sum_{n=1}^{\infty} \frac{2\delta \tan \beta_n}{\beta_n\left(\beta_n^2 + \delta^2 + \delta\right)} \mathrm{e}^{-\beta_n^2 D t / l^2}. \tag{2.29}$$

As $\delta \gg 1$ for a bulk diffusion controlled process and $\delta \ll 1$ for surface limited reactions, the main contribution to the sum in Eq. (2.29) comes from the first term [61]. Using the 1$^{\text{st}}$ degree Taylor expansion of the tangent in Eq. (2.27) and Eq. (2.29) $(\tan x \approx x)$ and $\left(\beta_n^2 + \delta^2 + \delta\right) \approx 2\delta$, the solution of the diffusion equation can be approximated by:

$$\frac{c(t) - c_\infty}{c_0 - c_\infty} \simeq \mathrm{e}^{-t/\tau}, \tag{2.30}$$

with a single saturation time $\tau = l/k_{\text{chem}}$ for surface controlled processes. The same result is obtained for diffusion limited processes with $\tau = l^2/(2\pi^2 D_{\text{chem}})$, where the exponential has a pre-factor of $(8/\pi^2)$ [63]. If changes in $P(\mathrm{O_2})$ are not too large, we can assume a linear relationship between the transients of the oxygen content and the film conductivity [43, 64]:

$$\frac{\sigma - \sigma_\infty}{\sigma_0 - \sigma_\infty} = \mathrm{e}^{-t/\tau}. \tag{2.31}$$

In the case of two parallel diffusion/reaction channels, one generally assumes a second relaxation process with a different relaxation time (see Eq. (4.1)).

Chapter 3

Experimental Methodologies

In this chapter a brief description of all experimental techniques used in this work will be given. The sample growth and preparation techniques are introduced in the sections 3.1 - 3.2. Samples are intensively studied using SQUID magnetometry, electrical measurements and X-ray diffraction techniques as described in 3.3, 3.4 and 3.5, respectively. The chapter is closed with the discussion of the home built *in situ* set-up for high temperature ECR measurements in section 3.6.

3.1 Deposition techniques of YBCO thin films

Physical properties of YBCO, as zero resistance up to strong magnetic fields, makes this material highly interesting for many different fields of applications. It has been shown that the angle between grain boundaries has major influence on macroscopic critical current densities. The supercurrents decrease exponentially with the grain boundary angle [65], due to charge localisation and suppressed d-wave pairing [24]. Therefore highly textured YBCO must be achieved. Several different physical and chemical deposition techniques have been developed and adapted for the growth of epitaxial superconducting films on single crystal and coated metallic substrates.

Commonly used techniques comprise pulsed laser deposition (PLD), sputter deposition, molecular beam epitaxy, thermal co-evaporation (all physical vapour deposition techniques), and chemical routes as chemical vapour deposition, liquid phase epitaxy and chemical solution deposition (CSD). The recently developed CSD transient liquid assisted growth (TLAG) method is another highly promising candidate for future superconducting tape production.

In the following two sections the PLD and CSD techniques will be discussed, as used in this work to obtain highly textured, epitaxial thin YBCO films. Films with good physical properties, as a critical temperature of around

90 K and high critical current densities (above 2 MA/cm^2 at 77 K) are achieved with both methods.

3.1.1 Sample growth via CSD trifluoroacetates route

Major benefit of this chemical route is its capability of depositing films at atmospheric pressure, making it a very cost effective method compared to expensive vacuum-based technologies. High performance and scalability have been shown [], making it an appealing alternative to already available commercial tape production lines.

The frontier of knowledge on CSD based on the use of trifluoroacetate solution and metal organic precursors has been pushed for many years by this research group. The description given here will closely follow the review of Obradors et al. [66].

MO-solution, deposition and pyrolysis

Starting point of any CSD route is a stable solution containing the stoichiometric amount of required metals for the final film. The precursor solution is based on trifluoroacetate salts dissolved in an alcoholic solvent as ethanol or methanol. A high purity solution is a requirement for good superconducting properties of the resulting layer.

The solution is deposited on a single crystal substrate by spin coating. The thickness and metallic concentration of the deposited layer determines the final film thickness. Another technique used in the group is the recently developed Ink-jet printing methodology which has certain improvements as high reproducibility, increased maximal thicknesses and reduction of solution waste.

The substrate is required to have a small in-plane lattice mismatch with the YBCO structure to allow defect-free, c-axis oriented growth. Films are grown on (100)-oriented $SrTiO_3$ and (100)-oriented $LaAlO_3$ squared single crystal substrates with a side length of 5 mm. Before the deposition substrates are annealed to 900 °C in an oxygen flow of 0.5 l/min to remove carbon-containing impurities and form terraces with the height of single unit cells. These terraces facilitate the nucleation of YBCO seeds in the next step of the synthesis.

The toxic component of fluorine is necessary to avoid the formation of $BaCO_3$, which decomposes only at very high temperatures. Instead the intermediate solid precursor BaF_2 is formed. There is ongoing research on reducing or eliminating the amount of fluorine necessary to synthesize YBCO to lower detrimental environmental effects.

Organic constituents are burned during the pyrolysis step at relatively low temperatures around 310 °C. A clear understanding of the ongoing decomposition processes is necessary to avoid negative strain releases, like buckling and cracking due to strong shrinkage and mass loss during pyrolysis. The optimization of parameters, as the heating ramps, firing temperature, oxygen and water pressure allows to grow homogeneous and epitaxial films.

Residual porosity is caused by fast gas escape during the decomposition stage. The mechanically unstable structure facilitates the formation of pores. These pores are thought to be highly important as diffusion path for oxygen during oxygen.

Nucleation and growth

At high temperatures the YBCO is nucleated and grown. During a fast heating ramp (25 °C/min) to 810 °C different intermediate phases are formed, limited by their formation kinetics. The $Ba_{1-x}Y_xF_{2+x}$ phase decreases its Y content from $x \approx 0.35$ after the pyrolysis to 0 at growth temperature and immediately Y_2O_3 is formed. The following reaction was identified to be the primary path for YBCO to be formed:

$$3CuO + 2Ba(O_xF_y)_2 + \frac{1}{2}Y_2O_3 + 2yH_2O \longrightarrow YBa_2Cu_3O_{7-\delta} + 4yHF \qquad (3.1)$$

The nucleation starts with many individual single seeds, which grow and coalesce to a continuous layer. YBCO can nucleate in different crystalline orientations, such as [001], [100] and [103], which have similar nucleation enthalpies. Obvious difficulties arise if heteroepitaxial YBCO layers are demanded. Therefore many process parameter have to be precisely controlled to achieve highly *c*-axis oriented films. The growth and nucleation rates depend among others on the temperature, oxygen partial pressure and water pressure. It has been shown that increased growth rates of TFA assisted growth decrease final film properties.

Thin layers grown within this there were typically 200 - 250 nm thick, highly *c*-axis oriented and exhibited current densities of 2 - 6 MA/cm^2.

Oxygenation

The oxygenation of YBCO is a complex process. Many steps are involved in the incorporation of oxygen into the structure to obtain good superconducting properties as explained in section 2.2. Here the standard oxygen process is described as used for many years within the group. After the growth the sample is slowly cooled to the dwell temperature for the oxygenation, typically 450

or 550 °C. When the temperature falls below 600 °C the oxygen partial pressure is increased to 1 bar. After a dwell of 210 min the sample is cooled with 10 °C/min to room temperature in an oxygen flow of 0.12 l/min.

3.1.2 Sample growth via pulsed laser deposition

The process of pulsed laser deposition is a physical vapour technique working in a low pressure environment. PLD can be used to grow epitaxial thick films of high quality. Its broad flexibility makes it a highly interesting fabrication method. An overview of this and other deposition techniques can be found in [67].

A high energy pulsed laser beam locally heats a target of the desired material. The short wavelength of the laser limits the interaction of the photons to free electrons of the target. These excited electrons subsequently interact with phonons leading to a sudden increase of temperature and an explosive removal of atoms from the surface layers. This material evaporate into a plasma plume, formed of neutral and charged particles. These particles are subsequently deposited on a substrate, which is mounted on a heater parallel to the material target. Using this technique monolayers, thick films and complex multilayer systems can be produced. High fabrication and maintenance costs for the laser and vacuum system are the main drawback of this deposition method.

The targets used were produced by *Oxolutio SL* and consist of pressed and sintered, stoichiometric YBCO powder.

Stable YBCO can only be formed in a certain region of the oxygen partial pressure $P(O_2)$- temperature phase diagram. The working pressure of the PLD technique is usually in the order of 10^{-1} mbar. To provide fast diffusion of the deposited adatoms on the substrate, the temperature of the heater is set close to the YBCO stability line on the high temperature side of the phase diagram. The process parameters strongly determine essential steps as the nucleation, phase formation and film growth. The parameters used for the deposition of YBCO films on single crystal substrates are shown in Table 3.1. The final thickness of the film is determined by the number of laser pulses during growth (under the conditions used: 26 pulses $\triangleq$ 1 nm). After the deposition the film was cooled immediately by switching off the heater. In the standard process oxygen flux is turned on below 600 °C and the pressure is raised to 1 bar to reach high T_c and J_c values.

T (°C)	800
$P(O_2)$ (mbar)	0.3
f (Hz)	5
Fluence (mJ)	97

TABLE 3.1: Parameter used for the growth of YBCO films using the Pulsed Laser Deposition method

3.2 Sample preparation techniques

Samples have been prepared for several types of measurements using photolithography and sputtering processes. A brief introduction will be given in the following.

3.2.1 Photolithography

A photolithography process allows the precise patterning of thin layers into desired geometries or to deposit additional surface cover layers in certain structures. Therefore a thin layer ($\approx 1\,\mu$m) of positive photo-resist is deposited by spin coating onto the clean sample surface. To dry out the resin and remove organic content in the resist the film is baked for one minute at 100 °C. A digital prepared mask is transferred to the sample using a Micro-Writer from *Durham Magneto Optics LTD* located in the clean room facility of ICMAB. The pattern is written with a UV laser with spot widths of 0.6, 1 and 5 μm. The exposed sample is chemically developed for one minute. In this step the photo-resist is removed from the irradiated areas, while in the other areas the photo-resist still covers and protects the underneath YBCO. The sample is now readily prepared for further steps as silver deposition or etching.

Etching the YBCO layer, e.g. into tracks for transport measurements (see section 3.4.3), is done in diluted phosphoric acid (1:100 H_3PO_4) for several seconds. The reaction is stopped with distilled water and immediately after the sample is dried with nitrogen gas. At the end the remaining resist is removed by immersing the sample into acetone in an ultrasonic bath for some seconds.

3.2.2 Sputter deposition

Sputtering is a process of thin film deposition via ion bombardment on a target material. Emitted atoms are subsequently deposited on the sample/substrate. Many different classes of materials as simple metals, alloys and complex materials can be deposited via sputtering.

	Ag	Pt
p (mbar)	0.1	0.02
U (V)	350	400
I (A)	$\sim$0.1	0.02

TABLE 3.2: Parameters for argon pressure and voltage as used during sputter deposition and typical current values

An electron beam ionises an inert gas producing highly energetic particles. These ions are accelerated towards the target. They bomb the surface and transfer their momentum and energy to the atoms within the first layers. A cascade of collisions is set off. Atoms near the surface with an energy greater than the binding energy get emitted into the half sphere above the target. Since sputtering is due to momentum transfer and atoms are not extracted out of the target by thermal evaporation, also materials with high melting point can be deposited. Momentum transfer can be optimized to increase the sputter yield by choosing a sputtering gas with an atomic weight similar to the target material.

In this work an argon DC sputtering system from *TSST* is used to deposit silver and platinum layers of thicknesses between 20 and 100 nm on top of YBCO samples. Standard parameters of Ag- and Pt-deposition are shown in Table 3.2.

3.3 SQUID magnetometry

Sample properties as the critical temperature T_c and critical current $J_c(T, \mu_0 H)$ can be assessed using magnetometry. The evaluation of the measured magnetization is based upon the Bean critical state model introduced in section 2.1.4 in the previous chapter. All magnetic measurements have been conducted in a *Quantum Design MPMS XL-7 SQUID* magnetometer equipped with a superconducting solenoid magnet with a maximum field of 7 T and 0.01 % of field non-uniformity. The operational temperature lies between 1.9 and 400 K. Magnetization measurements are in general fast and non-destructive measurements with low consumption of liquid helium. The broad range of possible measurement temperatures and magnetic fields is an additional advantage over transport measurements, which are limited due to very high critical current densities at low temperatures and low fields.

The set-up consists of a second order gradiometer with three pick-up coils along the axial direction of the magnet. The samples are mounted perpendicular to the applied magnetic field. All measurements are performed using

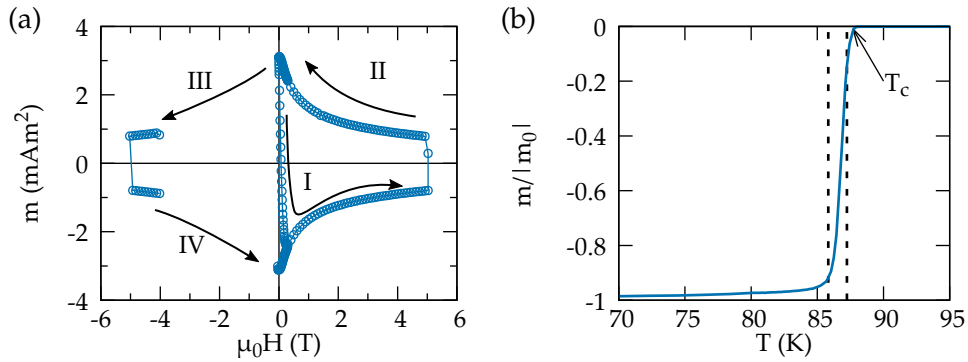

FIGURE 3.1: Magnetisation measurements using a SQUID magnetometer: (a) magnetisation measurement at 5 K, a 4-quadrant loop is performed to fully magnetize the sample as indicated with the black arrow lines. (b) the sample in Meissner state is warmed up in an applied field of 0.2 mT, all magnetic field is expelled out of its interior; the black lines indicate the transition width and $T_{c,onset}$ is labelled

the *Reciprocating Sample Option* (RSO). In this option the sample is periodically displaced in vertical direction (with a small amplitude of typically 3-10 mm) within the gradiometer. This movement is detected as an oscillating AC-signal in the SQUID sensor. The frequency of the sample movement was set to 4 Hz and each measurement point consists of 25 cycles. The current generated in the pick-up coils varies linearly with small variations in the position. The magnetic moment is automatically computed by the SQUID software via a linear fit through all repeated cycles.

Compared to direct current SQUID magnetometry the reciprocating sample technique has increased sensitivity, due to less influence of field inhomogeneities and thus caused reversals of the magnetization close to the surface and less relaxation of the trapped magnetization profile due to shorter measurement times.

3.3.1 $J_c(\mu_0 H, T)$ measurement

To calculate critical current densities using the Bean model [28, 29] one needs to measure the irreversible magnetic moment m_{irr} of the saturated $m - H$ hysteresis loop. Saturation is reached by sweeping the magnetic field through all four quadrants as shown in Fig. 3.1 (a) for a standard $m(H)$ measurement. Starting at zero applied field, the field is increased to +5 T and subsequently reversed to -5 T following the numbers I - III in the Figure. For full saturation

also at small positive fields the $\mu_0 H$ is increased from -5 T to +0.3 T (IV). For $\mu_0 H > 0$ the irreversibility moment can be calculated using

$$m_{irr}(\mu_0 H) = \frac{1}{2}\left(m_{dec}(\mu_0 H) - m_{inc}(\mu_0 H)\right), \tag{3.2}$$

with the magnetic moments measured with decreasing and increasing applied magnetic field.

To measure the temperature dependence of the total magnetisation, the sample is fully magnetised at 5 K with a loop to +3 and -3 T and then slowly warmed up at zero field. In this case m_{irr} is assessed only from the branch of increasing magnetic field (at 0 T).

The critical current densities as a function of temperature and applied magnetic field $J_c(T)$ and $J_c(\mu_0 H)$ can be calculated using the equations given in section 2.1.4.

3.3.2 T_c measurement

To measure the critical temperature the sample is zero field cooled. At the starting temperature (usually 10 or 50 K) a small magnetic field of 0.2 mT is applied. The sample is now in the Meissner state and fully expels the external magnetic field from its interior. The sample is continuously warned up with 0.5 K/min while the magnetisation is being measured. Above T_c the diamagnetic signal of the sample vanishes as shown in Figure 3.1 (b). T_c is defined as the temperature where the measured signal drops below $1e^{-7}$ Am^2. The transition width ΔT is defined by 10 and 90 % of the magnetisation m_0 extrapolated to 0 K, as it is indicated with dashed vertical bars in Fig. 3.1.

3.4 Low temperature electrical measurements

Electrical measurements at low temperatures have been performed using a *Physical Properties Measurement System* (PPMS). The sample is fixed on a sample holder using adhesive copper tape to ensure good thermal contact. Electrical contacts are made with a conductive silver paint from *RS components* and Ag wires onto the sample surface. To improve the electrical contact four small silver contacts of $400 \times 400\ \mu$m^2 with a thickness of 100 nm have been deposited by argon sputter deposition at the corners of the surface. After placing the sample inside the sample chamber, the system is purged and pumped to low pressures to avoid any damage on the system and the sample. The system is cooled using liquid helium and allows measurements in a temperature

range from 2 to 400 K. A superconducting magnet enclosing the sample chamber can operate at fields up ± 9 T.

Electrical measurements allow to obtain key physical parameters of a superconducting material as the transition temperature Tc, the resistivity $\rho(T)$, the charge carrier density $n\mathrm{H}(T)$ and the charge mobility $\mu(T)$, giving insight into the physical properties of the superconducting state. Measurements are carried out with an applied current of 100 µA in AC mode, which means that the direction of current is inverted once per measurement.

3.4.1 Van der Pauw measurements

Van der Pauw has shown that the resistivity of a sufficiently two dimensional, simply connected sample can be measured by attaching four contacts on the edge of the specimen [68, 69]. While this technique is valid for any arbitrary shape without holes, the case of a squared sample will be discussed, as used in this work. The resistance $R_{\mathrm{AB,CD}}$ is defined as the voltage drop between D and C per applied current through the contacts A and B. Analogously $R_{\mathrm{AB,CD}}$ is defined by permutation of the contacts. For the labelling of the contacts see Fig. 3.2. Van der Pauw's theorem states that the following expression holds for thin films with resistivity ρ and homogeneous thickness t:

$$\exp\left[-\frac{\pi t}{\rho}R_{\mathrm{AB,CD}}\right]+\exp\left[-\frac{\pi t}{\rho}R_{\mathrm{BC,DA}}\right]=1 \tag{3.3}$$

To calculate the sample resistivity ρ, Equation (3.3) can be transformed into Eq. (3.4) using $R^{\pm}=R_{\mathrm{AB,CD}}\pm R_{\mathrm{BC,DA}}$ and a function $f(R^+,R^-)$ only depending on the measured resistances:

$$\rho=\frac{d\pi}{\ln 2}\frac{R^+}{2}f(R^+,R^-) \tag{3.4}$$

The approximate solution of the function $f(R^+,R^-)$ for $R^+/R^-\approx 1$ is given by

$$f(R^+,R^-)\approx 1-\left(\frac{R^-}{R^+}\right)^2\frac{\ln 2}{2}-\left(\frac{R^-}{R^+}\right)^4\left(\frac{(\ln 2)^2}{4}-\frac{(\ln 2)^3}{12}\right) \tag{3.5}$$

3.4.2 Hall measurements

Hall measurements are based on the Hall effect, discovered by E. Hall [70] in 1879. Electrical point charges q in an external magnetic field $\vec{B}$ experience a

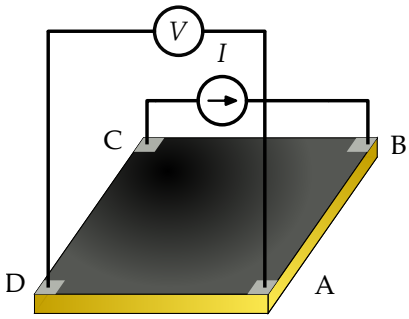

Method	Configuration	
Resistivity	V_{CD}	I_{AB}
	V_{AB}	I_{BC}
Hall	V_{AC}	I_{BD}
	V_{BD}	I_{AC}

FIGURE 3.2: Schematic of a sample with an electrical contact in each corner to measure resistivity using the van der Pauw technique; the table lists the two configuration used to average for resistivity and Hall measurements

Lorentz force $\vec{F}_L$ perpendicular to their direction of velocity $\vec{v}$

$$\vec{F}_L = q(\vec{E} + \vec{v} \times \vec{B}) \tag{3.6}$$

resulting in a deviation from the ideal straight path through a material. Due to their different sign, electrical positive and negative charges will be separated inside a current-carrying conductor to different sides. Any excess charge on one side creates a transverse electric field which opposes further charge separation and leads to a new equilibrium situation. In many materials the potential difference U_H between the two faces is proportional to the driving current I, the perpendicular magnetic field component B and material dependent Hall coefficient R_H:

$$U_H = \frac{R_H B I}{t}, \tag{3.7}$$

with the film thickness t. The sign of R_H is determined by the type of the charge carrier (electrons or holes) and its absolute value is related to the number of charges. For a p-type conductor with a single type of determinant charge carriers (holes), one can write:

$$R_H = \frac{1}{q n_H} \tag{3.8}$$

with the elementary charge $q = 1.602 \cdot 10^{-19}\,\mathrm{C}$ and the charge carrier density per unit volume n_H. As for many different material classes, Equation (3.8)

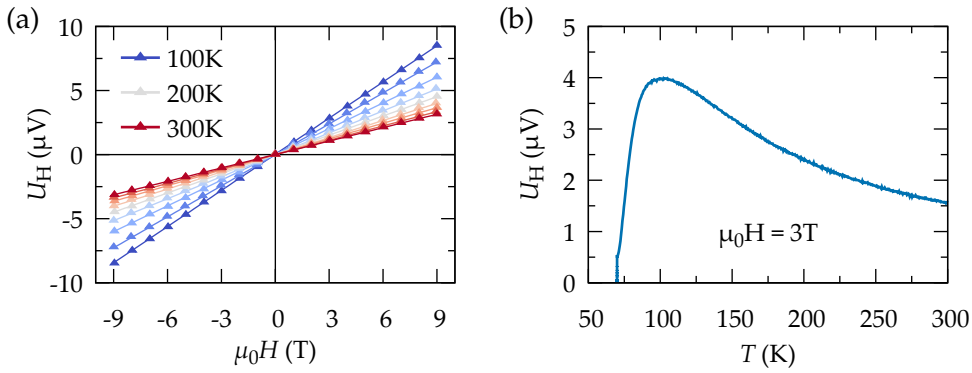

FIGURE 3.3: Hall effect measurements: (a) sweeping magnetic field at constant temperature to extract R_H from the linear slope of the Hall voltage and (b) in the case of vanishing voltage offset at zero field, the temperature dependence of $R_H(T)$ can be measured with a single temperature sweep at a constant applied field (3 T).

is used to calculate the charge carrier density n_H of YBCO, even though the validity of this equation is at its limits.

For every point in the $(\mu_0 H, T)$-diagram, the Hall voltage is measured in two configurations as indicate in the table of Fig. 3.2 and averaged to consider any electrical offset due to sample inhomogeneities and/or resistive contributions within the contacts. The magnetic field is swept between -9 and 9 T at constant temperature (see Fig. 3.3(a)). The Hall coefficient is extracted from the slope of the linear Hall voltage respond $R_H = \frac{t}{I\mu_0}\frac{dU_H}{dH}$. In the case of a vanishing voltage offset at zero magnetic field over all temperatures, the temperature dependent Hall coefficient $R_H(T)$ can be calculated from a single temperature sweep at constant applied field using Equation (3.7). A typical temperature dependence measurement at 3 T is shown in Fig. 3.3(b).

3.4.3 Electrical transport measurements

To obtain the critical current density J_c of a superconducting sample, electrical transport measurements can been performed using the standard four point technique. This method allows the characterisation of the critical current density of thin films as a function of temperature, field, and the orientation of the field in respect to the c-axis of the material: $J_c(T, \mu_0 H, \theta)$.

YBCO exhibits very high J_c values and therefore high currents would need to be applied to drive the superconductor into an energy dissipative state. To enable transport measurements samples have to be patterned to bridges with

widths of 10 - 100 μm. To avoid local heating and guarantee good electrical contacts an annealed interlayer of silver is necessary to obtain measurements of good quality.

3.5 X-ray diffraction measurements

X-ray diffraction techniques are very useful tools to obtain structural information of crystalline materials. Different methods can be used to probe chemical composition and defect structure, in-plane and out-of-plane parameters, film epitaxy and crystallite orientations, strain state and thickness of the film. In this work mainly two diffractometers are used: a *Bruker D8 Discover* with a monochromatic X-ray source and a *SIEMENS D5000*.

Diffraction measurements are based on the constructive interference of an electromagnetic wave, scattered by a periodic, long-range ordered structure, e.g. parallel planes of atoms. The wavelength of x-ray beams is of the same order of magnitude as interatomic distances in crystals, therefore they can be used for diffraction between atomic planes. The angles, where constructive interference produces a diffraction peak, is given by Bragg's law

$$n\lambda = 2d_{hkl}\sin\theta \tag{3.9}$$

where n is a positive integer, λ the wavelength of the incident X-ray beam, θ the angle between the surface and the incident wave and d_{hkl} the distance between two planes under consideration. The interplanar spacing for a system with orthorhombic symmetry reads

$$\frac{1}{d_{hkl}^2} = \frac{h^2}{a^2} + \frac{k^2}{b^2} + \frac{l^2}{c^2} \tag{3.10}$$

with the unit cell parameters a, b, c and the crystallographic direction $[hkl]$.

3.5.1 c-parameter measurement

The out-of-plane cell parameter c is determined by measurements with $\theta - 2\theta$ configuration. Using this geometry the diffraction vector $\vec{q}$ is always perpendicular to the surface plane since the incident angle of the beam ω is kept half of the detector angle 2θ. A typical pattern is shown in Figure 3.4. The $(00l)$ YBCO peak family and the substrate peaks $(h00)$ are clearly resolved with high intensities.

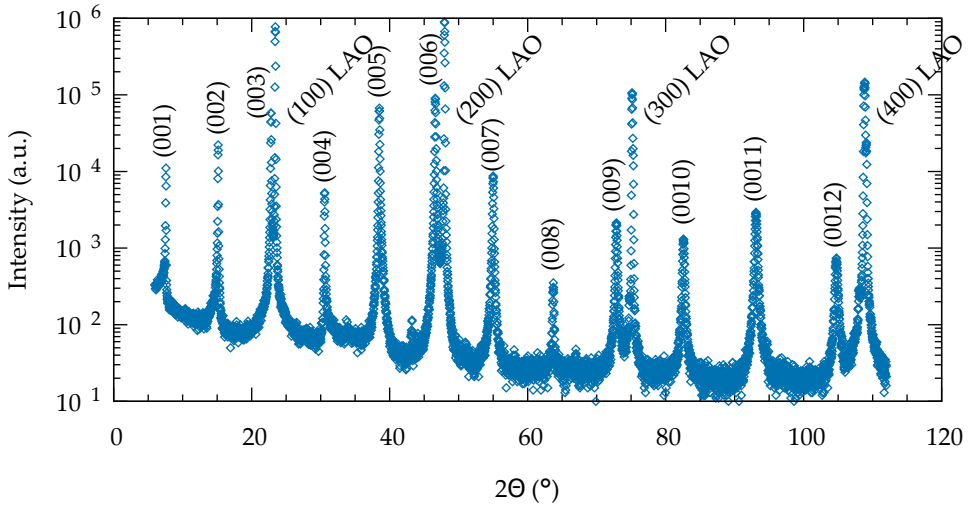

FIGURE 3.4: High resolution $\theta - 2\theta$ XRD measurement of a YBCO thin film on a LAO substrate. $(00l)$ YBCO peak family is labelled above peak, substrate peak labels are placed to their right side

Substrate	a (Å)	(100)	**(200)**	(300)	(400)
$LaAlO_3$	3.791	23.438	**47.959**	75.143	108.795
$SrTiO_3$	3.905	22.754	**46.472**	72.567	104.192

TABLE 3.3: Unit-cell parameters for STO and LAO substrate used to calculate diffraction angles. (200) reflections are used for sample calibration in $\theta - 2\theta$ measurements.

Calibration and post correction

The (200) substrate peak is used to calibrate the measurement for both, LAO and STO substrates. The substrate cell parameters are listed in Table 3.3, along with the corresponding diffraction angles. While for STO literature values have been take, the LAO cell parameter was refined from a powder diffraction measurement using the Rietveld technique.

A post correction is performed to minimise the error in the 2θ position. Therefore all substrate peaks are fitted and their offset to the expected position is corrected by a polynomial of second degree. This correction is applied to the whole spectrum.

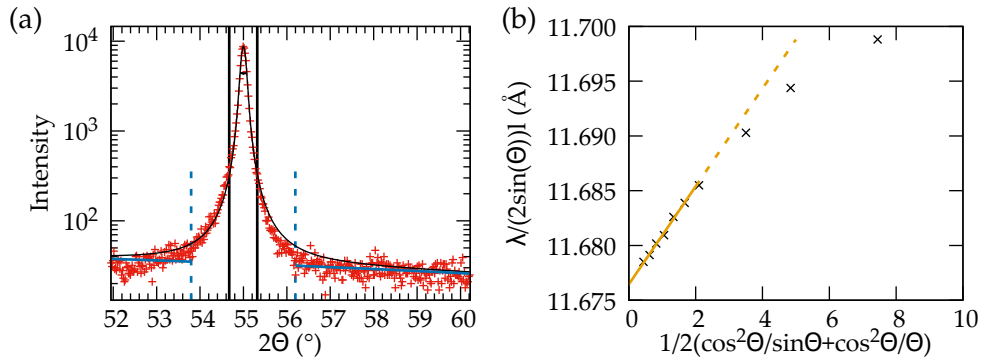

FIGURE 3.5: (a) Fitting procedure for the (007) YBCO peak; a linear background is fitted to the data in the visible area exempt between the two blue dashed bars; the peak itself is fitted to a pseudo Voigt within the area of the two black bars (b) Extrapolation of the c-parameter using Nelson-Riley criteria

Peak fitting

A key step of the analysis of diffraction measurements is the precise fitting of the peaks. This is done by using a home written fitting routine for gnuplot. Often, peaks cannot be simply described by a purely Lorentzian or Gaussian curve. Therefore the Voigt function is frequently used as a better approximation of real XRD patterns. This function is a convolution of a Lorentzian and a Gaussian. In the present fitting routine a pseudo Voigt function is used to fit the peak shape. It reads

$$I\left(2\theta - 2\theta_0\right) = I_{\max}\left[\eta l\left(2\theta - 2\theta_0\right) + \left(1-\eta\right) g\left(2\theta - 2\theta_0\right)\right] \tag{3.11}$$

and is the sum of a normalised Lorentzian l and normalised Gaussian g, weighted by the Lorentz fraction η. While precision is not significantly compromised, the computational effort is strongly reduced by using a pseudo Voigt instead of a Voigt profile. Up to four scalable fit parameters are used, corresponding to the position of the peak $2\theta_0$, its maximum intensity $I_{\max}$, the Full Width Half Maximum (FWHM) and the Lorenz fraction. The exact fitting steps are as following (see also Fig. 3.5 (a)):

1. A region of the full XRD spectrum is chosen, confining a single peak
2. Initial values for peak height and position are defined by the point with maximum intensity $I_{\max}$ and the corresponding $2\theta_0$ value. Additionally, an initial FWHM is defined by the closest points to $1/2 I_{\max}$ on the left and right side of the peak

3. A linear background is fitted to both sides of the peak, while the area of 4 FWHM around I_{max} is excluded from the fit
4. The linear background is subtracted from the spectrum
5. A pseudo Voigt function is fitted within the range of usually 2 FWHM around the peak
6. Step 5 is repeated with refined values for I_{max}, $2\theta_0$ and an adopted fit range to the new peak position

In case of the *SIEMENS* diffractometer a non-monochromatic source is used and the Cu K(α_2) line has a strong contribution. Therefore an additional pseudo Voigt profile has to be added in the fitting procedure. The position of the peak must be fixed to the corresponding peak position of the Cu K(α_1)

$$2\theta_{0,k\alpha_2}(2\theta_0) = 2\arcsin\left(\lambda_{k\alpha_2}/\lambda_{k\alpha_1} \cdot \sin(2\theta_0/2)\right) \tag{3.12}$$

Evaluation of the *c*-parameter

Two methods have been used to evaluate the out-of-plane lattice parameter:

Bragg condition When using Bragg's condition for several $(00l)$ peaks and plotting l over corresponding $2\sin(\theta)/\lambda$ values, the c-parameter can be calculated as the slope of a linear regression.

Nelson-Riley Several systematic errors decrease with increasing incident angle and would vanish at $2\theta = 180\,°$. Thus various extrapolation methods have been proposed since the early stage of XRD diffraction to diminish the influence of systematic errors and calculate cell parameters at the highest possible angle. The best extrapolation was obtained using following function [71]:

$$\frac{1}{2}\left(\frac{\cos^2(\theta)}{\sin(\theta)} + \frac{\cos^2(\theta)}{\theta}\right). \tag{3.13}$$

An example for an extrapolation to obtain the c-parameter as the intercept at $x = 0$ is shown in Figure 3.5 (b). Only peaks with $l \geq 6$ are used for the fitting.

3.5.2 Nanostrain analysis

Local, inhomogeneous deformation of the crystallite structure leads to the occurrence of nanostrain ϵ. This form of strain can be evaluated using a methodology developed by Williamson and Hall [72]. It correlates the increasing

broadening of the coherent XRD reflections with the increasing reflection angle:

$$\beta^2 \cos^2(\theta) = \frac{\lambda_{K_\alpha}}{L} + 16\epsilon^2 \sin^2(\theta) \tag{3.14a}$$

$$\beta \cos(\theta) = \frac{\lambda_{K_\alpha}}{L} + 4\epsilon \sin(\theta), \tag{3.14b}$$

where the different contributions to the broadening add up quadratically, as for the case of the convolution of Gaussian peak profiles (Eq. (3.14a)), or simply linear, if the peaks a defined by a Lorentzian profile (Eq. (3.14b)). β corresponds to the experimental broadening of the (00l) Bragg peaks, corrected by the instrumental broadening, λ_{K_α} is the wavelength of the Cu K_α radiation and L is the height of the crystallite. The nanostrain ϵ can be obtained by a linear fit in a plot of $\beta^x \cos^x(\theta))$ *vs.* $\sin^x(\theta)$, with $x = 1, 2$ for Lorentzian or Gaussian peak shapes, respectively.

3.6 *In situ* high temperature ECR measurements

Electrical conductivity relaxation (ECR) measurements are a very useful technique to measure reaction and transport kinetics of a solid material. Therefore the evolution of conductivity with time due to changes in external parameters as temperature and atmosphere is recorded. It provides insight into fundamental processes and one can obtain materials properties as the surface exchange constant k_{chem} and the chemical diffusion coefficient D^{chem}. It is an *in situ* analysis method and has a rather simple set-up, low measuring costs and a broad range of possible working temperatures. Measurements can be performed in vacuum, and different low and high pressure atmospheres. ECR measurements are of integral type and typically do not provide spatial resolution.

There are several other techniques to analyse solid state exchange reactions, such as *in situ* X-ray diffraction, thermogravimetry and secondary ion mass spectroscopy. The latter method allows to measure frozen-in profiles with spacial resolution. Optical adsorption spectroscopy is an example for an *in situ* method with spatial resolution.

Mainly three different driving forces are used in oxygen exchange experiments. To distinguish the nature of exchange one denotes k^δ and D^δ in case of chemically driven exchange due to change in partial pressure, k^* for isotope exchange in ^{18}O tracer experiments and k^{Q} for electrochemically overpotential driven measurements.

3.6.1 Measurement set-up

The ECR measurement set-up is home build and is made up of a furnace, an electrical set-up for the ECR measurements and a system to control the atmosphere inside the furnace. The whole set-up has been revised and main improvements as the automation of the whole process has been made during this work. The measurements are controlled and recorded by a LabView program via serial and GPIB connections.

Furnace

The furnace is of cylindrical shape with a bore of 30 mm in diameter in axial direction. A glass tube of 22 mm diameter inside the furnace bore is enclosed between the gas control unit on the entrance side and a two gas bubbler system on the exit to avoid gas exchange with environment. An external power unit controls the heating via a Eurotherm 902 Thermocontroller. The maximum heating rate is about 80 °/min while cooling is limited to 5-15 °/min above 300 °C (see the cooling characteristics for different temperatures in Fig. 3.6). The standard heating rate used for ECR measurements is 10 °/min from room temperature to the first dwell temperature.

Atmosphere control

On the entrance side three gas mass flow units (one of 3 ml/min, and two of 0.6 l/min) enable different oxygen partial pressures $P(O_2)$ by mixing O_2 and N_2 gases with purity above 99.995 %. The atmosphere is changed between dry and wet gas and different $P(O_2)$ by switching electro-valves with a digital relay. The standard total gas flow used is 0.6 l/min at atmospheric pressure. Partial pressures of oxygen between 1 bar and 10^{-5} bar (pure N_2) can be established.

Sample holder and sample mounting

The sample holder consists of three thin ceramic bars with two holes each for wiring purposes, mounted on a metallic plug. The central one is used for a K-type thermocouple with copper leads, providing the furnace temperature close to the sample position. Thick silver wires of 0.25 mm diameter are inserted into the holes of the other two bars and fixed at the end of with a high temperature silver paint from CDS Electronique. After manufacturing the sample holder these contacts were initially dried out at 800 °C.

Thin Ag wires of 0.125 mm are wrapped around theses contacts and fixed with silver paint in the corners of the samples surface. Typically silver contact

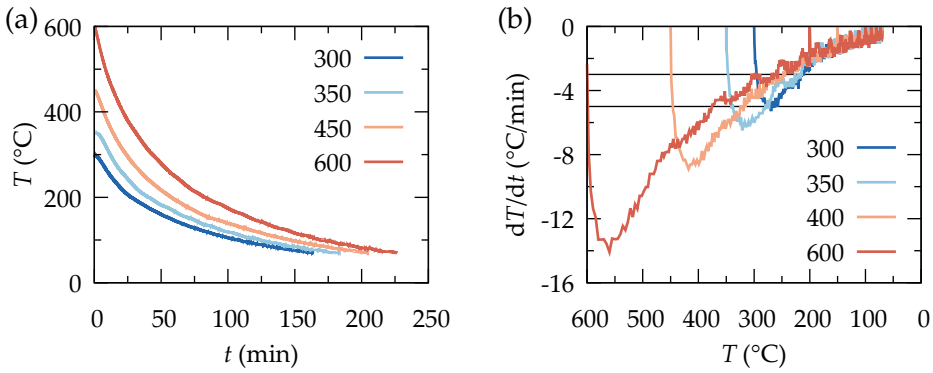

FIGURE 3.6: Furnace cooling characteristics with gas flow; a) b) Maximum cooling rates depending on last dwell temperature

pads between 20 and 100 nm were sputtered before onto the sample to guarantee good electrical contact. Before mounting the sample, it was cleaned for several minutes in acetone in an ultrasonic bath and dried with dry air or nitrogen gas.

Electrical measurement set-up

Electrical conductivity is measured using the van der Pauw method. A current of ±100 µA is applied using a Nanosourcemeter. The voltage drop is measured by a Keithley Nanovoltmeter 2182. The integration time of the A/D voltage converter is 20 ms to allow fast read out rates with good noise performance. While any electrical offset, e.g. due to thermal gradients, is considered by current reversal, no permutation of the voltage and current contacts is made. In general the material investigated is rather homogeneous, therefore measuring two Van der Pauw configurations is not absolutely essential, but to add this feature is recommended for a further update of the set-up. Time resolution is limited to 1 sec due to the slow read out of the furnace temperature and heating parameters and to guarantee a stable current supply during the voltage measurement.

Chapter 4

Study of YBCO oxygen kinetics via *in situ* electrical conductivity relaxation measurements

Normal state electrical and superconducting properties of YBCO crucially depend on its overall oxygen content. The importance of oxygen for cuprate high temperature superconductors (HTS) as hole dopant was realised soon after its discovery and research has been ongoing since [22, 63, 73].

Oxygen kinetics in YBCO has been studied by many different authors and techniques (for a thematic review see *e.g.* [74]). However, a fundamental and complete understanding of the ongoing processes in the oxygen exchange of YBCO thin films is still missing in literature. In recent years vast effort has been undertaken in finding materials for intermediate solid oxid fuel cells (SOFC), where high electronic and ionic conductivity, and oxygen exchange kinetics are required [75–78]. We have transferred this knowledge and have applied methodologies, developed for the analysis of oxide materials for cathodes in SOFC, to YBCO.

In this chapter a general analysis of oxygen exchange kinetics using electrical conductivity relaxation (ECR) measurements will be presented and the rate determining step of oxygen exchange will be identified. We will study the influence of surface coating and effects of different YBCO microstructures, due to different growth techniques, embedding of nanoparticles, calcium doping and internal macroscopic strain introduced by substrate lattice mismatch in reduced film thicknesses.

In the following the terms oxidation, or in-diffusion will be used to describe the process of oxygen incorporation into the YBCO structure due to an increase of oxygen partial pressure (forward reaction). Further, reduction and out-diffusion refer to the release of excess oxygen (excorporation) due to a new, lower oxygen chemical potential, achieved by decreasing $P(O_2)$ (backward reaction).

Two electron holes per oxygen are doped into the structure. Therefore the charge carrier density of the p-type conductor increases with the oxygen content $O_{7-\delta}$, as does the conductance. An accompanied change in valence state of copper (Cu^{1+}, Cu^{2+} and Cu^{3+} are observed in $Y_1Ba_2Cu_3O_{7-\delta}$) ensures charge neutrality within the unit cell [79]. From the bulk phase diagram a phase transition to the tetragonal phase ($\delta > 0.65$) is only expected for $T \geq 600\,°C$ within the pressure range of operation (compare with YBCO phase diagram on page 10) [21, 80]. However, a transition within different orthorhombic phases is expected and hence emerging effects as oxygen ordering [81].

4.1 Introduction into ECR measurements of YBCO thin films

Electrical conductivity relaxation (ECR) measurements are a very useful tool in obtaining information about the process of oxygen exchange of a material with atmosphere. Therefore the evolution of the samples conductivity is recorded over time during the transition from an initial to a final equilibrium state, induced by a jump in oxygen pressure at constant temperature. In the following we will introduce the necessary methodology to perform and analyse ECR measurements.

4.1.1 ECR experimental procedure

The specimen is mounted onto a sample holder and electrically contacted using a high temperature silver paint and silver electrodes. For measurements the sample is placed and sealed inside the furnace, as outlined in section 3.6 and the evolution of the films conductance is recorded during the whole measurement process. A typical temperature profile used to study the kinetics of YBCO is shown in Fig. 4.1. The measurement is usually started at 600 °C or 650 °C and sequentially reduced in steps of 25 or 50 °C. The initial heating rate is set to 10 °/min. The cooling rate is 5 °/min and 3 °/min above and below 450 °C respectively, to avoid deviations from the programmed profile. Every temperature dwell consists of three segments. The initial phase of several minutes serves to stabilize the temperature and equilibrate the sample to the new conditions. In a second and third phase the oxygen partial pressure is switched from 1000 mbar to 5 mbar and reverse, respectively. Therefore initial and final point of each dwell is in an oxygen rich atmosphere, as is the heating segment.

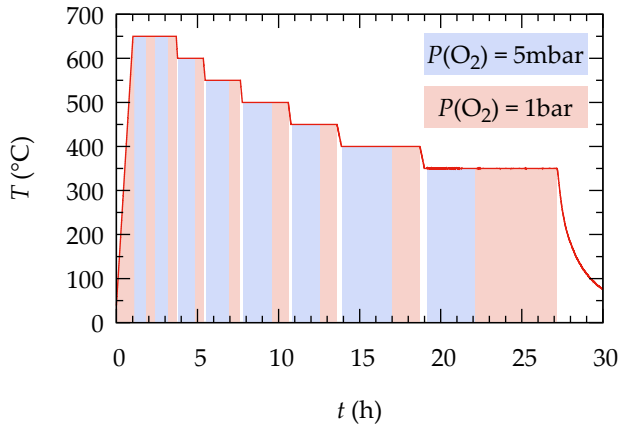

FIGURE 4.1: Standard temperature profile of *in situ* measurement, starting at high and going to low temperatures. At every temperature dwell the oxygen partial pressure is changed from high (red) to low (blue) and back to high. Temperature changes are always performed in high $P(O_2)$, but background colour is omitted for better clarity of the individual dwells.

While the measurement setup allows to establish any oxygen partial pressure between 0.01 mbar and 1 bar, the standard low $P(O_2)$ is set to 5 mbar to balance the trade off between sufficiently big steps in oxygen concentrations (changes in conductance) and reasonable short saturation times, as will be discussed in the following sections.

As oxygen diffusion and exchange at the surface are thermally activated processes, the dwell time is increased at lower temperatures to compensate slower oxygen kinetics. At high temperatures (600 °C) the low and high $P(O_2)$ phases are typically 30 min, while at lower temperatures the times are increased up to several hours.

Different start and end temperatures, step intervals and dwell times result in a broad variety of different total annealing times among all measured samples. The influence of annealing time and inversion of the measurement direction (starting at low temperatures and subsequently increasing temperature) and arising complexities will be discussed in the next chapter.

4.1.2 Results and Discussion of ECR measurements

The evolution of conductivity for a standard 250 nm thick pristine CSD film is depicted in Fig. 4.2. The atmosphere is indicated by background colouring

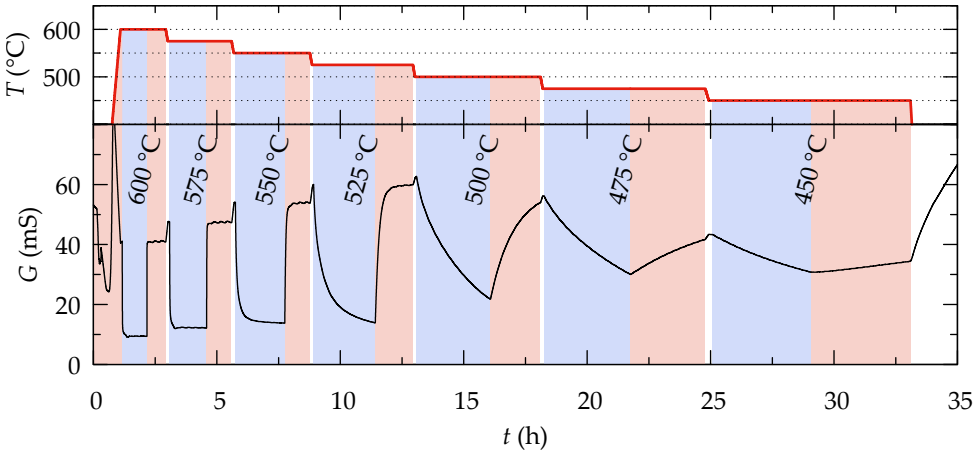

FIGURE 4.2: Conductance G of pristine 250 nm CSD YBCO film as a function of time. Changes in G are due to alternating steps in $P(O_2)$ at different temperatures. Corresponding temperature profile is shown on top.

whereupon red and blue imply high and low oxygen partial pressure, respectively. At the beginning of the measurement at high temperatures saturation can be reached in short times, while at low temperatures and after long annealing times equilibrium values are not reached within the duration of the experiments. The spikes in conductance between the dwells are due to the increase of conductance with lowering the temperature, as it is the increase at the end of the measurement, when the sample is cooled to room temperature.

Each segment can be analysed individually and the time evolution of its conductance can be fit to the solution of the diffusion equation (see section 2.2.3) using two exponential terms:

$$G(t) = \left[a\mathrm{e}^{-t/\tau_1} + (1-a)\,\mathrm{e}^{-t/\tau_2}\right] \cdot (G_0 - G_\infty) + G_\infty, \tag{4.1}$$

with saturation times τ_1 and τ_2, a weighting factor a and the initial and final equilibrium conductances G_0 and G_∞. The two relaxation times are commonly assumed to correspond to different regions of the surface with independent exchange rates [82, 83]. The data is fitted using *Gnuplot*'s least-squares fit routine. One example each, for the oxidising and reducing case, is shown in Fig. 4.3(a) and (b), respectively. When the atmosphere is electronically switched, the segment time is automatically set to zero. An initial fit value for G_0 is chosen by the average of the first five measured points of each segment.

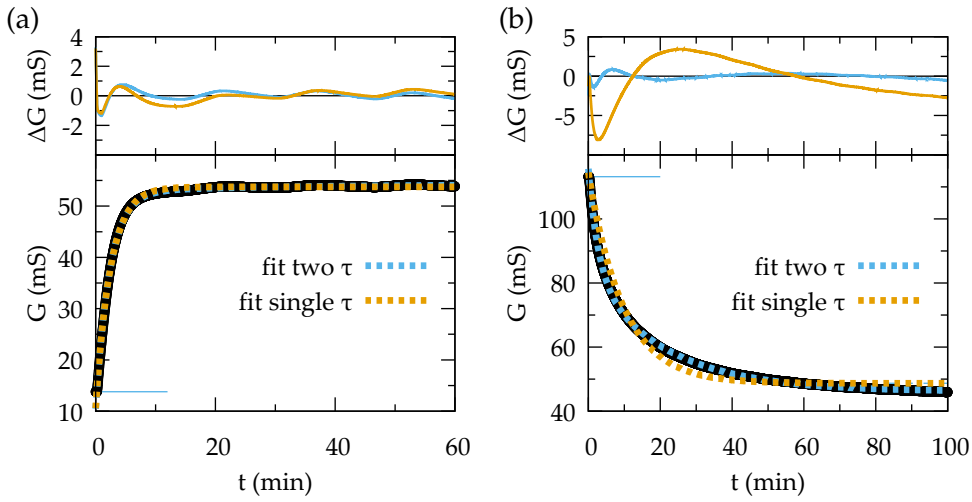

FIGURE 4.3: Time evolution of conductance of 250 nm CSD YBCO at 550 °C after a change in oxygen partial pressure: (a) the process of oxygen incorporation can be well described with a single exponential term while (b) oxygen loss in the structure needs to be modelled using two parallel exchange mechanism. The deviation ΔG of measured data and fits is shown on top.

These first seconds are not yet affected by the switching, since the respond time of the system is longer. The fitting process of two parallel exponential decays is more delicate to errors. Therefore sometimes it is necessary to feed the routine with starting values for G_∞ and τ_1 from a single exponential fit.

As shown in Fig. 4.3(a) and typically found in this thesis for the case of oxygen incorporation, one single saturation time linked to a single process, is sufficient to describe the evolution of $G(t)$. No further accuracy is gained by the second exponential term. In this case a in Eq. (4.1) is either very close to unity or the resulting difference of the two saturation times is smaller than the fitting error ($\tau_1 \cong \tau_2$).

On the other hand, the reduction process cannot be sufficiently modelled by a single process, as can be seen in Fig. 4.3(b). Using a two τ fit model results in high fit accuracy and accurate saturation values for $G_\infty(t \to \infty)$. In the upper panel of Fig. 4.3(a & b) the deviation $\Delta G(t) = G(t) - G_F(t)$, between the measured conductance $G(t)$ and the fit values $G_F(t)$ for one and two exponential terms is shown.

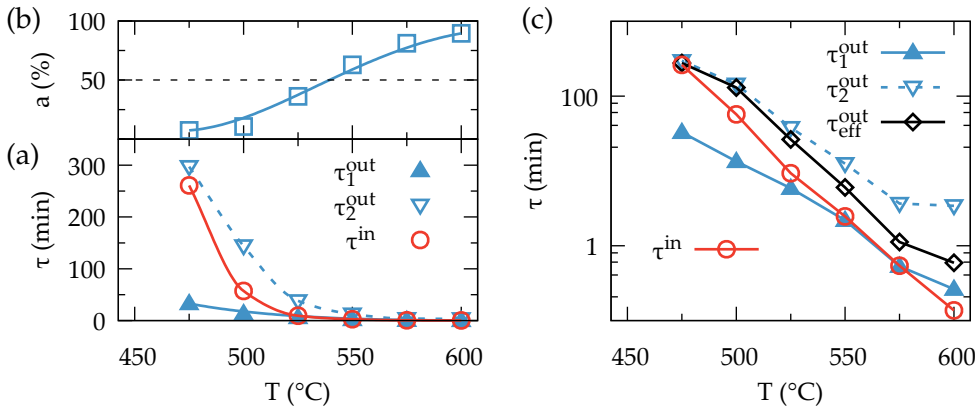

FIGURE 4.4: Analysis relaxation times of 250 nm CSD-YBCO sample: (a) Temperature dependence of τ for oxidising (in) and reducing (out) atmospheres, (b) weight a using 2 τ model for the case of reduction and (c) comparison of weighted effective saturation time τ_{eff} for out-diffusion process with original τ values.

The temperature dependence of the saturation times is shown in Fig. 4.4(a) for both, the out- and in-diffusion process. The time to equilibrate the samples conductance increases exponentially with decreasing temperature, as expected for a thermally activated process. In case of oxygen reduction a shift from one exchange mechanism to a second parallel mechanism is observed, as seen in the temperature dependence of the weight parameter a in Fig. 4.4(b). In some cases the further analysis can be facilitated by introducing an effective saturation time τ_{eff}

$$\tau_{eff} = a\tau_1 + (1 - a)\,\tau_2, \tag{4.2}$$

which is the weighted arithmetic mean value of the two separate saturation times. Its temperature evolution is depicted in Fig. 4.4(c). At high temperatures it is very close to τ_1^{out}, while it shifts to τ_2^{out} at lower temperatures. While for the analysis of activation energies it is necessary to consider both contributions separately, τ_{eff} is useful in the comparison among different samples of the same thickness.

As can be seen in Fig. 4.4(c), in-diffusion saturation times are shorter than effective out-diffusion relaxation times. This asymmetry is unexpected for purely bulk controlled diffusion and is an indicator that surface exchange reactions play a crucial role in YBCO thin films. This matter will be subject to detailed discussion in section 4.4.

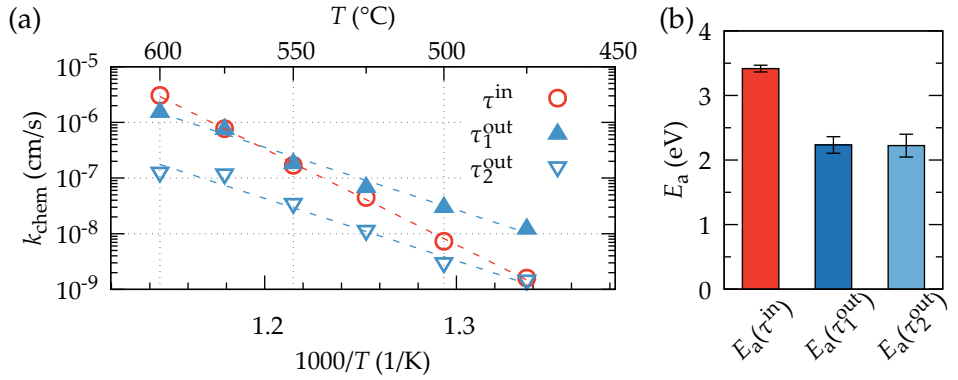

FIGURE 4.5: (a) Arrhenius plot for in- and out-diffusion process of pristine 250 nm CSD YBCO film; activation energy can be extracted with a linear fit in the log-lin plot and (b) extracted E_a values for oxidation and two parallel reduction processes.

The analysed samples are thin films grown on single crystal substrates. Thus, we consider only the top surface participating in the exchange process, which is reasonable as the thickness is much smaller than the top surface dimensions of the thin film. We assume a constant oxygen stoichiometry of the substrate and therefore no oxygen exchange effects at the film-substrate interphase. The measured saturation times are related to the total amount of oxygen ions being exchanged. If the rate determining step is one of the processes associated to surface exchange, the saturation time τ depends on a reaction rate constant related to the oxygen exchange at the surface and the thickness of the sample. The thickness independent parameter in quest is the so called chemical surface exchange coefficient and it reads:

$$k_{\text{chem}} = \frac{t}{\tau}, \tag{4.3}$$

with the sample thickness t. It is shown in Fig. 4.5(a) in an Arrhenius plot, which reveals information about the effect of temperature on the chemical reaction rate constant. Using an Arrhenius equation in the form of

$$k_{\text{chem}} = k_0 \mathrm{e}^{-E_a/k_B T} \tag{4.4}$$

with the Boltzmann constant k_B and a pre-exponential factor k_0 with the units of a velocity, one can obtain the activation energy E_a of the process by fitting (see Appendix A.1 for details). The activation energy is the minimum kinetic energy required for reactants to form the reaction product and corresponds to

the slope in a log-lin plot. The exponential term is called Boltzmann factor and gives the probability of the reaction to occur. The pre-exponential factor k_0 is the theoretical surface reaction rate constant at $1/T = 0$. Arrhenius equations for reactions are typically valid only within a small temperature range. In fluid chemistry k_0 is considered the total rate of collisions independent of their energy, while k_{chem} is the number of collisions per time leading to a reaction [35].

The extracted activation energy in the range of 475 °C until 600 °C for oxygen incorporation is 3.4 eV, which is considerably higher than for the reverse process of oxygen reduction, with an activation energy of 2.2 eV for both of the two parallel mechanism (τ_1 and τ_2, Fig. 4.5(b)). The values found are significantly higher compared to literature, usually reported to be around 1 eV. Even thought there are methodological differences, as different temperature ranges [84], assumed proportionality between time evolution of the oxygen content and resistance, rather than conductance [85] and different film growth techniques [86], an increase by a factor 2 - 3 is not expected solely by different methodologies. Additional, in several studies exchange kinetics were analysed in the aspect of diffusion limitation, also resulting in lower activation energies [64, 87].
This issue will be discussed again in Chapter 5, taking into account a deactivation of the surface exchange rates due to degenerative effects.

In summary we have shown that ECR measurements are a useful tool to investigate oxygen exchange kinetics of YBCO and its activation energies and presented a first sign, that incorporation of oxygen is limited by a surface reaction.

4.2 Surface coating with silver: Introducing a catalytic effect

In the typical multilayer architecture of second generation HTS coated conductors, the REBCO layer is terminated with a thin layer of silver ($<1\,\mu$m). The Ag coating is protecting and stabilising the underlying superconducting thin film and serves as a diffusion barrier for the surrounding copper stabilizer. Additionally, silver is known to present a catalytic effect for the process of oxygen exchange [42]. The deposition of silver on the surface before oxygen loading is the most used method by wire manufactures. We here want to study its effect on the oxygenation process.

We have deposited silver on the YBCO surface by sputter deposition. Photolithography is used to prepare a mask on the sample surface prior to silver sputtering. Different mask geometries (shape, size and number of Ag pads)

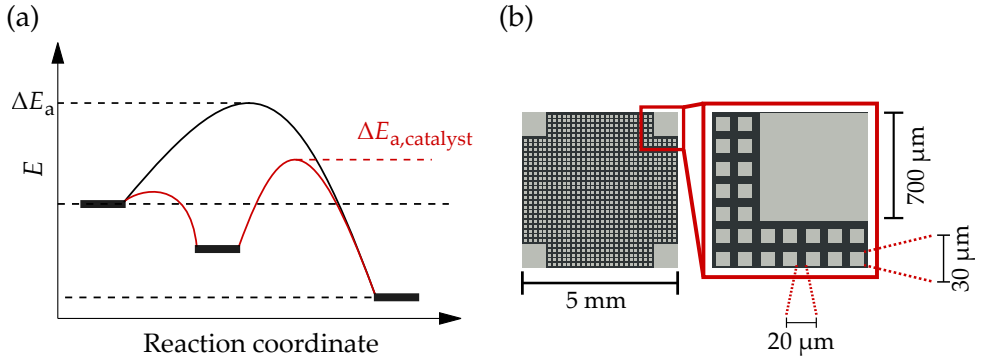

FIGURE 4.6: (a) Schematic description of the principle of the catalytic effect, offering an energetically preferable reaction path and (b) scheme for silver patterning for electrical measurements.

have been tested to enable resistivity measurements in the normal state of YBCO without short-cutting through the silver coating. The finally used pattern is drawn in Fig. 4.6(b) which did not influence electrical measurements, allowing a proper determination of the normal state resistivity and charge carrier density of YBCO. The mask consists of four squared electrodes in the corners with a side length of 700 µm for good electrical contact for ECR measurements. Additionally, all over the sample small squares (30×30 µm) are arranged, resulting in a coverage of the surface with silver of about 40 %.

4.2.1 Possible influences of silver coating on oxygen exchange kinetics of YBCO films

The coating with silver of the pristine YBCO surface could influence several parameters. Oxygen can be adsorbed on silver and diffused along the surface as O_2, or through the silver bulk to the YBCO layer in the form of oxygen ions O^{2-}. Also the triple phase boundary (TPB) of Ag, YBCO and the atmosphere could lead to modified surface kinetics [88]. The oxygen molecule might be ionised by an electron provided by silver and dissociated in close vicinity to the catalyst, while the resulting oxygen ion is directly absorbed into the YBCO surface layer, as observed for other oxides [89]. The possible influences of silver coating under consideration are the following:

- **Modification of adsorption rate and density:**
  Silver coating could lead to an increase of the sticking probability and the adsorption site density. A higher density of possible adsorption sites

for oxygen and therefore more particles participating in the reaction increases the exchange rate of surface related mechanism (as adsorption, ionisation, dissociation, surface diffusion and incorporation; see step 1-5 in Table 2.1).
The sticking probability can be expressed by the ratio of the rate ϕ_{ads} of adsorbed gas particles at the surface to the rate of all impinging molecules at the surface ϕ_{tot}: $s = \phi_{\text{ads}}/\phi_{\text{tot}}(100-\theta)$. The factor $(100-\theta)$ is the probability that the adsorption site is not filled for a given surface coverage θ. ϕ_{tot} can be obtained from Maxwell-Boltzmann gas theory and reads $\phi_{\text{tot}} = \frac{1}{4}P\bar{v}/(k_{\text{B}}T)$, with the average particle velocity $\bar{v}$, the pressure P, Boltzmann constant k_{B} and temperature T. The adsorption rate ϕ_{ads} is a material parameter that depends on the surface termination. Thus, s can be increased by surface coating with a material with higher ϕ_{ads}.

- **Catalytic effect of silver for oxidation reactions:**
  Catalysis is the acceleration of a chemical reaction due to the participation of an additional substance of very minor proportion. A catalytic material provides a new reaction path with a lower activation energy but the same educt and product. A schematic draft of a catalysed reaction is shown in Fig. 4.6(a). Transition metals, as Ag, Au and Pt are catalytically active for the process of oxygen dissociation [90] and often used in the catalysis of redox reactions. In the case of catalysed oxygen adsorption, an electron is transferred from the silver 5*s* orbital to the anti-bonding π^* O_2 orbital. This charge transfer weakens the chemical bonding of the O_2 molecule resulting in a chemically adsorbed state and a lowered activation energy for the process of dissociation. Therefore, catalytic activity of silver might enhance the oxygen exchange steps 1-3 (adsorption, ionisation and dissociation), as listed in Table 2.1 on page 18.

- **Surface protection and stabilisation:**
  A surface coating can protect the YBCO layer from environmental detrimental factors, as e.g. reactivity with the atmosphere and air moisture [91]. Further it might prevent the contamination of grain boundaries and generally the surface from impurities, which might cause a modification (degradation) of oxygen exchange kinetics, as discussed in Chapter 5. Additionally in the production of REBCO coated conductors Ag coating is used as electrical and chemical stabilizer to avoid interfacial reactions with the surrounding Cu coating, which is necessary as quench protection layer [92].

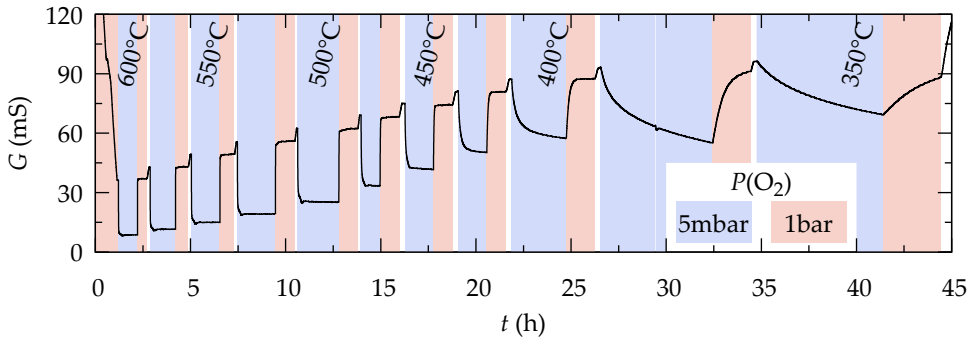

FIGURE 4.7: Time evolution of the conductance of a 250 nm CSD-YBCO film with surface silver coating measured in steps of 25 °C starting at 600 °C. Note that oxygen kinetics are faster below 450 °C as compared with a YBCO film without a silver layer.

4.2.2 Exchange kinetics of Ag coated YBCO thin films analysed by ECR measurements

To understand the influence of silver coating on oxygen exchange, ECR measurements were repeated with CSD YBCO 250 nm thick films with an Ag layer of 100 nm on top. The evolution of the samples conductance due to changes in oxygen partial pressure is measured from 600 °C down to 350 °C in steps of 25 °C. The *in situ* conductance is shown in Fig. 4.7. Saturation is reached in very short times and down to very low temperatures. Even at low temperatures as 350 °C, oxygen can be removed and incorporated into the structure in reasonable times. These results are in strong contrast to the ones found for the case of pristine YBCO films (see Fig. 4.2).

The saturation times of a pristine sample and one with a silver coated surface are compared in Fig. 4.8(a) in a semi-log plot. At 600 °C, the first analysed temperature, the time constants for both films are very similar. With decreasing temperatures, τ values for in- and out-diffusion for the pristine sample strongly increase. On the other hand, the silver coated sample shows a much weaker dependence on temperature. At low temperatures the non-silver coated film could not be analysed because no saturation in oxygen exchange was obtained. In the case of silver coated samples we observe an upwards deviation from an approximately power law T-dependence below 450 °C, demonstrating that oxygen exchange kinetics get into a slower phase. The asymmetry between in- and out-diffusion rates is observed as well for Ag coated YBCO films. Oxidation is faster than reduction and the time constant

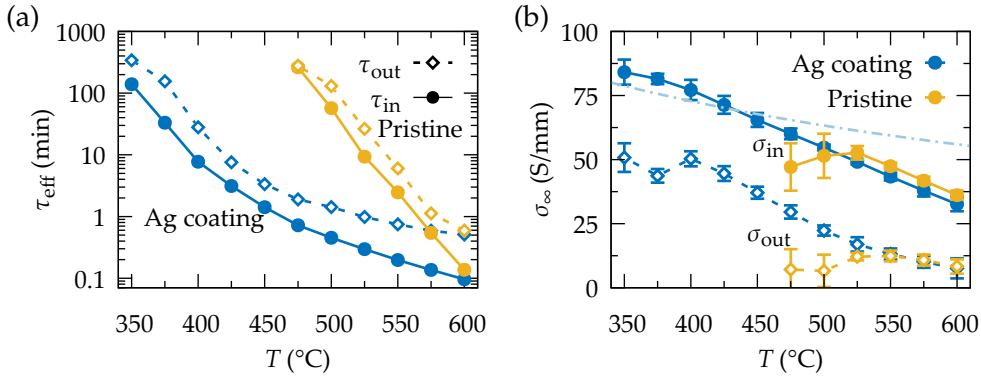

FIGURE 4.8: Comparison ECR measurements on YBCO with and without Ag coating: (a) saturation times τ_{eff} and (b) saturation conductivity values σ_∞ for reduction and oxidation; the light blue double broken line is the extrapolation of conductivity of the Ag sample below 300 °C during cooling.

ratio τ_{in}/τ_{out} exhibits similar values as in the case of pristine YBCO, between 0.2 and 0.4. Thus, also for a silver coated YBCO sample the rate determining step is a mechanism related to surface exchange reactions (see section 4.4). One can define a characteristic thickness t_c as the ratio of the chemical diffusion coefficient and the surface exchange coefficient:

$$t_c = \frac{D_{chem}}{k_{chem}}. \tag{4.5}$$

Typically exchange kinetics are limited by surface reactions if $t_c \gg t_{film}$ and by bulk diffusion if $t_c \ll t_{film}$. Using the empirically found relation for $D_{chem}(T)$ reported in [93]

$$D_{chem} = 0.033 \exp\left[-\frac{1.24}{k_B T}\right], \tag{4.6}$$

with the Boltzmann constant k_B in eV/K and the film thickness t_{film}, one can obtain an upper limit for k_{chem} for a surface limited process: $k_{max} = D_{chem}/t_{film}$. k_{max} is drawn in Fig. 4.9(a) (red line). The measured surface exchange coefficient is at least one order of magnitude smaller then the upper limit, confirming the assumption of a surface limited process even in the case of silver coated YBCO.

The saturation conductivities $\sigma_\infty \propto G_\infty$ for pristine and Ag coated samples are shown in Fig. 4.8(b). Open symbols correspond to the fit values ($t \to \infty$) of the reduction (5 mbar), closed symbols to the oxidation process (1000 mbar). It is worth noticing that until 525 °C the temperature dependence of $\sigma_{\infty,in}$ for

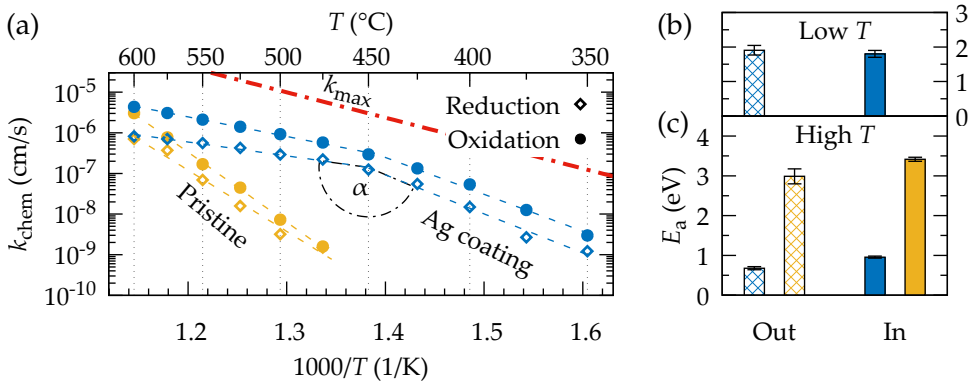

FIGURE 4.9: (a) Arrhenius plot for Ag coated and pristine CSD film, and activation energies for (b) Ag coated sample for 350 - 450 °C and (c) both samples for $T > 450$ °C (blue: Ag, yellow: pristine). The red line in (a) indicates the upper limit of k_{chem} for surface limited processes.

both samples is very similar, while saturation times already differ by more than one order of magnitude. This means that the same oxygen content can be reached in the temperature range of 525 - 600 °C for both samples, though the kinetics are very different . Below 525 °C, saturation is not reached for the pristine film and the uncertainty in the determination of σ_∞ increases. The saturation conductivity for a silver coated sample increases almost linearly with decreasing temperature until the last measured point at 350 °C for oxidation and reduction, respectively. The absolute difference between σ_{in} and σ_{out} remains similar between 350 and 600 °C. Therefore we expect no phase transition to the tetragonal phase within the analysed (p,T) range.

The conductivity of YBCO is known to scale over a broad temperature range with T^{-1}, as it is common for many metallic conductors. In the studied samples this dependency is typically observed below 300 °C and almost down to the critical temperature T_c.
After the last dwell step at 350 °C, the sample is cooled down to room temperature in oxygen rich atmosphere. Below 300 °C the linear dependence of the resistivity on T ($\rho = 1/\sigma \propto T$) is fitted with a straight line (not shown). In Fig. 4.8(b) the extrapolation of this fitted data is shown by the double broken light blue line. Above 450 °C the saturation conductivity deviates downwards from the extrapolation and therefore decreases faster than expected for a metal. This is understood by the decrease of the equilibrium overall oxygen content with increasing temperatures and the corresponding decrement of the charge carrier density.

The evaluation of activation energies for both films is presented in Fig. 4.9. For temperatures above 450 °C E_a is reduced by approximately a factor 3 for YBCO upon silver coating for both processes, the incorporation of oxygen into YBCO (full bars), and its release (patterned bars). In case of the silver coated sample, a second linear regime is found below 450 °C with a higher activation energy (see Fig. 4.9(a & b)). This result will be discussed in detail in the following section.

4.2.3 Analysis of two activation energy regimes caused by parallel exchange mechanisms

If two different processes participate in the oxygen exchange, the overall exchange coefficient can be assumed in a first approximation to be the sum of the particular rates k_1 and k_2 of the involved mechanisms:

$$k(T) = \underbrace{k_{0_1} e^{-E_{a_1}/k_B T}}_{k_1} + \underbrace{k_{0_2} e^{-E_{a_2}/k_B T}}_{k_2}, \tag{4.7}$$

with the individual activation energies E_{a_i} and pre-exponential factors k_{0_i} [54, 94]. The mechanism with lower E_a will start at lower temperatures to be active and is expected to provide the main reaction path at low T. With increasing temperature the second process will start contributing. In this intermediate temperature range, the parallel activity of two processes causes a deviation from linearity in an Arrhenius plot. At higher temperatures, the second mechanism will become more and more important, resulting in the return to a linear dependence with a different (higher) slope. This is schematically drawn in Fig. 4.10(a), using Eq. (4.7) with $E_{a_1} < E_{a_2}$ and $k_{0_1} < k_{0_2}$. The dashed line would correspond to the measured kinetics. This behaviour is commonly observed in diffusion limited systems, where the predominantly contribution changes from grain boundary diffusion to bulk diffusion.

In Fig. 4.10(b) the fractional quota for each mechanism is presented. The weight shifts with increasing temperature from the process with lower activation energy to the one with higher k_0 at elevated temperatures. In the case that one process has the smaller E_A and a higher k_0, it will indisputable provide the main reaction path over the full temperature range.

The presented data of the measurements is contrary to these considerations. At 450 °C a relatively sharp kink is observed in the Arrhenius plot for the Ag sample, with a higher activation energy at lower temperatures (see Fig. 4.9(a)). This downwards bending is observed for both, oxidation and reduction. Thus, it is not assumed to be correlated with a shift in the weight a in the two τ model (see Eq. (4.1)) used for the evaluation of the out-diffusion

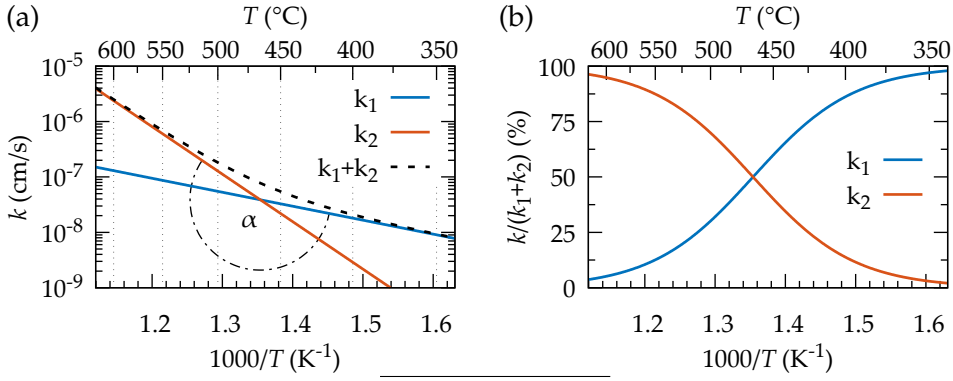

	E_a	k_0
k_1:	0.5	1
k_2:	1.7	1.5e8

FIGURE 4.10: Simulation of two parallel processes with different activation energies and k_0 values (see Eq. (4.7), with $E_{a_1} < E_{a_2}$ and $k_{0_1} < k_{0_2}$): (a) exchange coefficient for individual processes and their sum and (b) fractional portion of single mechanism on total exchange rate.

mechanism. Thus, the observed behaviour cannot be explained by two active parallel processes over the full temperature range.
Similar behaviour was found in a study of YBCO polycrystalline bulk specimen and thin films, where bulk diffusion is thought to be the limiting step [87]. It was proposed that the deviation to a lower activation energy is due to the lower equilibrium oxygen content at higher temperatures. An increased oxygen vacancy density causes an enhancement of the oxygen diffusion rate, additional accelerated by an increase of the lattice parameter c. This expansion in volume decreases the energy necessary to temporarily displace the crystal atoms during the jump of a diffusing atom from one site to the next.
In the presented case, where surface exchange is proposed to be the rate limiting reaction, an alteration in the surface coverage of charged ions could be responsible for the change in the activation energy.
Two different linear regimes of activation energy were as well observed for the oxygen transport through silver by several authors ([95, 96], and references therein for other materials), due to different control mechanism of oxygen transport, possibly trapping. The observed activation energy E was ascribed as the sum of the trap energy E_T and a thermal activation energy E_a. Higher activation energies at lower temperatures were attributed to a change in E_T,

causing a higher efficiency of traps, such as vacancies and interstitial impurities. However, in the next chapter we will be able to explain these results by taking into account surface degradation effects.

In this part it was shown, that silver exerts significant influence on the oxygen exchange kinetics. This was ascribed to its catalytic activity. YBCO films coated with silver have strongly increased exchange rates over the full analysed temperature range and decreased activation energies compared to pristine samples. This was found for both, oxidation and reduction processes.
The fact that the modification of the surface leads to an enhancement of exchange kinetics is another evidence that oxygen exchange in YBCO is limited by surface reactions. The asymmetry between in- and out-diffusion rates is kept upon silver coating. Therefore we conclude that bulk diffusion is still much faster compared to surface exchange kinetics enhanced by silver.

4.3 Environmental high temperature XRD analysis of YBCO exchange kinetics: a comparative study to ECR

XRD analysis is highly bulk sensitive and a fully integral technique. We have therefore performed *in situ* XRD measurements at elevated temperatures and under different atmospheres to proof the validity of ECR measurements and provide complementary information about the investigated YBCO thin films. Two XRD sessions of several days were performed at the Institut Català de Nanociència i Nanotecnologia (ICN2). These measurements were carried out in collaboration with Dr. Jessica Padilla and Dr. José Santiso from ICN2, with proactive support of short term research assistant Alex Gomez.

ECR measurements do not provide spatial resolution. Thus possible implications may arise if sample inhomogeneities lead to spatial variations in the chemical diffusion coefficient D_{chem} and a heterogeneous oxygen content distribution within the sample. If the method is not fully integral but only sensitive to some parts of the sample, the interpretation of the extracted data would have to be modified. Two phenomena are being discussed in the following, which might influence the measured relaxation times using electrical measurements:

- **Percolation currents:**
  Electrical percolation is the movement of electrons through a porous or inhomogeneous material, with zones of different resistivity. The grain boundary network in YBCO, even if grains are all *c*-axis oriented, might

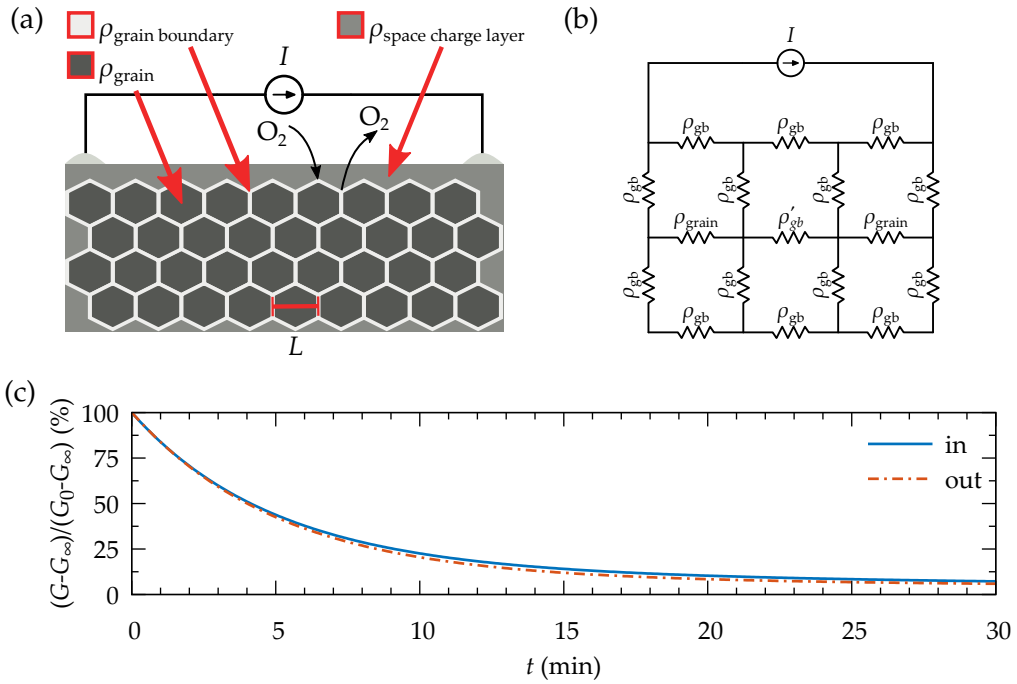

FIGURE 4.11: (a) Sketch of percolation phenomena caused by areas with different diffusion coefficients, resulting in zones with different resistivities. (b) Electronic circuit for the simplest model containing two grains interconnected with a network of grain boundaries and (c) corresponding simulated time evolution of normalised conductance for oxidation and reduction processes.

provide a percolation path altering the results for reduction and oxidation measurements.

Grain boundaries are considered high diffusivity paths for oxygen with a higher diffusion coefficient than bulk. Thus, the oxygen content in grain boundaries might adapt faster to changes in $P(O_2)$ than the overall bulk. A schematic of the percolation phenomena is depicted in Fig. 4.11(a). In the case of oxygen incorporation, the higher diffusion rate of grain boundaries may cause a network of well oxygenated, low resistive paths along the grain boundaries. The resistivity of the grains changes retarded. A reduction process may then cause the loss of oxygen first in the grain boundaries, resulting in a high resistive grid. The grains remain longer in a low resistance state. An asymmetry might be found for the oxidation and reduction, which could affect the measured relaxation times of the different processes in different direction.

A simple 2D model has been designed to analyse the effect of percolation currents, containing two grains, interconnected and surrounded by a network of grain boundaries, see Fig. 4.11(b), with the resistivities $\rho(t)_{\text{grain}}$ and $\rho(t)_{\text{grain boundary}}$. We consider grains of squared shape with the length l surrounded by grain boundaries with a width of $l/20$. The circuits equivalent resistance as a function of time is simulated. The time evolution of the inverse resistances ($\equiv$ conductances G) of the grains and the grain boundaries are assumed to follow an exponential decay, with two different time constants τ_{G} and τ_{GB}, while we assume the same initial and final values: $\rho(t)_{\text{grain}} = \rho(t)_{\text{grain boundary}}$ for $t = 0$ and $t = \infty$, with initial and final conductances as typically observed in the measurement. We have analysed several cases with τ_{GB} being between 3 and 100 $\times$ faster than τ_{G}, but we have not obtained significant differences between these scenarios. A simulation is shown in Fig. 4.11(c), normalised to initial and final conductance values, with $\tau_{\text{G}} = 50\,\text{min}$ and $\tau_{\text{GB}} = 5\,\text{min}$.
A fast initial change in the normalised conductance due to a small τ of the grain boundaries is observed, followed by a long tail with only small variations in G over time, caused by the slower equilibration of the grains. After 30 min the normalised $G(t)$ yields about 10 %. Only in the intermediate region, differences between in- and out-diffusion are observed, where the reduction is slightly faster (assuming same bulk diffusion rates and no surface exchange). Both processes can be well fit using a two τ model as in Eq. (4.1). The fitted relaxation times are within an error of less than 5 % to the initial values fed to the simulation if τ_{GB} is sufficiently larger than τ_{G}.
In a first approximation, this excludes that any grain boundary effect is responsible for the asymmetry observed, which in fact has been ascribed to surface exchange kinetics in the previous section.

- **Ionosorption model:**
  In the field of metal oxide gas sensors the ionosorption model is often used to describe their gas sensing properties [97]. The chemical adsorption of oxygen leads to a coverage of different charged species (O^-, O^{2-}, O_2^-) at the surface. A space charge layer is formed in close proximity to the surface. For several p-type materials it is observed that the carrier density of the majority charge increases due to the trapped electrons from the valence band in the surface. This accumulation of charges causes a decrease in resistivity.

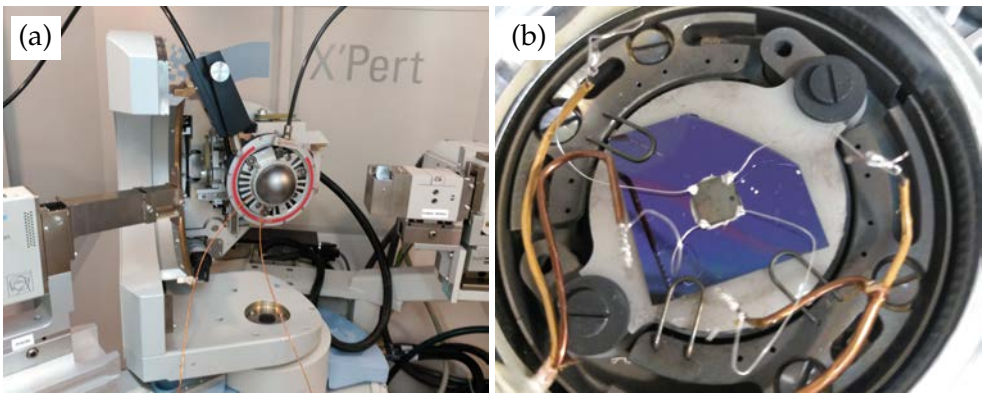

FIGURE 4.12: (a) Measurement setup used for *in situ* XRD measurements and (b) sample holder with mounted sample, contacted with four electrodes for simultaneous ECR measurements.

The dimension of the space charge region can be estimated using the Debye length λ_D, which scales proportional to $\sqrt{T/n_H}$, with the temperature T and the charge carrier density n_H. A high coverage of ionosorbed oxygen species is observed on p-type materials [98]. Thus a possibly continuous low resistance percolation path at the surface of the film might cause a parallel resistor model. In this case the low resistance path is mainly determining the total resistance.
Optimally doped YBCO exhibits a comparatively high charge carrier density, so fluctuations in local charge densities are screened within short distances. On the other hand the charge carrier density n_H is reduced by up to 2-3 orders of magnitude during the performed oxygen exchange measurements. A space charge layer could be formed during the out-diffusion measurement which might affect the symmetry of in- and out-diffusion processes.

Subsequent a study using environmental high temperature XRD measurements is presented. This *in situ* technique allows to detect stoichiometric changes by following the XRD pattern of a thin film. This method is highly bulk sensitive and is not expected to be influenced by the above mentioned phenomena. Thus *in situ* XRD measurements can be used to test the validity of ECR measurements as shown in the following two subsections.

4.3.1 Analysis of XRD *in situ* measurements

In situ X-ray diffraction measurements are performed using an X'Pert PRO MRD diffractometer from *PANalytical*, equipped with a 1D detector form *PIXcel* and a domed hot stage model from *Anton Paar*. The setup is shown Fig. 4.12. A monochromatic Cu Kα_1 source is used. The 1D detector has 255 channels aligned in 2θ direction with a resolution of about 0.01 °. Therefore a range of 2.51 ° can be simultaneously measured. A graphite dome is used to seal the sample chamber from environment. Different atmospheres above the sample were established using a flow of 0.5 l/min of either dry air (21.0 % O_2), or a mixture of nitrogen and oxygen for low $P(O_2)$ atmospheres. A detailed description of the setup and experimental methodology can be found elsewhere [99].

With a 1D detector, variations in 2θ peak positions can be directly observed and correlated to changes in the average cell parameter. For the *in situ* measurements the (006) reflection of YBCO is chosen due to its high intensity and proximity to the (200) substrate reflection, which is used as a reference in control scans. The tail of the LAO reflection is negligible. The scanned 2θ range is set to 44.5 ° - 47 ° and the resolution in time is about 10 sec per scan. From previous *ex situ* measurements with a fully deoxygenated sample in pure N_2 gas flow, a maximal peak shift of less than 0.5 ° is expected and considered in the chosen 2θ range.

For the study of oxygen kinetics by XRD we have used a 250 nm thick CSD YBCO film coated with a silver layer of 100 nm. Relaxation measurements were performed at temperatures between 600 and 400 °C. The oxygen partial pressures used were 5 mbar and 210 mbar for reduction and oxidation, respectively. The latter is the maximum possible $P(O_2)$ in this setup, and therefore lower in comparison to the standard high $P(O_2)$ of 1 bar used ECR measurements in our setup.

At the beginning and end of every temperature dwell a control scan was performed recording a wider 2θ range, including the LAO (200) and YBCO (007) reflections to ensure correct alignment and detect potential phase changes. Additional control scans were performed before and after the whole temperature process. The initial control scans at room temperature and 600 °C are shown in Fig. 4.13(a). From this two measurements the thermal expansion coefficient of the $LaAlO_3$ substrate *a*-lattice parameter is obtained to be $9.8 \cdot 10^{-6}\,K^{-1}$, which is close to the reported one of $8.8 \cdot 10^{-6}\,K^{-1}$ [100]. The shift in the *c*-parameter of YBCO is bigger and about 0.21 Å, compared to 0.02 Å for LAO. The thermal expansion coefficient of YBCO is reported to be about $13 \cdot 10^{-6}\,K^{-1}$, for thin films as well as bulk material [101–103]. From the presented measurements an expansion coefficient of $32 \cdot 10^{-6}\,K^{-1}$ is obtained,

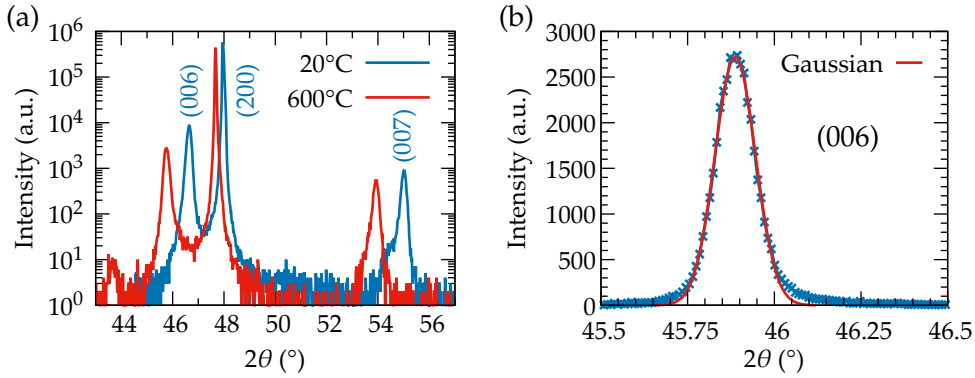

FIGURE 4.13: (a) Control scan at 20 °C and 600 °C, including the (006) and (007) YBCO reflection and the LAO substrate peak (200) and (b) Gaussian fit of XRD pattern within the 2θ range of the 1D-detectors to calculate the c-parameter.

which is more than twice the purely thermal expansion coefficient. This additional expansion is expected due to the loss of oxygen during annealing in dry air atmosphere at elevated temperatures. From the bulk phase diagram at 600°C and 0.21 bar of oxygen, one would expect an oxygen content of the YBCO film of about $O_{6.65}$ [21, 80].
A recent study reported that α shows only a very weak dependence on oxygen stoichiometry [104]. Thus, it is reasonable to assume that the reported YBCO thermal expansion coefficient is valid within the analysed temperature and YBCO oxygen stoichiometry range and one can calculate the corresponding c-parameter at room temperature from the measured one at 600 °C, c_{T_2}, using:

$$c_{T_1} = \frac{c_{T_2}}{1 + \alpha(T_2 - T_1)} = 11.798, \tag{4.8}$$

with $c_{T_2} = 11.887$ and T_1 and T_2 being 20 and 600 °C, respectively. With the relation between the c-parameter and the oxygen content reported in [105, 106], one can assess the oxygen content of the annealed sample at 600 °C to be $O_{6.50}$, which is slightly lower than the one expected from the phase diagram. This discrepancy might be explained by either a thermal expansion coefficient $\alpha(O_{7-\delta})$, depending on the oxygen content $(7 - \delta)$, or a systematic error in the evaluation due to the used reference values. The estimation of the oxygen content will be more thoroughly addressed at the end of this section. The given results for YBCO are based on the evaluation of the (006) and (007) reflections, which are found to be very similar.

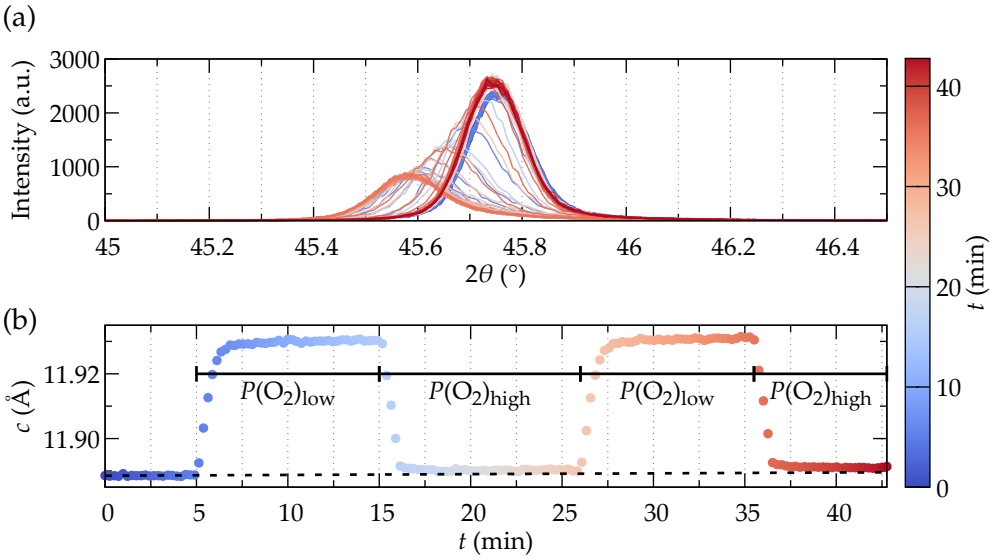

FIGURE 4.14: (a) Time evolution of YBCO (006) peak at 600 °C. Changes are induced by variations in the oxygen partial pressure. (b) Extracted c parameters from the 2θ scans in (a).

During the following *in situ* measurements, only the (006) reflection was recorded. Each individual scan of the peak is fitted with a Gaussian as shown in Fig. 4.13(b). From the 2θ position of the reflection the c-parameter is calculated using Bragg's law $c = \frac{\lambda}{2\sin\theta} l$.

The time evolution of the YBCO (006) reflection at 600 °C due to changes in the atmosphere is shown in the upper graph of Figure 4.14. The colouring of the different lines corresponds to the time. Smooth transitions between two stable positions are observed. In Fig. 4.14(b) the extracted c-parameter values are depicted and the switches in atmosphere are indicated.

The atmosphere is switched first from an oxygen rich to an oxygen poor one. The crystal structure expands due to the loss of oxygen and the reflection shifts to lower 2θ values. The c-parameter changes from 11.89 Å to 11.93 Å, a relative expansion of 0.34 %. The new equilibrium state is reached within minutes. The time evolution of c can be modelled by an exponential law with a certain relaxation time τ with $c(t) \propto e^{-t/\tau}$. Similar to ECR measurements, the out-diffusion process can be better modelled using a second parallel exponential decay, taking into account the observed small drift after the initial big change in c.

The black broken line in Fig. 4.14(b) is the extrapolation of the initial unit cell parameter. A small shift to higher values is observed with subsequent alternating steps in $P(O_2)$. The same is detected for the reduction process,

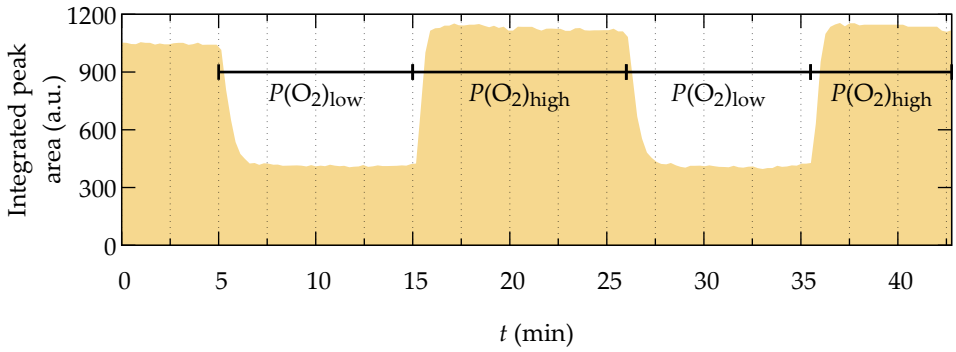

FIGURE 4.15: Dependence of integrated peak area of YBCO (006) reflection on external $P(O_2)$ at 600 °C.

but the change is less significant. Similar phenomena are reported, *e.g.* for $La_2NiO_{4+\delta}$ thin films [99, 107], where this irreversibility was attributed to effects at the film-substrate interface and partial decomposition under N_2 atmosphere.

The dependence of the integrated peak area on the $P(O_2)$ is shown in Fig. 4.15. The area decreases by a factor of about 2.7, upon switching to a low oxygen atmosphere at 600 °C. This is caused by a change of the crystals structure factor due to overall modifications of the electron density along the unit cell, mainly by the removal of oxygen in the chain sites. This influence of oxygen doping on interatomic distances, bond lengths and electron distribution within the unit cell was studied *ex situ* and reported in detail previously [108, 109]. For all analysed temperatures, a drop in the integrated peak area of a factor 2-3 is observed, but no clear temperature dependence was found.

Several isotherms are measured to extract the temperature dependence of relaxation times with the aim to compare it with in-house ECR measurements. Such a comparison is shown in Fig. 4.16(a) for normalised conductance $G(t)$ and $c(t)$ parameter values at 500 °C. While the out-diffusion pressure of 5 mbar was the same in both measurements, the in-diffusion pressure was limited to 0.21 bar for XRD and to 1 bar for ECR measurements.
Small differences in the time dependence between ECR and XRD measurements are detected for oxygen in- and excorporation at 500 °C, with the electrical measurement being the faster one. For the normalisation of X (representing G and c) of the in-diffusion process shown in Fig. 4.16(a), X_0 and X_∞ are swapped for clarity (representing $1 - \exp[-t/\tau]$ instead of $\exp[-t/\tau]$).

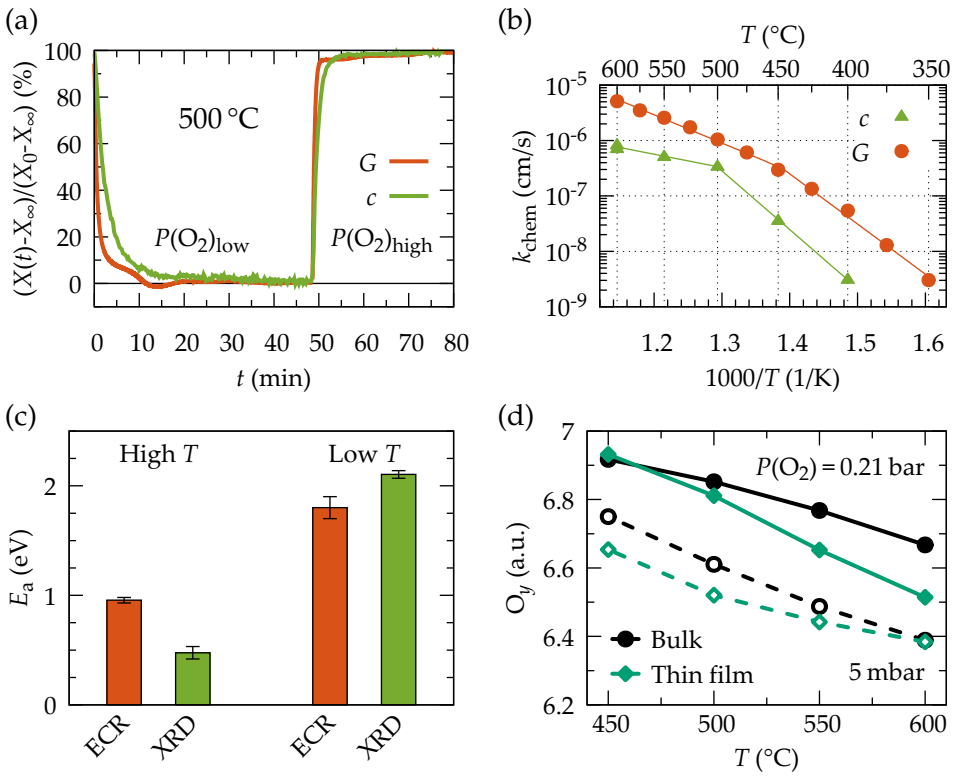

FIGURE 4.16: Comparison of XRD and ECR kinetic measurements of Ag coated CSD YBCO samples performed in different setups: (a) normalised conductance G and c-parameter values for an out- and in-diffusion process at 500 °C; for in-diffusion X_0 and X_∞ in normalisation are swapped for better representation: $(X(t) - X_0)/(X_\infty - X_0)$. (b) Arrhenius plot and (c) extracted activation energies for oxidation measurements. (d) Estimated oxygen content for $YBa_2Cu_3O_y$ from *in situ* c-parameter measurements compared to expected bulk values from the phase diagram.

Bigger differences between the two measured samples are observed in an Arrhenius plot for the oxidation process, shown in Fig. 4.16(b). The XRD measurement reveals the same general trend, with a kink around 500 °C and two activation energy regimes, but significant changes in the exchange rates can be observed. The extracted activation energies for the oxidation of silver coated samples are shown in Fig. 4.16(c). At high temperatures XRD measurements show a 50 % lower activation energy, while at low temperatures E_a obtained for both techniques are about 2 eV.
At this point it is not clear, whether the observed differences in exchange rates

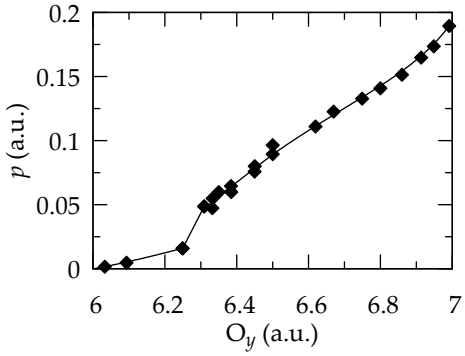

FIGURE 4.17: Plot used to estimate oxygen content O_y from calculated doping p, reproduced from [106] with permission.

and E_a arise due to different setup characteristics, such as the gas flow above the sample, which is influenced by the total gas flow and the sample chamber geometry, microstructural differences in the measured samples or real differences in the sensitivity of the measurement techniques. The different oxygen partial pressures for the oxidation process are not thought to be the main reason, since same trends are observed for the reduction process, where 5 mbar are used in both measurement setups. Though, as shown in section 4.4.3, the step size in $P(O_2)$ might affected the E_a and a contribution to the observed differences cannot be excluded.

We have analysed the oxygen content as a function of temperature and pressure. Therefore, as described in the beginning of this section, we have projected the measured c-parameter to room temperature using Eq. (4.8), assuming the thermal expansion coefficient α to be independent of the oxygen content. With the corresponding room temperature c-parameter, the doping level of the sample can be calculated using the empirical equation:

$$p = 9y + 1.5 \cdot 10^9 y^6, \tag{4.9}$$

with $y = 1 - c/c_0$ and $c_0 = 11.925\,\text{Å}$, which was found in [105] for 30 nm thick YBCO films. A similar formula was reported previously for YBCO single crystals, with different pre-factors [106]. The estimated doping in turn is used to assess the oxygen content using Fig. 4.17, reproduced from [106].

The analysis of the oxygen content of the thin film is shown in Fig. 4.16(d) and compared to bulk phase diagram values from literature [21]. Open symbols correspond to low, full ones to high $P(O_2)$, respectively. We observe the expected trend of increasing oxygen content with decreasing temperature, but

measured values deviate up to 0.15 from the reported values. For the incorporation process a deviation towards lower oxygen content O_y than expected from bulk, is observed at high T (the measured c-parameter is larger than expected from bulk). For reduction (open symbols) a similar trend is seen but with a deviation at low T.
We note, that the empirical formula used to estimate the doping, was obtained for 30 nm thick YBCO films. As it will be shown in section 4.6.1, for such thin films, macroscopic strain induced by lattice mismatch of the layer with the substrate causes a decrease of the oxygen content and therefore an increase of the c-parameter. This could introduce a systematic error in the evaluation of the oxygen content. Additional errors could arise from an oxygen content dependent thermal expansion coefficient $\alpha(\delta)$ and artefacts due to a smaller thermal expansion of the substrate.

We can summarize the presented *in situ* XRD measurements that we found very similar trends for oxygen exchange kinetics as compared to electrical conductivity measurements, including similar time constants and different activation energy regimes. The observed differences in absolute values could arise due to the differences in the ECR and XRD measurement setups. To exclude this factor we have performed simultaneous measurements as described in the following section.

4.3.2 Simultaneous ECR and XRD *in situ* oxygen exchange measurements

To perform both, ECR and XRD measurements simultaneously, a sample is glued with silver paint to a silicon wafer, which is then mounted to the hot stage. Prior four thin silver electrodes with a length of several centimetres are fixed to the corners of the sample using high temperature silver paint and dried out over night in a dry box. The wires are then connected to the contacts provided inside the XRD sample chamber in a delicate preparation step (see Fig. 4.12(b)). The chamber contacts are embedded into a thin aluminium ring, which is fixed in between the hot stage and the sealing graphite dome, blocking measurements at low angles.

Kinetic measurements are performed at 550, 500 and 475 °C. Before a current is applied, an initial $P(O_2)$ cycle is measured using only x-ray diffraction technique. Subsequent a current of 100 µA is applied for simultaneous ECR measurements, with positive, negative and zero bias. The resolution in time is about 1 s for the ECR technique and 10 s for XRD. Applying a small current to the sample does not lead to any change in the measured c-parameter

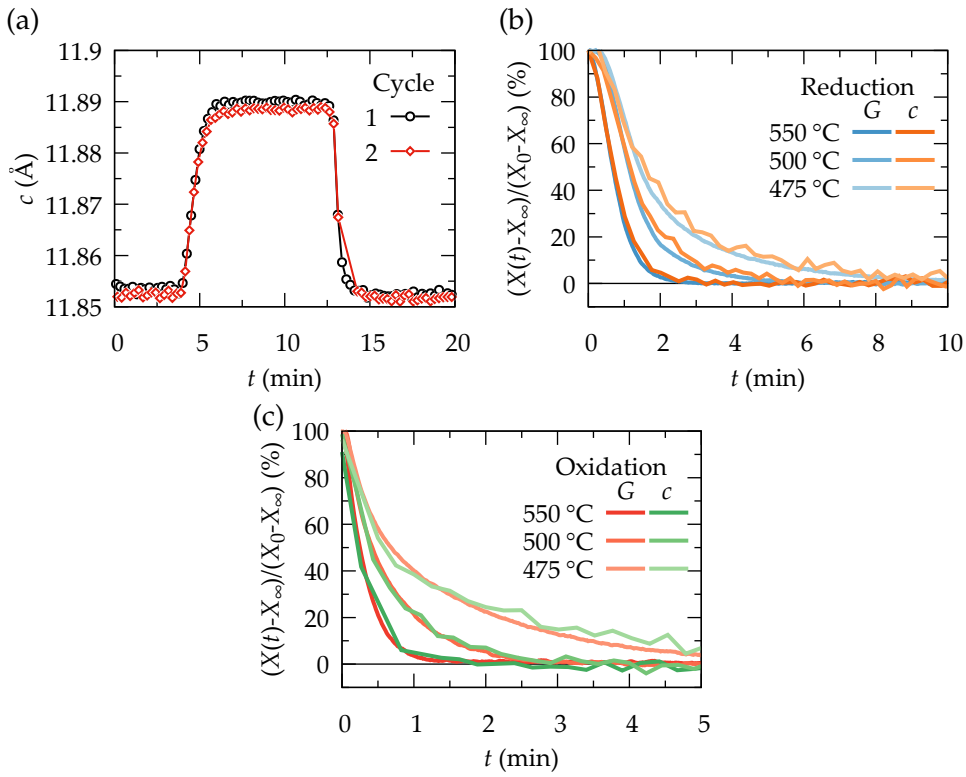

FIGURE 4.18: (a) XRD scan without (1st cycle) and with applied current (2nd) for ECR measurements at 550 °C. (b) & (c) Comparison of simultaneous XRD and ECR kinetic measurements: Normalised *in situ* data for conductance G and the lattice constant c at different temperatures for reduction and oxidation, respectively.

(see Fig. 4.18(a) where at the beginning of the second cycle a current is applied). Rather a small shift in saturation values of c is observed as previously in Fig. 4.14(b) due to some irreversibility of the process.

The main findings of the simultaneous measurements are shown in Fig. 4.18(b) and (c), where the normalised conductance G and c-lattice constant are compared for the process of oxygen excorporation and incorporation, respectively. At all three temperatures investigated the time dependence of c and G is very similar, respectively. Therefore, it is concluded that both techniques are equally bulk sensitive and fully integral, excluding the influence of percolation currents due to grain boundaries or spatial inhomogeneities of the diffusion coefficient and surface related effects. Therefore the observed asymmetry

between in- and out-diffusion exchange rates can be excluded to be an artefact of the measurement process.

4.4 Rate determining step of YBCO oxygen exchange kinetics

The loading of oxygen into the YBCO structure is an important step in the fabrication of long length coated conductors. The understanding of the ongoing processes is necessary to optimize the final oxygen content and conductor properties for operations. For oxygen in- and excorporation one can distinguish between mechanisms related to the surface and to the bulk.
In the field of mixed ionic-electronic conductors (MIEC), which are widely used as cathode material in solid oxide fuel cells (SOFC), the oxygen exchange is subject to intensive research for more than a decade [34, 110, 111]. There is a broad consensus that a mechanism related to the surface is limiting the oxygen exchange rates for thin oxide films [37]. Historically within the YBCO community mainly bulk diffusion was considered as the rate determining step (RDS), which holds for single crystals with low defect concentrations [74, 85, 112]. Already at the early stage of YBCO thin film production several authors proposed that surface exchange processes have to be taken into account [113, 114], but only in the following decades its overall importance for YBCO became clear [63, 82].
As it was shown in previous sections, an asymmetry for in- and out-diffusion rates indicated the significance of surface exchange mechanisms, as did the enhanced exchange rates due to surface modifications by silver coating. In section 2.2 we have introduced all relevant transport and reaction mechanisms under consideration (see step 0-6 in Table 2.1 on p. 18). The oxygen partial pressure above the sample can be changed sufficiently fast in our setup, so that step 0 can be excluded to be the RDS. In the following we will present a study to determine which of the remaining steps 1-6 is the RDS of silver coated CSD-YBCO thin films.
We have used Ag coated films to shorten measurement times and enable the analysis of oxygen exchange also at low temperatures. As we will see in Chapter 5, silver coating effectively changes the RDS. Therefore all conclusions from this section are valid *only* for Ag coated YBCO thin films.

4.4.1 Bulk *vs.* surface: the importance of surface reactions for YBCO oxygen exchange kinetics

In the analysis of oxygen exchange one generally distinguishes between surface and bulk related mechanisms. In a first step we assume that oxygen incorporation from the gas phase into the bulk (far from the surface) consists of only two elementary steps:

- **Surface mechanism:** Firstly, simplified within one single step, the direct incorporation of oxygen into a vacancy (including dissociation and charge transfer by oxidation) into the first atomic surface layer [39]:

$$1/2\mathrm{O}_2 + \mathrm{V}_\mathrm{O}^{\bullet\bullet} \rightleftharpoons \mathrm{O}_\mathrm{O}^\mathrm{x} + 2h^\bullet \tag{4.10}$$

- **Bulk diffusion:** Secondly, the diffusion of atomic oxygen within the bulk, along and across internal interfaces (neglecting corresponding holes, as electrical conductivity is high):

$$\mathrm{O}_\mathrm{O}^\mathrm{x}(x) \rightleftharpoons \mathrm{O}_\mathrm{O}^\mathrm{x}(x') \tag{4.11}$$

If one assumes that surface reactions are much faster than bulk diffusion, the first layer below the surface is *quasi* instantaneously balanced to any change in atmosphere. Due to the fact that for diffusion processes $\vec{k} = \overleftarrow{k} \equiv k$, the problem reduces to a concentration gradient across the bulk of the material with the net reaction rate:

$$\Re = k\left([A] - [B]\right) = k\Delta c \tag{4.12}$$

In this case the incorporation and release of oxygen corresponds to the exact same process, but with flipped sign of the concentration gradient $\frac{\mathrm{d}c}{\mathrm{d}x}$, corresponding to Fick's first law [115]:

$$j = D_\mathrm{chem}\frac{\mathrm{d}c}{\mathrm{d}x} \tag{4.13}$$

with the net diffusion flux j. Therefore, no difference in the measured saturation times between oxygen in- and excorporation is expected. This assumption still holds even if the diffusion coefficient D_chem depends on the vacancy defect concentration, when measured with a fully integral method. Additional effects, *e.g.* as measurement artefacts due to percolation currents were already excluded in the previous section from contributing to an asymmetry.

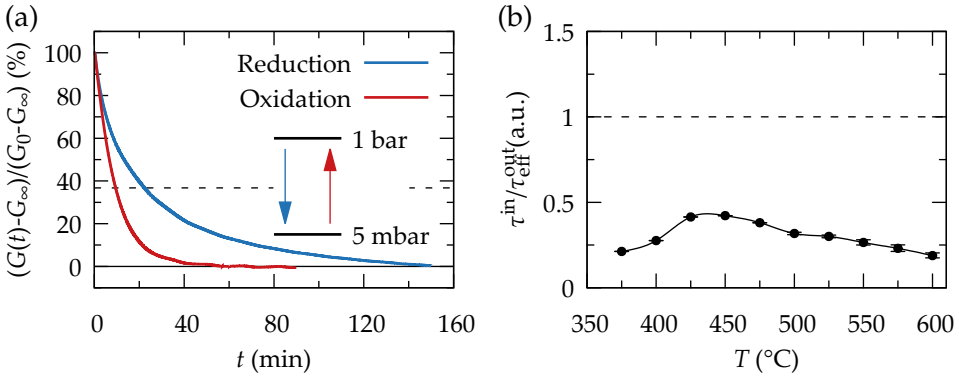

FIGURE 4.19: Observed asymmetry of reduction and oxidation processes of Ag coated 250 nm CSD film: (a) normalised conductances at 400 °C reveal differences in time evolution, (b) ratio of saturation times for different temperatures.

To confirm that the RDS is a surface mechanism we look specifically at the exchange rates of the oxidation and reduction process in a two step, binary oxygen pressure measurement, where the pressure is changed between $P(O_2)_{high}$ and $P(O_2)_{low}$, as described above. One can normalise the measured conductance using Eq. (4.1) to its initial and final values to obtain a clear plot of the time evolution. This is done for a silver coated, 250 nm thick CSD film in Fig. 4.19(a) for a reduction process with an initial pressure of 1000 mbar and a final pressure of 5 mbar and the subsequent oxidation, with the reverse change in pressure, as depicted in the inset of the graph. Oxidation is faster by a factor of ≈ 3 compared to reduction, with $\tau^{in} = 9.3$ min and $\tau^{out}_{eff} = 26.4$ min. For a single rate controlled process the intersection of the data with the dashed horizontal line at $1/e \approx 37\,\%$ defines the saturation time τ.

A typical example of the ratio of the relaxation times of oxidation and reduction as a function of T is shown in Fig. 4.19(b). For the case of out-diffusion the effective saturation time is used. The ratio is far below unity for all investigated temperatures. The deviation from unity can only be explained if the RDS is linked to an elementary step within the surface, as their reaction rates depend on the oxygen partial pressure via the surface coverage, as discussed in detail in section 2.2. Differences in the forward and backward Gibbs free enthalpies $\vec{G}$ and $\overleftarrow{G}$ of *e.g.* dissociation and recombination of O_2 (step 3) or of vacancy formation and annihilation (step 5) could contribute as well to the asymmetry between oxidation and reduction rates. Additionally the activation energies of the different steps might be pressure dependent and therefore the rate determining step itself might change in the analysis at different pressures. We will address this issues in the next section. However, we can

conclude here that bulk diffusion (step 6) is not the RDS in YBCO thin films, which is in agreement with enhanced reaction rates upon surface modifications (Ag coating).

4.4.2 Origin of oxidation and reduction reaction rate differences

At the beginning of this chapter we have shown that oxidation is faster than the reverse process, the reduction ($k_{\mathrm{in}} > k_{\mathrm{out}}$), even though activation energies were lower for out-diffusion as compared to in-diffusion ($E_{\mathrm{a,out}} < E_{\mathrm{a,in}}$), as determined in section 4.1. In the previous section we argued that any asymmetry in activation energy and reaction rates can only be related to surface exchange reactions and we were able to exclude step 6 to be the rate determining step. Remaining possible candidates for the RDS are step 1-5, comprising all surface processes of adsorption until incorporation into a vacancy.

In this section we will address the three possible origins for the asymmetry of oxidation and reduction that can be inferred from differences in Eq. (2.13) and Eq. (2.13) for both processes:

(a) differences in the pressure dependence of surface exchange coefficients for oxidation $k_{\mathrm{chem,in}}$ and reduction $k_{\mathrm{chem,out}}$ due to a different surface coverage

(b) differences in the forward and backward free enthalpies $\vec{G}$ and $\overleftarrow{G}$ and pre-exponential factors $\vec{k}_0$ and $\overleftarrow{k}_0$.

(c) different rate determining steps for in- and excorporation because the activation energies of the particular steps depend on oxygen pressure.

Case (a): To analyse the influence of the surface coverage on surface reaction rate constants we have performed a new type of *in situ* experiment, where the pressure is changed between three values (1000, 5 and 0.01 mbar) in 4 steps. The procedure of these ternary measurements is schematically drawn in the inset of Fig. 4.20(b). The $P(O_2)$ is lowered from 1000 mbar in two steps, first to 5 mbar (I↓) and then to 0.01 mbar (II↓). Subsequently, the pressure is raised to 5 mbar and then to 1000 mbar (II↑ and I↑, respectively). In this experiment one can extract in- and out-diffusion kinetics in the case of the same coverage $\Theta_{\mathrm{out}} = \Theta_{\mathrm{in}}$ by comparing I↓ and II↑.

The conductance as a function of time for a ternary $P(O_2)$ measurement at 450 °C is shown in Fig. 4.20(a) for a 250 nm thick CSD-YBCO (Ag) film. The background colouring indicates the different oxygen atmospheres. One can observe that I↓ saturates faster than II↓, as well as I↑ reaches equilibrium in shorter time compared to II↑.Thus, for oxidation and reduction processes reaction rate constants are higher at higher final oxygen pressures.

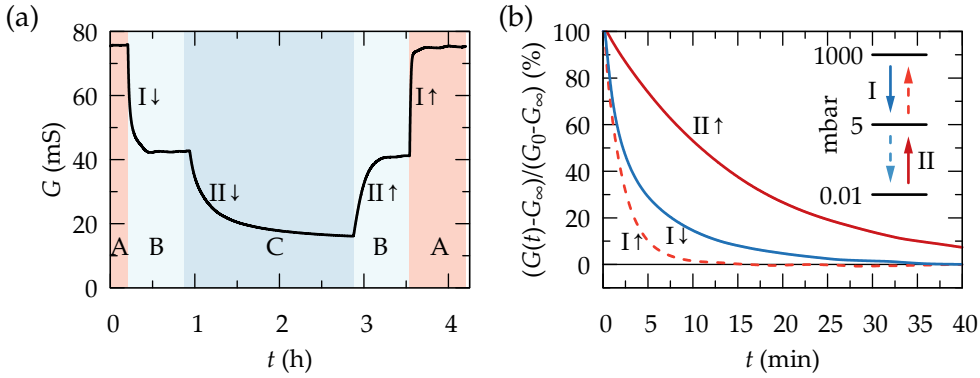

FIGURE 4.20: 3-step (ternary) pressure measurements at 450 °C for 250 nm CSD-YBCO (Ag) film: (a) G as a function of time; atmosphere is switched from A $\overset{\text{I}\downarrow}{\rightarrow}$ B $\overset{\text{II}\downarrow}{\rightarrow}$ C $\overset{\text{II}\uparrow}{\rightarrow}$ B $\overset{\text{I}\uparrow}{\rightarrow}$ A, with A=1000 mbar, B=5 mbar, C=0.01 mbar as indicated with different background colouring. (b) Normalised G for oxidation (red) and reduction (blue) process with final $P(O_2)$ of 5 mbar; dashed red line corresponds to oxidation at 1000 mbar, as indicated in the inset.

P_{low}	P_{high}	P_{final}	τ_{in}/τ_{out}
0.01	1000	5	**3.1**
1	100	10	**2.4**±0.4
10	1000	100	**2.6**

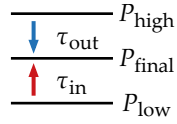

TABLE 4.1: Tertiary $P(O_2)$ measurements with different final pressures at 450 °C; all pressures are given in mbar.

To highlight this finding we compare the normalised conductances for the case of oxidation (red lines) with final pressures of 5 mbar (II↑) and 1000 mbar (I↑) in Figure 4.20(b). The oxygen incorporation process is substantially slower if performed at lower oxygen partial pressure. The same is found for the process of oxygen excorporation (comparison not shown). These results confirm that the different oxygen surface coverages in binary measurements contribute to the observed asymmetry between in- and out-diffusion, as in-diffusion saturation times are obtained at higher pressure than out-diffusion relaxation times.

Case (b): We focus now on the oxidation and reduction process with the same final pressure of 5 mbar II↑ and I↓, respectively (solid lines in Fig. 4.20(b)). In both cases the process is triggered by a jump in $P(O_2)$ of about $2\frac{1}{2}$ orders of magnitude.

Under this conditions we find that the reduction process is significantly faster than oxidation.

The oxidation saturation time τ_{in} is about 15 min, while $\tau_{out,eff} \approx 5$ min for reduction. The ratio $\tau_{in}/\tau_{out,eff}$ is given in Table 4.1 and it is compared to results of ternary measurements with different step sizes in pressure (all at 450 °C). Independent of the initial and final partial pressure and therefore hole and vacancy concentrations, it is found that the reduction process is about a factor 2.5 - 3 faster than oxidation at 450 °C.
Equivalent to the discussion in section 4.4.1, no difference in reaction rate constants is expected for any diffusion limited process, which is only based on variations in concentration of one particular specie. The fact that we find an asymmetry for oxidation and reduction surface reaction rate constants ($k_{chem,in} \neq k_{chem,out}$) at the same final pressure, allows us to exclude the mechanism of surface diffusion of oxygen ions (step 4 in Table 2.1) to be the rate determining step in Ag coated YBCO.

We conclude that the reduction process is significantly faster than oxidation if measured at the same oxygen pressure at 450 °C. This asymmetry goes beyond the typically observed differences strongly governed by changes in the coverage and it is directly linked to different forward and backward free enthalpies $\vec{G}$ and $\overleftarrow{G}$ and pre-exponential factors k_0. Forward and backward reaction rate constants can be written as

$$\vec{k}_{in} = \vec{k}_0 \exp\left[-\frac{\Delta\vec{G}}{k_B T}\right] \tag{4.14}$$

and

$$\overleftarrow{k}_{out} = \overleftarrow{k}_0 \exp\left[-\frac{\Delta\overleftarrow{G}}{k_B T}\right]. \tag{4.15}$$

Differences in $\vec{k}_{in}$ and $\overleftarrow{k}_{out}$ at the same $P(O_2)$ might arise due to different chemical barriers $\vec{G}$ and $\overleftarrow{G}$ for adsorption to and desorption from the surface, O_2 dissociation and recombination and in- and excorporation into/from the lattice structure of oxygen ions, respectively.

Case (c): Further we have studied if the activation energies of the oxidation and reduction process depend on the oxygen partial pressure itself. Therefore we have performed ternary measurements, as shown above in Fig. 4.20(a), at several temperatures. The resulting surface exchange coefficients are shown in an Arrhenius plot in Fig. 4.21(a) for the two oxidation steps at 5 mbar and 1 bar, with activation energies of 0.9 eV and 0.8 eV, respectively. That the E_a

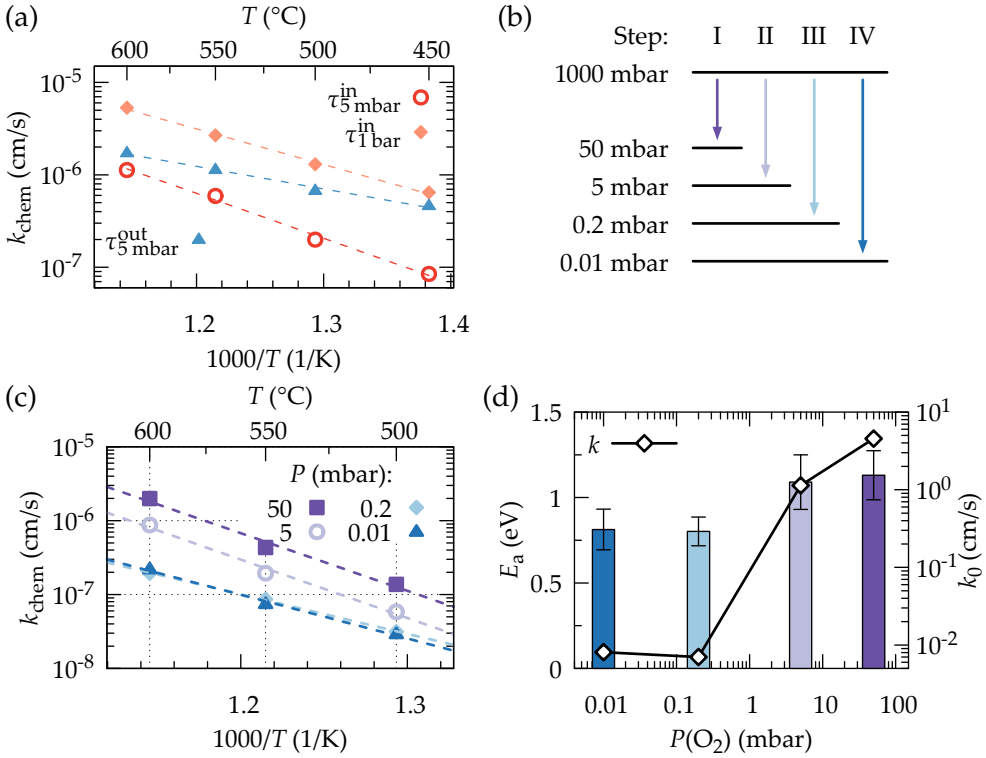

FIGURE 4.21: 250 nm Ag coated CSD-YBCO film: (a) Arrhenius plot of oxidation processes at final pressures of 5 mbar and 1 bar, extracted from ternary measurements at different temperatures and k_{chem} for reduction at 5 mbar. (b), (c) & (d) Multi-step $P(O_2)$ measurement: (b) Schematic of the experimental procedure for the analysis of the pressure dependence of the reduction process. (c) Arrhenius plot for reduction processes at different atmospheres and (d) corresponding activation energies (bars) and k_0 values (diamonds, right scale).

is the same (within the errors) for both oxidation processes indicates that the RDS does not vary within the analysed pressure range. In the field of chemical solution reactions, collision theory interprets k_0 as the total number of collisions per time. Only the fraction $\exp[-E_a/k_BT]$ (probability factor) of k_0 leads to a reaction [35, 116]. Correspondingly, the increase of k_0 can be linked to the increase of surface coverage and the resulting gain of particles participating in the exchange process. The reduction process at 5 mbar is drawn as well in Fig. 4.21(a), with an activation energy of 0.5 eV. The different energy barriers for oxidation and reduction at the same final pressure of 5 mbar demonstrate

that forward and backward reactions have not the same Gibbs energies, as anticipated above.

The pressure dependence of E_a for the case of reduction was analysed in a multi-step $P(O_2)$ measurement as shown schematically in Fig. 4.21(b), where the pressure is decreased from the same initial pressure of 1 bar to various lower ones. The surface exchange coefficients k_{chem} for out-diffusion processes at different oxygen atmospheres are shown in Fig. 4.21(c) in an Arrhenius-type plot. At any given temperature the surface exchange coefficient k_{chem} increases with increasing oxygen partial pressure.

The extracted E_a and k_0 values are shown in Fig. 4.21(d) as a function of the oxygen pressure. The activation energies of the reduction process below 1 mbar are about 0.8 ± 0.1 eV and above approximately 1.1 ± 0.1 eV. This values are by a factor 2 higher than generally observed for Ag coated CSD films of comparable thickness. This is expected to be due to the long measurement duration of this kind of measurement, as increased activation energies were found as well for oxygen incorporation. This issue will be addressed in Chapter 5. However, the important result is that the observed variation in E_a over $P(O_2)$ is small, thus we assume that the same RDS is limiting the oxygen exchange within the analysed pressure and temperature ranges. On the other hand, the pre-exponential factor k_0 strongly increases with increasing $P(O_2)$ (right scale in Fig. 4.21(d)). This again shows the crucial importance of the surface coverage Θ for the process oxygen exchange, as previously concluded for **case (a)**.

Only in the simplest case of Langmuir-type adsorption for non charged particles, the adsorption energy does not depend on the surface coverage, and therefore on $P(O_2)$ [47–49]. As we generally assume that charged ions play a crucial role in the overall exchange process, we would expect a pressure dependence of the activation energy in the case that adsorption is the rate determining step. However, we do not observe such a dependence of E_a on the pressure, for neither oxidation nor reduction. This indicates that adsorption (step 1) is comparatively fast and does not limit the overall oxygen exchange reaction, as we will confirm in the next section.

We complete this section with the analysis of the temperature dependence of the equilibrium constant $K_{eq}(T)$

$$K_{eq}(T) = \frac{\vec{k}_{in}(T)}{\overleftarrow{k}_{out}(T)} \propto \frac{\tau_{out}(T)}{\tau_{in}(T)}. \tag{4.16}$$

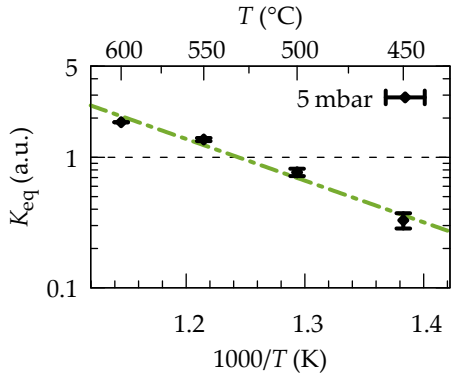

FIGURE 4.22: Van 't Hoff representation of equilibrium constant K_{eq} obtained at 5 mbar to extract standard enthalpy change of oxygen exchange reaction.

The equilibrium constant at 5 mbar is shown in Fig. 4.22 in a semi-log plot over the inverse temperature (van 't Hoff plot). We find that below approximately 525 °C reduction is faster than oxidation, thus $K_{eq} < 1$ and *vice versa* at higher temperatures. This is caused by different activation energies and k_0 values for the process of oxygen in- and excorporation. At low temperatures reduction is faster, because it is governed by a lower E_a. At high temperatures the kinetic energy of a sufficient amount of particles is high enough to surpass the activation energy barrier. Thus the pre-exponential factor k_0 becomes the determining parameter, which is higher for the case of oxidation.
The temperature dependence of the equilibrium constant K_{eq} can be expressed by the standard enthalpy change ΔH via the van 't Hoff equation [117]:

$$\frac{\mathrm{d}\left(\ln K_{eq}\right)}{\mathrm{d}(1/T)} = -\frac{\Delta H}{R}, \tag{4.17}$$

with R being the ideal gas constant. H is extracted by a linear fit from the van 't Hoff plot in Fig. 4.22. We observe an increase of K_{eq} with increasing T, thus the underlying reaction is an endothermic process with $\Delta H \approx 0.6\,\mathrm{eV} > 0$. Therefore the process of oxygen incorporation adsorbs energy in the form of heat. The fact that K_{eq} crosses 1 means that oxidation is either faster or slower than reduction depending on the temperature.

We are ready now to conclude on the origin fo the asymmetry of oxidation and reduction rates. In the binary electrical conductivity relaxation measurements, we conclude that the main contribution comes from the surface

coverage, which strongly depends on the oxygen partial pressure. With increasing pressure the surface coverage increases, leading to faster exchange rates. This can explain the difference in the saturation times observed in binary measurements, where reduction relaxation times are assessed at lower $P(O_2)$ than oxidation relaxation times. A second contribution comes from different free enthalpies and pre-exponential factors k_0 of the RDS for forward and backward reaction rates. This allows us to exclude surface diffusion (step 4) to be the RDS, as in any diffusion process forward and backward activation energies are identical.
Finally, from the multi-step measurements, we can conclude that the RDS does not change in the analysed temperature and pressure ranges, within the accuracy of our experiments.
In summary, case (a) and (b) contribute to the asymmetry of oxidation and reduction, while case (c) was not observed.

4.4.3 Analysis of the pressure dependence of reaction rates of YBCO thin films

Up to this point we were able to exclude the transport mechanisms (step 0, 4 and 6 in Table 2.1) to be the RDS of oxygen exchange in silver coated CSD-YBCO thin films. Also the adsorption reaction (step 1) was found implausible to govern the overall oxygen exchange. To identify the RDS among the remaining candidates we thoroughly study the pressure dependence of the involved kinetics by $P(O_2)$ multi-step measurements. In these isothermal measurements, $P(O_2)_{low}$ is varied over several orders of magnitude while $P(O_2)_{high}$ is kept constant and *vice versa* respectively, as schematically shown in Fig. 4.24(c) and Fig. 4.25(b).
The following analysis can be performed due to the fact that the RDS does not vary within the investigated pressure range, as we have shown in the last section.

Reaction rates far from equilibrium

If a single step is rate determining, the analysis of the reaction rate $\Re$ can provide further insight to the physicochemical origin of the RDS. In this section we will follow the methodology for the analysis of reaction rates developed by Merkle and Maier in [36]. We recall that the net reaction rate $\Re$ can be generally written as:

$$\Re = \vec{\Re} - \overleftarrow{\Re} = \vec{k}_{in}\,[A] - \overleftarrow{k}_{out}\,[B]\,. \tag{4.18}$$

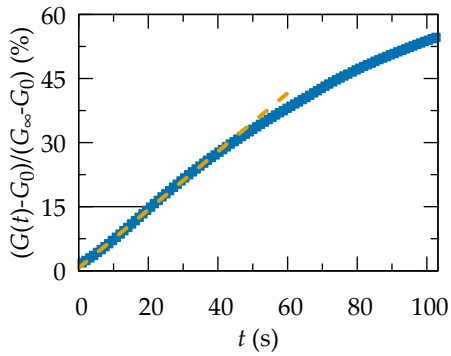

FIGURE 4.23: Evaluation of initial reaction rate for Ag/YBCO of 250 nm at 500 °C for a reduction process. $\Re|_{t\approx 0}$ is obtained by a linear fit of the experimental data below 15 %.

If the equilibrium is disturbed by large changes in the oxygen partial pressure, the reaction rate $\Re$ is determined in the beginning of the relaxation process by either the forward reaction rate $\Re \approx \vec{\Re} = \vec{k}_{\text{in}}\,[\text{A}]$ in the case of a jump to higher $P(O_2)$, or by the backward reaction rate $\Re \approx \overleftarrow{\Re} = \overleftarrow{k}_{\text{out}}\,[\text{B}]$, when the partial pressure is lowered. In this initial phase one can assume the defect concentrations to be similar to the original concentrations of the preceding equilibrium state. Thus, one can write the initial reaction rate $\Re|_{t\approx 0}$ for a forward (oxidising) step as:

$$\Re|_{t\approx 0} \approx \vec{\Re} = \vec{k} \cdot (P(\text{O}_2))^n \left[\text{O}_\text{O}^\times\right]_{\text{eq}}^x \left[h^\bullet\right]_{\text{eq}}^y \left[\text{V}_\text{O}^{\bullet\bullet}\right]_{\text{eq}}^z, \tag{4.19}$$

with the reaction rate constant $\vec{k}$ of the RDS and the initial educt equilibrium concentrations of oxygen ions, electron holes and oxygen vacancies. For a decrease in pressure (backward/reduction reaction) the initial reaction rate $\Re|_{t\approx 0}$ can be expressed as:

$$\Re|_{t\approx 0} \approx \overleftarrow{\Re} = \overleftarrow{k} \cdot \left[\text{O}_\text{O}^\times\right]_{\text{eq}}^x \left[h^\bullet\right]_{\text{eq}}^y \left[\text{V}_\text{O}^{\bullet\bullet}\right]_{\text{eq}}^z. \tag{4.20}$$

The initial reaction rates $\Re|_{t\approx 0}$ of experiments based on large $P(O_2)$ changes, can be extracted from the initial slope of the conductance $G(t)$:

$$\Re|_{t\approx 0} \sim \left.\frac{\mathrm{d}G(t)}{\mathrm{d}t}\right|_{t\approx 0}, \tag{4.21}$$

where we obtain $\mathrm{d}G(t)/\mathrm{d}t$ from fitting $(G(t) - G_\infty)/(G_0 - G_\infty) < 15\,\%$ by a straight line, as exemplarily shown in Fig. 4.23.

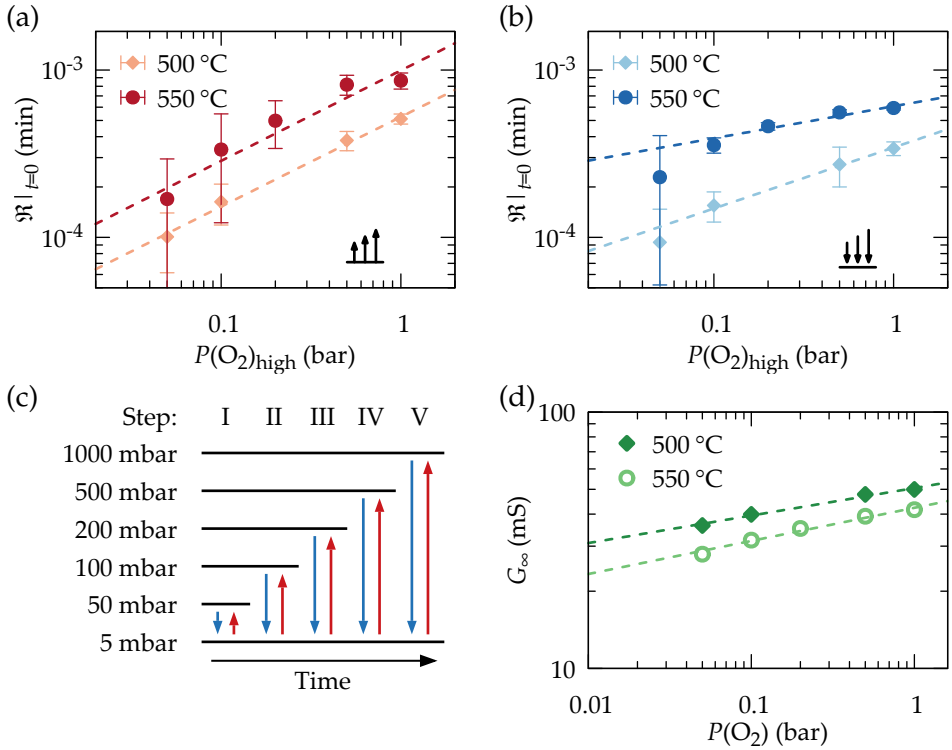

FIGURE 4.24: Pressure dependence of initial reaction rate of 250 nm CSD-YBCO (Ag): (a) Forward reaction rate $\Re|_{t\approx 0}$ for a series of large upward $P(O_2)$ jumps from same low pressure of 5 mbar at 500 and 550°C, (b) backward reaction rate for a set of large downward jumps in $P(O_2)$ to the same final pressure and (c) schematic of measurement procedure: red (blue) arrows indicate forward (backward) reactions. (d) Dependence of equilibrium conductance on oxygen pressure of 250 nm thick Ag-YBCO.

We start with the analysis of a series of large upward jumps to various higher pressures from the **same initial low** $P(O_2)$ ↟, as schematically shown with red arrows in Fig. 4.24(c). For all upwards jumps from the same initial pressure the pre-equilibrium defect concentrations are kept constant and the pressure dependence of Eq. (4.19) reduces to $\Re|_{t\approx 0} \sim P\,(O_2)^n$.
If we look at the reaction rate equations (2.17a-f), we see that the explicit pressure dependence n is either 1 if the determining mechanism involves molecular oxygen of any charge (O_2, O_2^-, O_2^{2-}, step 1-3), or $n = 0.5$ for a RDS only containing atomic oxygen (O^-, $O_O^\times$, step 4-6).
The experimentally obtained pressure dependence of $\Re|_{t\approx 0}$ for a silver coated

250 nm thick CSD YBCO film is shown in Fig. 4.24(a). We find $n = 0.54$ for $T = 500$ and 550 °C, very close to $n = 0.5$, indicating that only atomic oxygen is involved in the RDS of oxygen incorporation. In our analysis above we have shown that the transport steps 4 and 6 are not limiting the overall oxygen exchange process. Therefore we can conclusively identify the incorporation of oxygen ions into vacancies (step 5) to be the rate determining step of Ag coated CSD-YBCO thin films.

We have performed as well the reverse analysis for reduction, as schematically shown with blue arrows in Fig. 4.24(c). This experiment consists of various large jumps to the **same final low** $P(O_2)$ $\downarrow\downarrow\downarrow$. The obtained initial reaction rates are shown in Fig. 4.24(b). We find $n = 0.19 \pm 0.03$ for 550 °C and $n = 0.36 \pm 0.04$ for 500 °C for large jumps to the same final pressure of 5 mbar. If we assume that forward and backward reaction are limited by the same mechanism, namely step 5, we can write the pressure dependence for large downward jumps using Eq. (2.17e) as:

$$\Re|_{t\approx 0} \approx \overleftarrow{\Re} \propto \left[O_O^{\times}\right]_{eq} \left[h^{\bullet}\right]_{eq} \propto P(O_2)^{n_O + n_h} \tag{4.22}$$

with the defect pressure dependencies n_h and n_O for holes and incorporated oxygen and thus $n \equiv n_O + n_h$. The pressure dependences for holes and oxygen are expected to be linked via $n_h = n_O$ [45].
We can obtain the pressure dependence of holes by analysing the saturation conductance at different pressures, as shown in Fig. 4.24(d), due to the fact that $G \propto \sigma \propto [h^{\bullet}]$ in p-type conductors, as YBCO. For the presented sample we find $n_h \approx 0.15 \pm 0.03$ for $T = 500$ and 550 °C, while generally we obtain values between 0.15 and 0.2 in our experiments. From reported defect models for YBCO one would expect $n_h \leq 0.25$ at comparatively (high) oxygen partial pressures [40, 118], reasonable close to our results.
If we compare now the experimentally obtained pressure dependence of the initial reaction rate n with the $P(O_2)$ dependence of holes n_h, we indeed find that $n \approx 2n_h = n_O + n_h$ holds within the accuracy of our measurements.

For the sake of completeness we have additionally analysed the pressure dependence of the steps 1-3, where we obtain $n = 4n_h$ and $n = 3n_h$ for step 1 and 2, respectively. These relations do not hold for the experimentally obtained values of $n_h \approx 0.15$ and the averaged $\Re|_{t\approx 0}$ $P(O_2)$ dependence $\bar{n}_{avg} \approx 0.28$. Therefore step 1 and step 2 cannot account for the RDS. The process of dissociation (step 3) exhibits the same $P(O_2)$ dependence as step 5, and thus cannot be distinguished using this approach.

To persuade the reader of the validity of the methodology using initial reaction rates we show a series of large downward jumps from the **same initial high** $P(O_2)$ $\downarrow\downarrow\downarrow$. The dependence of $\Re|_{t\approx 0}$ on $P(O_2)$ is shown in Fig. 4.25(a). For

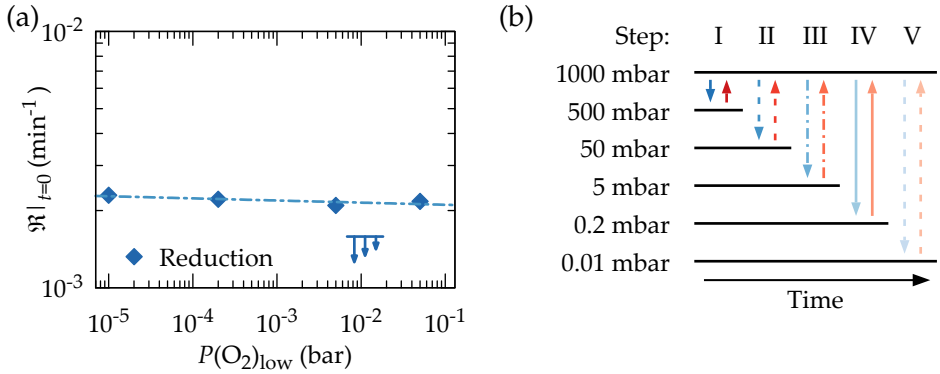

FIGURE 4.25: (a) Pressure dependence of initial reaction rate $\Re|_{t\approx 0}$ for large downward steps to the same final $P(O_2)$ of silver coated 250 nm CSD-YBCO at 600 °C. (b) Schematic diagram for multi-step measurement with constant initial/final high $P(O_2)$.

a series of atmosphere changes from 1 bar to various lower $P(O_2)$ (reduction), $\Re|_{t\approx 0}$ is found to be constant. This result is expected as the initial hole and vacancy concentrations are the same for all downward jumps and $\overleftarrow{\Re}$ does not explicit depend on the $P(O_2)$ (see Equation (4.20)).

Reaction rates close to equilibrium

In this section we analyse the equilibrium reaction rate $\Re^0$. Deviations from equilibrium are triggered by small jumps in oxygen partial pressure. We can analyse the equilibrium reaction rate $\Re^0$ for small perturbations in $P(O_2)$ using [38]:

$$\Re^0 = \sqrt{\overrightarrow{k}_{in}\,[A]_{eq} \cdot \overleftarrow{k}_{out}\,[B]_{eq}} \propto \sqrt{\frac{1}{\tau_{in}}\frac{1}{\tau_{out}}}, \tag{4.23}$$

with the saturation times of in- and out-diffusion processes. The reaction rate of each particular step in the process of oxygen in- and excorporation is linked to a certain pressure dependence, as given in Equation 2.17 for each relevant mechanism. By comparing the experimental pressure dependence with the calculated one we can provide a second method to identify the RDS and verify the analysis performed above for reaction rates far from equilibrium.

The $P(O_2)$ dependence of $\Re^0$ of Ag/YBCO triggered by small $P(O_2)$ steps is shown in Fig. 4.26(a). We observe a power-law dependence of $\Re^0$ over 2 orders of magnitude in pressure, with $\Re^0 \propto P(O_2)^n$ and $n = 0.35$ and 0.26 for 450 and 550 °C, respectively. With increasing step size of the change in oxygen

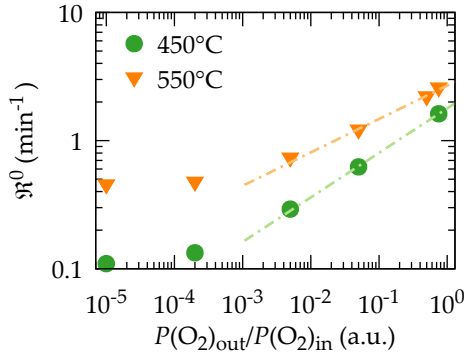

FIGURE 4.26: Pressure dependence of equilibrium reaction rate $\Re^0$ for small steps in $P(O_2)$ for silver coated 250 nm CSD-YBCO.

n_h	Step 1	Step 2	Step 3	Step 5
0.15	1.1	0.95	0.8	0.25
0.25	1.3	1.1	1	0.25

TABLE 4.2: Pressure dependence of $\Re^0$ considering the particular mechanism is the RDS for different hole concentration pressure dependencies n_h ($[h^\bullet] \propto P(O_2)^{n_h}$). We have used $n_h = n_O = -n_V$.

partial pressure, the assumption of proximity to equilibrium is no longer valid and a deviation from a power law dependence can be seen in Fig. 4.26(a).

We have calculated the pressure dependence of $\Re^0$ for two different pressure dependencies n_h of the hole concentration ($[h^\bullet] \propto P(O_2)^{n_h}$), as listed in Table 4.2, with $n_h = n_O = -n_V$ as assumed in reported defect models for YBCO [44]. $n_h \simeq 0.15$ corresponds to the value obtained in this work (see Fig. 4.24(d)), while $n_h = 0.25$ is the literature value [118]. However, in both cases the measured pressure dependence n of $\Re^0$ is very close to the one calculated for step 5 and far from the expected dependencies for the other steps. Thus, we conclude that step 5 is the RDS, as we have found in our analysis of reaction rates far from equilibrium.

Mosleh, Søgaard, and Hendriksen have performed a detail analysis of many different possible reaction mechanism containing between one and four elementary steps and different types of charges [39]. Our calculations are in very good agreement with their results for a process, where all charges are provided by the formation of holes in the valence band (see mechanism 12

and 13 in Appendix C in [39]), as *e.g.* they obtain a pressure dependence of $1/4 < n < 1/2$ for the step of oxygen incorporation into a vacancy.

This result confirms that the RDS of oxygen incorporation for Ag/YBCO thin films is the last charge transfer to reach the ionisation state of the bulk with accompanied recombination with an oxygen vacancy.

In this section we have shown evidence, that oxygen exchange kinetics of silver coated YBCO are strongly influenced by the surface coverage of adsorbed oxygen ions and are therefore determined by a surface related exchange mechanism. In- and out-diffusion relaxation times increase with decreasing pressure, linked to a decrease in oxygen coverage. In a binary oxygen pressure measurement, oxidation is faster than reduction due to the higher coverage Θ at all investigated temperatures. If reduction and oxidation reaction rates are analysed for the same final pressure, reduction is found to be faster at low temperatures, while oxidation is faster at high temperatures. This temperature dependence is understood to be due to different activation energy barriers and k_0 values of the two processes. From this asymmetry at the same pressure, surface diffusion (and in general any diffusion process) can be excluded of being the RDS as diffusion has the same activation energy E_a for forward and backward reaction.

We have further shown that the rate determining step must only consist of atomic oxygen. The analysis of the reaction rates close to equilibrium $\Re^0$ and the initial reaction rate $\Re|_{t\approx 0}$ far from equilibrium at different temperatures consistently leads to the conclusion that oxygen in- and excorporation for thin YBCO films coated with Ag is limited by the last elementary step related to the surface (step 5), consisting of charge transfer and oxygen incorporation into a vacant oxygen site within the crystal lattice.

Also for the case of non-Ag coated YBCO films a surface related mechanism limits the overall oxygen exchange. At the end of Chapter 5 we will be able to conclude on the RDS of pristine YBCO.

4.5 Microstructural influences of different growth techniques on oxygen exchange kinetics

The research on HTS coated conductors is driven by various requirements for different applications, operating either at high T and low magnetic fields, at intermediate temperatures and fields or at low T and high magnetic fields. Researchers follow numerous approaches to improve superconducting properties for these conditions by *e.g.* the implementation of artificial defects of various dimensionality to pin magnetic vortices at different temperatures, or by

cation substitution to increase self-field critical currents by increasing the condensation energy. We will analyse the influence of several such approaches on the oxygen exchange kinetics, as modifications of the microstructure might have crucial impact on the oxygenation process.

Bulk diffusion in YBCO single crystals was found to be up to 10^6 times faster in the superconducting CuO_2 planes along the *ab*-direction than perpendicular to it in *c*-direction [119]. Therefore it is assumed that diffusion along the (00l) direction is bypassed by high diffusivity channels as grain boundaries and via pores [74, 104]. Different growth techniques cause variations in the microstructure affecting the amount of pores, grain size and grain boundary density, *etc*. We remind that surface reactions were found to be the rate determining step of oxygen exchange in pristine Ag and non-Ag coated YBCO thin films. However, a modification of the microstructures could potentially decelerate bulk diffusion in YBCO. Therefore we have investigated samples with *e.g.* decreased pore densities, or high numbers of $YBa_2Cu_4O_8$ intergrowths due to incorporated nanoparticles in the Y123 structure. On the other hand, bulk modifications can propagate to the surface and change the surface composition, topology and roughness. This changes could modify the oxygen exchange at the surface, especially as grain boundaries and other defects at the surface are believed to be highly active in the process of oxygen exchange [57].

In the following sections results of *in situ* ECR measurements for samples with different microstructures are presented. These microstructural variations were obtained by cation substitution, embedding of nanoparticles and/or different growth techniques, as a flash heating process, a pore-free CSD approach using fluorine free precursor solutions and a pulsed laser deposition method (PLD).

4.5.1 Oxygen exchange of calcium doped $Y_{1-x}Ca_xBa_2Cu_3O_{7-\delta}$

The substitution of yttrium with calcium is known to increase the charge carrier density within the CuO_2 planes and therefore it is an interesting approach to reach the overdoped region of the YBCO phase diagram. Calcium is generally found in the divalent state Ca^{2+}, while the valence state of yttrium is Y^{3+} in YBCO [120]. The extra charge introduced by Ca doping is partially screened by an increased oxygen vacancy density which comes along with the modification of the microstructure [121, 122]. With increasing calcium content, the critical temperature is reported to decrease rapidly [123], which is compensating the beneficial effect of additional charges and thus increased charge carrier densities for high operation temperatures (77 K).

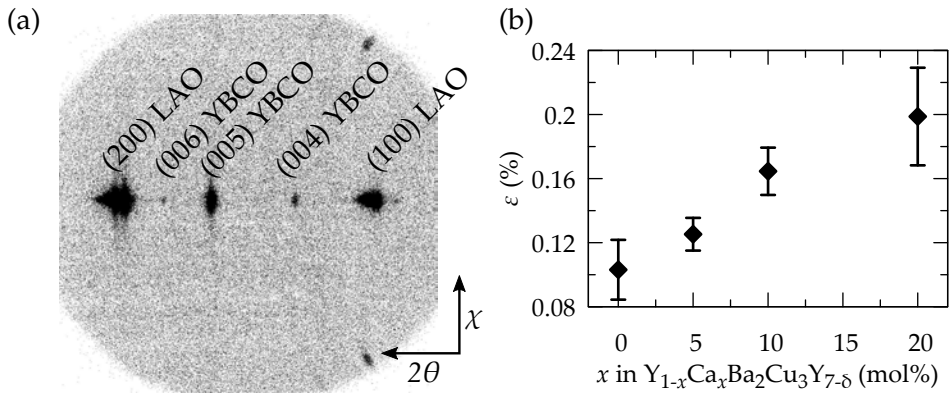

FIGURE 4.27: (a) GADDS analysis of 20 mol% calcium doped sample and (b) evolution of nanostrain with increasing doping.

Within this thesis YBCO films with a calcium content of 5, 10 and 20 mol% in respect to yttrium were produced. Therefore a specific amount of calcium acetate from *SIGMA ALDRICH* is dissolved in the stoichiometric YBCO precursor solution and stirred over night. The deposition via spinning, pyrolysis and growth are not modified from the standard fabrication process for pristine YBCO as described in Chapter 3. Since Ca is added to the stoichiometric YBCO solution, the excess of yttrium is expected to form yttrium oxide Y_2O_3. This phase is stable within the YBCO matrix and is thought to be a preferential artificial pinning site up to a certain extend [124].

The epitaxial texture of the calcium doped thin layers is verified using a general area-detector diffractometer system (*GADDS*), a two-dimensional X-ray diffraction system. In Fig. 4.27(a) a typical scan is shown for a 20 mol% calcium doped sample in a range of 17.8 - 52.4° and 56 - 125° for 2θ and χ, respectively. The YBCO reflections have a peaked intensity distribution, no rings in χ are observed, confirming the epitaxy of the nanolayer.

The nanostrain ϵ is evaluated using the Williamson-Hall methodology as described in section 3.5.2. Values for samples containing different amounts of calcium are shown in Fig. 4.27(b). The distortion of the matrix through excess Y_2O_3 leads to an increase of the measured nanostrain, as typically observed due to the incorporation of nanoparticles [125]. This has been associated to an increase of stacking faults.

The samples physical properties at low temperatures are analysed using SQUID magnetometry and electrical measurements, as shown in Fig. 4.28. The critical temperature drops from around 90 K for pristine YBCO to below 80 K, for the 20 mol% Ca-doped samples, as expected from literature for Ca-doped YBCO [126, 127]. The average charge carrier density is only slightly

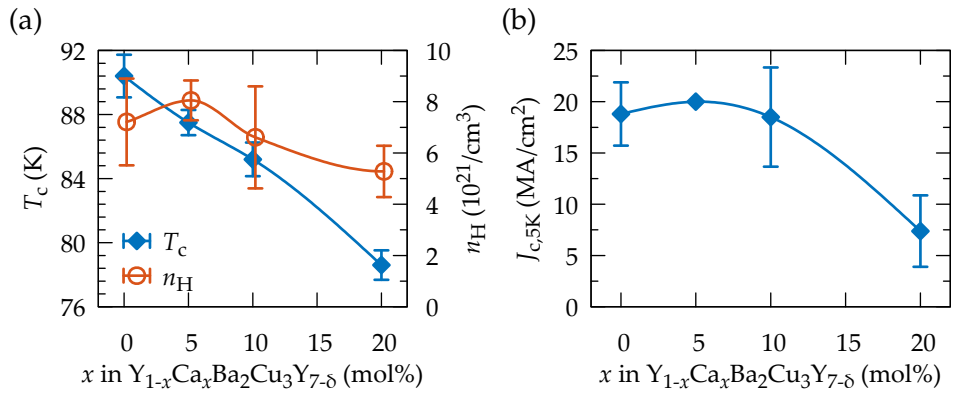

FIGURE 4.28: Dependence of low temperature physical properties on Ca x in $Y_{1-x}Ca_xBa_2Cu_3O_{7-\delta}$: (a) critical temperature and charge carrier density n_H(300 K), (b) critical current at 5 K.

increased for low calcium doping, but does not exceed the mean variation of pristine films and decreases above 10 mol%. The critical current density at 5 K is preserved up to 10 mol% and strongly decreases for higher calcium doping. The relatively low J_c values shown for the pristine films are far below the maximum currents reached in this thesis and generally for thin films grown by CSD (about a factor 2 lower), but they are the ones obtained in pristine YBCO during the period, when Ca-doping was studied. The exact reason is not known but the origin is thought to be one or several of the detrimental factors as high humidity, high water content in the precursor solutions, lower purity of metalorganic precursor, *etc*.

Oxygen incorporation of Ca doped YBCO studied by ECR

In- and out-diffusion kinetics are studied between the temperature range of 650 and 400 °C. Oxygen was removed from the structure by exposing the calcium doped sample to an oxygen partial pressure of 5 mbar. The reverse process of oxidation is obtained in a 1 bar atmosphere. The measured surface exchange rates are shown in an Arrhenius plot in Fig. 4.29(a). As in our previous studies we find that oxygen incorporation is faster than reduction. The oxidation process has an activation energy of 0.91±0.03 eV. In case of reduction, two parallel processes are active, with saturation time τ_1 and τ_2 as shown with full and open triangles. They exhibit similar temperature dependences but differ in about one order of magnitude in absolute values. At 500 °C both contributions show a kink to a higher activation energy at lower temperatures. For the high temperature regime E_a reads 0.66 eV (0.52 eV) for the process with the relaxation time τ_1 (τ_2), while at lower temperatures it increases to 1.10 eV

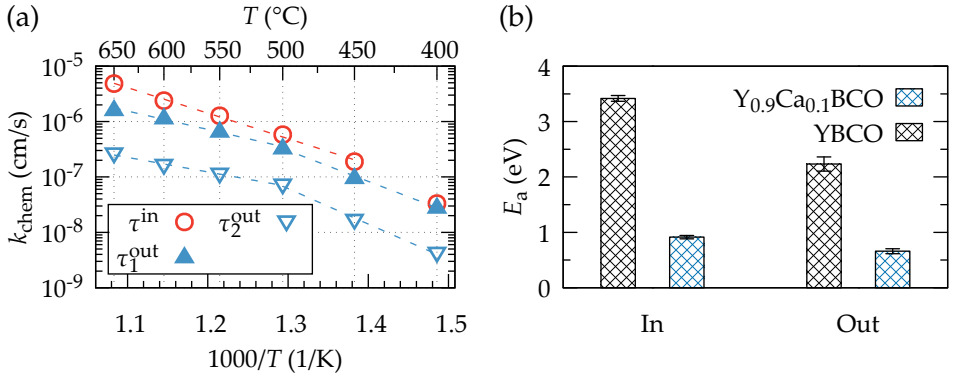

FIGURE 4.29: (a) Arrhenius plot for 10 % calcium doped sample and (b) activation energies for pristine and calcium doped YBCO thin films for the high temperature regime (450-600 °C).

(1.27 eV). The activation energies for Ca doped films are significantly lower than for pristine YBCO films ($E_{a,in} = 3.4$ and $E_{a,out} = 2.2$ eV), as shown in Fig. 4.29(b).

We compare the effective out-diffusion saturation times of a pristine YBCO film, a YBCO layer with a silver surface coating and a calcium doped sample in Fig. 4.30(a). At 600 °C all three samples have similar reaction rates. When decreasing the temperature, the calcium sample follows the trend of the silver coated one, showing a weaker temperature dependence and much smaller time constants at low temperatures. Calcium doping and the accompanied changes in the microstructure and strain landscape, grain size, surface morphology, *e.g.* allows to exchange oxygen down to 400 °C.

Saturation conductivity values are shown for the in-diffusion process in Fig. 4.30(b) for a Ag coated pristine film and non-Ag coated 10 and 20 mol% calcium doped YBCO layers. A very linear dependence of σ_∞^{in} on temperature is observed for all three samples. As discussed in section 4.2.2, the deviation from metallic behaviour ($\sigma \propto T^{-1}$) is caused by changes in the oxygen stoichiometry. While calcium doping has a strong effect on the exchange kinetics (Fig. 4.30(a)) and corresponding activation energies (Fig. 4.29(b)), the temperature dependence of the equilibrium oxygen content (Fig. 4.30(b)) does not show significant dependence on the microstructural modifications, similar to the case of pristine and silver coated YBCO.

In summary the substitution of yttrium by calcium did not yield a significant increase in charge carrier and critical current densities. We address this to the lack of optimisation of the pyrolysis and growth process for stoichiometric

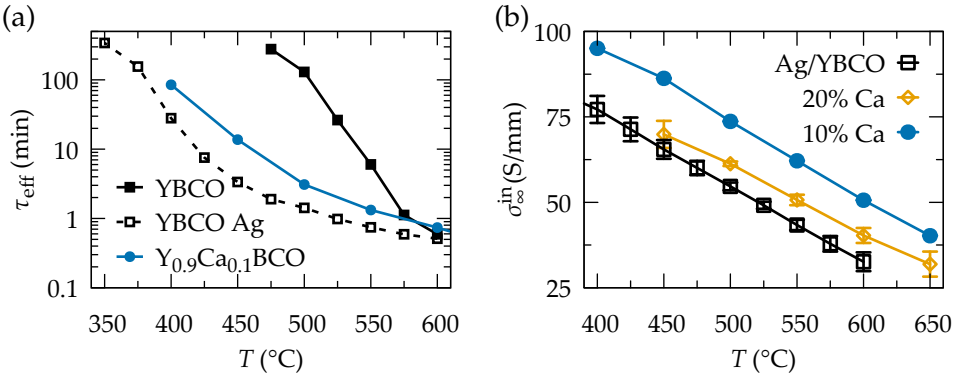

FIGURE 4.30: (a) Semi-log plot of out-diffusion saturation times of a 10 mol% calcium doped sample in comparison to non-Ag and Ag coated pristine YBCO. (b) Saturation conductivity of the oxidation process for Ag coated pristine and non-Ag coated 10 and 20 mol% calcium doped YBCO.

$Y_{1-x}Ca_xBa_2Cu_3O_{7-\delta}$ which was beyond the framework of this thesis. However, we have shown that the oxygen incorporation is favoured for Ca doped thin films, an advantageous prerequisite for further research.

4.5.2 Oxygen kinetics of YBCO CSD nanocomposite thin films

The embedding of nanoparticles into the YBCO crystal structure grown by a CSD methodology, was found to be a promising route to push the superconducting limitations of in-field applications. Higher critical current densities in external magnetic fields can be obtained by introducing pair-breaking regions into the superconductor, which effectively pin magnetic vortices within their normal state volume [125, 128, 129]. Many approaches haven been studied for successful implementation of nanoparticles [130–133]. Several parameters must be precisely controlled to fully exploit their potential, as particle size, shape, density and distribution to avoid issues as coarsening, segregation and reactivity, *etc*.

Nanocomposite (NC) YBCO films were grown under different routes by Dr. Pablo Cayado and Dr. Ziliang Li during their PhD studies and NC samples were generously provided by them for further analysis. Two approaches were followed to obtain stable nanoparticles within the YBCO matrix. In the first, nanoparticles are spontaneously segregated and formed during the

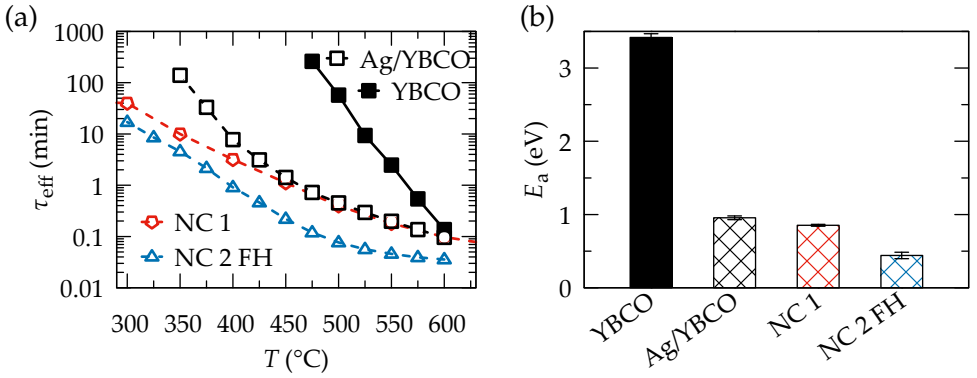

FIGURE 4.31: (a) In-diffusion relaxation times for non-silver and silver coated pristine YBCO thin films and silver coated nanocomposites with spontaneously segregated 5 mol% BZO + 6 mol% BYTO (NC 1) and 20 mol% BZO preformed nanoparticles using a flash heating growth technique (NC 2 FH). (b) Surface exchange activation energies corresponding to samples shown in (a).

growth process of YBCO, while in the latter preformed nanoparticles of desired amount and size are added and stabilized in the precursor solution. Detailed discussions can be found in the theses [134, 135] and in literature [136, 137].

In the following we will analyse a nanocomposite film obtained by spontaneous segregation with a composition of 5 mol% BZO + 6 mol% BYTO (NC 1) and a film with 20 mol% preformed BZO nanoparticles of 5-6 nm (NC 2 FH). The latter was grown using a flash heating process with a much faster heating ramp (20 °/s), which avoided nanoparticle coarsening in a large extend. All percentages are given in respect to 1 mol of yttrium. The studied nanocomposites were coated with a patterned 100 nm layer of silver on the surface.

Oxidation time constants at different temperatures are shown in Fig. 4.31(a). For comparison the saturation times of a non-silver coated and a silver coated pristine YBCO layer are drawn too. As in the case of calcium doping, the modification of the microstructure leads to an acceleration of oxygen exchange kinetics, especially for NC 2 FH. The temperature dependences of NC 1 and the pristine YBCO film with Ag coating are very similar down to 450 °C. Below 425 °C much higher kinetics are observed for the nanocomposite films.

We have calculated activation energies in the range of 450 - 600 °C for all presented samples, as shown in Fig. 4.31(b) for the case of in-diffusion. The silver coated pristine YBCO film has a similar E_a as NC 1. For the flash heated sample NC 2 we obtain an ever lower activation energy of 0.44 eV.

To conclude, nanocomposite YBCO thin films do not only exhibit preferential pinning behaviour but also show excellent oxygen exchange kinetics, with very low activation energies. Low activation energies and fast exchange kinetics at low temperature are a prerequisite for low T oxygenations, necessary to maximise the oxygen content within the structure.

4.5.3 Oxygen incorporation into porous-free CSD YBCO obtained by a fluorine free growth process

The most widely used growth technique of YBCO via chemical solution deposition is based on trifluoroacetate (TFA) solutions. During the growth process some toxic fluorine is released. Thus, a highly desired goal for the synthesis of YBCO using a chemical solution route is to decrease the necessary amount of fluorine in the precursor solution. Therefore, a new methodology is being developed within the SUMAN group avoiding the use of trifuloracetates based on a novel transient liquid assisted growth technique, which enables ultra fast YBCO growth rates up to 100 nm/s, making it extraordinarily interesting for R-2-R production.

Owing to the fact that in this technique the YBCO crystallisation is based on a liquid-solid reaction, very porous free layers are obtained. It is not the intention of this thesis to compare the different CSD methods, but to explore oxygen kinetics from very porous free films, taking into account that porosity has always been ascribed as one of the best channels for oxygen diffusion. At the time of the analysis of these samples, this novel growth technique was being optimized. The analysed fluorine free samples were grown by Dr. Laia Soler and Júlia Jareño within their PhD studies and generously provided for further study.

From bulk YBCO studies it is well known, that diffusion along the *ab* plane is faster by orders of magnitude than along the *c* direction [138]. Any kind of defects thus are expected to provide the main path of diffusivity normal to the surface. Among grain boundaries, porosity is thought to play an important role for oxygen diffusion in *c*-direction. SEM images of the surface of a TFA-CSD and a fluorine free sample are shown in Fig. 4.32. Pores are exemplary marked with red circles in both images. In the case of the FF-CSD sample porosity is strongly reduced.

In Figure 4.33(a) the temperature dependence of the surface exchange coefficient for the incorporation of oxygen is shown. Two different samples obtained by a fluorine free growth process are compared with two standard TFA-CSD films. The sample FF Ag, marked with triangles, was grown with a fast heating ramp of 20 °C/s at a $P(O_2)$ of 10 mbar. This sample is epitaxial and has an onset critical temperature of about 90 K but less than 1 MA/cm^2 at

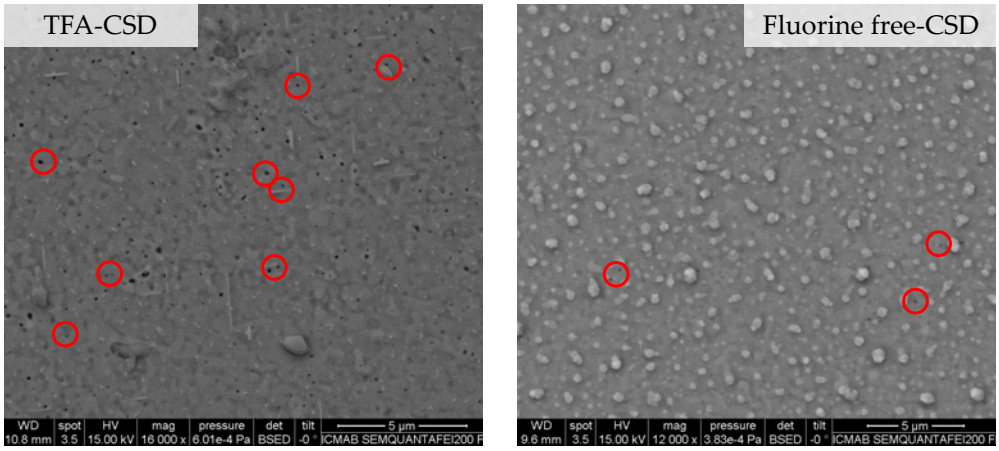

FIGURE 4.32: SEM images of the surfaces of two YBCO films obtained by different CSD growth techniques: standard TFA-CSD and low-porous fluorine free CSD. Pores are exemplary marked with red circles.

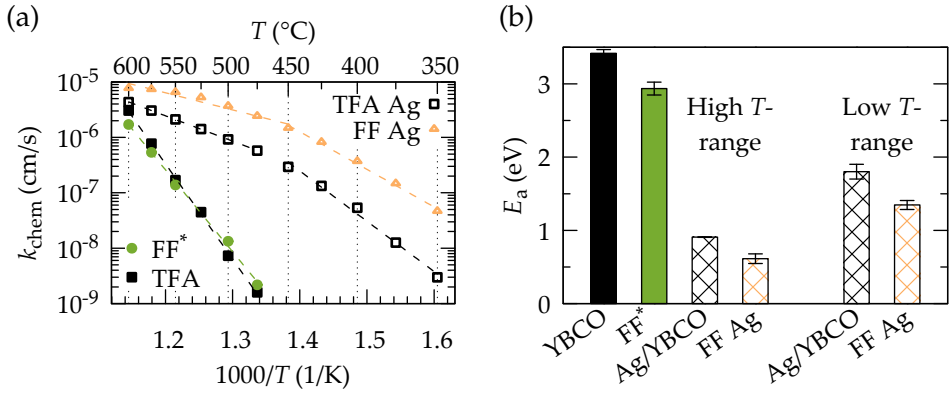

FIGURE 4.33: (a) Surface exchange rates for oxygen incorporation of films obtained by the TFA-CSD route and a fluorine free (FF) CSD growth process and (b) corresponding activation energies of oxidation process, with second E_a regime at low temperatures for FF Ag and Ag/YBCO

77 K. The sample FF* was grown using a low $P(O_2)$ route, where the pressure is increased after reaching growth temperature, so that the previous formation of undesired phases at lower temperatures is prevented. This sample has a J_c(77 K) of 2.3 MA/cm^2. FF* shows very similar exchange rates as the pristine TFA film. Although the porosity is strongly reduced, bulk diffusion is still faster than the surface exchange rates. Thus overall exchange kinetics are not altered significantly. The activation energy for FF* is about 3 eV, similar to 3.4 eV for pristine TFA-CSD YBCO, as shown in Fig. 4.33(b).
The exchange kinetics of the Ag coated fluorine free CSD film grown by the temperature route (FF Ag) are accelerated in respect to silver coated standard CSD-YBCO (Ag/YBCO) and comparable to strained nanocomposites. Granularity is still a major issue in the growth of fluorine free YBCO and causes decreased critical current densities in these samples. On the other hand the enhanced exchange rates are also expected to be due to granularity and generally faster surface kinetics at grain boundaries [52].
In both silver coated films Ag/YBCO and FF Ag we observe a deviation to, by a factor 2 higher activation energies at lower temperatures (<450 °C), as depicted in Fig. 4.33(b).

The fluorine free growth of YBCO is a highly interesting approach for the production of HTS CCs, with its very high growth rates, potential high critical current densities and reduced detrimental influence on environment. Pristine FF CSD YBCO films show similar oxygen exchange kinetics as pristine TFA CSD YBCO, although the pore density at the surface is strongly reduced. Upon silver coating, exchange rates can be significantly enhanced, especially at low temperatures. This shows that also in FF thin films low temperature oxygenation processes are achievable with the aim to maximise the oxygen content of the YBCO layer.

4.5.4 Oxygen exchange of YBCO deposited by PLD

Pulsed layer deposition is one of the most common growth methods in the commercial production of HTS coated conductors and holds record critical current values for long length tapes [131]. It is therefore an interesting candidate to study and compare its exchange kinetics with chemical solution derived YBCO films.

Images of the microstructure with atomic resolution obtained by transmission electron microscopy show the same type of defects, *i.e.* stacking faults, but the density, length and distortion induced in the CuO_2-planes show clear differences between the two growth techniques (Fig. 4.34(a) and (b)). The pristine CSD film (a) exhibits strongly distorted CuO_2 planes and a high density

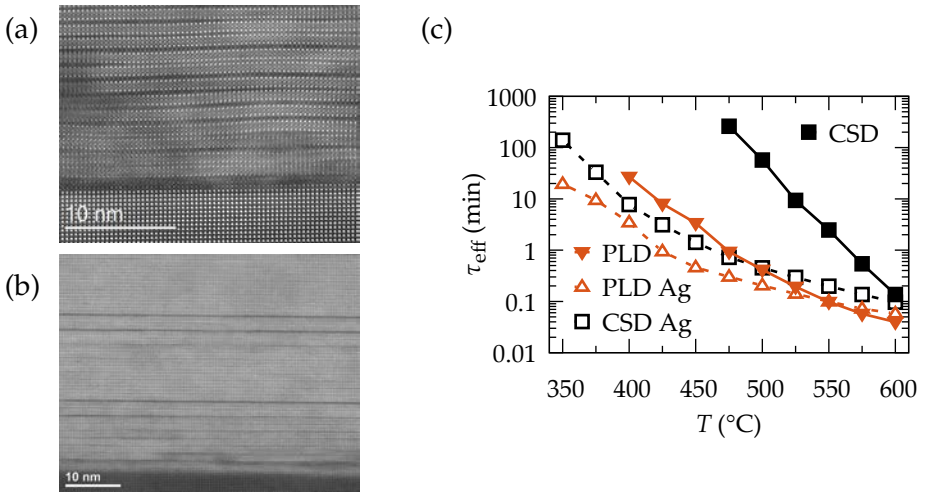

FIGURE 4.34: TEM images of thin films grown by (a) CSD and (b) PLD on a $LaAlO_3$ and $SrTiO_3$ substrate, respectively. (c) Effective oxidation relaxation times for YBCO films derived by chemical solution and pulsed laser deposition.

of short CuO intergrowths (stacking faults). The defect density of the PLD layer (b) is lower with uniform planes in *ab* direction and only a few but long stacking faults. These images were taken by the TEM experts of our group Dr. Bernat Mundet and Dr. Roger Guzman.

Electrical conductivity relaxation measurements are performed at temperatures between 600 and 350 °C in steps of 25 °C using 200 nm thick PLD-layers. During the isothermal annealings the oxygen partial pressure is switched between the standard pressures of 1 bar and 5 mbar. The saturation times for the oxidation process of selected samples are shown in Fig. 4.34(c). The pristine PLD film shows much faster kinetics than the CSD one. The same trend is observed for the case of reduction (not shown). Initially the opposite result was expected since the modified and enhanced defect landscape of CSD films was expected to provide a rich variety of adsorption sites on the surface and fast diffusion paths in the bulk. Upon silver coating both growth routines exhibit a similar temperature dependence, with the PLD having nonetheless by a factor of 2 faster rates. It is observed that in the case of PLD the influence of silver coating is much weaker. The Ag surface layer effectively enhances exchange rates compared to as-grown surfaces only at lower temperatures, after several cycles of out- and in-diffusion.

The activation energy for oxygen incorporation is 1.4 eV for the pristine PLD film, thus reduced by more than a factor 2 in comparison with pristine YBCO grown via CSD ($E_a = 3 - 4$ eV). On the other hand, silver coated PLD

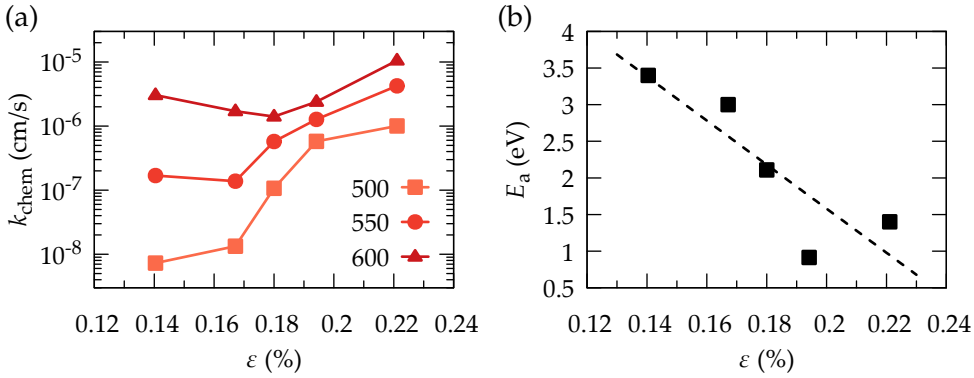

FIGURE 4.35: (a) Dependence of surface reaction rate constant for oxidation on nanostrain of various sample types at different temperatures (LTR samples with increasing strain: CSD-TFA, FF*, FF, 10 %Ca, PLD; all samples without Ag coating) and (b) activation energy of oxidation for the same specimen. Straight line in (b) is a guide to the eye.

films have an oxidation activation energy of about 0.8 eV at high temperatures. Further a deviation from a single E_a regime is observed below 450 °C with an average value of about 1.5 eV. These energies are very similar to the ones obtained for Ag coated CSD films (0.9 and 1.8 eV, respectively). In the next chapter we will discuss some additional facts that need to be considered when evaluating films without Ag coating, that might explain the difference here observed between CSD and PLD pristine films. We anticipate that the modification of the surface during annealing plays a crucial role in the evaluation of oxygen exchange kinetics.

4.5.5 Summary: Role of nanostrain on oxygen exchange kinetics

We have shown that most analysed types of microstructures have improved exchange rates compared to pristine YBCO films grown by CSD-TFA. In all analysed films oxygen in- and excorporation is limited by surface reactions, since out-diffusion time constants were found to be larger than for incorporation. Exchange kinetics could be enhanced upon the deposition of a thin catalytic layer of silver on the surface.
As the surface is limiting oxygen exchange processes, purely bulk modifications caused by different growth techniques cannot account for the observed variations of exchange rates. Modified surface composition, as different grain boundary densities with its faster exchange rates [52, 57], and porosity are

expected to play an important role on the exchange kinetics. A common defect that we have observed in all layers, is the stacking fault, with different degrees of density. Therefore, we have analysed the nanostrain ϵ, since this is the physical parameter that is able to quantify the local distortions induced by the stacking fault density [125]. We have analysed the nanostrain ϵ for the above discussed cases and compare the surface exchange reaction rate as a function of ϵ among all sample types in Fig. 4.35(a) (non Ag coated films). We find a strong dependence of k_{chem} on ϵ at an intermediate temperature of 500 °C. Exchange kinetics are significantly increased with increasing nanostrain. This dependence is weakened with increasing temperature, as can be seen for $T = 600$ °C, where only a weak dependence on ϵ can be observed.
This can be understood by looking at the activation energies for the same samples in Fig. 4.35(b). The nanostrain ϵ effectively decreases the activation energy of the oxidation process. At high temperatures a sufficient amount of particles surpasses the energy barrier, where differences in E_{a} only play a minor role. With decreasing temperature the effect of nanostrain and lowered activation energies become more important, resulting in the observed differences of the surface exchange rates.
Nanostrain is a measure of very local inhomogeneities in the crystal structure, and therefore within the bulk. On the hand, surface exchange rates are limited by a surface mechanism and not by bulk diffusion. Therefore, nanostrain must have an effect as well in the top bulk layer at the interface with the gas phase. As we have made this analysis for non-Ag coated YBCO films, any surface step (step 1-5 in Table 2.1) might be affected. Possible effects of nanostrain on surface exchange kinetics might be the modification of the vacancy volume (step 5) and/or a reconfiguration of the electronic structure of the surface leading to modified adsorption, ionisation and dissociation rates (steps 1-3).

In this section we have studied the influence of different YBCO microstructures on exchange kinetics. Modifications of the microstructure were introduced via Ca doping, embedding nanoparticles and the use of different growth techniques as a TFA flash heating process, a low-porosity fluorine free CSD route and pulsed laser deposition. In all cases we observed enhanced exchange kinetics. This was explained by a varied nanostrain landscape induced by different growth techniques affecting exchange energy barriers, modifications of the surface composition and different grain boundary densities, which are expected to severe as highly active exchange sites at the surface.

4.6 Influence of strain in YBCO oxygenation process: A thickness dependence study

Many examples in the material class of functional oxides are found, where the oxygen vacancy density is closely linked to the charge carrier density and thus is crucial to *e.g.* electronic or ionic conduction and magnetic properties [139]. For thin films of the superconducting compound $La_{2-x}Sr_xCuO_{4-\delta}$ it was found, that the superconducting transition temperature is correlated with the strain state and can be enhanced or decreased by compressive or tensile strain induced via substrate mismatch [140–142]. Successive investigations have been performed to gain better understanding of mechanical stress on the energy barriers of solid state reactions. This phenomena is called mechano-chemical coupling and can alter reaction and diffusion kinetics due to changes in the oxygen defect formation enthalpy and adsorption energy, the migration energy barrier and or dissociation and charge transfer barrier [143–145].

Tensile strain is often identified to decrease the oxygen vacancy formation energy in functional oxides [146–148]. On the other side, compressive strain is found to increase vacancy migration and formation energies in perovskite oxides [149]. Theoretical modulations intend to explain the influence of mechanical stress on formation enthalpies in terms of changes in the vacancy formation volume [148] and weakening of interatomic lattice bonds for tensile strain [144]. In this section we will analyse the dependence of physical properties and oxygen exchange rates on film thickness and related substrate induced macroscopic strain within the lattice.

4.6.1 Thickness dependence of physical properties of PLD-YBCO thin films

To study the influence of film thickness on physical properties and oxygen exchange kinetics of YBCO thin films, layers with a nominal thickness down to 25 nm were grown by Pulsed Laser Deposition (PLD). Tensile or compressive strain is introduced into the thin film by a mismatch between the in-plane cell parameter of the substrate and YBCO bulk material. We have grown YBCO onto $LaAlO_3$ and $SrTiO_3$ single crystal substrates, as commonly used for the epitaxial deposition of HTS materials [150]. Lattice parameters and crystal structure of the utilised substrates are shown in Table 4.3. The mismatch is

Substrate	Crystal system / structure	a (Å)	Mismatch δ to bulk (%) a	b	ab	Strain
$LaAlO_3$	pseudocubic / perovskite	3.791	-0.86	-2.44	-1.66	Compressive
$SrTiO_3$	cubic / perovskite	3.905	2.12	0.49	1.30	Tensile

TABLE 4.3: Overview of crystal structure and lattice parameters of the substrates used. Mismatch calculated using YBCO bulk values $a = 3.824$ Å and $b = 3.886$ Å [22].

calculated relative to YBCO bulk with the lattice parameter a_{bulk} using[1]:

$$\delta = \frac{a - a_{\text{bulk}}}{a_{\text{bulk}}}, \tag{4.24}$$

with a being either the substrate or the thin film lattice parameter. The mismatch of the substrate with the bulk defines the maximal deviation, while a thin film is likely to exhibit an intermediate state. It is useful to introduce a strain parameter s which defines the actual strain state of the sample

$$s = \frac{\delta_{\text{film}}}{\delta_{\text{substrate}}} = \frac{a_{\text{film}} - a_{\text{bulk}}}{a_{\text{substrate}} - a_{\text{bulk}}} \begin{cases} = 100\,\%, & \text{fully strained,} \\ = 0\,\%, & \text{fully relaxed,} \end{cases} \tag{4.25}$$

with $\delta_{\text{substrate}}$ and δ_{film} being the mismatch of YBCO bulk with the substrate and the thin film, respectively. For a partially strained thin film, s will vary between the fully relaxed bulk state with $s = 0\,\%$ and the fully strained situation with $s = 100\,\%$.

In-plane lattice parameters are obtained by reciprocal space maps. These measurements were performed in the XRD facilities of ICN2 in a set of $\omega - 2\theta$ scans. The reciprocal space wave vectors Q_x and Q_z parallel and perpendicular to the surface are defined via

$$Q_x = \frac{\lambda}{2} \sin\theta \sin(\theta - \omega) \tag{4.26}$$

$$Q_z = \frac{\lambda}{2} \sin\theta \cos(\theta - \omega). \tag{4.27}$$

[1] In literature δ is also defined relative to $a_{\text{substrate}}$ or a_{film}. The here used definition indicates the right sign for compressive (-)/tensile (+) strain and allows a straight forward introduction of the strain parameter s.

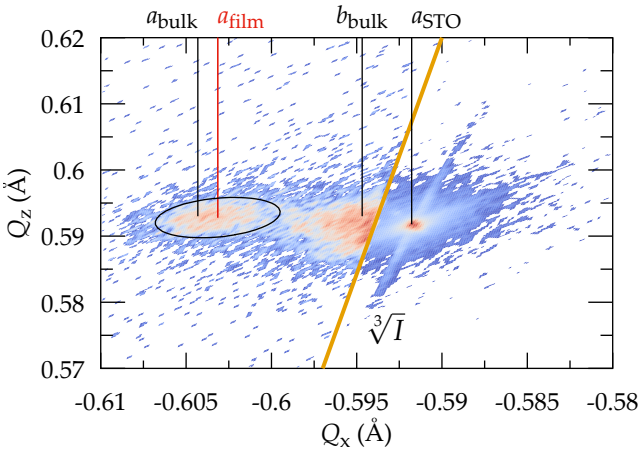

FIGURE 4.36: Reciprocal space map of 50 nm thin PLD-YBCO film grown on STO showing YBCO (-309) and (0-39) and substrate (-303) reflections. Fully relaxed bulk lattice constant values are indicated by vertical black lines. To the right of the orange line the intensity is scaled with $\sqrt[3]{I}$ for better clarity of the film peak.

YBCO peaks close to a substrate peak are chosen to allow a precise calibration of the position using the well defined substrate peak position. A two dimensional elliptical Gaussian function is used to fit the YBCO reflections of obtained by reciprocal space maps:

$$I(Q_x, Q_z) = I_0 \mathrm{e}^{-\left(w_1(Q_x-Q_{x_0})^2+w_2(Q_x-Q_{x_0})(Q_z-Q_{z_0})+w_3(Q_z-Q_{z_0})^2\right)}. \tag{4.28}$$

The centre positions of the reflection are used to calculate the lattice parameters via

$$a = \frac{h}{Q_{x_0}}, \tag{4.29}$$

$$c = \frac{l}{Q_{z_0}}, \tag{4.30}$$

with the Miller indices h and l.

An example is shown in Fig. 4.36 for a 50 nm thin film grown on a STO substrate. For better clarity, to the right side of the orange line the intensity is scaled with $\sqrt[3]{I}$. A well defined peak for the STO substrate is observed. The centre of the YBCO (-309) reflection of the thin film is marked with a red straight line. The black lines indicate the fully relaxed bulk lattice constants.

Substrate	t (nm)	a (Å)	b (Å)	δ_a (%)	δ_b (%)	s_a (%)	s_b (%)	s_{ab} (%)
STO	25	3.840		0.41		19.4		≤ 19.4
STO	50	3.832		0.20		9.5		≤ 9.5
LAO	50	3.823	3.874	-0.04	-0.31	4.1	12.7	8.4
LAO	200	3.824	3.886					0

TABLE 4.4: Evaluated in-plane parameters from XRD measurements and corresponding mismatch and strain values, obtained using .

The in-plane lattice parameter a of the YBCO layer is shifted towards the substrate. The black ellipse indicates the contour of the fitted Gaussian, where the intensity drops to 1/e. In the chosen $\omega - 2\theta$ region the b-parameter for films grown on STO cannot be evaluated due to the close proximity of the corresponding reflection to the substrate peak.

The results for different substrates are presented in Table 4.4 and visualised in Figure 4.37. The strain parameter s increases with decreasing thickness, as tabled for STO. The relaxation of strain with thickness is also shown in Fig. 4.37(b). The dashed line is a guide to the eye.
Additionally it is observed that an increasing difference between the in-plane parameter of film and substrate leads to a higher strained state, as shown in Table 4.4 for the YBCO b-parameter of a 50 nm sample on LAO ($s_a < s_b$). The values for s_{ab} for films grown on STO are maximum values, since the b-parameter is closer to the substrate in-plane cell parameter and therefore expected to be less strained than a.
A 25 nm film grown on LAO was measured as well, but the intensity of the YBCO reflection is too low for a reliable evaluation, though the right trend of a shift towards the substrate is observed.

The Poisson effect describes the phenomena of a materials expansion perpendicular to the direction of compression, and vice versa for tensile stress. Thus, changes in a and b are expected to propagate and alter the out-of-plane lattice constant c accordingly. The c-parameter of a set of several thin samples is analysed and presented in Fig. 4.38(a). The unit cell expands a long the c-direction for samples grown on LAO with decreasing thickness. Thin layers deposited on STO exhibit only a very weak dependence on thickness between 25 and 200 nm. Besides the expected c-axis contraction due to tensile strain, a contrary expansion caused by lower oxygen content needs to be considered, as we will see later. This is likely to explain the *quasi* thickness independence of STO samples (*destructive interference* of opposite effects on the c-parameter). The same effect of oxygen content on the c-parameter is

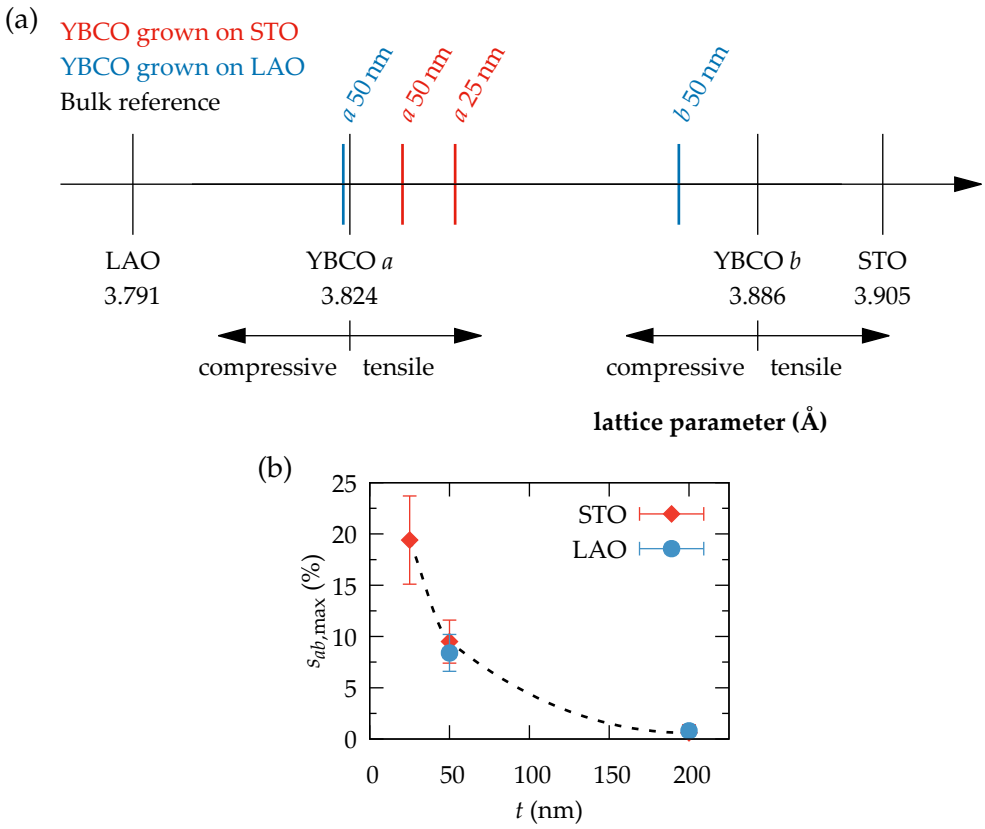

FIGURE 4.37: (a) Visualisation of in-plane lattice parameters for LAO and STO substrates, YBCO bulk and measured thin films, grown on different substrates, respectively. (b) Maximum in-plane strain state over film thickness.

expected for films grown on LAO but in constructive superposition to the expansion due to strain.

To gain better understanding of the influence of strain on the oxygen content, the deviation of the lattice parameters a and c of the thin films from bulk is shown in Fig. 4.38(c). To calculate the deviation $\Delta c = c_{\text{film}} - c_{\text{bulk}}$, $c_{\text{bulk}} = 11.695\,\text{Å}$ is used. A compression in one direction is correlated with an expansion in the other. The dashed line indicates a purely Poisson-like deformation in a first order approximation for small values:

$$\nu \approx -\frac{\Delta a}{\Delta c}, \tag{4.31}$$

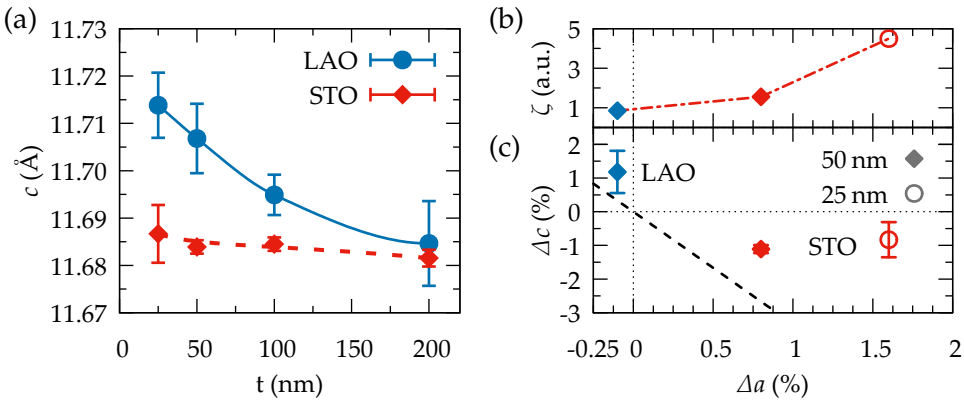

FIGURE 4.38: (a) Variation of c-parameter of PLD-YBCO films grown on different substrates with decreasing thickness, (b) deviation from expected Poisson deformation $\zeta = |\Delta c - \nu \Delta a|$ and (c) deviation of out-of-plane over in-plane cell parameter from bulk, $\Delta x = x_{\text{film}} - x_{\text{bulk}}$ for a and c, with $a_{\text{bulk}} = 3.824$ Å and $c_{\text{bulk}} = 11.695$ Å, respectively. Dashed line in (c) indicates purely Poisson-like deformation.

with $\nu_{\text{YBCO}} = 0.3$ [151]. All points lie above the deformation related to the Poisson effect, which means that all measured c-parameters are larger than expected for pure Poisson expansion/compression.
The deviation ζ from a Poisson-like deformation is shown in Fig. 4.38(b), with $\zeta = |\Delta c - \nu \Delta a|$. ζ strongly increases for the 25 nm thick film. This superposed expansion is caused by a change in the oxygen content, namely a loss of oxygen, due to the introduced macroscopic strain by lattice mismatch with the substrate. The equilibrium oxygen content of YBCO at constant temperature T and pressure p is defined by the minimum of the Gibbs free energy G:

$$G(T, p, \mu_i) = U + pV - TS - \mu_i N_i, \tag{4.32}$$

with the internal energy U, volume V, entropy S and chemical potential μ_i and particle number N_i of the ith chemical component. In the presence of internal strain the conjugated pair pV must be generalised to the product of the stress tensor $\hat{\sigma}$ and the volume V multiplied by the strain tensor $\hat{\epsilon}$ [152]:

$$pV \longrightarrow V \sum_{mn} \sigma_{mn} \epsilon_{mn} \tag{4.33}$$

The mechanical work pV is modified by substrate induced strain. Correspondingly the minimum of G is altered leading to a change in the equilibrium oxygen content of YBCO.

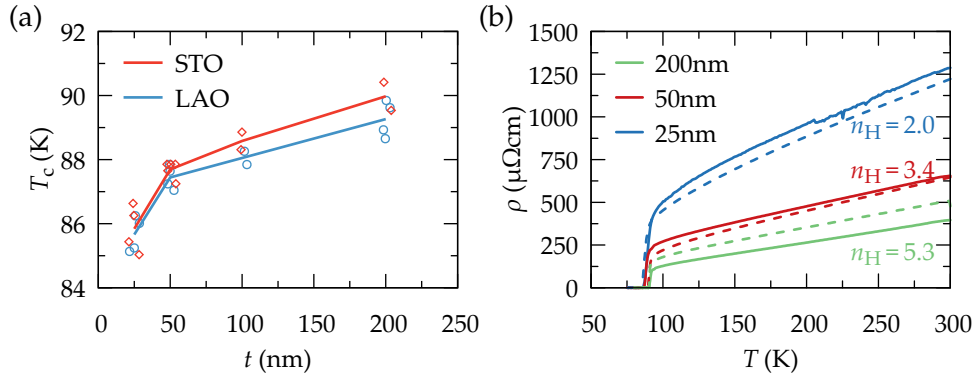

FIGURE 4.39: (a) Thickness dependence of critical temperature for thin PLD films on different substrates and (b) resistivity $\rho(T)$ for films of different thickness on LAO and STO (broken lines), the charge carrier density n_H (10^{21} cm^{-3}) at 300 K is indicated for each film grown on LAO.

Indeed, low temperature measurements are in agreement with the analysis of in-plane strain. With decreasing thickness a decrease in critical temperature is observed (Fig. 4.39(a)). This was reported previously and described as well due to an increase of macroscopic strain [153]. Additionally we observe an increase of resistivity with decreasing film thickness. This increase of ρ with decreasing thickness is linked to lower charge carrier densities, as shown in Fig. 4.39(b) for films grown on LAO and STO with continuous and broken lines, respectively.

The (005) reflection for a 25, 50 and 200 nm thick film grown on LAO is depicted in Fig. 4.40(a). The data is normalised to its minimum and maximum intensity within the shown range. An increase of the full width at half maximum with decreasing layer thickness is observed. The inset shows the integrated peak area (I.P.A., full bars) for the three samples on a logarithmic scale. The I.P.A., normalised to the thickness of the sample, is additionally drawn in the inset (mesh pattern, corresponding logarithmic y-axis not shown). The normalised I.P.A. for the 25 and 50 nm thick film is constant, while an increase for the 200 nm sample can be observed.

The increase in FHWM can be linked to a modified strain landscape within the sample. The nanostrain ϵ is shown for samples of different thickness grown on LAO and STO in Figure 4.40(b). High nanostrain values are found for the 25 nm thick films. With increasing thickness, ϵ decreases and saturates around 0.3 %. The values for 200 nm samples are high as compared to pristine CSD films, which are typically around 0.1 % [125]. The found dependence on thickness is expected due to substrate induced stress and resulting strain

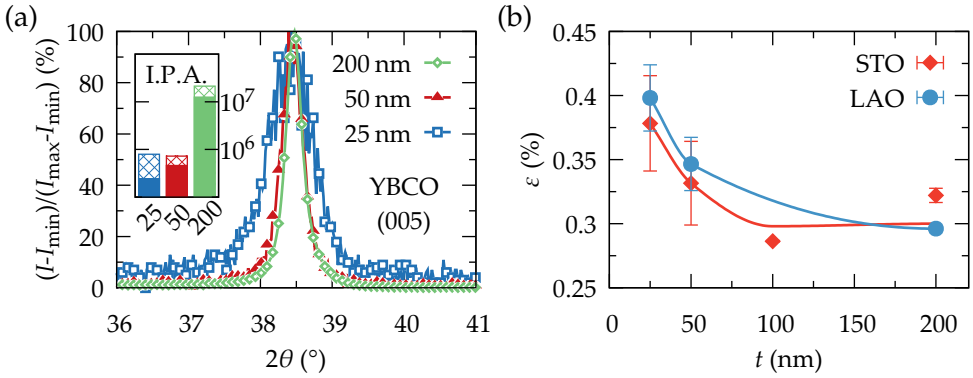

FIGURE 4.40: XRD analysis for PLD thin films grown on LAO: (a) normalised (005) reflection of layers with different thickness, inset shows the integrated peak area on a logarithmic scale (full bars) and normalised to the sample thickness (mesh pattern) and (b) evolution of nanostrain ϵ with decreasing film thickness; lines are guides to the eye.

on different length scales. Additionally, strain might be released during the longer deposition time at growth temperature for thicker films. This could be caused by fast atomic diffusion in the crystal lattice already during the deposition process.

In summary, PLD-YBCO thin films were found to exhibit increased macroscopic strain with decreasing thickness due to lattice misfit with the substrate. Tensile and compressive strain was introduced due to the growth on STO and LAO substrates, respectively. For thicker films stress is released, lowering the internal strain. The same trend is observed for nanostrain, which decreases with increasing film thickness. We have seen that higher strain values correlate with an increased oxygen vacancy density and therefore lower critical temperatures and decreased charge carrier densities.

4.6.2 Thickness dependent oxygen kinetics of pristine YBCO by PLD

We have seen that with decreasing thickness nano- and macrostrain values raise, accompanied by a decrease of the overall oxygen content. In the following section we will analyse the influence of thickness on oxygen exchange kinetics.

In Fig. 4.41(a) the *in situ* resistivity during the heating stage with a constant rate of 10 °C/min in 1 bar of oxygen is shown for layers of different thickness

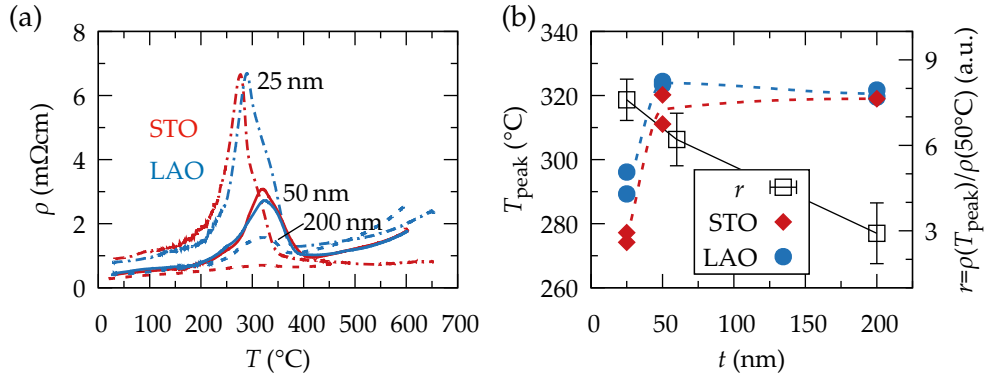

FIGURE 4.41: (a) Heating ramp with peak in resistivity for 25 nm (double broken), 50 nm (full) and 200 nm (dashed line) thick films on LAO and STO and (b) extracted peak temperature and resistivity ratio (right scale) over thickness; the ratio for 50 nm is shifted to the right for better clarity.

on LAO and STO respectively. Below 200 °C we observe a linear increase of ρ with temperature. Above, a strong upwards deviation is observed, resulting in a peak between about 280 and 320 °C. The height of the peak decreases with the thickness of the films.
The extracted peak temperatures are presented in Fig. 4.41(b). As thickness increases, initially the peak position shifts to higher temperatures and above 50 nm it saturates at about 320 °C. Within the same thickness, the peak temperature is lower for films grown on STO in respect to LAO for all studied samples.

A peak in resistance during heating in a similar temperature range has been observed previously by different authors and was ascribed to be due to oxygen re-ordering within the mobile sublattice of the structure [154, 155]. The authors claimed that during such a process oxygen is slightly moved from its initial crystal position resulting in a temporary higher disorder state and hence additional scattering occurs, resulting in the peak in resistance.

To the right scale in Fig. 4.41(b) the ratio r of the resistivity at the peak temperature to the initial resistivity at 50 °C is shown. The open black squares are the average ratio values for films with the same thickness. The ratio decreases with increasing film thickness. This thickness dependence cannot be explained by a simple re-ordering within the structure as this effect should be thickness independent and homogeneous across the whole sample. We address the occurrence of the peak to the onset of oxygen incorporation, where oxygen initially occupies interstitial lattice sites, causing a higher disordered state. The thickness dependence is expected as only near surface layers are

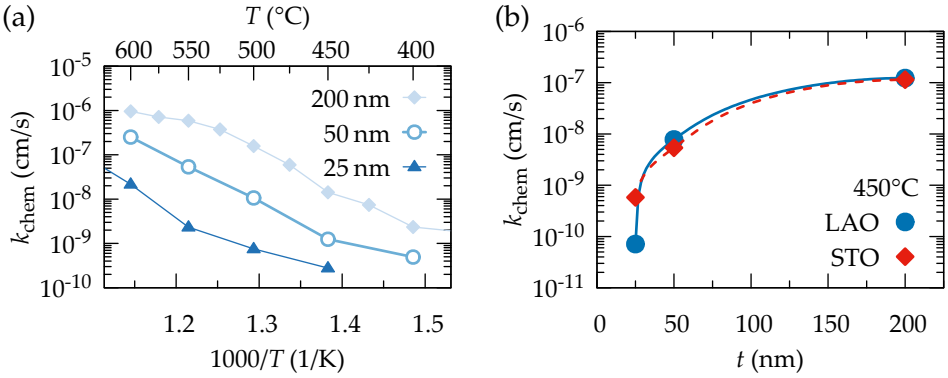

FIGURE 4.42: (a) Surface exchange coefficient k_{chem} for reduction process of 25, 50 and 200 nm thick films on LAO and (b) in-diffusion k_{chem} as a function of thickness at 450 °C.

affected. The higher strain state of thin films might additionally influence the disorder state, thus contribute to the increase of ρ. The occurrence of this peak, its influence on the oxygenation process and its dependence on surface coverage and heating ramp will be discussed in more detail in section 6.1.

The oxygen exchange kinetics of YBCO thin films was found to be limited by the surface, which means that the flux of ions through the surface is limiting the overall reaction rate. This flux is proportional to the surface area but independent of the volume underneath. On the other hand, electrical conductivity relaxation measurements are sensitive to the bulk conductivity and relative changes in oxygen concentration. The measured saturation times τ are proportional to the volume of the sample. For comparison among different film thicknesses, we need to use the surface exchange coefficient $k_{chem} = t/\tau$, as done in the following.

We compare the surface exchange coefficients as a function of the inverse temperature for pristine PLD-YBCO films of different thickness (25, 50 & 200 nm), grown on LAO substrates, in Fig. 4.42(a). All three cases obey a thermally activated behaviour, with faster kinetics at higher temperatures. We observe that the surface exchange rate k_{chem} strongly depends on the film thickness and increases with increasing thickness.

In Figure 4.42(b) we compare the oxidation kinetics as a function of film thickness for films grown on STO and LAO. As in the case for reduction, oxidation surface exchange rates significantly increase with film thickness in the investigated range between 25 and 200 nm. A dependence of the kinetics on the different strain types induced by different substrates is observed for the 25 nm films, were strain was higher, as will be discussed in section 4.6.4.
A thickness dependence study of oxygen surface exchange in LSMO by Yan

and Salvador in [156] obtained similar results of decreasing exchange rates with decreasing thickness. The authors proposed a model consisting of two different surface regions, namely a native dislocation-free surface and an area in proximity of dislocations. Defect-rich zones in the surface layer are known to be highly active in the overall oxygen exchange mechanism [57] and are expected to have faster exchange rates than the pristine surface: $k_{\text{chem,dislocation}} > k_{\text{chem,pristine}}$. The total exchange rate k_{chem} can then be written as:

$$k_{\text{chem}} = A_{\text{D}} k_{\text{chem,dislocation}} + (1 - A_{\text{D}}) k_{\text{chem,pristine}}, \tag{4.34}$$

with the area fraction A_{D} of the surface mediated by dislocations. The enhanced exchange kinetics of thicker films are thus explained by an increase of the dislocation density with increasing thickness, as dislocations are formed in thicker films to relax substrate induced strain [156].
We propose that in YBCO thin films a similar situation is present, in agreement with our observation that strain is released with increasing film thickness. As the film thickness is directly proportional to the high temperature annealing time, sintering effects already during growth might contribute to the decrease of strain within the matrix, as *e.g.* by the formation of misfit dislocations. However, the exact mechanism of strain relaxation remained unclear within our studies.

4.6.3 Thin film exchange reactions upon silver surface coating

As in the case of CSD-YBCO films, we have as well studied the oxygen exchange kinetics of thin PLD layers upon silver coating. Therefore we have prepared a new set of samples with nominal thicknesses of 25, 50, 100 and 200 nm, grown on LAO and STO substrates. The surface of the pristine films was coated with silver by sputter deposition. The same geometry as shown in Fig. 4.6 was used to enable electrical measurements. The thickness of the deposited silver layer was 20 nm for the 25 and 50 nm thick PLD films and 100 nm for thicker layers.

In situ ECR measurements were performed as described in the previous sections. Figure 4.43(a) shows the surface exchange coefficient for oxidation for films of different thickness grown on LAO substrates for non-silver (blue) and silver coated (orange) samples in a Arrhenius-type plot. The exchange kinetics of the 25 and 50 nm non-Ag samples decrease the fastest with decreasing temperature. As ascribed above, a strong dependence on thickness was found for pristine samples. We find the same trend for the case of silver coated samples, where oxygen exchange rates are lower for thinner films. However, we observe a more similar temperature dependence for all thicknesses, in

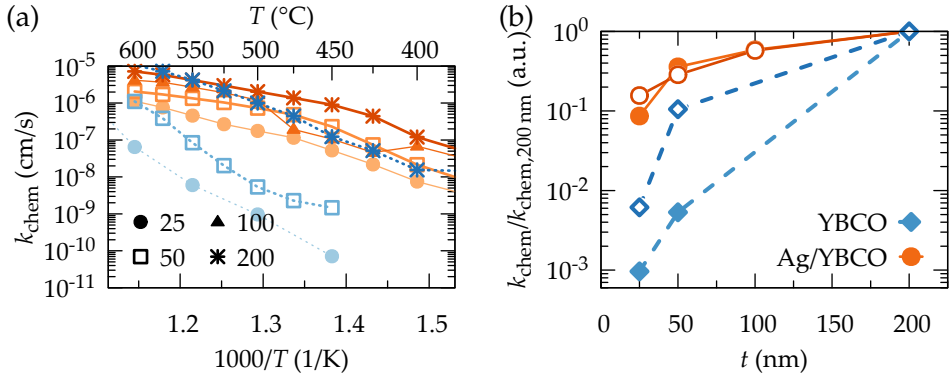

FIGURE 4.43: (a) Oxidation surface exchange coefficient over inverse temperature for pristine (blue) and silver coated (orange) YBCO films of different thickness on LAO. (b) k_{chem} as a function of thickness normalised to $k_{chem,200\,nm}$ values; open (full) symbols correspond to data obtained at 600 °C (500 °C).

comparison to non-Ag pristine films. The thickness dependence is depicted for the temperatures of 500 and 600 °C in a log-lin graph in Fig. 4.43(b). For clarity the surface exchange coefficients of the silver (non-Ag) coated samples are normalised to the corresponding k_{chem} value of the 200 nm thick Ag (non-Ag) sample at each temperature. The open and closed symbols correspond to 600 °C and 500 °C, respectively.

We observe an increase of exchange rates with thickness for non-Ag and Ag coated films at both temperatures. In the case of silver coated YBCO the dependence on thickness is significantly decreased for all analysed temperatures: a 200 nm thick Ag coated film exchanges oxygen with the atmosphere about 10 times faster than a layer with a thickness of 25 nm. In comparison, a 200 nm, Ag free YBCO layer has a factor 100-1000 faster exchange rates than a non-Ag YBCO film of 25 nm.

The activation energies of Ag coated YBCO thin films obtained at temperatures above 450 °C are shown in Fig. 4.44. For the oxygen reduction process we find that E_a only varies weakly with film thickness and substrate, with a tendency to smaller energies with decreasing thickness for STO. On the other hand, the oxidation activation energies show some dependence on thickness and substrate. For films deposited on STO substrates we find an increase of E_a with increasing film thickness, while for the case of LAO the activation energy decreases in thicker films.
However, major differences between films grown on different substrates are only observed for the case of 25 nm thick films, as will be discussed in the following.

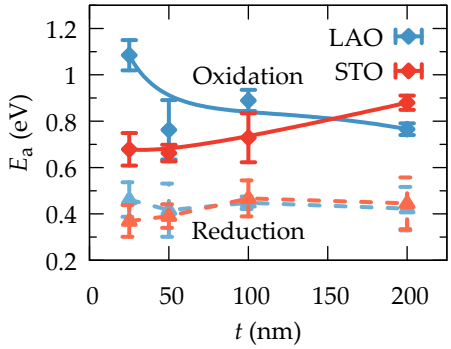

FIGURE 4.44: Activation energies E_a for oxidation (continuous) and reduction (dashed lines) process of silver coated PLD films grown on $LaAlO_3$ (blue) and $SrTiO_3$ (red) substrates as a function of the film thickness t.

4.6.4 Strain influence on oxygen kinetics for 25 nm thick films

In the previous section we have shown, that macro- and nanostrain are reduced with increasing thickness. Additionally we have found a strong dependence of surface exchange rates on the film thickness, with faster rates in thicker films. This trend is opposite to what we would have expected from our analysis of different microstructures in section 4.5, where we have found that exchange kinetics are enhanced with increasing nanostrain. This alleged contradiction was resolved by assuming a significant contribution to the overall exchange rate of enhanced kinetics at defected areas, resulting from strain release.

To solely analyse the influence of macrostrain due to the mismatch with the substrate on the oxygen kinetics, we focus here on 25 nm thick films. The oxygen exchange of these strained films was analysed between 650 and 450 °C in steps of 50 °C.

The resistivity versus temperature during the heating stage with a constant rate of 10 °C/min in a 1 bar oxygen atmosphere is shown in Fig. 4.45(a). As discussed above, a peak in ρ is observed. This peak is shifted to a lower temperature for the film grown on STO compared to LAO (see inset). In the exhibited example, the temperature is reduced from $T_{\text{peak, LAO}} = 290\,°\text{C}$ to $T_{\text{peak, STO}} = 277\,°\text{C}$, which is a first indicator that kinetics are changed due to substrate induced strain.

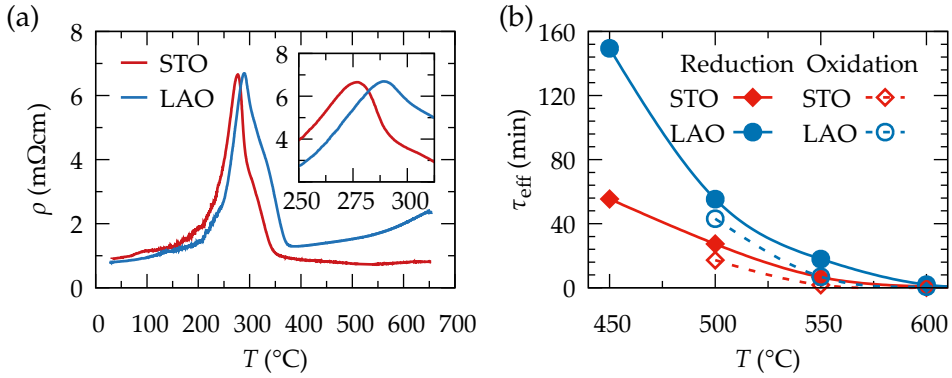

FIGURE 4.45: ECR measurement on strained 25 nm thick non-Ag YBCO layers on STO and LAO: (a) resistivity during constant heating period and (b) reduction (filled) and oxidation (open symbols) saturation times as a function of temperature.

In Fig. 4.45(b) the saturation times for the reduction and oxidation process are displayed. Tensile strained films on STO exhibit faster oxygen exchange rates than compressive strained YBCO on LAO over the full temperature range for oxidation and reduction processes. These results are in agreement with literature outlined in the beginning of this section, where it was reported that tensile strain causes faster kinetics compared to compressive strain. Also for 25 nm thick films in-diffusion is found faster than its reverse process independent of the film substrate, thus a surface mechanism is limiting the overall oxygen exchange.

Figure 4.46 shows an Arrhenius plot for the oxidation process and the activation energies, obtained by Power-law fits, for oxygen ex- and incorporation. Consistently, with previous results, it is found for both substrates that the reduction process has a lower activation energy than oxidation. Further we obtain lower activation energies for tensile strained layers grown on STO than for compressed ones on LAO. The activation energies are reduced by about 40 % and 20 % for out- and in-diffusion, respectively. Again, the lowering of activation energies due to tensile strain compared to compressive strain in 25 nm thick films is in agreement with reported studies on other oxides [145, 147, 148]. The pre-exponential factor k_0, depicted with diamonds in 4.46(b), is higher for oxidation than for reduction, but also varies with the substrate, indicating that k_0 is influenced as well by strain.

In this section we have investigated the influence of thickness and macroscopic strain on exchange kinetics and physical properties. Compressive and

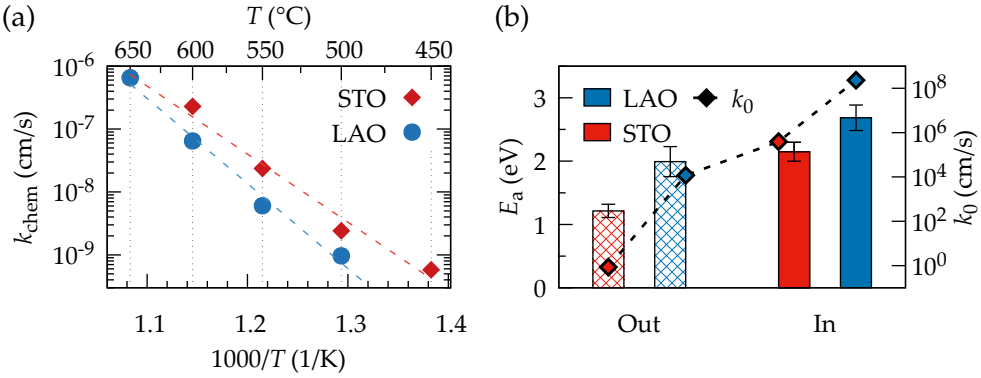

FIGURE 4.46: (a) Arrhenius plot for oxidation process of 25 nm Ag-free PLD thin films and (b) extracted activation energies and k_0 values (black diamonds) for in- and out-diffusion.

tensile strain was introduced into thin films by lattice mismatch with the substrate. We found that strain relaxes rapidly with increasing film thickness. Strained films exhibit a decreased oxygen stoichiometry. Oxygen exchange rates are drastically reduced for thinner films. In films of 25 nm thickness we could observe a significant difference between tensile and compressive strain, where tensile strain enhances oxygen exchange kinetics and lowers the activation energies of oxygen in- and excorporation.

4.7 Conclusions

In this chapter we have shown, that *in situ* electrical conductivity relaxation measurements are a very useful tool to study the oxygen exchange kinetics of epitaxial YBCO thin films. Its methodology and full integral sensitivity to the bulk was proven by simultaneous *in situ* XRD measurements.
A one dimensional oxygen diffusion model, based on Fick's second law and a first order surface exchange mechanism was used to described the measurements. The time evolution of conductivity could be well fit using a single exponential decay in the case of oxygen incorporation, while two parallel processes had to be assumed for the oxygen reduction mechanism. The weighted contribution of these two processes to the overall rate changes with temperature from one to the other. The physical origin of this second process could not be identified within this work, but might be related to different areas of the surface as grains and grain boundaries or dislocation-free and defect-rich regions.

We have studied the dependence of the exchange rates on temperature and oxygen partial pressure. For a standard relaxation measurement triggered by changes in $P(O_2)$ between $P(O_2)_{high}$ and $P(O_2)_{low}$, oxygen incorporation is faster than removing O from the crystal. Based on this asymmetry found for in- and out-diffusion processes, it was concluded, that exchange kinetics in thin YBCO films are limited by a surface mechanism.

Further, we have found, that the coating of YBCO with silver significantly increases exchange rates and lowers activation energies for reduction and oxidation. Yet, another evidence that oxygen exchange kinetics of thin YBCO films are determined by surface reactions. We address the enhancement of kinetics to the catalytic activity of silver for oxygen reduction reactions, which will be further discussed in the next chapter. The RDS is kept within the surface, as the asymmetry between in- and out-diffusion rates is as well observed for silver coated films.

While oxygen exchange rates are strongly affected by the oxygen partial pressure due to the change in coverage, activation energies were found to be independent of the pressure over several orders of magnitude. Therefore it was concluded that the RDS does not vary within the analysed pressure range.

Analysing out- and in-diffusion processes at the same final pressure (*ergo* with the same surface coverage) revealed that reduction rates are faster than oxidation rates at low temperatures. At high temperatures, oxidation becomes faster. This temperature dependence is in agreement with lower activation energies and lower k_0 values for oxygen excorporation. From this asymmetry at the same pressure and different activation energies of oxidation and reduction, surface diffusion can be excluded of being the RDS as it is assumed to be the same for both processes.
The analysis of the pressure dependence of initial and equilibrium reaction rates led us to the conclusion that the last ionisation and incorporation step of a surface oxygen ion (step 5 in Table 2.1) is the RDS for oxygen incorporation into Ag coated YBCO thin films. This is in agreement with the result, that only atomic oxygen is involved in the RDS.

We have studied the influence of different YBCO microstructures on exchange kinetics. Modifications of the microstructure were introduced via doping of Ca into the structure, embedding of nanoparticles and the use of different growth techniques as a TFA-CSD flash heating process, a liquid-based CSD growth and pulsed laser deposition. Exchange kinetics were found to be enhanced for Ca-doped YBCO, nanocomposites and films deposited by PLD. We address this to a modified nanostrain landscape. Nanostrain was found to mediate the activation energy of the rate determining step.

Further we have analysed the influence of thickness and macroscopic strain, introduced into thin YBCO films due to lattice mismatch with the substrate, on physical properties and oxygen exchange kinetics. Maximum strain values of about 20 % were obtained in 25 nm thick films grown by PLD. With increasing film thickness strain is released. The strained lattice was found to influence the thermodynamics of YBCO, resulting in lower oxygen contents with increasing strain values. The occurrence of macroscopic strain is accompanied by an increase in nanostrain, which was proposed to be due to very short growth times. In agreement with literature tensile strain was found to enhance oxygen exchange kinetics compared to compressive strain for the thinnest films. However, with increasing thickness exchange rates were strongly enhanced. It is suggested that a strain relaxation mechanism leads to a defected surface with enhanced surface exchange rates, causing faster kinetics in thicker films. Independent of the film thickness and surface coating, it was concluded that a surface mechanism limits the exchange of oxygen with environment.

Chapter 5

Microstructural and surface changes in YBCO by oxygen exchange processes

In the last chapter we have studied the overall oxygen exchange process for YBCO with environment and we have concluded that a surface reaction step is limiting the overall rate of oxidation and reduction processes. However, the optimisation of the manufacturing process of HTS coated conductors requires not only the deep understanding of the oxygen incorporation mechanism, but the general effect of thermal treatments on the microstructure and surface of the superconducting layer, as it will impact the superconducting properties of the final conductor.
Therefore, as discussed in this chapter, additional sets of ECR measurements are performed to investigate the influence of annealing history, as the dependence on temperature and total annealing time, on the samples microstructure and its surface. This analysis will allow a thorough understanding of oxygen exchange kinetics of YBCO thin films and provide conclusions on observations made in Chapter 4, as *e.g.* different activation energy regimes.

5.1 Dependence of oxygen exchange process on measurement history

The oxygen exchange kinetics of YBCO are analysed by changes in oxygen partial pressure during isothermal annealings at various temperatures. Up to now, we have followed the standard procedure of starting at high temperatures and subsequently decrease the temperature, as established in preceding works [134, 157]. The reproducibility of the measurement is usually tested during the first dwell with repeated cycles at high temperatures and reassured by the analysis of several similar samples.

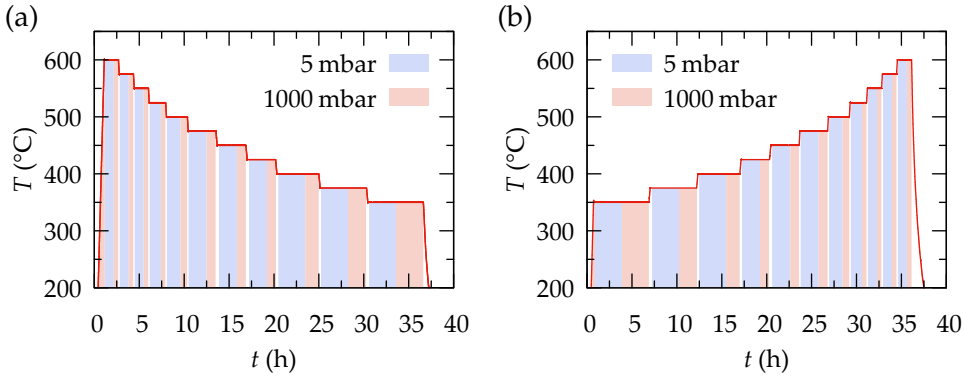

FIGURE 5.1: Thermal profile for (a) standard (*T-down*) and (b) time reversed (*T-up*) ECR measurement. Oxygen partial pressure is indicated by the different background colouring.

To analyse any kind of history dependence on the measurement, the standard temperature profile is reversed in time, as shown in Fig. 5.1. While the two processes are identical in terms of dwell times, the heating and cooling rates are slightly modified. In the standard process (in the following abbreviated as *T-down*) the sample is heated with 10 °C/min to 600 °C. The cooling rate between the dwells is 5 °C/min above 475 °C and reduced to 3 °C/min due to slow furnace cooling at lower T.
The reverse process (*T-up*) starts with a dwell at low temperature, typically 350 °C or 450 °C, and T is subsequently increased. The heating rates are 3 and 5 °C/min below and above 450 °C, respectively, to avoid any overshoot in temperature. As in the standard procedure, during every dwell the oxygen partial pressure is switched from high to low and back to high. In the following we will analyse the influence of inverting the measurement direction in pristine and silver coated CSD and PLD films.

5.1.1 Time reversed (*T-up*) ECR measurement in pristine CSD YBCO

The time evolution of the conductance G for a *T-up* process is presented in Fig. 5.2(a) for a pristine CSD film with a thickness of 250 nm. The oxygen atmosphere is indicated by the background colouring, at which blue and red mark low (5 mbar) and high (1 bar) $P(O_2)$, respectively. The corresponding temperature is presented in the upper part of the graph.
We observe very fast transitions of G to the new equilibrium states. Even at 450 °C saturation is reached within minutes for a pristine YBCO layer without

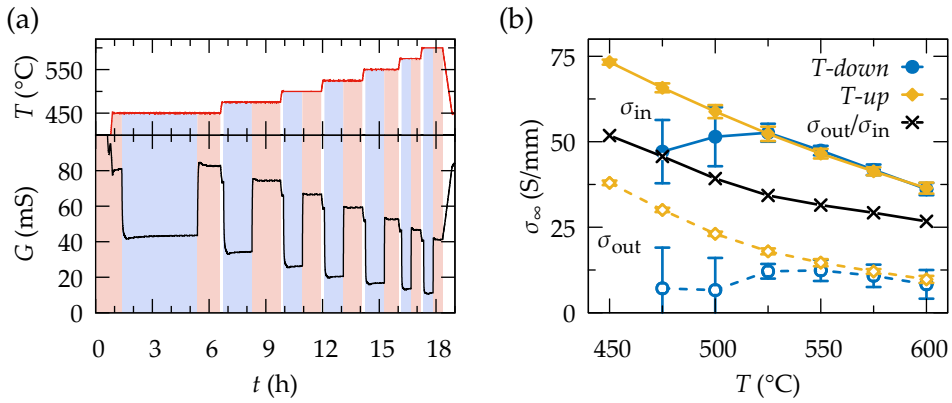

FIGURE 5.2: (a) Time evolution of conductance of 250 nm pristine CSD YBCO film starting at low temperatures; corresponding temperature is shown in the upper graph. (b) Saturation conductivities for CSD films measured in *T-down* and *T-up* direction (open symbols: out-diffusion, filled symbols: in-diffusion). The ratio of conductivities shown for *T-up* (black line) has the same y scale but is given in %.

Ag coating. This is in strong contrast with results of the standard ECR measurements of section 4.1, where at 450 °C saturation was not reached within hours.

The saturation conductivities σ_∞ for oxidation and reduction are shown in Fig. 5.2(b) for a *T-down* and *T-up* process. For the latter the oxidation saturation values increase linearly with decreasing temperature down to 450 °C, while for a *T-normal* process this trend stops below 525 °C due to slow kinetics. The linear temperature dependence is the superposition of mainly two contributions. The conductivity decreases with increasing T due to a thermally activated increase of the phonon concentration causing increased lattice scattering of the charge carriers, as expected for metallic behaviour. Secondly, oxygen is being released from the structure with increasing temperature. A higher oxygen vacancy concentration lowers the electronic conductivity due to a lowered amount of free charges.

The ratio of $\sigma_{\infty,\mathrm{out}}/\sigma_{\infty,\mathrm{in}}$ for the sample measured following the *T-up* process, is depicted in Fig. 5.2(b) with the same scale to the left but in %. The ratio increases with decreasing temperature. This means that the change in oxygen stoichiometry between $P(O_2)_{\mathrm{high}}$ and $P(O_2)_{\mathrm{low}}$ decreases with decreasing temperature. One can also notice that σ_{out} at 450 °C has about the same value as σ_{in} at 600 °C. This is in good agreement with the expected equilibrium oxygen content from the YBCO bulk phase diagram [21], wherein the phase points at (450 °C,5 mbar) and (600 °C,1000 mbar) have an oxygen content of about $O_{6.75}$.

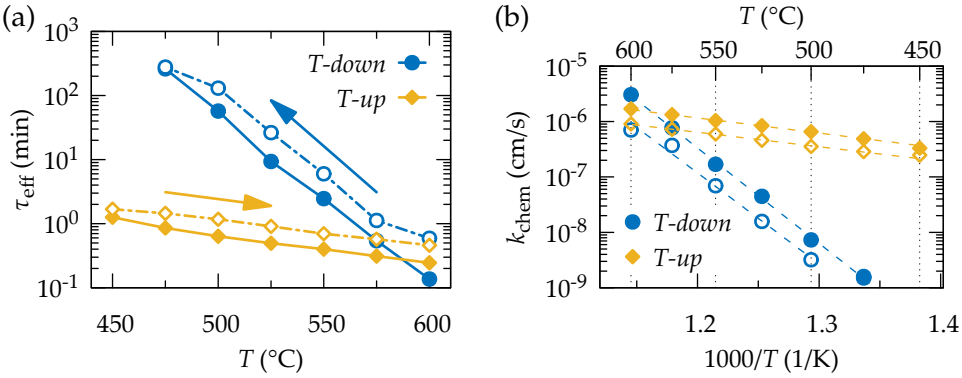

FIGURE 5.3: (a) Relaxation times for *T-down* and *T-up* process. Open and filled symbols correspond to oxygen release and uptake, respectively and (b) Arrhenius plot to extract activation energies for the measured temperature range by linear fits.

The main contribution to the temperature dependence of G therefore must come from the stoichiometric change of oxygen and not from the increase of scattering. This further implies that not only the time evolution of the measured conductance is proportional to changes in the stoichiometry but also the relative changes in conductance are proportional to the oxygen content.

The extracted saturation times for a *T-down* and *T-up* process are compared in Fig. 5.3(a). The measurement directions are indicated with arrows. We observe a strong contrast between the two measurement procedures, for both, oxidation (full symbols) and reduction (open symbols). Relaxation times of the *T-up* process are very short at low temperatures and exhibit a much weaker dependence on temperature, as compared to the *T-down* measurement. At 475 °C τ values are decreased by more than two orders of magnitude upon changing the measurement direction.
The asymmetry between in- and out-diffusion saturation times is kept upon reversing the measurement direction (starting at low T), with similar ratios τ_{in}/τ_{out} of about 0.5. For oxygen incorporation (solid symbols) a crossover between the two measurement directions occurs between 575 and 600 °C. Only at the first temperature at 600 °C *T-down* shows faster kinetics, while *T-up* has shorter saturation times at all lower temperatures. The same trend is observed for the out-diffusion process, with similar time constants only at the initial dwell of the normal process at 600 °C.

The data is presented as well in Fig. 5.3(b) in an Arrhenius plot and activation energies are extracted. For the *T-up* process we obtain $E_a = 0.48$ and 0.58 eV for oxygen ex- and incorporation, respectively. These values are

strongly reduced compared to 2.2 eV (reduction) and 3.4 eV (oxidation) obtained by the *T-down* measurement procedure.

5.1.2 Time reversed (*T-up*) ECR measurements in Ag coated CSD YBCO

We have found that the direction of the measurement has a crucial impact on the observed oxygen exchange kinetics of pristine YBCO films. Saturation times can be decreased by more than two orders of magnitude by starting at low temperatures. The resulting exchange rates are comparable to silver coated films obtained by a *T-down* process. To better understand these results we have repeated oxygen exchange measurements with silver coated CSD thin films, following the *T-up* procedure (350 - 600 °C).

Reduction time constants for both measurement directions are shown in Fig. 5.4(a) for silver coated films (open symbols). For comparison the pristine samples are drawn as well (closed symbols). The two silver coated layers have a similar temperature dependence, as does the pristine *T-up* film. As shown above, the pristine *T-down* sample strongly deviates.

It is worthwhile to mention that at the first temperature dwell at 450 °C the pristine sample equilibrates the fastest to a new atmosphere. Also at higher temperatures this sample has the same exchange rates as a silver coated sample.

If we concentrate on the silver coated samples measured in different directions (open symbols), we can observe a crossover of saturation times at 425 °C. The process starting at 600 °C exhibits shorter relaxation times at higher temperatures, whereas the reverse process *T-up* saturates faster at lower temperatures. We have observed a crossover of saturation times of the two different measurement directions for many different pairs of samples, as *e.g.* Ag coated 250 nm thick CSD films and silver coated thin PLD layers (25-200 nm). The temperature of the crossing varies between 400 and 475 °C. Typically in our measurements, the point in time of the crossover corresponds to about half of the total measurement duration. This is a first indicator that the annealing time has an impact on the observed oxygen exchange kinetics of YBCO, as will be discussed in detail in section 5.3.

In Figure 5.4(b) we show the out-diffusion surface exchange rate constants for a silver coated film (*T-up* process). The reduction process is fit using two parallel processes (2τ model) at each temperature. The weight shifts from τ_1 with almost 100 % at 600 °C to about 50 % each below 500 °C. Over the full measured temperature range a single linear activation energy can be extracted

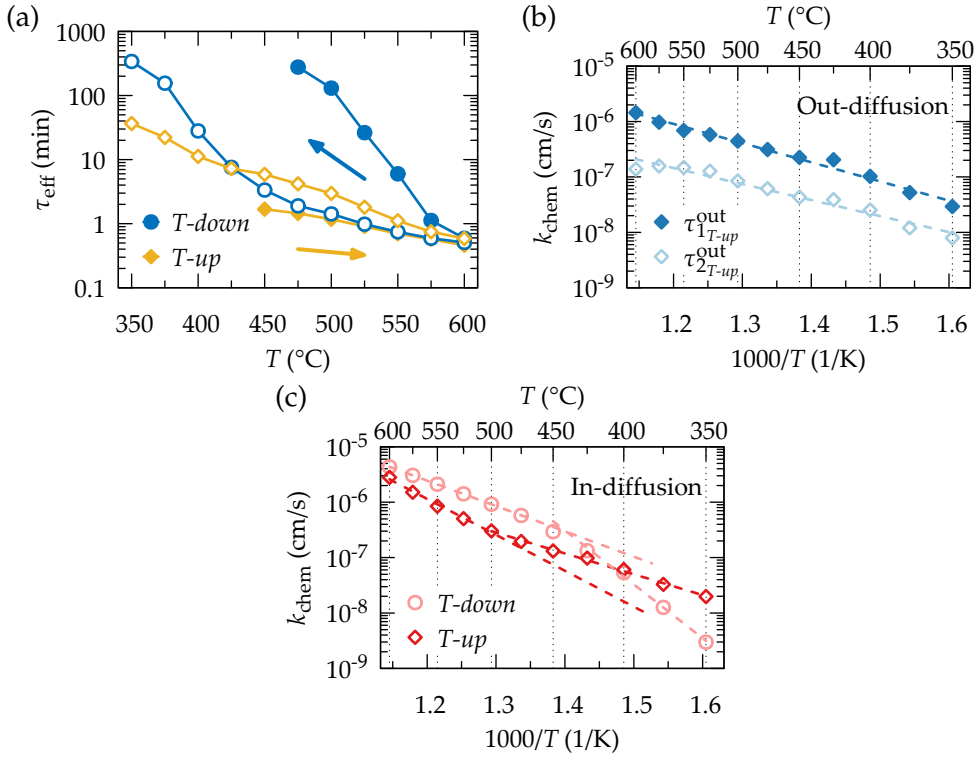

FIGURE 5.4: (a) Effective out-diffusion relaxation times of pristine (closed symbols) and silver coated (open symbols) 250 nm thick CSD YBCO films measured in different directions. (b) Out-diffusion surface exchange constants (of two parallel processes) of silver coated *T-up* sample. (c) k_{chem} of in-diffusion process for *T-down* and *T-up*.

for the out-diffusion process with $E_a(\tau_1) = 0.69\,eV$ and $E_a(\tau_2) = 0.57\,eV$, respectively. This is contrary to the *T-down* process, where we found two temperature regimes with $E_a(\tau_1) = 0.56\,eV$ at high T and $E_a(\tau_2) = 1.77\,eV$ at low T, where either one of the two parallel mechanism is predominantly contributing, as discussed previously (Chp. 4.2.2).

The in-diffusion surface exchange rates for a *T-down* and a *T-up* process are shown in Figure 5.4(c). As previously discussed for the *T-down* procedure, we find a deviation from one single activation energy regime in the case of the *T-up* measurement. However, in contrast to previous measurements, the low temperature range exhibits the lower activation energy ($E_a = 0.76\,eV$). At temperatures above 500 °C a second linear activation energy regime occurs

with higher pre-exponential factor k_0 and activation energy. At high temperatures both measurement procedures exhibit similar activation energies of $E_a \approx 1$ eV.
We would like to emphasise that in the initial phase of both processes (*T-down* and *T-up*) we find small activation energies and subsequently we observe a kink to higher activation energies. This is another indicator of the importance of thermal history/annealing time.

In summary, we have found a dependence of oxygen exchange kinetics on the measurement history. Its influence is particularly pronounced in pristine YBCO films, but also observed upon silver coating. A crossover of saturation times of the two measurement directions occurs around 425 °C for silver coated samples, with faster kinetics at low T in *T-up* and at high T in *T-down* measurements, respectively. Additionally we find a deviation to higher activation energies as the time of the experiment increases, which hints to a possible influence of annealing time.

5.1.3 Transformation of surface silver coating during annealing processes

In the analysis of silver coated films after oxygen exchange measurements we have observed that an initially thin and homogeneous silver layer transforms into islands during the annealing process, similar to the dewetting effect at solid-liquid interphases. This transformation could possibly contribute to the asymmetry between the two different measurement directions *T-down* and *T-up*, although it is observed as well in pristine YBCO. However, the analysis in this section will help to understand the role of silver as a catalytic agent of Chapter 5.3.

We have studied the transformation of a 20 nm thin silver film, deposited on a $LaAlO_3$ substrate, under different heat treatments, as shown in Figure 5.5. In Fig. 5.5(a) SEM images are shown for the case of the as deposited silver layer (initial), after an annealing for two hours at 400 °C (#1) and 600 °C (#2). The statistical analysis of the particle size is performed using an *Image J* routine within an area of 29.9 µm × 25.8 µm in the centre of the surface. The initial distribution of Ag is a homogeneous layer over the full surface. On top of this layer a small amount of submicrometer Ag islands is accumulated.
After annealing (case #1) we find a high density of small particles with an average (maximum) diameter of 100 nm (230 nm) on top of the YBCO surface. After a dwell at higher temperature (#2), less but bigger islands are formed with a mean diameters of 175 nm and and a maximum particle size of 350 nm.

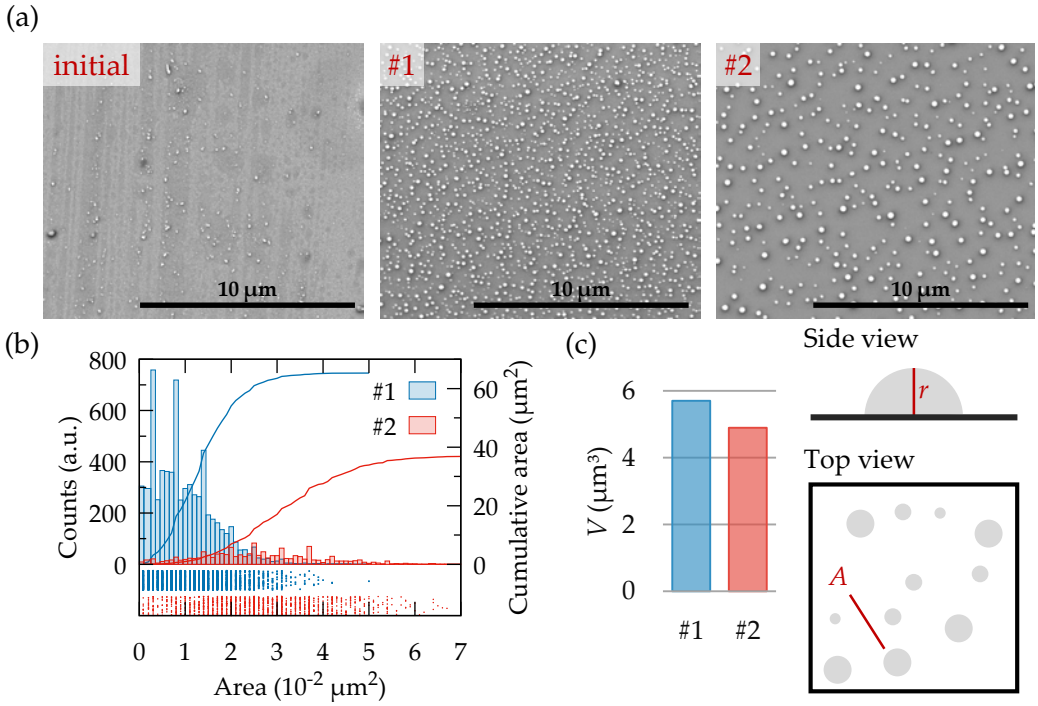

FIGURE 5.5: (a) SEM images of a 20 nm thick layer of silver on top of LAO after deposition (initial), a two hour heat treatment at 400 °C (#1) and 600 °C (#2). Statistical analysis of (b) island sizes from SEM images for a surface area of 29.9 µm × 25.8 µm (continuous lines correspond to cumulative area) and (c) the total volume of silver using a model of half spheres.

This coarsening effect is likely caused by the higher mobility of the silver particles at higher temperatures.

The distribution of the particle size is shown in Fig. 5.5(b). The continuous lines mark the cumulative surface area of the silver particles. The total analysed surface is about 770 µm^2. Hence, the fraction of surface covered by silver is strongly reduced to about 9 % for (#1) and almost further halved to 5 % by (#2). The Ag particles are assumed to be of half sphere shape to analyse the total amount of silver, respectively its volume, on the surface. The volume counts 5.7 µm^3 after annealing at 400 °C and 4.9 µm^3 after 600 °C, as shown in (c). The difference could be caused by partial sublimation of silver at 600 °C.

The temperature T_F, where the formation of the silver islands starts, can be extracted from electrical *in situ* measurements. Therefore we have coated the full surface of a YBCO thin film with a 100 nm thick Ag layer. Silver electrodes are fixed to the corners of the silver coated surface.
The *in situ* resistance as a function of temperature is shown in Fig. 5.6(a) in

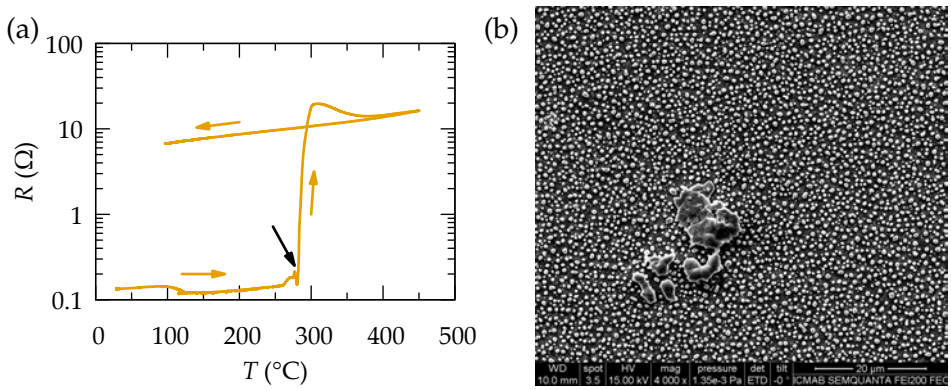

FIGURE 5.6: (a) Resistance as a function of temperature of a fully Ag coated YBCO film, the arrow marks the temperature where islands are formed and a continuous current percolation path only through silver is broken. (b) SEM image after thermal treatment of initially fully covered YBCO surface with a 100 nm thick Ag layer.

a semi-log plot. At the beginning of the measurement, the total resistance is determined by the low resistance path through the Ag layer in parallel to YBCO, resulting in a very low measured value until 280 °C. At this point the continuous current percolation path through silver is interrupted. We observe a sharp transition and above 290 °C the system starts to be sensitive to the YBCO film.
The measurement was performed with a heating ramp of 10 °C/min. As the formation process of islands is thermally activated and during the heating the system is out of equilibrium, T_F might be lowered to a certain extend by reducing the heating rate. Note, the derived temperature of 280 °C is the point where the percolation path is fully interrupted, therefore the transformation of the full layer might start already before. As soon as the islands are formed, the measured resistance profile follows the same trends as a pristine YBCO sample, *e.g.* with a linear slope during cooling.

The resulting coverage is shown in Fig. 5.6(b) after annealing at 450 °C for 2 h. The 5 × thicker initial silver coating leads to much bigger islands, as compared to (#1) in Fig. 5.5(a), with an average diameter of 600 nm and maximum particle sizes above 1 µm. Also the fractional coverage of the surface with silver is increased to about 28 %, which is approximately 5 × larger than the ones reported before.

Since the formation of islands happens at an early stage (during the heating ramp), it is not expected to have major influence on the further measurement procedure and it is not assumed to be responsible for the detected asymmetries of the *T-down* and *T-up in situ* process, especially as this was found as well for pristine films. We recall that the initial coverage due to the patterning of the silver layer is about 40 %, which reduces to a final coverage of the surface with silver to 5-10 %. We have performed ECR measurements with thicknesses of the silver coating between 20 and 100 nm. However, no influence on the initial thickness was found on the oxygen exchange rates. Thus we conclude that the fractional coverage does not play a considerable role above a critical value of 5-10 %.

5.1.4 Outlook: possible mechanism giving rise to thermal history dependence

In this section we have shown that the measurement history strongly affects the oxygen exchange kinetics of YBCO thin films. This impact was found for pristine and in attenuated manner as well for silver coated YBCO obtained by different growth techniques. The following options could explain the results due to the influence of surface and microstructural changes on oxygen exchange kinetics of YBCO:

(A) A breaking of the grain and twin boundary coherence through the thickness of the film due to the formation of stacking faults (two dimensional defect along the *ab*-plane) could drastically reduce the rate of oxygen transport within the material, making bulk diffusion the rate determining step. Additionally, CuO-intergrowths can cause a modification of the present strain landscape and the films equilibrium oxygen content.

(B) Changes in the surface due to the thermal history could lead to a modified surface exchange rate k_{chem}, causing a variation of the overall kinetics. A restructuring of the surface, cation segregation and phase instabilities might change the overall composition, chemistry and morphology of the surface.

While (B) is considered to only affect the exchange kinetics (saturation times), (A) might alter the materials conductivity due to changes in the equilibrium oxygen stoichiometry and defect landscape (residual resistivity). In the next two sections 5.2 and 5.3 we will focus on the raised assumptions (A) and (B), respectively.

5.2 Thermally activated effects on microstructure, normal state and superconducting physical properties

We have found that YBCO oxygen exchange reaction rates are strongly affected by the measurement history. This dependence might be caused by thermally activated changes of the films microstructure, as the formation of stacking faults. Grain and twin boundaries are considered fast diffusivity channels for oxygen ions. The intercalation of a CuO double layer could break the twin boundary coherence along the crystals *c*-direction for CSD films as demonstrated in [158, 159], effectively slowing down oxygen diffusion. If the bulk diffusivity D_c along *c* gets reduced until $D_c \ll k_{\text{chem}} t$, with the film thickness t, bulk diffusion becomes the RDS.

In this section we will analyse the impact of thermal treatments on the microstructure and physical properties in the normal and superconducting state. Further we will study if modifications of the bulk can explain the observed effect of measurement history on YBCO exchange kinetics, as *e.g.* the rigorous slow down of reaction rates in pristine YBCO.

5.2.1 Study of post annealed YBCO microstructure by STEM analysis

In the following we will study the microstructural differences between two 200 nm thick YBCO films after oxygen exchange measurements. These films were deposited by PLD on $LaAlO_3$ substrates. The oxygen exchange rates of sample *Y-Td* were analysed following the procedure *T-down*, starting at high temperatures (600 - 350 °C), while sample *Y-Tu* was measured in *inverse* direction, going up in temperature.

The film microstructure is investigated by scanning transmission electron microscopy. This analysis was performed in collaboration with STEM experts of the group. The resulting STEM images are shown in Fig. 5.7(a) and (b) for *Y-Tu* and *Y-Td*, respectively. Two $YBa_2Cu_4O_{8-\delta'}$ intergrowths (stacking faults) are exemplarily marked with arrows in both images, which consist of double CuO chains in between BaO planes of the YBCO structure. These defects are well observable due to their high contrast. In both samples a high amount of stacking faults (SF) is found with a density of 10^{12}/cm. This is in contrast to as grown PLD YBCO films, which exhibit a low density of intergrowths (compare with STEM image in Fig. 4.34(b) on p. 99). These high SF-densities are also by orders of magnitude higher than in standard CSD YBCO films [160] and usually only observed in YBCO nanocomposites with embedded nanoparticle concentrations [125].

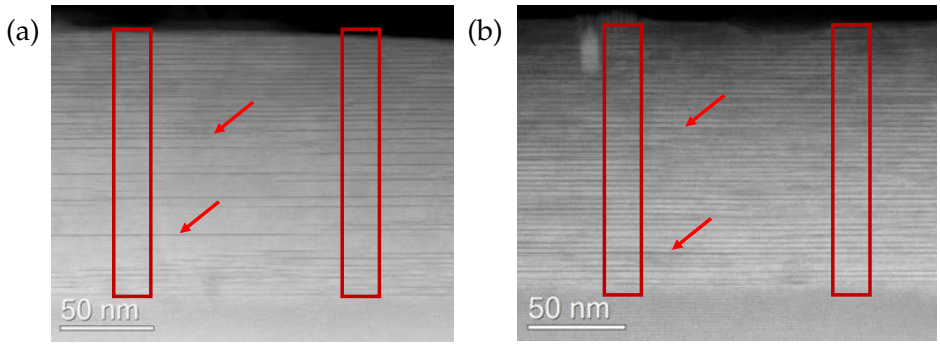

FIGURE 5.7: STEM images of 200 nm thick PLD films after *in situ* measurements starting (a) at low (*Y-Tu*) and (b) high (*Y-Td*) temperature. In both samples we find a very high stacking fault density.

The standard procedure of oxygen exchange measurements (*T-down*) provokes the formation of a higher amount of stacking faults with a mean separation of intergrowths in *c*-direction by about 2.5 nm, while the inverse process (*T-up*) has a mean distance of 4 nm between neighbouring SFs along *c*. The observed stacking faults of *Y-Td* are larger than 200 nm, extending the image width at least on one side. On the other hand, in the case of *Y-Tu* short intergrowths can be seen close to the interface with the substrate. Therefore the mean length of the SFs seems to be shorter in this sample.

The origin of the different intergrowth landscapes of the two samples is not clear. We assume that the formation of SFs is a thermally activated process and favoured in the presence of a distorted matrix. Therefore in the *T-down* process SFs are rapidly formed already at the beginning of the measurement at high T and further expand during the subsequent steps at lower temperatures. In the *T-up* process Y124 intergrowths only slowly start to form at low temperatures and rapid development is withhold until the dwells at elevated temperatures.

5.2.2 Bulk analysis of as-grown and post annealed films by XRD

In this section we will study the modification of the films X-ray diffraction pattern due to thermal annealing. TEM analysis revealed a high $YBa_2Cu_4O_8$ intergrowth density in post annealed YBCO films. The *c*-parameter of Y124 is with 13.61 Å [161, 162] larger than 11.68 Å of Y123, due to the double CuO-chain. Thus, the (00l) peak family of Y124 bulk is shifted to lower 2θ values as compared to Y123.

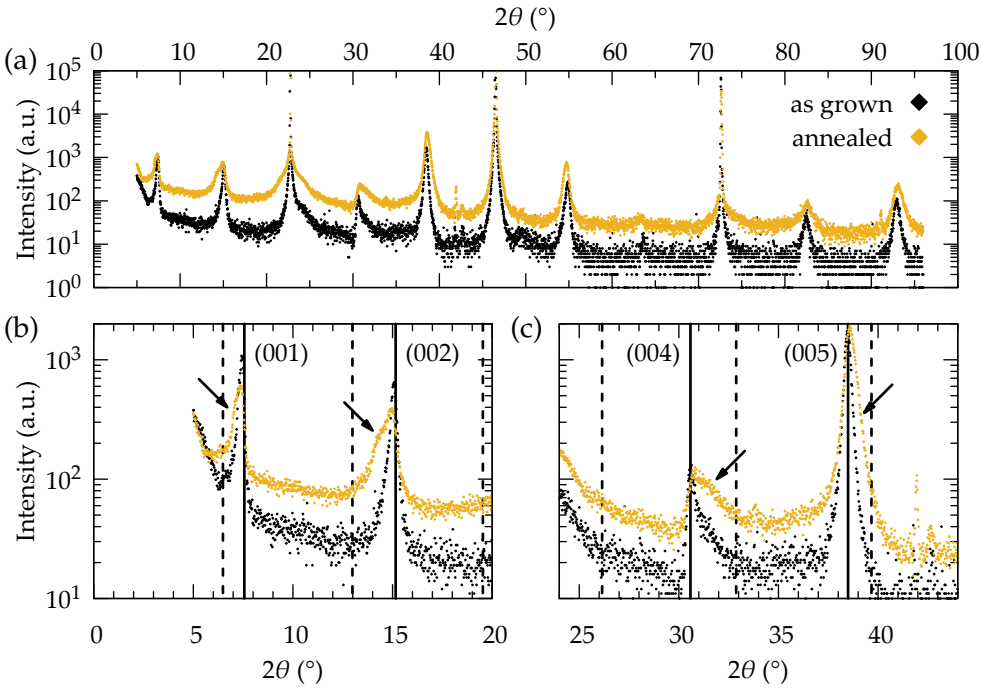

FIGURE 5.8: XRD scan of a 100 nm PLD film previous to and after *in situ* measurement: (a) full range and extracted regions (b) and (c), with theoretical Y123 and Y124 (00l) peak positions marked with solid and broken lines, respectively. In the post annealed film we observe shoulders in the Y123 peaks towards the closest Y124 reflection (marked with arrows).

The full 2θ XRD profile of a 100 nm thick PLD YBCO film grown on $SrTiO_3$ before and after annealing (*T-up*) is shown in Fig. 5.8(a). For clarity the intensity of the post annealed film is shifted to higher values. Both profiles show the (00l) $YBa_2Cu_3O_{7-\delta}$ reflections and the (h00) substrate peaks. No impurity phases are detected and the XRD profile does not show coherent reflection related to the Y124 phase. Additionally, we do not observe major modifications of the patterning after annealing, as for example the arising of new peaks or a broad shift of certain reflections to a different angle.
However, from STEM measurement we know that a significant amount of stacking faults is formed during post growth annealing processes. The lack of a significant shift of the coherent reflections is opposite to some reports in literature, where the formation of stacking faults causes severe changes in the peak position [159, 163, 164] and the stacking fault density can be evaluated using the Hendricks and Teller model [165].

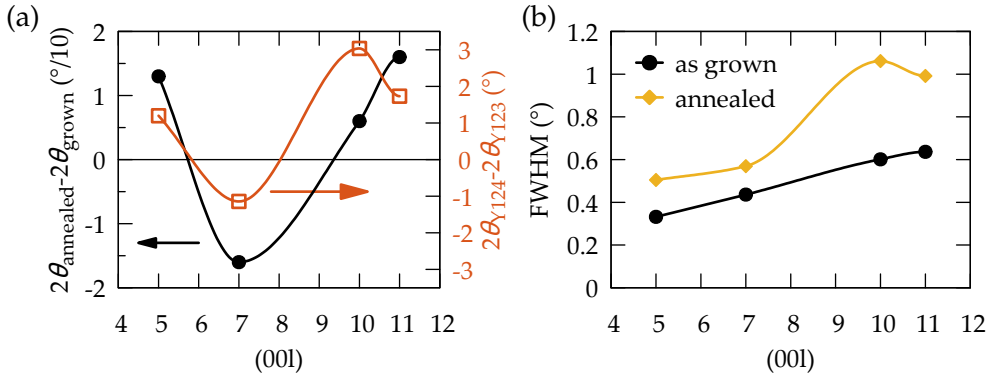

FIGURE 5.9: (a) Relative peak shift after annealing (left scale) compared to the distance of the bulk Y123 and Y124 reflections (right scale) and (b) comparison of the FWHM of higher angle (00l) peaks before and after annealing.

The first four YBCO reflections, not overlapping with the substrate peak, are enlarged shown in the sub-figures (b) and (c). Theoretical (00l) peak positions of the $Y_1Ba_2Cu_3O_7$ phase are indicated by solid vertical lines, while the dashed lines correspond to the Y124 bulk phase. Although the Y124 structure is not reproduced by defined peaks, an asymmetric broadening of the Y123 peaks into the direction of the closest Y124 bulk reflection is observed for all shown peaks. The shoulders are marked by arrows.

An analysis of the peak movement for higher angle reflections is shown in Figure 5.9(a). Due to the strong deformation respectively substrate overlap, the low order (00l) peaks with $l < 5$ could not be fit properly and are excluded from further analysis. The black circles represent the ten times magnified shift of each measured peak position after annealing to its as grown state. The orange squares (right scale) mark the distance between the theoretical positions of the Y123 peaks and its closest Y124 neighbour. As the measured shift in 2θ (black line) follows the same trend as the difference of Y123 and Y124 bulk reflections (orange line), we conclude that the first is heavily influenced by the formation of stacking faults during the heat treatment. This effect interferences with the sensitivity of the *c*-axis to the overall oxygen content.

A general broadening of the peak shape due to thermal annealing is observed for the higher angle reflections, as shown in the analysis of the full width at half maximum (FHWM) in Fig. 5.9(b). The FHWM of the (00l) peaks increases over the full spectrum. The peak broadening is symmetric in respect to the peaks 2θ position. Thus it is not directly caused by the larger Y124 unit cell (as the asymmetric shoulder for low angle reflection), but by a stronger distorted YBCO matrix and thus increased inhomogeneous strain within the

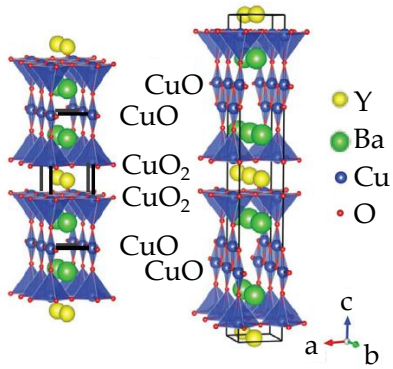

FIGURE 5.10: Unit cells of the orthorhombic $Y_1Ba_2Cu_3O_7$ and $Y_1Ba_2Cu_4O_8$ phase.

microstructure. The extracted nanostrain value increases from $\epsilon = 0.28\,\%$ in the as grown state to $\epsilon = 0.33\,\%$ after annealing.

Significantly stacking faulted YBCO layers (as observed by STEM) do not exhibit a coherent Y124 phase in their X-ray diffraction pattern. However, the high defect density influences the peak shape and position of the Y123 peak family. We found a shift of the (00l) YBCO reflections to the closest Y124 neighbour. In the case of low angle reflections the evolution of a shoulder on one side of the peak is observed. Additionally the formation of stacking faults causes an increase of nanostrain within the film.

We have found that stacking faults are formed during post growth annealing processes. The Y124 intergrowth structure contains an additional CuO chain within its unit cell with respect to Y123. The unit cells of the $Y_1Ba_2Cu_3O_7$ and $Y_1Ba_2Cu_4O_8$ phase are shown in Fig. 5.10. It has been shown [66] that the YBCO matrix only contains the stoichiometric amount of copper related to the Y123 phase. Thus, the formation of stacking faults is accompanied by the occurrence of Cu vacancies V_{Cu}, and therefore local copper off-stoichiometry [166]. It was experimentally found by STEM studies that these nanoscaled defects are balanced by the formation of complex point defects within the CuO double chain [166], in the form of Cu di-vacancies. Further, it was proposed and supported by density functional theory calculations, that this di-vacancies are decorated by three oxygen vacancies, forming a stable defect cluster. If the defect density is high enough, this might affect the overall oxygen stoichiometry of the thin film.

Additionally, in a recent study of YBCO thin films by means of several TEM techniques, oxygen vacancies were observed for the first time experimentally within the apical oxygen site position in the BaO-planes [167]. This defect was found to be linked to the presence of Y124 intergrowths, as the occurrence is limited to the close proximity of stacking faulted regions within the YBCO matrix. Y124 has a larger *c*-parameter as compared to Y123. Thus, Y124 intergrowths cause a local distortion of the crystal at the edge of the partial dislocation, contributing to an increased strain state of the structure. On the other hand the formation of oxygen vacancies in the BaO-plane was found to reduce the *c*-parameter. Thus it was suggested that the system generates $V^{\bullet\bullet}_{O(apical)}$ in adjacent cells of the intergrowth to compensate the mismatch with the surrounding.

To conclude, a lowering of the oxygen concentration might be expected with an increasing stacking fault density within the YBCO due to the formation of oxygen vacancies at different crystal sites to reduce internal strain and the Gibbs free energy of the distorted lattice.

5.2.3 Influence of thermal treatments on normal state and superconducting physical properties of YBCO thin films

We have seen in the previous sections that during thermal annealings to measure the oxygen exchange kinetics of YBCO the microstructure is strongly modified by the formation of $YBa_2Cu_4O_8$ intergrowths. The time mirrored processes *T-down* and *T-up* were found to cause different densities of Y124 intergrowths. Further we have argued that this defect could possibly modify the Gibbs free energy of the system, resulting in an increased oxygen vacancy density. In this section we will investigate the influence of the two different thermal processes on normal state and superconducting physical properties.

The charge carrier density n_H of post annealed PLD films with different thicknesses is shown in Figure 5.11. The values are averaged over several samples grown on $LaAlO_3$ and $SrTiO_3$ substrates for the same thickness. We find that the *T-up* process results in a higher final charge carrier density for all thicknesses. This could be related with the last temperature dwell, which is performed at low *T* for *T-down* and at high *T* for *T-up*. To exclude this possibility we have performed *T-up* measurements, where after reaching the last dwell at high temperature a low temperature dwell was repeated (*e.g.* dwells at 350, 375,..., 600, 350 °C). However, this modified procedure leads to the same conclusion that the *T-up* process results in higher charge carrier densities. Thus, a lower charge carrier density n_H in *T-down* measurements could be linked to the higher density of stacking faults and consequent defects, as discussed in the previous section.

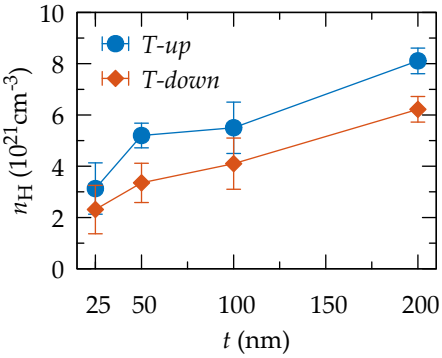

FIGURE 5.11: Charge carrier density n_H of post annealed PLD films with different thicknesses: the *T-up* procedure always leads to higher n_H as compared to *T-down*.

We will focus here on the influence of the thermal history on two samples of 200 nm thickness, grown by PLD on $LaAlO_3$ substrates, by comparing their states before and after ECR measurements. On both films a patterned 100 nm layer of silver was deposited previous to all presented measurements.
As in section 5.2.1, the kinetics of sample *Y-Td* were analysed following the process *T-down*, starting at high temperatures and subsequently going down. On the other hand sample *Y-Tu* corresponds to the process *T-up*. The ECR *in situ* analysis of the latter sample was completed with a repeated dwell at 350 °C. Therefore, according to the YBCO equilibrium phase diagram, both samples should be in the same state, due to the last annealing dwell at 350 °C.

The critical current densities obtained by magnetisation measurements (SQUID), are shown in Fig. 5.12(a). Initially both samples have a $J_c(5\,K)$ of about 35 MA/cm^2 and very similar temperature dependence. After the thermal treatment the critical current density at 5 K drops by about 30 % for *Y-Td*, while in the case of *Y-Tu* J_c is reduced by less than 10 %. The performance of the *T-down* sample is worsened over the full temperature range. The inset shows the critical currents normalised to the J_c value at 5 K. Both samples in the pre-annealed state and additionally the post annealed state of *Y-Tu* have very similar dependences on temperature. *Y-Td* after annealing deviates from this behaviour, revealing changes in the contributions to the critical current.
This feature is enhanced in 50 nm thick films which were annealed following the *T-down* and *T-up* process, respectively. Their normalised self-field critical currents are shown in Fig. 5.12(b). As well as for the 200 nm thick samples, the temperature dependence of the initial state of both samples is very similar (continues lines). After annealing we observe strong deviation from this

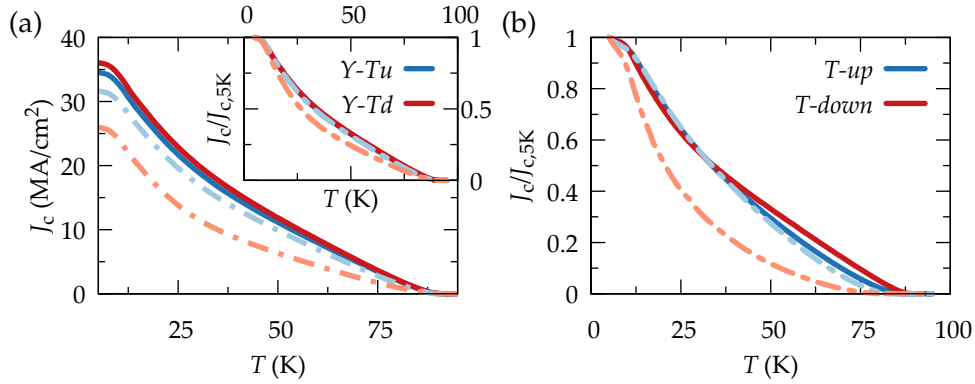

FIGURE 5.12: (a) Critical current densities for *Y-Tu* and *Y-Td* before (continuous lines) and after annealing (broken lines); the inset shows the J_c normalised to the value at 5 K. (b) Normalised critical current densities of pre- (continuous) and post-annealed (broken lines) 50 nm thick films, grown by PLD.

n_H (10^{21}/cm^3)	Pre-annealed	Post annealed
Y-Tu	5.3	8.1
Y-Td	5.1	6.2

TABLE 5.1: Charge carrier densities of 200 nm thick PLD films before and after thermal treatment.

temperature dependence for the *T-down* sample, while the temperature dependence is kept for the film annealed following the *T-up* process. In absolute values of J_c, *T-down* looses about 90 % at 5 K, while the *T-up* heat treatment causes a reduction of less than 50 %.

The charge carrier densities of *Y-Td* and *Y-Tu* are given in Table 5.1. The amount of mobile charges within the structure increases for both samples with the different temperature treatment. As mentioned above, the *T-up* process results in a higher n_H value. The increase of n_H of sample *Y-Td* combined with a decrease of J_c can be understood by looking at T_c measurements performed by different methods. The magnetic superconducting transitions, measured by SQUID, of the two samples are drawn in Fig. 5.13(a), where the initial as grown states are represented by continuous lines, while the post annealed transitions are drawn with dashed lines. The onset critical temperatures are about 89.7 K for both as grown samples, with a transition width of about 3 K. After the thermal treatment the transition temperature T_c is insignificantly reduced to about 89.3 K for both samples. The main difference between the

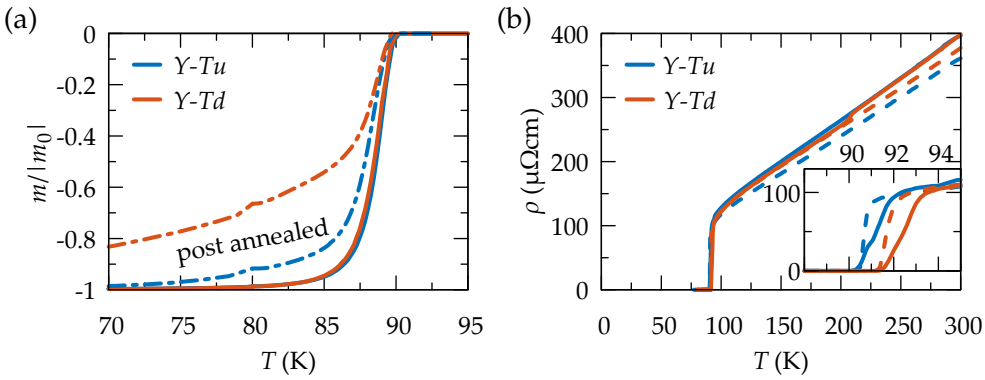

FIGURE 5.13: Superconducting transitions of *Y-Tu* and *Y-Td* obtained by (a) magnetic measurements (SQUID) and (b) electrical resistivity measurements. The pre-annealed state is indicated by continuous lines, the post annealing one with broken lines.

initial state and the post annealed sample and within the two different temperature processes is the transition width. Especially for *Y-Td* the transition is strongly broadened, with some parts of the sample becoming superconducting at temperatures as low as 50 K. The broader transition has to be correlated with an increased inhomogeneity within the samples microstructure.
Electrical measurements to extract T_c are shown in Fig. 5.13(b). The inset expands the region around T_c, showing a very sharp transition for both films after annealing (dashed lines). The resistivity at room temperature is slightly decreased in agreement with higher charge carrier densities in post annealed films.
The obvious differences in the transition widths between electrical and magnetic T_c measurements can be ascribed to the measurement method. The former technique measures a percolation current, bypassing non-superconducting normal zones, resulting in sharp transitions. In the latter, some regions with poor oxygen stoichiometry generating inhomogeneities, which cause a broadening of the transition, as SQUID measurements are sensitive to the full bulk. These defects are incoherent and distributed across the bulk and might be related with the formation of $YBa_2Cu_4O_{8-\delta}$ intergrowths and accompanied strained regions. The broader transition of the sample *Y-Td* is in agreement with a higher defect concentration as observed by STEM in section 5.2.1 for *T-down* samples.

In summary, we have shown that the direction of thermal annealings has substantial influence on normal state and superconducting properties. We

observe the formation of stacking faults and oxygen deficient zones, resulting in an inhomogeneous microstructure caused by thermal treatments between 350 and 600 °C in different oxygen atmospheres ($P(O_2) \leq 1$ bar). We have proposed that the mechanism leading to these transformations is thermally activated and accelerated in the presence of a distorted lattice. Therefore, measurements starting at high temperature (*T-down*) result in a higher stacking fault density, lower charge carrier density and stronger degraded critical current density, as compared to the inverse process *T-up*, as we have observed in our measurements.

5.2.4 Breaking of twin boundary coherence

YBCO thin films grown on single crystal substrates are typically highly twinned. Twin boundaries (TB) consist of thin, disordered planes with increased oxygen deficiency [168]. When oxygen is incorporated into the CuO-chains in *b* direction, strain is generated due to the simultaneous increase of the lattice parameter *b* and decrease of *a* [169]. TBs are generated during the tetragonal - orthorhombic phase transition to release stress inside the matrix. TB are aligned parallel to the crystal *c*-axis and are coherent across the whole film thickness in pristine YBCO layers. Grain boundaries and other defect rich regions were found to exhibit high diffusivity rates [57, 119]. Thus, TBs are thought to play a crucial role in fast oxygen transport through the bulk material in YBCO, as diffusion along *c* direction in bulk is orders of magnitude smaller than within the *ab*-planes [138]. Even though *c*-axis oxygen diffusion is significantly slower than along the *ab*-direction, it is still much faster than surface incorporation, making the latter the RDS of oxygen exchange in YBCO as shown in the previous chapter. In [158] it was concluded that the formation of Y124 intergrowths, which are 2D defects within the *ab*-planes, breaks the vertical coherence of twin boundaries (with a beneficial effect on the pinning properties).

If we assume that twin boundary channels are interrupted by CuO intergrowths, bulk diffusion might become the slowest, and therefore the rate determining step for oxygen exchange. This might also explain the observed asymmetry between oxygen kinetics measurements in two different measurement directions. The transformation of the microstructure is likely a thermally activated process, therefore its rate is enhanced at higher temperatures. If the measurement is performed following the *T-up* procedure, the twin boundary landscape of a pristine YBCO film is still intact at low temperatures, allowing fast oxygen transport rates. On the other hand, in the *T-down* process, structural changes occur during the first dwells at high temperatures limiting fast oxygen exchange at the following low temperature $P(O_2)$ cycles.

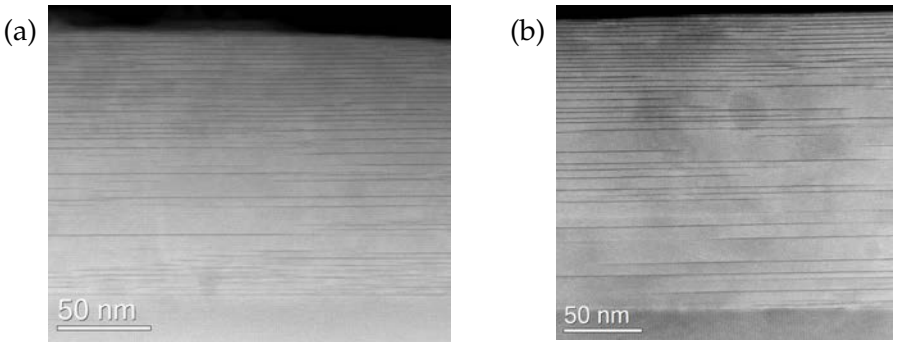

FIGURE 5.14: TEM images of (a) post annealed PLD film and (b) pristine CSD YBCO layer grown using a flash heating process.

To test this assumption, we have characterised pristine CSD YBCO films grown using a flash heating (FH) process, which were produced and provided generously by Dr. Ziliang Li, during his PhD in our group. Samples produced by this technique exhibit a very high density of stacking faults as shown in Fig. 5.14. The left image shows a PLD film after long *in situ* measurements, while the image to the right is the as grown microstructure of a flash heated sample. Both samples exhibit a similar intergrowth architecture, with a high density of long length stacking faults.

If the appearance of stacking faults causes the degeneration of oxygen exchange due to the breaking of twin boundary coherence, an initially stacking faulted specimen is expected to exhibit slow oxygen kinetics at low temperatures, even when the measurement is performed starting at low temperatures (*T-up*).

Such *T-up* ECR measurement of a pristine flash heated CSD film is shown in Fig. 5.15(a). The kinetics are analysed in the temperature range from 450 °C up to 600 °C in steps of 25 °C. The new equilibrium state after a change in the oxygen partial pressure is reached within very short times, already at the lowest temperature. This very fast relaxation is kept until 600 °C.

The in- (diamonds) and out-diffusion (circles) saturation times of the FH sample are compared to a standard pristine CSD film in Fig. 5.15(b). Both measurements were performed following the *T-up* procedure and the samples were not coated with a silver layer. We find a very similar temperature dependence of the two samples with very short relaxation times within the analysed temperature ranges. The initially stacking faulted FH sample exhibits comparable reaction rates as a pristine CSD film. Thus we can conclude that the presence of Y124 intergrowths and the associated breaking of twin

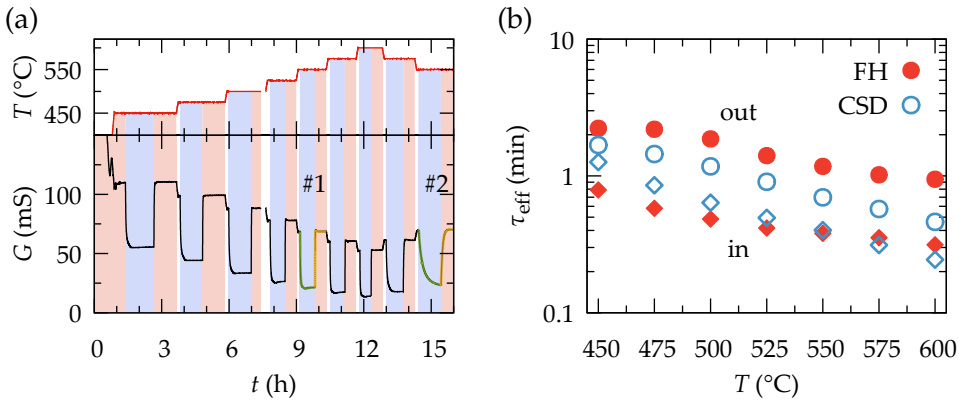

FIGURE 5.15: ECR measurement of a pristine FH CSD film (a) conductivity as a function of time (oxygen partial pressure indicated via background colouring); after reaching 600 °C, measurements are repeated at 575 and 550 °C. (b) Relaxation times of standard and flash heated CSD sample of oxidation (diamonds) and reduction (circles) measured in inverse direction (*T-up*).

boundary coherence is not responsible for slow exchange kinetics. The drastic deactivation observed in *T-down* measurements at low temperatures must be caused by another mechanism.

As shown in Fig. 5.15(a), after reaching 600 °C, the temperature is reduced again in steps of 25 °C and ECR measurements are repeated at 575 and 550 °C. The first and second dwell at 550 °C are indicated with #1 and #2 and the electrical conductivity relaxation data is further analysed in Fig. 5.16(a). Therein we compare the ECR for in- and out-diffusion measurements of the two dwells (with continuous and broken lines for #1 and #2, respectively). One can observe a drastic slowdown of the exchange rates for oxygen loading and the process of oxygen excorporation, while the conductivity saturation values are only slightly affected from one measurement to the other.

In Figure 5.16(b) we compare in-diffusion saturation times obtained by *T-up* processes for a CSD and a FH film (starting at (1) and going to (2)). The two *T-up* measurements are completed with repeated in- and out-diffusion cycles at lower temperatures after reaching 600 °C. Repeated dwells were performed at 575 and 550 °C in the analysis of the FH sample (3) and at 450 °C for the standard CSD film (4).

The high contrast between *T-up* and *T-down* measurements was already discussed previously. The interesting, new finding is the strong increase of saturation times in the repeated cycles of the *T-up* measurements. This strong upward deviation of τ after inverting the temperature cannot be related to the

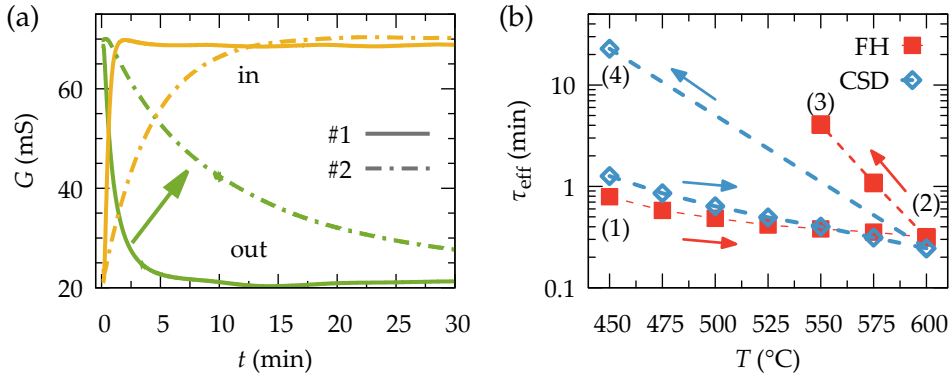

FIGURE 5.16: (a) 250 nm pristine FH CSD YBCO: $G(t)$ of for in- and out-diffusion at 550 °C before (continuous) and after (dashed lines) reaching $T_{max} = 600$ °C (extracted from Fig. 5.15(a)). (b) In-diffusion time constants for *T-up* measurements of a FH and a standard CSD film starting at (1) and going up to (2); after reaching 600 °C measurements are repeated at lower temperatures ((3) and (4) for FH and CSD, respectively).

formation of Y124 intergrowths at high temperatures, as the initially stacking faulted FH sample has fast kinetics at low temperatures. We therefore suggest that a surface related process is responsible for the deactivation of exchange rates, as will be discussed in the next section.

In this chapter we have shown that thermal treatments under different oxygen partial pressures ($\leq$ 1 bar) generate high amounts of $YBa_2Cu_4O_8$ intergrowths of long lengths, as observed with STEM measurements. The direction of the thermal history of the oxygen exchange measurements seems to play a crucial role, as we have found different defect characteristics of the SFs, as density and length, for a *T-down* and *T-up* process. A qualitative analysis using XRD has revealed the influence of SFs on the XRD pattern of YBCO. Although we did not observe coherent peaks related to the Y124 phase, a deformation of the Y123 reflections occurs, indicating the formation of stacking faults. We have shown that measurement history has additionally strong impact on the oxygen exchange kinetics and superconducting properties of our thin films. Even tough the dwell time per temperature is equal, starting at high temperatures results in a stronger reduction of critical current densities. From the presented measurements we can exclude that the formation or presence of intergrowths in the form of stacking faults causes the significant increase of saturation times at low temperatures in *T-down* processes.

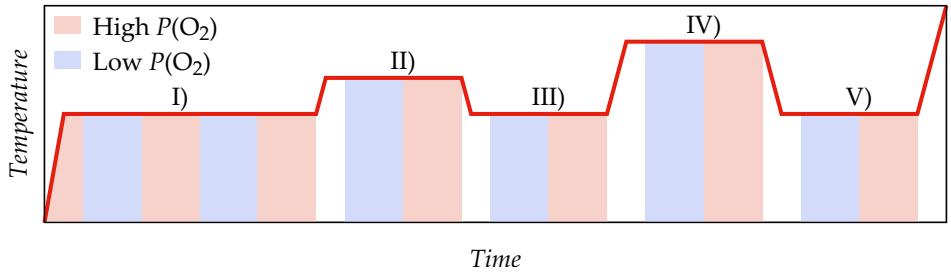

FIGURE 5.17: Profile of *in situ* ECR measurement to find temperature, where oxygen exchange starts to degenerate, consisting of several forward and backward steps in temperature.

5.3 Surface modification giving rise to irreversibility of oxygen exchange measurements

In previous sections we have found an asymmetry between *T-up* and *T-down in situ* measurements. This irregularity could not be explained by a modification of the microstructure nor a transformation of the silver surface coating. In this chapter we will study the parameter triggering the observed irreversibility and the role of deactivation of the surface oxygen exchange mechanism.

5.3.1 Temperature range of surface oxygen exchange deactivation

In the previous section 5.2.4, a decrease of oxygen kinetics was observed after reverting the temperature at 600 °C (see Fig. 5.16(a & b)). We found a sharp deviation to higher saturation times in repeated cycles at lower T. This finding suggests that the underlying mechanism has a high activation energy and deactivation of fast kinetics is caused at high temperatures.

A new set of modified *in situ* ECR measurements was performed to find the temperature where the underlying phenomena noticeably affects the oxygen exchange kinetics of YBCO. This experiment consists of several steps to higher and lower temperatures (T-step measurement), which in- and out-diffusion processes at each temperature. The temperature profile is shown in Fig. 5.17 and the individual steps are described in the following:

I) Several initial out-/ in-diffusion cycles to ensure stability and reproducibility of the measurement at 450 °C

II) Out- and in-diffusion cycle at 500 °C

III) Out- and in-diffusion cycle at 450 °C, to be compared with I)

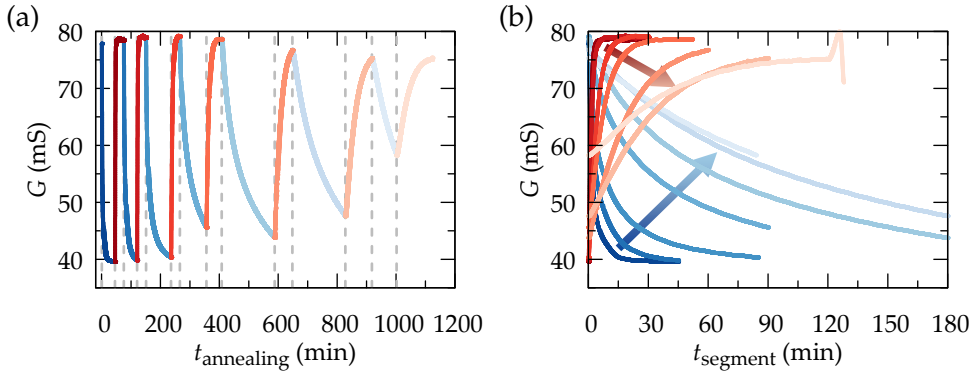

FIGURE 5.18: Several repeated out- (blue) and in- (red) diffusion measurements at 450 °C (250 nm CSD YBCO): (a) In chronological order, where the beginning of each pressure segment (change in the atmosphere) is indicated with dashed vertical line. (b) Conductance as a function of segment dwell time of each $P(O_2)$ segment (arrows indicate total annealing time).

IV) Out- and in-diffusion cycle at 550 °C

V) Out- and in-diffusion cycle at 450 °C, to be compared with I) and III)

VI) Continue until kinetics are affected

Oxygen exchange deactivation of pristine CSD YBCO at 450 °C

The history dependence of a pristine 250 nm thick CSD film is studied by a T-step measurement, precisely step I). We have performed several cycles of changes in atmosphere at 450 °C as shown in Figure 5.18(a), where the conductance G is plotted as a function of the total annealing time. The vertical bars indicate the point where the oxygen atmosphere is switched (start of next pressure segment). During the first cycles saturation is reached very fast, while with increasing annealing time, the process of oxygen exchange becomes significantly slower. This can be clearly observed in Fig. 5.18(b), where the conductance is shown over the segment dwell time. With subsequent $P(O_2)$ steps, thus with increasing total annealing time, the relaxation times become substantially longer. Even with extended dwell times of each segment, equilibrium saturation is not reached.

For each pressure segment we extracted the relaxation time constant and plotted it as a function of the total annealing time in Fig. 5.19(a) (precisely the annealing time $t_{annealing}$ at the start of the particular $P(O_2)$ segment). The

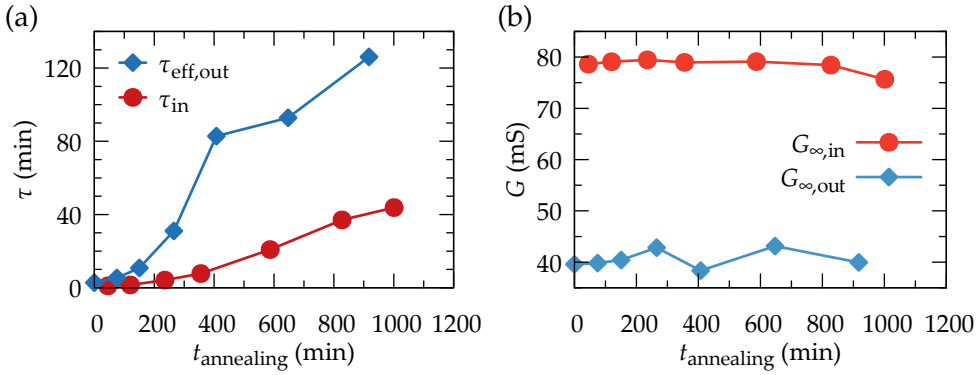

FIGURE 5.19: (a) Evolution of relaxation times during isothermal annealing at 450 °C and (b) corresponding conductance saturation values for in- and out-diffusion of a pristine 250 nm CSD YBCO sample.

relaxation times strongly increase with advancing annealing time. The exchange rate of the excorporation process decreases significantly faster. After an annealing of 1000 min $\tau_{eff,out}$ is about 25 × larger than its initial value, while τ_{in} increases from 1 min at the beginning to about 45 min.
The evolution of the saturation conductance for in- and out-diffusion, obtained by fitting the results of Fig. 5.18(a), is shown in Fig. 5.19(b). Notice that we do not observe any influence of the annealing time on the films saturation conductance. However, we have found a strong reduction of surface limited oxygen exchange rates with increasing annealing time, while bulk determined conductance is unaffected. This leads us to the assumption that the origin of degeneration of oxygen exchange kinetics is lying within the surface.

Oxygen exchange irreversibility of pristine PLD YBCO investigated by T-step measurements

So far we have only analysed step I) of a T-step measurement. In Fig. 5.20(a) we present the results of the full analysis of a 200 nm pristine PLD film consisting of 5 steps [I-V)]. Oxidation (circles) and reduction (diamonds) saturation times are drawn on a logarithmic scale as a function of $t_{annealing}$. The temperature profile is shown on top, with the labelling of the individual steps.

First we focus on the coloured symbols (blue and red), which correspond to saturation times measured only at 450 °C. As in the case of CSD-YBCO we see a strong increase of relaxation times, τ with the annealing time $t_{annealing}$. The yellow line corresponds to a quadratic fit (in a lin-lin plot) of the in-diffusion saturation times of step I) at 450 °C: $\tau_{in} = a \cdot t^2_{annealing} + b$, with

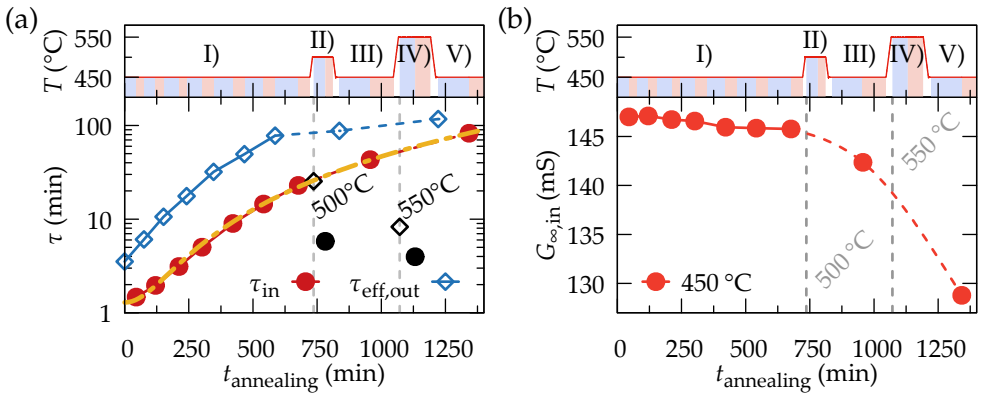

FIGURE 5.20: T-step measurement of 200 nm PLD YBCO film: In- (circles) and out-diffusion (diamonds) saturation times as a function of total annealing time at 450 °C (coloured symbols), and 500, respectively 550 °C (black symbols); yellow line indicates quadratic fit $\tau_{in} \propto t^2_{annealing}$. (b) Oxidation saturation conductance at 450 °C, τ values at intermediate temperature steps are omitted. The corresponding temperature profile is shown on top in (a) and (b).

scaling parameters a and b. The τ values of phase III) and V) follow the extrapolation of the quadratic trend. Thus, it does not seem that the higher temperatures during phase II) and IV), and the heating and cooling stages have additional impact on the deactivation of the oxygen exchange rates. Therefore we conclude that the main parameter causing the deactivation of surface reactions is the annealing time, an ageing effect.

The black symbols are relaxation times at 500 and 550 °C, corresponding to step II) and IV), respectively. Relaxation times $\tau(t_{annealing} < 350\,\text{min})$ at 450 °C are smaller than those obtained at higher temperatures. This implies that thermally enhanced kinetics at higher temperatures can not surmount oxygen exchange deactivation caused by ageing.

The evolution of the in-diffusion equilibrium conductance $G_{\infty,in}$ at 450 °C is shown Figure 5.20(b). Points at higher temperatures are omitted. As previously found in the case of CSD films, the saturation conductivity basically remains unchanged in phase I), with $G_{\infty,in} \approx 146$ mS. A significant decrease in conductance is observed after step II) and IV), where the temperature is raised to 500 °C and 550 °C, respectively.

The decrease of conductivity of YBCO at 450 °C, after annealings at higher T, can be related to two different phenomena: either the depletion of available charges in the conduction band (or rather free electron holes in YBCO), *e.g.* as accompanied by stoichiometric changes due to the increase of the oxygen

vacancy concentration or by the introduction of defects and impurities into the lattice structure. However, both effects are expected to be bulk related and should not be linked to the degradation of the oxygen surface exchange rate.

In this section we have described the occurrence of two different effects taking place during post growth thermal annealings. The first phenomena is related with annealing time. This ageing effect strongly degrades the capability of pristine YBCO films to exchange oxygen with environment. Already at 450 °C a substantial adverse effect was observed. Incorporation and excorporation reaction rates are affected and saturation times approximately increase proportional to $t^2_{\text{annealing}}$. A second mechanism observed seems to modify the electronic bulk properties and is related with changes in electrical conductance after changes in temperature. The observed decrease of the electrical conductance might be related with stoichiometric changes of oxygen and/or the formation of defects within the film.

5.3.2 Influence of oxygen partial pressure

We have shown that oxygen exchange kinetics degrade with annealing time at constant temperature in alternating oxygen atmosphere. In this section we will address the role of oxygen partial pressure on the deactivation of exchange rates to identify if high or low $P(O_2)$ atmosphere is the responsible for the slow down of oxygen kinetics. We will consider a third possibility as well, namely that the actual change of $P(O_2)$ (and corresponding microstructural modifications) is the origin of the detrimental effect.

The influence of low and high oxygen partial pressure is analysed by an experiment as shown in Fig. 5.21(a), referred to as *single cycle* (*sc*) in the following. The CSD YBCO film is heated in 1 bar of oxygen and annealed for 10 hours at 450 °C. The conductance is constant during this stage. Subsequent the atmosphere is changed to a low $P(O_2)$ of 5 mbar for 2 h and back to 1 bar. During the low $P(O_2)$ segment saturation is not reached within two hours. The back transition in oxygen rich atmosphere occurs faster and equilibrates at the same conductance value as the initial state before the cycle.

The saturation times for oxidation and reduction of this *single cycle* (open symbols) are shown in Figure 5.21(b) and compared to relaxation times from multiple $P(O_2)$ changes. The latter were obtained in step I) of a T-step experiment (see *e.g.* Fig. 5.19(a)) and will be referred to as *multi cycle* (*mc*).

At first we compare relaxation times of these two measurements regarding the number of changes of the atmosphere (cycles). Therefore we look at the first cycle of the (*mc*) experiment. For example, we obtain in the initial cycle

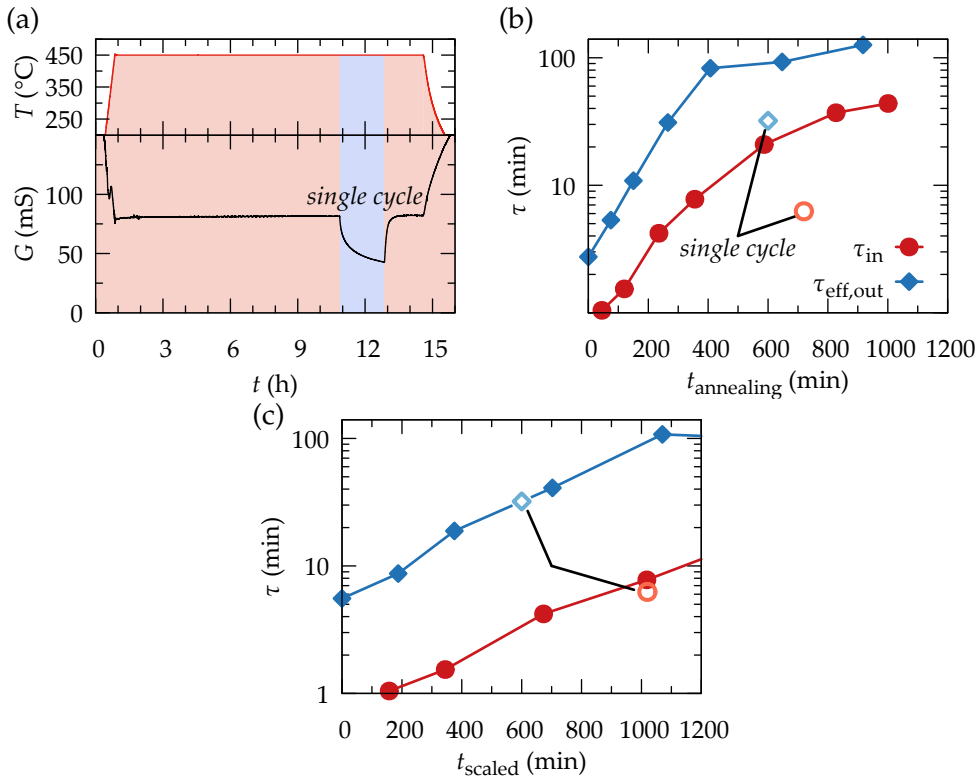

FIGURE 5.21: (a) *Single cycle* ECR measurement of 250 nm CSD film at 450 °C after long initial annealing in high $P(O_2)$. (b) & (c) Comparison of oxidation (red) and reduction (blue) relaxation times of *single cycle* (open) and *multi cycle* (full symbols) measurements as a function of (b) annealing time and (c) rescaled annealing time to account different detrimental impact of low and high $P(O_2)$ atmospheres.

for the case of out-diffusion $\tau_{mc} \approx 3$ min and $\tau_{sc} \approx 30$ min, see Fig. 5.21(b). When the first atmosphere change is performed after an annealing of 10 h (*sc*), the relaxation times are much longer as compared to the initial cycle of the (*mc*) experiment.
Thus, we can conclude that the annealing time (before the first cycle) itself has a strong deactivating effect on oxygen exchange kinetics. Further, microstructural changes within the bulk induced by changes in the $P(O_2)$, as variations in length of lattice parameters, increase/release of stress, *e.g.*, can be excluded to be the main source of the degradation.

If we compare the two experiments with respect to the total annealing time (at $t_{annealing} = 600$ min), the film with multiple cycles in atmosphere exhibits

longer relaxation times than the *single cycle* sample, *e.g.* for the case of out-diffusion we find $\tau_{mc} \approx 90\,\text{min}$ and $\tau_{sc} \approx 30\,\text{min}$. However, in this case τ values are of the same order of magnitude. At this point, both films were annealed for the same time (600 min) and we have seen above that the number of cycles is not the main source for the deactivation of exchange rates. Therefore we will consider in the following that high and low $P(O_2)$ have different detrimental influences on the exchange kinetics, to explain the differences between the saturation times of the (*mc*) and (*sc*) experiments.

We can write the total annealing time $t_{\text{annealing}}$ as the sum of the preceding pressure segments i with length t_i at high and low $P(O_2)$:

$$t_{\text{annealing}} = \sum_i \left(t_{i,P_{\text{high}}} + t_{i,P_{\text{low}}} \right) = t_{P_{\text{high}}} + t_{P_{\text{low}}}, \tag{5.1}$$

with t_P being the cumulative dwell times of the particular atmosphere. To account for a pressure dependent impact on the degradation, a rescaled time is introduced with the weighting parameters a and b:

$$t_{\text{scaled}} = a \cdot t_{P_{\text{high}}} + b \cdot t_{P_{\text{low}}} \tag{5.2}$$

The trivial case of $a = b = 1$ corresponds to graph shown in Fig. 5.21(b). The weights a and b are tuned until in- and out-diffusion time constants fall onto the same line for both measurements:

$$\tau_{\text{single cycle}}(t_{\text{scaled}}) = \tau_{\text{multi cycle}}(t_{\text{scaled}}). \tag{5.3}$$

This is shown in the lower plot of Fig. 5.21(b), with $a = 1$ and $b \approx 3.5$, leading to a reasonable well collapse. $b > a$ might suggest, that low $P(O_2)$ has a more destructive influence on the oxygen exchange kinetics. This simple approach is only thought to point out the possible various influences of different atmospheres and to be a starting point for further research.

The final conductance at 450 °C is not affected by the interim change in oxygen partial pressure as can be seen in Fig. 5.21(a). On the other hand, conductivity and charge carrier density n_H at room temperature and critical current densities at 5 and 77 K are decreased by about 15-20 % after thermal annealing compared to their original values. XRD 2θ measurements were performed before and after the *in situ* measurement. A shift to lower angles, as depicted for the (005) reflection in Figure 5.22(a), is observed for all (00l) peaks, caused by the expansion of the *c*-parameter. Additional to the shift in position a shoulder occurs around 39.2 °, which we were able to correlate to the formation of Y124 intergrowths. The evaluation of the nanostrain is shown in Fig. 5.22(b). A subtle increase of the nanostrain ϵ from 0.14 to 0.18 %

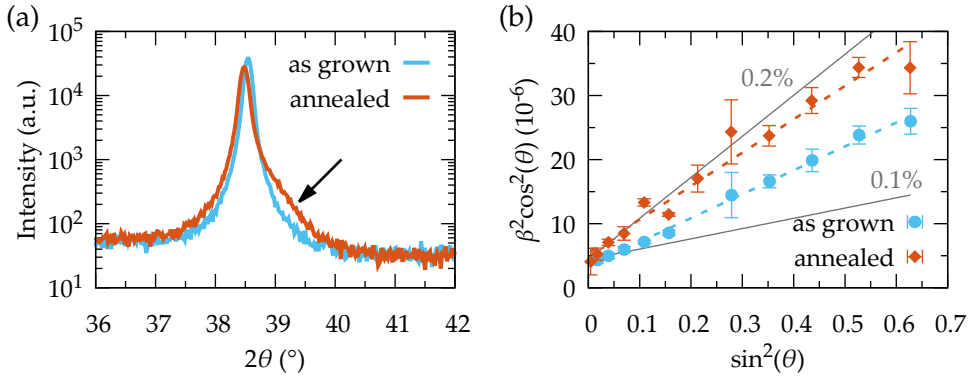

FIGURE 5.22: XRD analysis of 250 nm CSD film before and after single cycle measurement at 450 °C: (a) (005) YBCO reflection and evolving of shoulder at 39.2 °and (d) evaluation of nanostrain.

is found after the thermal treatment. The origin is very likely the strained region associated to the edges of the Y124 intergrowths.
These measurements show that stacking faults can already be generated at intermediate temperatures as 450 °C as a thermally activated process. The films final conductance is invariant to preceding changes in atmosphere and is not sensitive to the amount of structural deformations induced by the Y124 intergrowths generated.

To summarize, annealing in high and low oxygen partial pressure was found to detrimentally influence exchange kinetics. This finding is of relevance as it affects the possibility to properly re-oxygenate pristine YBCO after certain manufacturing steps causing a loss of oxygen, as *e.g.* during the fabrication of superconducting joints. Additionally, we found trace of the formation of stacking faults at low temperatures as 450 °C and long annealing times by means of XRD measurements, while *in situ* conductivity measurements are not sensitive to the formation of this defect at least at those densities.

5.3.3 Surface modifications during annealing

In the previous sections it was shown that oxygen kinetics of pristine films are dramatically reduced with increasing annealing time, while the film conductance G is invariant to the history of changes in atmosphere (at constant T). While the conductance is predominantly governed by the bulk, the exchange kinetics are surface limited. This suggests, that the origin of the deactivation effects on exchange rates lies within the surface.

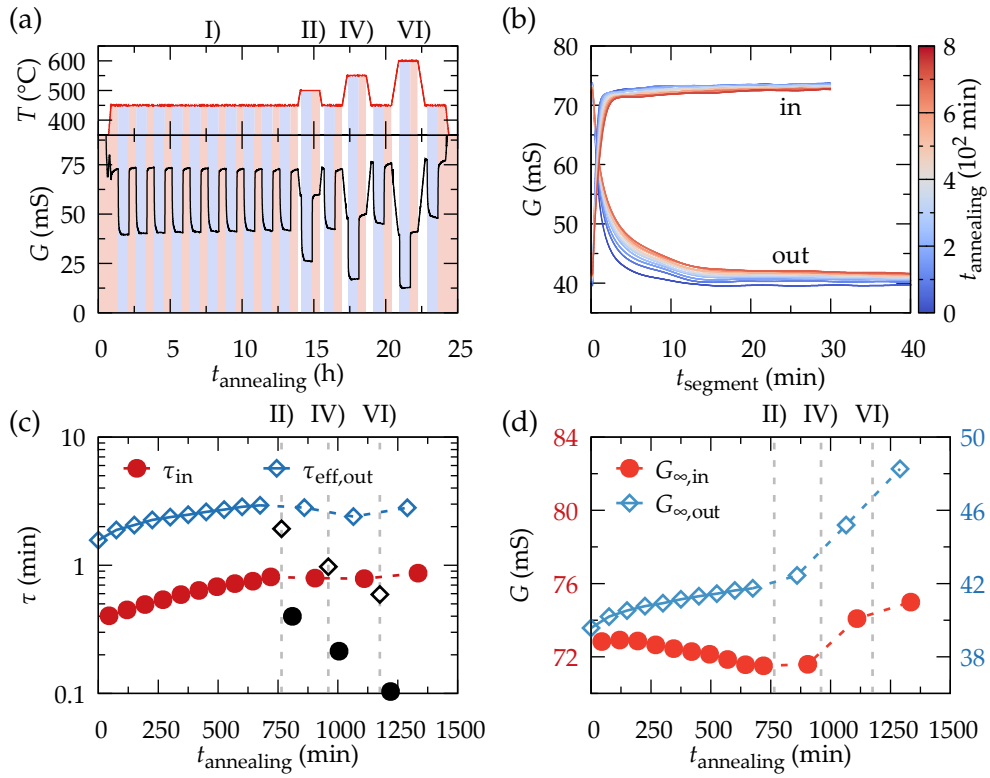

FIGURE 5.23: T-step measurement with Ag coated CSD film (a) $G(t)$ with indication of atmosphere, (b) segments from phase I) put on top of each other, the colour of each lines corresponds to the annealing time. (c) Saturation times over annealing time (in colour for 450 °C and black for higher T during phase II), IV), VI)). (d) Equilibrium conductances at 450 °C.

T-step measurements are repeated using silver coated YBCO, as shown for a 250 nm CSD film in Fig. 5.23(a). Phase I) consists of ten reduction and oxidation cycles. In the phases II), IV) and VI) the sample is heated to 500, 550 and 600 °C, respectively, with dwells at 450 °C in between. Already at first sight it is obvious that the evolution of G with annealing time strongly differs upon silver coating, as compared to T-step measurements of pristine YBCO. Saturation is reached within short time for all cycles, even after more than 20 h of annealing.

The data of phase I) is also presented in Figure 5.23(b), as a function of the elapsed time since the last change in atmosphere. The line colours correspond to the total annealing time.

We find only small variations in the electrical conductivity relaxation measurements over more than 10 h of annealing time. This is in strong contrast with previous measurements on pristine YBCO films (compare with Fig. 5.19(a)).

The relaxation times as a function of the total annealing time are shown in Fig. 5.23(c). The coloured symbols correspond to measurements at 450 °C, the black ones to the intermediate phases II), IV) and VI) at 500, 550 and 600 °C, respectively. One can observe a small increase of τ at 450 °C with time but the deactivation of the exchange mechanism is strongly retarded.

Upon increasing the temperature (black symbols), τ values decrease, as expected for a thermally activated process. Using the time constants of the phases I)-VI) obtained at different T (450 - 600 °C), activation energies can be calculated using an Arrhenius plot (not shown), obtaining 0.73 eV and 0.45 eV for oxidation and reduction, respectively. This numbers are in reasonable agreement with values found for a *T-up* process ($E_{a,in} = 0.6$ and $E_{a,out} = 0.48$ eV).

The saturation values G_∞ at 450 °C are shown in Fig. 5.23(d). Small variations are seen during phase I), but bigger changes occur after heating to higher temperatures. $G_{\infty,out}$ increases by about 20 %. This could be ascribed to a lower amount of oxygen being released from the structure during reduction. On the other hand the increase in conductance could be the result of oxygen ordering at elevated temperatures as reported elsewhere [170, 171]. $G_{\infty,in}$ increases after going to higher temperatures, which is in contrast to pristine films, where a decrease was observed (as shown in Fig. 5.20(b)). However, the measured variation is limited to a few percent of its initial value.

The evolution of saturation times with annealing time is compared in a semilog plot in Fig. 5.24 for a pristine (full symbols) and a silver coated (Ag, open symbols) YBCO film. We observe remarkable differences between the two samples. The initial saturation times are fairly similar, with the Ag sample having a factor two shorter τ values. After annealing for 650 min this factor is boosted to about 35. The relaxation times of the silver sample increase linearly ($\tau_{Ag} \propto t_{annealing}$) over the full time range, while for the pristine film an approximately quadratic increase ($\tau_{pristine} \propto t^2_{annealing}$) is observed for the case of oxidation. The dashed lines represent a linear/quadratic fit for the Ag coated/pristine film for oxidation saturation times, respectively (note the representation in a semi-log graph). Two different time dependencies suggest that different mechanism cause the deactivation of oxygen kinetics.

This remarkable finding demands to question the role of silver. As it was described in the previous chapter (section 4.2), the initial fractional coverage of silver on the surface due to patterning adds up to about 40 %. The formation of Ag islands during heat treatments causes a further shrinkage, resulting in a coverage of about 10 % of the total surface.

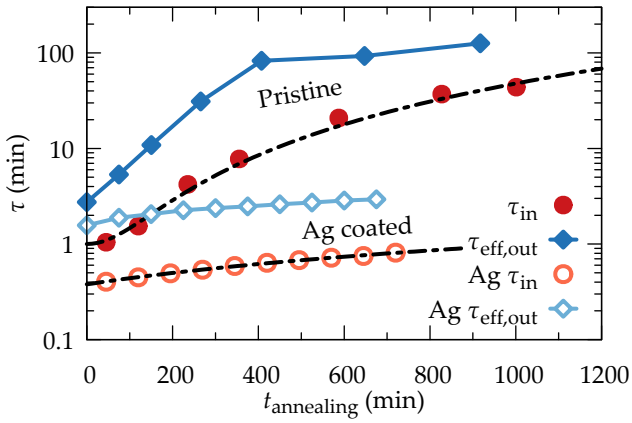

FIGURE 5.24: Saturation times of several $P(O_2)$ cycles at 450 °C for pristine (full) and silver coated (open symbols) 250 nm CSD film.

If silver is thought to serve as a protection layer, the final coverage seems very low for such drastic influence on the evolution of the exchange kinetics. A more plausible explanation incorporates the catalytic activity of silver combined with chemical instability of the surface as discussed in the following section.

5.3.4 Oxygen exchange deactivation model and the role of silver

In solid oxide fuel cells deterioration (ageing) effects on oxygen exchange at elevated temperatures under different atmospheric conditions were recently under investigation, as it remains a main issue for many cathode materials [172–175]. The surface composition has a very important role in the oxygen exchange of surface limited reactions. Surface sensitive techniques as X-ray Photoelectron Spectroscopy (XPS) [176, 177], Secondary Ion Mass Spectroscopy (SIMS) [178, 179] and Low-Energy Ion Scattering (LEIS) [175, 180] are used to characterise the chemical composition of the surface and the first atomic layers underneath. Degeneration might be caused by insufficient phase stability (surface decomposition) and cation segregation. In the presence of alkaline earth metals (as for example barium) a source of contamination and poisoning of the SOFC could be the formation of hydroxides and carbonates at operation temperature in contaminated atmospheres. An enrichment of rare earth cations close to the surface was found *e.g.* for $Nd_2NiO_{4+\delta}$ [172] and $La_2NiO_{4+\delta}$ [181] after annealing under oxygen exposure. The durability of conventional cathodes of SOFCs and its oxygen reduction reaction activity

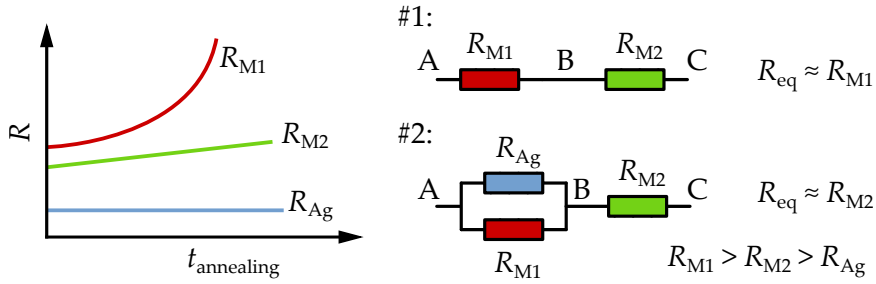

FIGURE 5.25: Schematic electrical analogue of oxygen exchange reactions (A⇌B⇌C) in YBCO consisting of two elementary steps in series: surface degradation causes decrease of exchange rates (increase of resistance) with time. (#1): Oxygen exchange in pristine YBCO is limited by step R_{M1}, exhibiting a fast degradation rate. (#2): Silver coating on the YBCO surface changes the RDS to R_{M2} by providing an alternative reaction path R_{Ag} bypassing R_{M1} in parallel.

were found to be enhanced by the modification of the surface. Using alkaline earth metal free cathode materials as a catalyst improve the overall performance because of their good oxygen exchange capability, high stability and capability of resistance against poisoning with contaminants [173, 182, 183].

To the best of our knowledge there is no literature on a deep study of the restructuring of the YBCO surface due to post-growth annealings under different atmospheric conditions.

In the preceding sections we have observed that Ag affects the deactivation rate of oxygen kinetics. We propose the following model to describe the overall influence of silver on the susceptible oxygen exchange kinetics of YBCO. Without compromise we can simplify our model for oxygen exchange at the surface by combining the involved processes into two elementary mechanism called M1 and M2, involving the different processes discussed in Chapter 2 and analysed in Chapter 4. M1 will comprise oxygen adsorption, ionisation and dissociation (step 1-3 in Tab. 2.1), while M2 defines the incorporation of oxygen into a vacancy (step 4). The latter is the rate determining step (RDS) in silver coated YBCO thin films, as we found in Chapter 4. We use an electrical analogue and ascribe a resistance R_{Mi} to each mechanism, assuming $R_{M1} > R_{M2} > R_{Ag}$. The resistances are connected in series, as the reactions are successive. A graphical visualisation of this model for the case of pristine YBCO is shown in Fig. 5.25(#1). The slowest process (equivalent to the highest

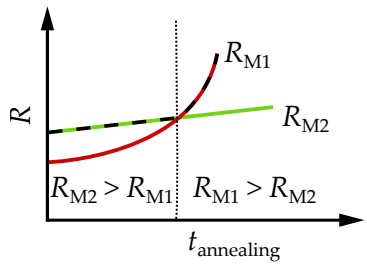

FIGURE 5.26: Schematic electrical analogue of oxygen exchange reactions of hypothetical case that initially $R_{M2} > R_{M1}$. As M1 and M2 have different deactivation rates, a kink is observed in the determining resistance (as indicated by the black dashed line).

resistance) is limiting the overall process[1]. Thus, oxygen exchange in pristine YBCO is limited at all time by R_{M1}, as will be elucidated below.
The case of silver coated YBCO is shown in Fig. 5.25(#2). Silver provides an alternative catalytic reaction path R_{Ag} for mechanism M1[2]. The activation energy for the alternative reaction is lower, therefore $R_{Ag} \ll R_{M1}$. As these two processes run in parallel, the reaction A⇌B is determined by the faster mechanism R_{Ag}. Therefore the overall reaction A⇌B⇌C is limited by R_{M2} for the case of silver coated YBCO.

The intrinsic exchange activities of YBCO degrade with time and the degradation rate differs for each mechanism. We consider a much faster degradation rate for M1 compared to M2, as shown in the schematic $R(t)$ diagram in Fig.5.25. The only partially coverage of the surface with silver does not serve as a protection layer to avoid chemical damage of the YBCO surface, but it provides a fast and highly active alternative reaction path for oxygen exchange. This model correctly explains the observed differences between pristine and silver coated YBCO (as shown in Fig. 5.24), as the greatly reduced deactivation rates in the latter and the different time dependencies of the two types of samples (linear in Ag coated and quadratic in pristine YBCO).

If initially pristine YBCO is limited by M2 as well, we would initially have $R_{M1} < R_{M2}$. Therefore we would expect a kink, when the determining mechanism changes, as shown in Fig. 5.26 due to different deactivation rates. This

[1]This is a general assumption in the field of physical chemistry [34]. However, a simple electrical analogue lacks a clear representation of this characteristic (compare with section 2.2).

[2]As mentioned in section 4.2, we only contemplate adsorption, ionisation and/or dissociation of oxygen to be enhanced by silver, all combined in process M1 in the present consideration.

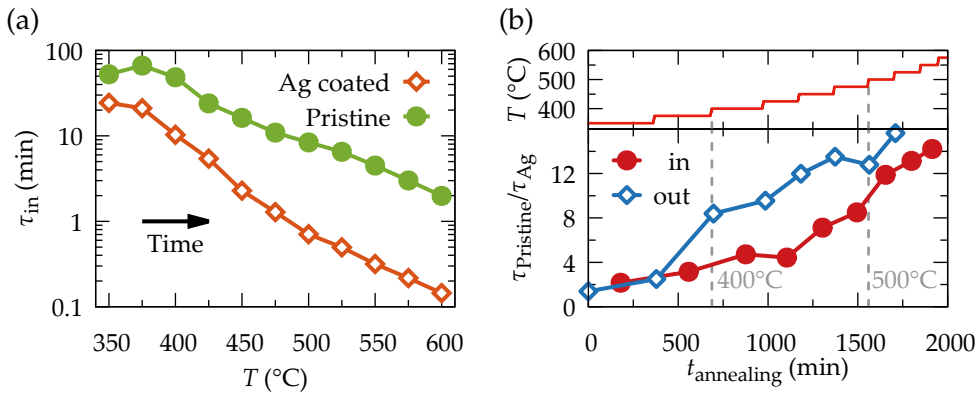

FIGURE 5.27: Analysis of *T-up* measurements: (a) In-diffusion saturation times of pristine and Ag coated YBCO starting at 350 °C. The ratio $\tau_{Pristine}/\tau_{Ag}$ with the data from (a) and additionally for out-diffusion saturation times, is depicted in the lower part of (b) as a function of total annealing time; upper graph shows corresponding temperature, as indicated by dashed bars for 400 and 500 °C.

is not observed in our experimental data (see Fig. 5.24). Additionally, we find saturation times in Ag coated films by about a factor 2 smaller and the onset temperature of oxygen incorporation is reduced upon silver coating, as discussed in Chapter 6.1.3. All these facts indicate a change of the RDS upon Ag coating.

Now, we will apply our considerations to *T-up* measurements on a pristine and silver coated CSD-YBCO film, as shown in Figure 5.27(a). Saturation times of the Ag coated sample decrease with increasing temperature, as described above. A similar trend is observed for the pristine film, with exception of the first two measurement points at 350 and 375 °C. We find faster relaxation at lower temperature: $\tau_{in}(350\,°C) < \tau_{in}(375\,°C)$. This clearly contradicts the expected behaviour of a thermally activated process. Lower τ values at lower temperatures were observed in several *T-up* measurements in pristine films of different thicknesses and grown by either PLD or CSD technique.
This finding can be explained by long annealing times at low temperatures, causing a considerable degradation of the surface exchange rates. At low temperatures this deactivation cannot be compensated by the increase in thermal energy with increasing temperature, resulting in the observed anomaly.

We now concentrate on the ratio of saturation times $\tau_{Pristine}/\tau_{Ag}$ of the two discussed *T-up* measurements. The ratio is plotted as a function of the annealing time in Fig. 5.27(b) for in- and out-diffusion saturation times and the corresponding temperature is shown on top. At first the different rate

determining steps of pristine and silver coated YBCO exhibit rather similar transport coefficients, as can be seen by a small ratio between their saturation times of about a factor 2 (as found in the comparison of T-step measurements in section 5.3.3). After some time, we observe a significant increase of the relaxation time ratio. As in our model considerations above, we address this to specific degradation rates of the two different RDS for pristine and Ag coated YBCO.

The specific degradation mechanism remains unclear and a deep study of the electrical and chemical reconstruction of the YBCO surface is out of the scope of this thesis. Nevertheless, further research can be guided by the intense studies performed in the field of SOFC, where a degradation of surface exchange kinetics has been observed previously [184–186] and the effect of surface termination is experimentally and theoretically studied [187, 188]. Short and long term chemical stability of the surface of cathode materials for SOFC is investigated *e.g.* using electrochemical impedance spectroscopy measurements [186, 189] and X-ray photoelectron spectroscopy (XPS) [176, 185].

In this section we have shown that the deactivation of surface exchange kinetics is directly related to the thermal annealing time. Already at low temperatures as 350 and 450 °C we can observe the degradation of exchange rates, while the conductivity of the bulk remains unaffected.
We suggest that a restructuring of the surface, cation segregation and phase instabilities cause a general change of the composition and chemistry of the surface. These changes adversely affect the elementary reaction steps, involved in the oxygen exchange process. A catalytic layer of silver on the surface provides an alternative reaction path, effectively changing the rate determining step of the reaction. Upon silver coating the degenerative effect of annealing time on saturation times is strongly reduced. We ascribe this to different degradation rates of the different limiting reaction mechanisms in pristine and Ag coated YBCO. Thus, we are assuming that surface degradation is always present, but with Ag we bypass its most severe effects.

5.4 Conclusions

In this chapter we have investigated the influence of oxygen exchange measurements at temperatures between 350 and 600 °C on the microstructure and surface of YBCO thin films. Throughout this chapter we have found similar results for samples obtained by PLD and CSD with thicknesses between 25 and 250 nm.

We have analysed the temperature dependence of oxygen reaction rates by either going down (*T-down*) or going up (*T-up*) in temperature. Following the latter process we obtain strongly reduced saturation times as compared to the first procedure, revealing a strong dependence of the observed kinetics on the thermal history. Additionally we have found a deviation to higher activation energies with increasing annealing time, thus in a *T-down*/*T-up* process at lower/higher temperatures.

Within this chapter we have identified the formation of stacking faults (SF). The generation of this defect in YBCO thin films, which consists of a double CuO-chain, is already enabled during annealings at intermediate temperatures (450 °C) and under an oxygen partial pressures of ≤ 1 bar.
Electrical conductivity relaxation measurements are not sensitive to this process in the present extent, but these defects can be observed as a modification in the XRD pattern of post annealed films. Precisely, we found the occurrence of shoulders in the low angle Y123 reflections, accompanied by a general increase of the FWHM and a shift of the Y123 peak position towards the closest Y124 reflection, while coherent reflections of the $YBa_2Cu_4O_8$ phase were not present in the observed spectra. A STEM study revealed high densities ($10^{12}\,cm^{-1}$) of long intergrowths in post annealed films.
We have shown that the formation/presence of SFs does not cause a deactivation of oxygen exchange kinetics. On the other hand, we have found that time reversed processes result in different SF densities, accompanied by different charge carrier densities and levels of inhomogeneity. *T-down* processes reveal a more detrimental influence on superconducting properties. We ascribe this to the thermally activated nature of the formation process which is promoted in a distorted lattice.

Consistently with results in the previous chapter, we concluded that a surface reaction is limiting the overall oxygen exchange rate in our thin films at all time. Initially, pristine YBCO exhibits a high oxygen activity and fast reaction rates k_{chem} at low temperatures, governed by a low activation energy for oxygen exchange. This characteristic is deactivated during measurements. We were able to correlate the deactivation of the surface oxygen exchange to annealing time. In fact, already at temperatures as low as 350 °C we found a degradation of the surface exchange rates. The capacity of the film to exchange oxygen with environment might be reduced by a surface modification due to phase instability, segregation and depletion or accumulation of cations and the formation of carbonate side products. However, the precise mechanism could not be identified and remains unclear.

Silver coating of the YBCO surface changes the rate limiting step and strongly reduces the detrimental impact of thermal annealing time. We have

developed a model for surface reaction, consisting of serial and parallel processes that might be activated by Ag coating. Within this model, we were able to explain the observed differences between pristine and silver coated YBCO thin films. We conclude that silver provides an alternative reaction path and changes the RDS of oxygen kinetics in YBCO. We have shown that already a fractional coverage of the surface with silver of 5-10 % is enough to activate this route. By assuming different degradation rates of the individual elementary steps we can conclusively explain our experimental observation.

Chapter 6

Overdoping YBCO thin films

In the previous two chapters we have thoroughly studied the mechanisms of oxygen incorporation and effects of oxygenation treatments on the microstructure and surface of YBCO films. In this last chapter we focus on the influence of the oxygenation process to the superconducting properties. Especially we are interested in the impact of different heat treatments and oxygenation procedures on the superconducting critical currents at different temperatures and magnetic fields.

We know that the total pinning force, F_p, can be written as the sum over the elementary pinning force $f_{\mathrm{p},i}$ for all defect sites N_p [190]:

$$F_\mathrm{p} = \sum_{i}^{N_\mathrm{p}} f_{\mathrm{p},i}(B,T) \tag{6.1}$$

As vortex pinning is essential for dissipation-free current transport, many different approaches are followed to increase the total pinning force [128, 191, 192], especially by increasing the pinning site density N_p, *e.g.* via the embedding of nanoparticles [125, 193, 194] or by introducing columnar defects by irradiation [195–197].
Less attention has been drawn to maximise $f_{\mathrm{p},i}$. Magnetic flux does not cause an energy change when their core is situated within a non-superconducting, normal region, where the superconducting order parameter ψ vanishes. On the other hand, if a magnetic vortex is placed into the superconducting region the system loses condensation energy. In the single flux regime the elementary core pinning force is equal to the negative maximum variation of the pinning potential energy U across the pinning centre with a radius r [190]:

$$f_\mathrm{p} = \left(-\frac{\partial U}{\partial x}\right)\Bigg|_{\max} \propto \xi \mu_0 H_\mathrm{c}^2 \begin{cases} |\psi| = 0 \text{ for } r < \xi \\ |\psi| = 1 \text{ for } r > \xi \end{cases} \tag{6.2}$$

with the superconducting coherence length ξ, which is the typical length scale of variations of ψ. The pinning force is proportional to the superconducting condensation energy $E_c = -\mu_0 H_c^2 V/2$, with the pinned volume V of the defect (*e.g.* $V = 4/3\pi\xi^3$ for point defects) and the thermodynamic critical field H_c. Therefore, the pinning force can be increased by maximising the condensation energy, which is linked to the oxygen content via doping [198–200]. In the underdoped regime the condensation energy is strongly suppressed due to the opening of the competing pseudogap [201]. On the other hand, in the strongly overdoped regime the condensation energy decreases due to the decreasing superconducting energy gap [202]. Thus, a peak in condensation energy is linked to the closing of the pseudogap at $p = 0.19$ [203], where J_c is maximised. Therefore we aim to dope YBCO to this critical doping point.

In the first part of this chapter we will present the different routes followed by means of different oxygen heat treatments and give an analysis of their impact on the basic superconducting properties. In the second part we investigate the doping state of thin films and focus on the doping dependence of superconducting and normal state electronic properties of YBCO.

6.1 Oxygenation - the impact of oxygen heat treatments on superconducting properties

The importance of oxygen stoichiometry for the properties of cuprate superconductors has been outlined since the advent of high temperature superconductors (HTS) and the oxygenation is known to be one of the key process steps to obtain high performance superconducting YBCO. Bulk YBCO is typically sintered and oxygenated for very long times up to several days [87].As the thin film production emerged, oxygenation processes where only subsequently modified. In the commercial fabrication of superconducting coated conductors (CC) up to now a complex process with several temperature steps is used to properly oxygenate the superconducting layer.

The growth process for CSD YBCO consists of a high temperature dwell at low $P(O_2)$, where YBCO nucleates and grows. Subsequent the film is directly oxygenated (case (I) in Fig. 6.1(a)) at intermediate temperatures. Therefore the atmosphere is changed to 1 bar of O_2 during cooling at 600 °C and the sample is oxygenated between 550 and 450 °C between 2 and 3.5 h. This thermal profile corresponds to the standard process within our group. However, in this thesis we have modified this process to be able to thoroughly analyse this process already from the initial oxygenation. Therefore the sample is cooled in low oxygen atmosphere to room temperature (case (II) in Fig. 6.1(a)). In this case the sample needs to be oxygenated in a post growth annealing. An

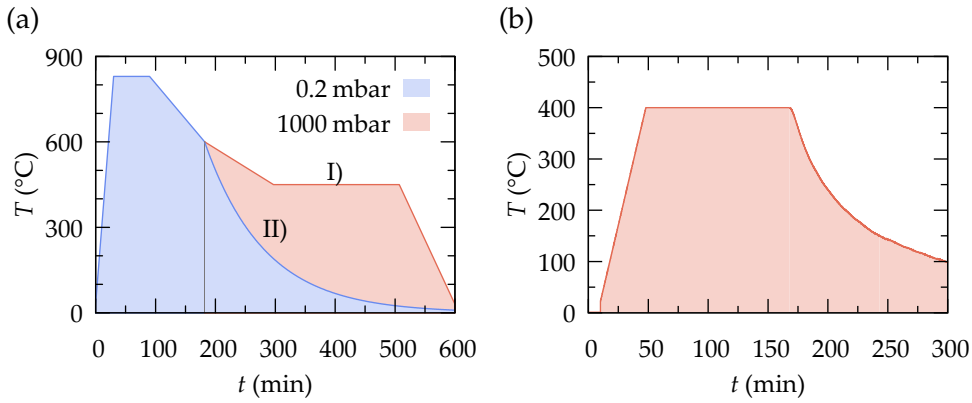

FIGURE 6.1: Temperature profile of (a) a standard YBCO growth process, where either the oxygenation is subsequent to the growth (I), or the film is cooled in low $P(O_2)$ atmosphere (II) and (b) a post growth heat treatment in oxygen rich atmosphere.

exemplary thermal profile is shown in Fig. 6.1(b). This second procedure allows to investigate the initial oxygenation using *in situ* electrical conductivity measurements.
A similar approach is followed for films grown by PLD. After the deposition in a low $P(O_2)$ atmosphere (0.3 mbar), the sample is cooled to room temperature without increasing the $P(O_2)$. Such as grown, non-oxygenated samples are poorly oxygen loaded, but already exhibit metallic behaviour with a low critical temperature < 60 K (*e.g.* see Fig. 6.8(b)), which indicates that the oxygen content is about $O_{6.5}$ with every second O-chain site filled.

We have studied the influence of oxygenation temperature (200 - 600 °C), surface coatings and dwell time (0 - 6 h) on the initial oxygenation and resulting superconducting properties, as will be presented below.

In this section we will study the initial oxygenation of YBCO and focus on the influence of different thermal annealings on the normal state and especially superconducting physical properties of YBCO thin films obtained by chemical solution and pulsed laser deposition. In the following we will restrict the comparison of CSD films to simultaneously grown samples, which were found to present similar properties. Additionally we use YBCO layers fabricated by PLD, where a better control of less process parameters increases the reproducibility of our results.

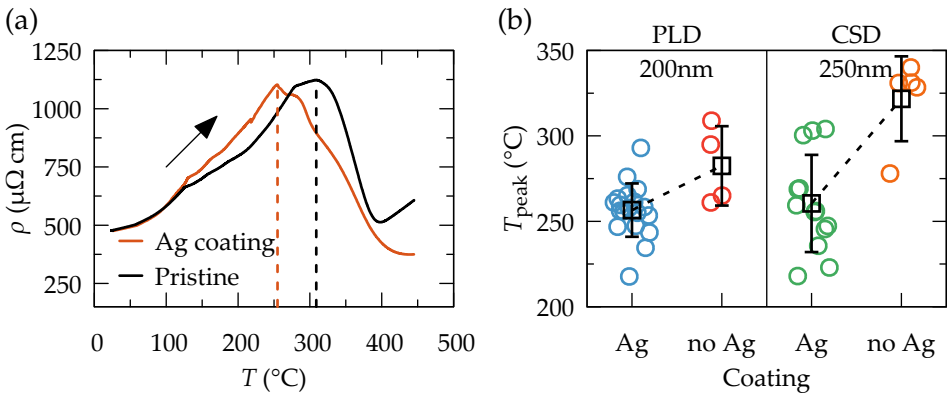

FIGURE 6.2: (a) Heating stage of initial oxygenation of pristine and Ag coated (100 nm) PLD-YBCO films of 200 nm and (b) analysis of peak temperature dependence on coating for PLD and CSD growth techniques.

6.1.1 *In situ* analysis of the initial oxygenation

As in the previous two chapters we use electrical resistivity measurements to obtain information about the ongoing processes during the initial oxygenation of YBCO thin films. Therefore we analyse as grown, non-oxygenated YBCO layers, obtained by CSD and PLD.

For the *in situ* analysis of the oxygenation process we have used the same setup as in the previous chapters (for details see section 3.6). Samples are individually mounted to a sample holder and electrically contacted with silver electrodes to record the time evolution of the resistivity ρ of the film during the oxygen heat treatment.

In Fig. 6.2(a) we compare $\rho(T)$ of the initial heating ramp (10 °C/min) from room temperature to 450 °C for a pristine and a silver coated PLD film, respectively. We observe a peak in resistivity during the heating process of the initial oxygenation. The same characteristic was first described in chapter 4.6.4 (ff.) for already oxygenated thin PLD films. The peak positions are indicated with dashed vertical lines for the two films shown in Fig. 6.2(a). The maximum in ρ of the silver coated specimen is reached at $T_{\mathrm{peak}} \approx 250\,°\mathrm{C}$, while the pristine sample peaks just above 300 °C. In both shown cases, and typically in the investigated samples, the maximum is followed by a minimum in ρ between 400 and 450 °C. The resistivity $\rho(T_{\mathrm{min}})$ is reduced by about 25 % for the silver coated sample compared to the pristine film. As the resistivity decreases with increasing oxygen content, the lower minimum resistivity suggests that up to this point more oxygen was incorporated into the Ag coated sample, in agreement with faster kinetics found in the previous chapters for Ag-YBCO

films. The ratio $\rho(T_{peak})/\rho(50\,°C)$ between the resistivity at the peak temperature and 50 °C is found to be typically between 2 and 3 and is only slightly reduced upon surface coating with silver.

We have analysed the temperature of the peak in ρ in pristine and silver coated YBCO layers grown by either PLD or CSD technique, as shown in Fig. 6.2(b). The black squares correspond to the average values of each sample group. Pristine CSD films have a higher peak temperature compared to pristine PLD specimen, in agreement with faster oxygen kinetics of YBCO obtained by PLD, as reported in Chapter 4. Upon silver coating the peak temperature is lowered for both growth methods to about 260 °C. The decrease is approximately 25 °C for PLD samples and more than 60 °C for the case of films grown by CSD.

As mentioned in Chapter 4, the observation of a peak in resistivity is reported in literature to be related to an increased scattering due to oxygen reordering, thus of purely bulk nature [154, 155]. However, we have found that surface coating has considerable influence on the peak position. Namely the temperature of its maximum can be shifted to lower temperatures upon silver coating. Additionally we found a thickness dependence of the magnitude of the peak in section 4.6.2. Thus, our results strongly suggest a correlation of the peak in resistance with kinetic effects at the surface. Within this picture, the fast decrease of the resistance above the peak temperature is ascribed to the increase of available charges due to the incorporation of oxygen. Therefore T_{peak} can be identified as the onset temperature of oxygen exchange. This implies that oxygen loading would be very much reduced at temperatures below the peak, or even hindered due to a different activation energy regime. The lowering of T_{peak} by silver coating indicates that Ag is a good catalytic agent activating the incorporation of oxygen at lower temperatures.

So far we have analysed the occurrence of the peak during a constant heating rate of 10 °C/min. As the situation during the heating stage is far from equilibrium and the peak in resistivity is related to oxygen kinetics, one would expect a dependence of the peak temperature on the heating rate. Therefore, we have analysed the dependence of the occurrence of the peak on the heating rate r, as shown in Fig. 6.3(a) for silver coated PLD films during the initial oxygenation.

Upon reducing the heating rate the resistivity peaks at lower temperatures. T_{peak} can be reduced from 270 °C to 220 °C by decreasing the heating ramp from 20 °C/min to about 1 °C/min. This can be understood in terms of a thermally activated process. We can represent the data in an Arrhenius-like plot in Fig. 6.3(b). Using the averaged peak temperature for each heating rate r, we can model the peak dependence on the heating rate by $r = r_0 \exp[-E_a/k_B T_{peak}]$, resulting in the straight line in the semi-log plot. The

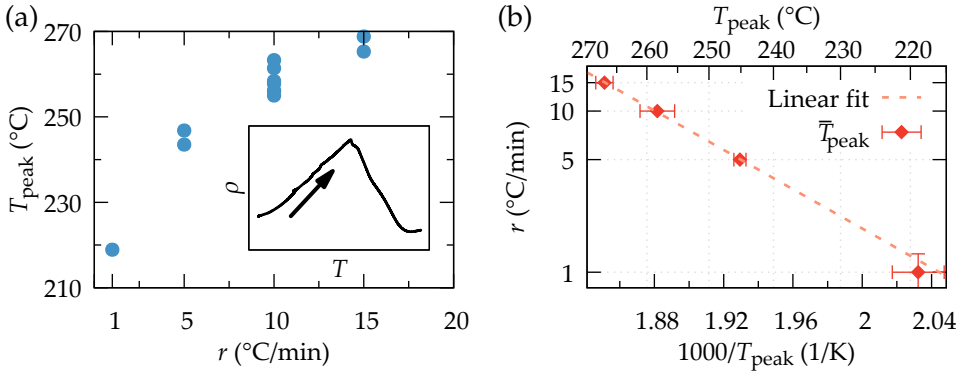

FIGURE 6.3: (a) Heating rate dependence of temperature, where resistivity peaks; inset shows an example for $\rho(T)$ during heating. (b) Arrhenius-like plot showing thermally activation, linear slope corresponds to the activation energy of the process.

obtained activation energy E_a for this process is 1.2 eV, which is similar to the activation energies obtained for oxygen incorporation for this type of films in Chapter 4. The further decrease of r might lower the observation temperature of the peak. However, an Arrhenius law is always valid only within a limited temperature range. We will come back to the relevance of the peak for the oxygenation at low temperatures (200-300 °C) in section 6.1.4.

6.1.2 Oxygenation at intermediate temperatures

Up to now we have investigated the heating stage of the oxygenation process up to 450 °C. In the following we study the further evolution of the *in situ* resistivity in the temperature range of 450 °C to 550 °C, which is the typical one for the oxygenation of YBCO thin films.

In situ resistivity data is shown in Fig. 6.4(a) for two silver coated YBCO samples oxygenated at 550 °C (Ag1) and 450 °C (Ag2)[1], respectively, as well as a pristine film annealed at 550 °C.
The silver coated films exhibit a very similar temperature dependence until 450 °C with the typically observed peak around 260 °C and a minimum above 400 °C. A similar behaviour is found in the pristine, non-Ag coated film but with a shift of the peak to higher temperatures, as observed in the previous section.

[1]The resistivity of sample Ag2 was rescaled by a factor of 0.66 for better clarity of the presented results, which does not compromise the further analysis.

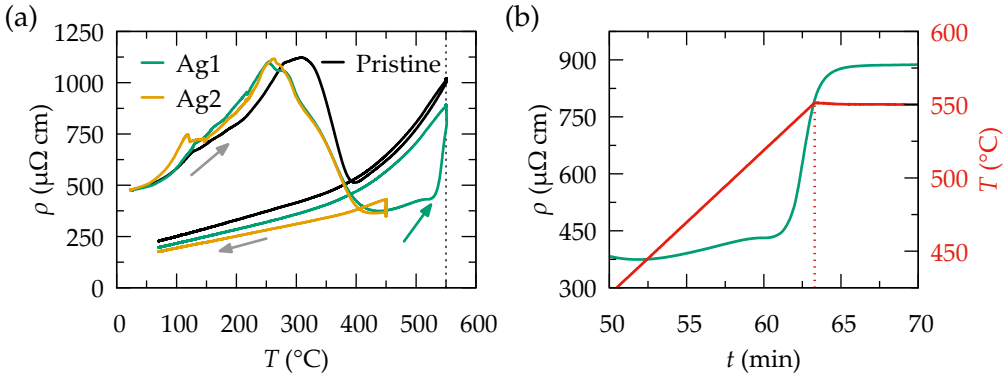

FIGURE 6.4: (a) Initial oxygenation of 200 nm PLD-YBCO films at 550 °C (pristine and Ag coated film Ag1) and at 450 °C (Ag2[1]); a strong upturn in ρ is observed for Ag1 (green arrow). (b) Resistivity over time of sample Ag1 close to the beginning of the dwell at 550 °C showing in detail the upturn in ρ.

During the dwell at 450 °C, sample Ag2 shows a small increase in resistivity. Upon cooling a linear behaviour is found below 350 °C, as expected for properly doped YBCO.

An interesting characteristic is found looking at sample Ag1: the peak in ρ is followed by a minimum around 430 °C and a subsequent approximately linear increase with T up to 530 °C, where a sharp upturn can be observed (green arrow). This strong increase in resistivity mainly occurs before the dwell temperature of 550 °C is reached as can be seen in the resistivity over time plot in Fig. 6.4(b). This upturn was found in all silver coated PLD-YBCO samples heated above 530 °C and is therefore of special interest to us.

In the case of the pristine sample no such behaviour was found, but the resistivity immediately increased significantly after surpassing a minimum at about 400 °C (Fig. 6.4(a)). Upon cooling, all three compared samples exhibit a very similar temperature dependence, which results in a linear proportionality $\rho \propto T$ below 350 °C. The same characteristics were found for pristine/silver coated CSD-YBCO films, including a constant increase/sharp upturn in ρ during heating between 400 and 550 °C and metallic behaviour during cooling.

The phenomena of the upturn occurs upon surface coating, so it might be associated to a kinetic effect of oxygen exchange. On the other hand, the increase in resistivity is not reversible, *e.g.* during a subsequent low temperature dwell ρ remains high. Possible origins of the upturn are though to be related with the overall oxygen content, oxygen ordering effects or a modification of the microstructure. As any of these effects might have significant influence

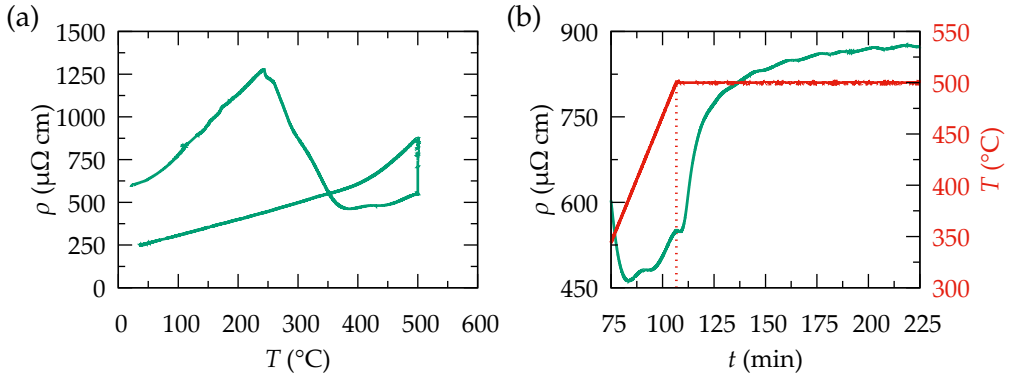

FIGURE 6.5: Initial oxygenation of 200 nm PLD-YBCO sample (Ag coated) (a) ρ over T and (b) detailed view of upturn of resistivity during constant temperature dwell.

on the final superconducting properties of the YBCO film we have devoted further research on the occurrence of this upturn.

With a heating ramp of 10 °C/min, the upturn occurs very precisely at 530 °C, observed in several different samples. Therefore we have performed oxygenations at this rate and reduced temperatures as 520 °C and 500 °C, respectively. The *in situ* resistivity of an oxygenation at 500 °C is shown in Fig. 6.5(a). Again, an upturn can be observed, but in this case the strong increase is retarded and develops during a dwell at constant temperature and $P(O_2)$, as shown in Fig. 6.5(b). The observed resistivity relaxation can be modelled assuming two parallel exponential processes (see Eq. (4.1)) with an effective time constant of about 12 min. An increase of ρ at constant $P(O_2)$ and T would correspond to a loss of charge carriers and therefore a loss of oxygen. In chapter 4.2 we have found for these conditions much faster kinetics (by a factor 4) and thus, it is unlikely to be linked to oxygen exchange.

At this point, however, any increase in resistivity is undesirable, as it is either originated by a loss of oxygen or the formation of defects within the structure. Both effects are thought to be of detrimental character to superconducting critical current densities. The microstructure of the samples Ag1 and Ag2, oxygenated at 550 and 450 °C, respectively is analysed by high resolution x-ray diffraction to trace any possible cause of the upturn in ρ.
The peak positions only vary within the second significant figure after the decimal point for all YBCO $(00l)$-reflections, as exemplary shown in Fig. 6.6(a) for the YBCO (005) reflection. The formation of stacking faults was previously found to cause the development of a shoulder to the right side of the (005) peak. The shown peaks are very symmetrical and of similar shape for both

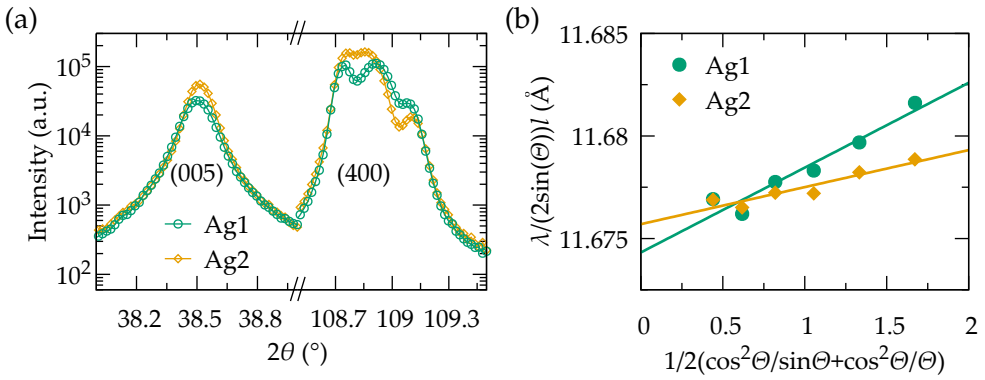

FIGURE 6.6: (a) XRD pattern of 200 nm PLD films oxygenated at 550 °C (Ag1) and 450 °C (Ag2), respectively: (005) YBCO peak and (400) $LaAlO_3$ reflection and (b) evaluation of c-parameter using Nelson-Riley extrapolation to $x = 0$.

samples. Thus there is no hint of an increased stacking fault density in the investigated sample showing an upturn in resistivity.

The (400) $LaAlO_3$ substrate peak shows an increased ab-twin domain structure for Ag2, annealed at 550°C. In $LaAlO_3$ a phase transition from a rhombohedral to a cubic perovskite structure occurs at $T_c = 540$ °C [204, 205]. Our data is not conclusively about a correlation between the splitting of the (400) peak and the sudden increase in resistivity, as twinning is observed as well in some cases after annealing at only 450 °C, and missing although an upturn in ρ was observed in samples annealed at 550 °C.

The evaluation of the c-parameter for Ag1 and Ag2 is shown in Fig.6.6(c) using the Nelson-Riley extrapolation to $x = 0$ for reflections of higher order ($l \geq 7$). We obtain the very close values of 11.674 Å and 11.676 Å, for Ag1 and Ag2, respectively. The nanostrain value ϵ is calculated to be 0.22 and 0.18 % for Ag1 and Ag2, respectively, not revealing a clear origin of the upturn in resistivity.
In contrast, the charge carrier density n_H is higher by about 20 % for Ag2 ($10.7 \times 10^{21}/\mathrm{cm}^3$) than for Ag1 ($8.8 \times 10^{21}/\mathrm{cm}^3$). As we will see in section 6.2, we find that the charge carrier densities are typically higher for films oxygenated at lower temperatures, as it is understood due to a lower configurational entropy for the ordering of oxygen vacancies at lower temperatures and thus higher equilibrium oxygen concentrations (see also section 2.1.2).

We have performed a thorough analysis to trace any microstructural differences caused by oxygen annealings above 500 °C. Even though we have observed a systematic upturn in resistivity of silver coated YBCO films above

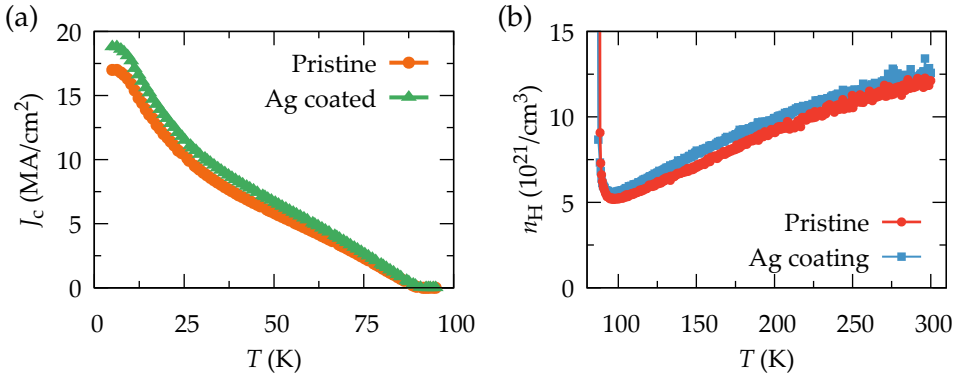

FIGURE 6.7: (a) $J_c(T)$ for 250 nm TFA-CSD samples: pristine surface and Ag coated (continuous layer of 100 nm Ag on top of YBCO surface). (b) Temperature dependence of charge carrier density of 200 nm thick pristine and Ag coated PLD films (Ag sample with standard patterning).

500 °C, we could not find any microstructural origin linked to this feature, as presented above by the analysis using XRD. Additionally performed electrical transport measurements (not shown) did not yield a clear origin. However, Hall measurements revealed a difference in the doping state, where samples annealed at higher temperatures exhibit lower charge carriers and *vice versa*.

6.1.3 Influence of surface coating on normal state and superconducting properties

In the previous section we have shown the strong influence of Ag surface coating on the onset temperature of oxygen incorporation. This result is in agreement with faster oxygen exchange kinetics of Ag coated YBCO as found in Chapter 4. Here we analyse the influence of a silver coating layer on the surface on the final superconducting properties.

Normal state and superconducting physical properties are measured by electrical and magnetic measurements on post oxygenated thin films. We start with the comparison of the self-field critical current density of a pristine and a silver coated CSD sample in Fig. 6.7(a). The latter film was fully covered with a continuous Ag layer of 100 nm thickness. Both films were grown simultaneously and oxygenated at 550 °C in 1 bar of oxygen.
The specimen exhibit the same temperature dependence and the deviation in absolute values is not significant. The rather low absolute values of J_c are not related with the oxygenation process but were a general issue of the batch of CSD samples used for this analysis. However, the same result was obtained

for PLD samples, where critical current densities were found to be independent of surface coating too. The superconducting transition is about 90.5 K for both films and the c-parameter was determined to be the same up to the fifth significant figure ($c = 11.693$ Å).
The charge carrier density as a function of temperature is shown for a silver coated and a pristine PLD film in Fig. 6.7(b). Again, we observe a qualitative very similar behaviour, while the quantitative difference is not significant. The same result is found for the resistivity $\rho(T)$ (not shown).

These results allow us to conclude that a thin catalytic surface layer of silver has influence on the oxygen exchange kinetics, while thermodynamics and thus bulk properties are not affected. This is in agreement with results in Chapter 4.2.2. As long as equilibrium is reached, electrical and superconducting properties after annealing are the same for pristine and silver coated films. This can be guaranteed by sufficiently high temperatures and sufficiently long annealing times. We reach the same conclusions analysing the post oxygenation physical properties of YBCO layers grown by PLD and CSD technique.

6.1.4 Minimum oxygenation temperature

The increase of point defects, as oxygen vacancies in the crystal structure with increasing temperature is caused by a higher configuration entropy. Up to a certain defect concentration the entropic energy exceeds the formation enthalpy of the vacancy, leading to a temperature dependent thermodynamic equilibrium defect concentration, as discussed in section 2.1.2. Thus decreasing the oxygenation temperature leads to a lower oxygen vacancy concentration, as shown in the phase diagram of the YBCO oxygen non-stoichiometry in Fig. 2.4. Low temperature oxygenations are therefore a promising method to overdope YBCO. The injection of holes by oxygen doping causes a higher charge carrier density in the copper oxygen planes, increasing the condensation energy and therefore, we would expect a possible increase of the critical current densities. We have shown in Chapter 5 that oxygen exchange kinetics of pristine, non-degraded YBCO films is fast, also at low temperatures. Thus, oxygen loading at low T should not be precluded by kinetics.

In the previous section 6.1.1, we have found an onset temperature for oxygen incorporation, indicated by a peak in resistivity. However, as it is a thermally activated process, the occurrence of the peak depends on the heating rate and could be lowered by reducing the heating rate, following an Arrhenius-type activation law. The extrapolation to a rate of 0.5 °C/min gives a peak temperature of 200 °C. Instead, we have performed a dwell corresponding to an infinite slow heating rate. Therefore, we have performed an

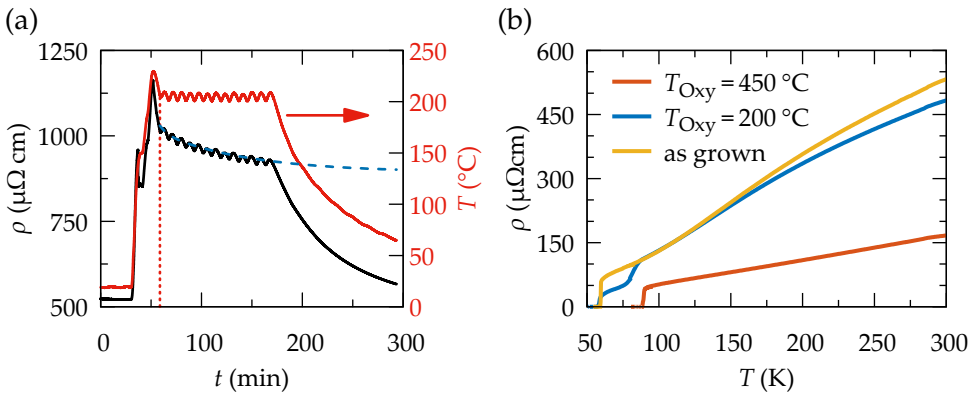

FIGURE 6.8: (a) Low temperature *in situ* oxygenation at 200 °C of 200 nm Ag coated PLD-YBCO film (dashed line indicates fit through relaxation process with $t > 60$ min) and (b) comparison of low temperature dependence of ρ of 200 nm PLD samples after growth and standard/low temperature oxygenation.

initial oxygenation of a 200 nm thick PLD-YBCO sample coated with Ag at 200 °C for 2 h. The corresponding *in situ* resistivity is shown in Fig. 6.8(a). The spike in ρ at $t = 50$ min is caused by an overshoot in temperature of the furnace, but this increased resistivity is not correlated to a peak in ρ as discussed above.

The actual begin of the dwell at 200 °C is marked by a vertical red line. The samples resistivity at $T = 200$ °C decreases from about 1000 $\mu\Omega$ cm to 900 $\mu\Omega$ cm. This is an insignificant decrease in comparison to the drop in ρ observed for the oxygenation processes at higher temperatures. We can model the relaxation process using Eq. (4.1) as indicated with a dashed line in Fig. 6.8(a) and find a saturation resistivity of ρ_∞ =890 $\mu\Omega$ cm. This suggests that a dwell longer than 2 h would have led neither to any further significant decrease of the films resistivity. We can compare ρ_∞ at 200 °C with resistivity values at 200 °C obtained during cooling from oxygen treatments at higher T (*e.g.* via Fig. 6.4(a)), where ρ(200 °C)$\approx$ 250 $\mu\Omega$ cm and thus almost by a factor 4 smaller. In addition we can compare the initial resistivity with the post annealed value at room temperature for different oxygenation treatments, as a strong decrease in ρ indicates an increased oxygen content. In the case of the 200 °C oxygenation ρ is reduced by less than 10 %, while for standard oxygenations we observe drops of 70 - 80 %.

These results indicate that at 200 °C a different activation energy regime governs the oxygen incorporation, with much higher activation energies and almost no oxygen exchange takes place. Hence, a proper incorporation of oxygen at 200 °C is not possible.

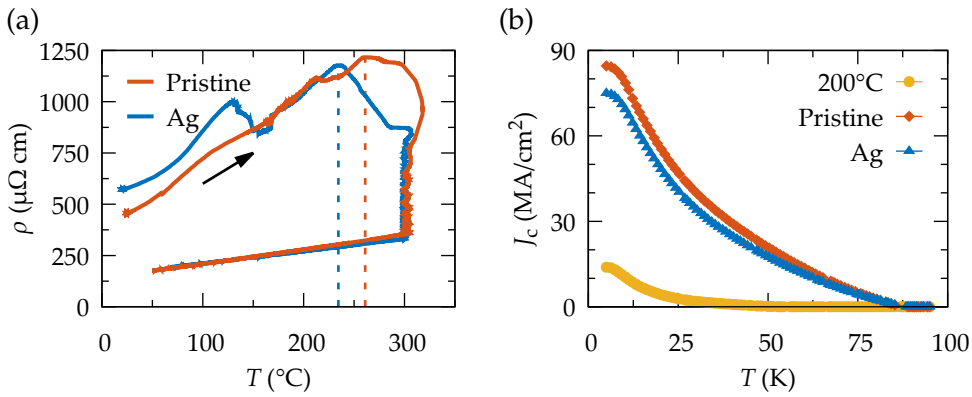

FIGURE 6.9: (a) *In situ* oxygenation at 300 °C of pristine and Ag coated 200 nm PLD films (arrow indicates the direction of time) and (b) corresponding post annealing self-field $J_c(T)$ compared to silver coated film oxygenated at 200 °C.

This is confirmed in Fig. 6.8(b), where the low temperature dependence of ρ is shown for an as-grown film (without oxygenation), a standard oxygenated YBCO layer ($T_{oxy} = 450$ °C for 2 h) and a specimen annealed at 200 °C (2 h). The latter only slightly deviates at room temperature from the non-oxygenated as-grown film, which is in the range of variations among different samples. Still, the sample has a slightly increased oxygen concentration since around 80 K some parts of the sample already become superconducting, while the full transition occurs only at 57 K. This is in agreement with the small reduction of the *in situ* resistivity during the oxygenation dwell as discussed above (see Fig. 6.8(a)).
The as-grown film exhibits a very similar critical temperature with $T_c = 58$ K. The standard oxygenated film, on the other hand, shows a linear T dependence and a sharp transition around 88 K. Therefore we conclude that a temperature of 200 °C is too low to enable proper oxygen incorporation into the full YBCO structure and we suggest that the oxygenation process has to be performed above the peak in resistivity to reach a high doping state.

Next, we have oxygenated PLD-YBCO thin films for 2 h at 300 °C, which is still considered to be a very low temperature for oxygenation. Examples are shown for a silver coated film (Ag) and a pristine sample in Fig. 6.9(a) (note that it was shown in Fig. 6.2(b) that for PLD films the peak occurs below 300 °C, independent of coating). A peak in ρ during the initial heating is observed for both samples with a magnitude of about 1200 $\mu\Omega$ cm. For the Ag sample the peak is shifted to a lower temperature (25 °C) and it is followed by a sharp decrease in resistivity. The pristine sample shows a less distinct, broader peak, but ρ rapidly drops during the dwell at 300 °C. The spike for the

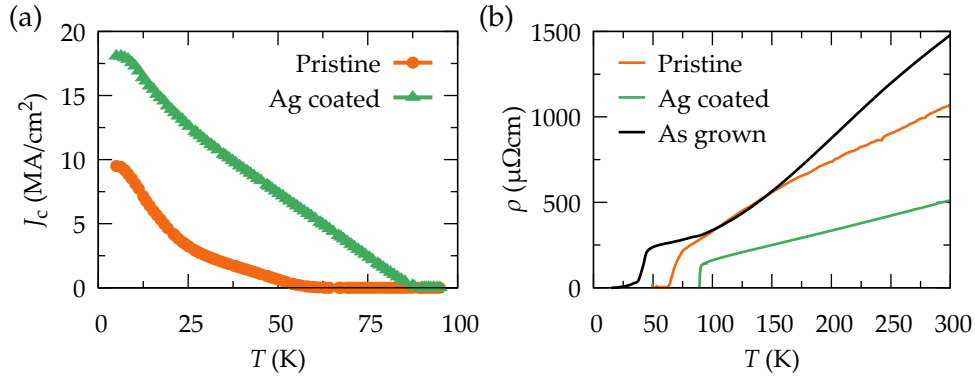

FIGURE 6.10: Pristine and silver coated CSD films oxygenated at 300 °C: (a) Temperature dependence of J_c and (b) film resistivity at low temperature, compared to as grown CSD film (without oxygenation).

Ag sample at around 130 °C is thought to be an artefact of the contacts. After a dwell of 2 h both samples end up with a much lower resistivity of about 340 $\mu\Omega$ cm, suggesting a very high oxygen content of the film. This is confirmed by measurements of the charge carrier densities at room temperature for both films ($n_H \approx 15 \times 10^{-21}/\text{cm}^3$).

The self-field critical currents of the two samples oxygenated at 300 °C are shown in Fig. 6.9(b). Additionally the $Jc(T)$ of a silver coated sample oxygenated at 200 °C is drawn. The oxygenation of PLD films at 300 °C results in excellent superconducting properties independent of Ag coating. These films are highly overdoped. On the other hand an oxygenation temperature of 200 °C is not sufficient to dope enough oxygen into the structure.

We have performed a similar analysis using YBCO films grown by chemical solution deposition. We compare pristine and silver coated 250 nm thick YBCO films, which were oxygenated for 5 hours at 300 °C. While pristine PLD films exhibit a peak in resistivity below 300 °C, the onset temperature of oxygen incorporation of pristine CSD films is around 320 °, while for Ag covered CSD and PLD films we found $T_{onset} \approx 260$ °C (compare with Fig. 6.2(b); heating rate 10 °C/min). The analysis of low temperature physical properties is shown in Fig. 6.10. We observe a clear difference in the self-field critical current densities of the pristine and the Ag coated sample. The J_c of the former is lower by a factor of 2 at low temperatures and rapidly decreases further with increasing T. The pristine sample becomes superconducting below 63 K, while the superconducting transition of the Ag sample occurs at 88.6 K, proofing a significantly higher oxygen content in the latter specimen. This is in agreement with Hall measurements determining the charge carrier densities

to be 6.2×10^{21} and 1.8×10^{21} cm^{-3}, for the Ag coated and pristine layer, respectively. As commented above, a comparison of J_c and n_H values between films grown by CSD and PLD is difficult due to the vast number of different parameters influencing the different deposition and growth processes. This topic will be further studied in section 6.2.

The resistivity of the films obtained by CSD is shown in Fig. 6.10(b). The Ag coated film exhibits the lowest ρ at all T, a very metallic behaviour ($\rho \propto T$) and a sharp transition at T_c. The resistivity of the pristine specimen oxygenated at 300 °C is higher by more than a factor of 2 at room temperature, it shows a deviation from linearity at lower temperatures (< 150 °C) and a broad superconducting transition. For comparison we present an as-grown sample too. This film was cooled after growth in low oxygen atmosphere ($P(O_2)_{growth} = 0.2$ mbar, $n_H = 1.1 \times 10^{21}$ cm^{-3}, $T_c < 40$ K). The as-grown layer has a higher resistivity and a lower charge carrier density and T_c. This indicates that some oxygen was incorporated into the YBCO matrix of the non-Ag coated film during the 5 h annealing at 300 °C. However, the oxygen kinetics of pristine CSD YBCO films is not sufficient to achieve an optimally doped state for YBCO at such low T.

In this section we have analysed low temperature oxygenations. We have shown that a proper oxygen loading into YBCO is limited by the onset temperature of oxygen incorporation, which is linked to a peak in the *in situ* resistivity. Oxygenations performed at temperatures below this peak only lead to a partial doping of the structure, while $T_{oxy} > T_{peak}$ results in a high and homogeneous oxygen content, with high J_c and n_H values. We showed that the catalytic activity of silver reduces the minimal temperature necessary to efficiently dope oxygen into the structure, by shifting the peak in resistivity to lower temperatures. However, the effect of silver coating is limited to oxygen exchange kinetics, as Ag and non-Ag coated thin films show similar superconducting properties, as long as the oxygenation is performed above the peak temperature.

6.1.5 Ozone assisted oxygenation

Ozone is a powerful oxidising agent, which is used in many industrial branches related to oxidation. In the growth of YBCO by molecular beam epitaxy (MBE) ozone is commonly used as it is more reactive than molecular oxygen O_2 and therefore oxidation efficiency is increased at lower oxygen pressure [67, 206]. As ozone enhances the partial pressure of atomic oxygen on the surface compared to O_2, the oxygen stoichiometry of the material could increase, as found

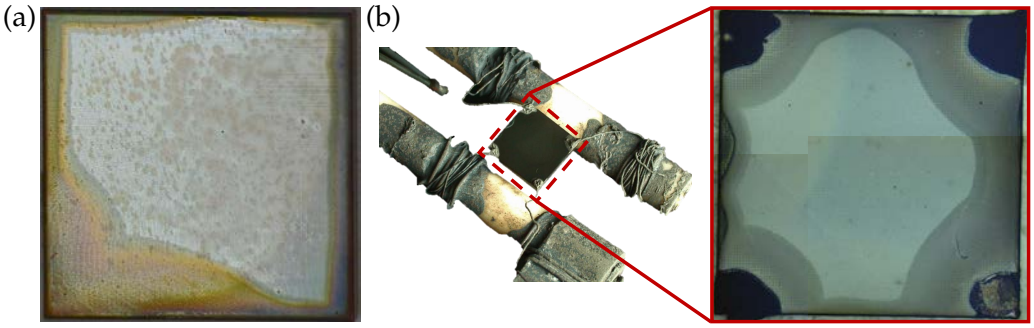

FIGURE 6.11: Optical microscopy images of PLD-YBCO films after annealing at 450 °C with (a) 6.5 % of ozone and (b) 1.8 %. Strong oxidation of silver electrodes and contact pads on the sample and the sample holder due to the ozone is observed.

for cobalt doped YBCO [207] and silver copper oxides annealing in ozone enriched atmospheres [208]. On the other hand, detrimental influences of ozone on YBCO and its Ag coating were reported for oxygenations at low temperatures in an oxygen/ozone mixture with less than 0.5 % O_3 [209].

We have used a commercial ozone generator from *Oxitres* yielding an O_2/O_3 mix with 0.8 - 6.5 % of O_3 and a total flow of 0.48 l/min. Optical microscopy images of the surfaces of post annealed PLD-YBCO films in different ozone atmospheres are shown in Fig. 6.11. Severe degradation of the surface can be observed for the highest ozone concentration of 6.5 % in Figure (a). Figure 6.11(b) shows the sample holder for electrical *in situ* measurements after exposure to 1.8 % of ozone at 450 °C with a sample mounted using silver electrodes. The Ag on the surface is largely oxidised, exhibiting the typical black appearance of silver oxide. The magnification of the sample shows different surface regions. This might be caused by shadowing effects of the silver contacts in the corners and turbulent gas flow above the sample. Thus a proper tuning of ozone conditions is needed, which was beyond the scope of this thesis.

Our interest here is to demonstrate the *in situ* resistivity of an ozone oxygenation, as presented in Fig.6.12(a) for a 200 nm thick PLD sample coated with silver. The film is heated with 10 °C/min to 450 °C with a continuous oxygen flow of 0.48 l/min with an ozone concentration of 1.8 %. For comparison a standard oxygenation of a 200 nm PLD-YBCO (Ag) in 100 % of O_2 is shown as well in Fig. 6.12(a). For the ozone enhanced oxygenation we observe a peak in $\rho(T)$ at a remarkable low temperature of 200 °C, followed by a strong decrease. This implies that ozone lowers the onset temperature of oxygen exchange activity of the material by about 50 °C (compare *e.g.* with Fig. 6.2(b)).

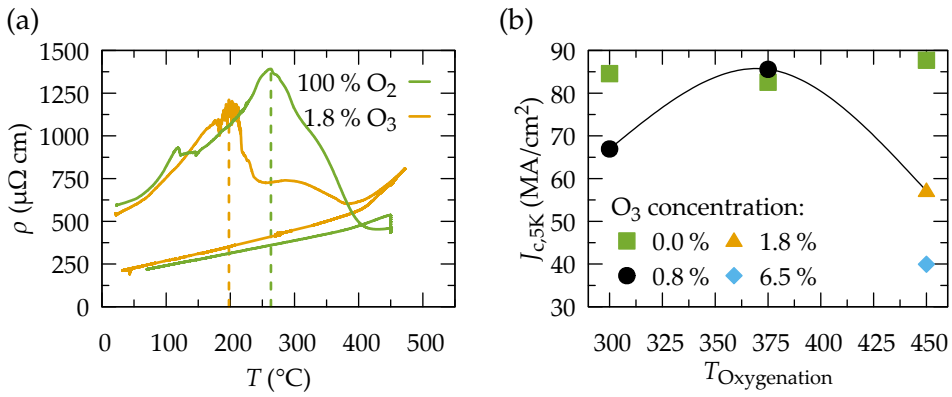

FIGURE 6.12: (a) *In situ* oxygenation of silver coated 200 nm PLD films, annealed in 1.8 % of O_3 and pure O_2. (b) Self-field J_c at 5 K *vs.* oxygenation temperature for different concentrations of ozone during the annealing.

A second peak can be seen at about 300 °C. We address this to the heating conditions far from equilibrium with ongoing incorporation of oxygen and increasing scattering due to the temperature increase. During the dwell of 2 h at 450 °C no change in ρ is observed. Upon cooling ρ decreases linearly with decreasing temperature below 400 °C, with a slope of 0.9 $\mu\Omega$ cm/K. The low slope and low resistivity at room temperature indicate a properly oxygenated sample, while the surface shows some signs of degradation as previously presented in Fig. 6.11(b), suggesting that further lowering the ozone concentration might be beneficial.

The self-field critical current at 5 K for samples oxygenated at different temperatures are compared in Fig.6.12(b). The ozone concentration of 0.8 % is the minimum, non-zero, ozone concentration possible in this setup. Upon reducing $P(O_3)$ from 6.5 % to 1.8 % at $T_{oxy} = 450$ °C J_c increases by about 40 %. J_c was further increased by lowering the $P(O_3)$ to 0.8 %. The lowered onset temperature of oxygen activity by ozone motivates to decrease the oxygenation temperature to increase the oxygen content within the structure and therefore the critical current densities. As shown in Fig. 6.12(b) the maximum J_c is obtained at 375 °C. Further lowering of T did not yield the expected increase in J_c at this stage, though further systematic work should be done. For comparison we added the best obtained J_c values for pure O_2 oxygenations at these temperatures (see section 6.1.3 and 6.1.4).

Critical current densities obtained by ozone assisted oxygenations are close to values achieved by standard methods. In the optimal case found (375 °C and lowest O_3 partial pressure) current densities are similar to the best films obtained within this thesis. In Fig. 6.13(a) the self-field $J_c(T)$-dependence is

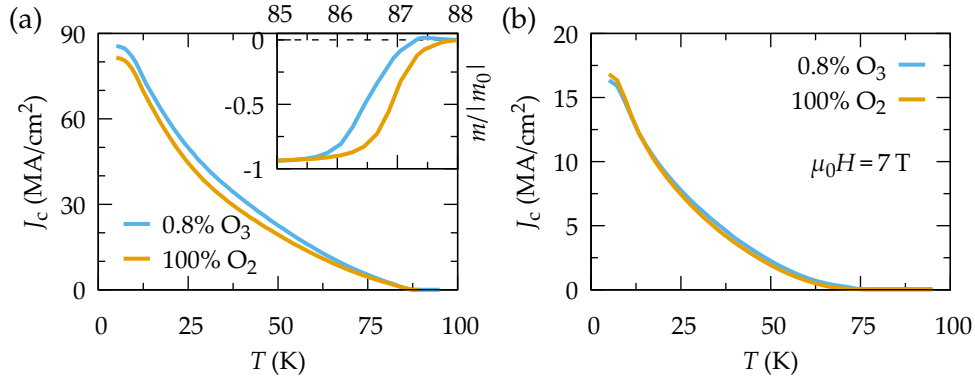

FIGURE 6.13: Temperature dependences of (a) self-field critical current densities and (b) $J_c(\mu_0 H = 7\,\mathrm{T})$ of 200 nm PLD YBCO films annealed at 375 °C in ozone enhanced and pure O_2 atmosphere. The inset in (a) shows a T_c measurement.

shown for two Ag coated films, both oxygenated at 375 °C. The two samples exhibit excellent superconducting properties. The inset shows the superconducting transitions obtained by magnetic measurements in a SQUID. The T_c of the ozone annealed sample is slightly reduced, which indicates an increase of the doping level. On the other hand, the critical current densities in an external field of 7 T reveal no difference, where a higher condensation energy due to increased oxygen content would be expected to cause a more significant increase in J_c.

We conclude that oxygenation using ozone might be an opportunity to enhance the superconducting properties of YBCO thin films due to the decreased onset temperature of oxygen incorporation, as O_3 is more reactive in comparison to O_2. We have been able to establish oxygenation conditions using ozone that do not deteriorate YBCO and allow high oxygen doping into the structure. Using an ozone concentration of 0.8 % we have achieved thin films with excellent superconducting properties, such as a J_c of almost 90 MA/cm^2 at 5 K. However, further studies should be done to tune and optimise the potential of O_3 assisted oxygenations, especially at lower temperatures.

6.2 The doping state of YBCO thin films

$YBa_2Cu_3O_{7-\delta}$ is a complex material with a non-stoichiometric triple perovskite structure. Its superlattice consists of two CuO_2-planes and one $CuO_{1-\delta}$ chain separated by spacer layers of either yttrium, or barium oxide [22] (see Fig. 2.3).

In general the temperature versus doping phase diagram of cuprate high-temperature superconductors is of intricate nature [10, 13]. It exhibits many different phases and peculiarities, as anti-ferromagnetic ordering at low doping, charge density wave order [210], a pseudogap above the superconducting transition [12], *etc.*, as shown in Fig. 2.2.

Due to the multilayer structure of YBCO and charge transfer and ordering effects, concepts as doping, charge carrier density and oxygen content cannot be used synonymously and need to be precisely defined as in the following:

- **Hole doping, p:**
  In most high-temperature superconductors the superconducting state arises upon positive or negative charge doping into the Mott-frustrated insulating material, precisely in cuprate materials into the CuO_2-planes. The doping p refers to the amount of charges (holes) per Cu in the CuO_2-planes. The doping level and therefore the Cu-valence state of the CuO_2-planes are of crucial importance to unconventional superconductivity as the critical temperature uniquely correlates with doping [211, 212]. The doping state $p = 0.16$, where T_c reaches is maximum is called optimal doping. The underdoped and overdoped region are at lower and higher doping values, respectively.

- **Oxygen content:**
  The oxygen stoichiometry of the unit cell changes with the oxygen content in the CuO chains. O_6 correlates to empty chains, and O_7 to fully filled chains. In the intermediate range oxygen ordering phenomena occur, as stripes with filled and empty chain sites (ortho-I, ortho-II phase and intermediate short range ordering) [213]. Because of this ordering effects the hole doping level p does not obey a unique dependence on the oxygen stoichiometry [106]. Upon oxygen incorporation into the unit cell, two electron holes are formed. By charge transfer between the CuO-chain and the CuO_2-plane only a small fraction of all holes are doped into the superconducting planes.

- **Charge carrier density, n_H:**
  The charge carrier density corresponds to the total amount of charges per unit volume and therefore to the charges available in the CuO-chains and CuO_2-planes. It is reported that upon crossing into the pseudogap phase, a transition from $\bar{n}_H \approx 1 + p$ to $\bar{n}_H \approx p$ occurs, where $\bar{n}_H$ is the charge carrier density per unit cell [214]. This is explained by a Fermi surface reconstruction, due to a metal-to-metal transition at $T = 0\,K$ (quantum critical point) [215, 216]. The charge carrier density can be modified by oxygen incorporation or cation substitution, as *e.g.* Ca^{2+} for

Y^{3+}. In any case, in general, a higher charge carrier density is correlated with a higher doping state of the CuO_2-planes.

The doping state of $YBa_2Cu_3O_{7-\delta}$ can be assessed via measurements of the ratio of Cu^{3+}/Cu^{2+} ions by the idiometric titration method [217, 218], angle-resolved photoemission spectroscopy (ARPES) [219] or by X-ray absorption measurements [79]. The oxygen stoichiometry of YBCO bulk can be determined by thermogravimetric (TGA) and evolved gas analysis (EGA) [220]. As these methods are destructive, very costly, highly complex and/or only available for bulk material other approaches were followed in literature to gain information about the oxygen content/charge carrier density of YBCO, *e.g.* by X-ray diffraction measurements [106, 221], via the determination of the critical temperature T_c, electrical measurements as resistivity and Hall effect measurements [222–224] and thermoelectric power (Seebeck coefficient) measurements [225, 226].

6.2.1 Assessing the doping state of YBCO thin films

In the following sections we will briefly introduce several techniques used in this thesis to obtain information about the electronic state of YBCO. As we do not have a direct measure of the doping state of the CuO_2-planes we will utilize all these parameters to evaluate it and try to establish a correlation with the critical current density in section 6.2.4.

Electrical resistivity measurements at low and high temperatures

We have performed resistivity measurements in the temperature range between room temperature (RT) and T_c and between RT and the oxygenation temperature. A typical example for the former is shown in Fig. 6.14(a). For HTS materials one usually finds a linear dependence of ρ on T in a broad temperature range:

$$\rho(T) = bT + \rho_0, \tag{6.3}$$

where the slope b and ρ_0 are reported to be doping dependent [227]. b and the resistivity at 0 K, ρ_0, are obtained by fitting the resistivity curve between 150 and 300 K.
The normalised resistivity $(\rho(T) - \rho_0)/(bT)$ is shown in Fig. 6.14(b) for a underdoped, optimally doped and overdoped YBCO film. This plot reveals the temperature dependent deviation of ρ from linearity. The normalised resistivity of the underdoped sample deviates downwards from unity around 200 K. The decrease of the normalised resistivity $(\rho(T) - \rho_0)/bT$ is linked to the opening of a pseudogap, whereupon a fraction of the total carriers migrates

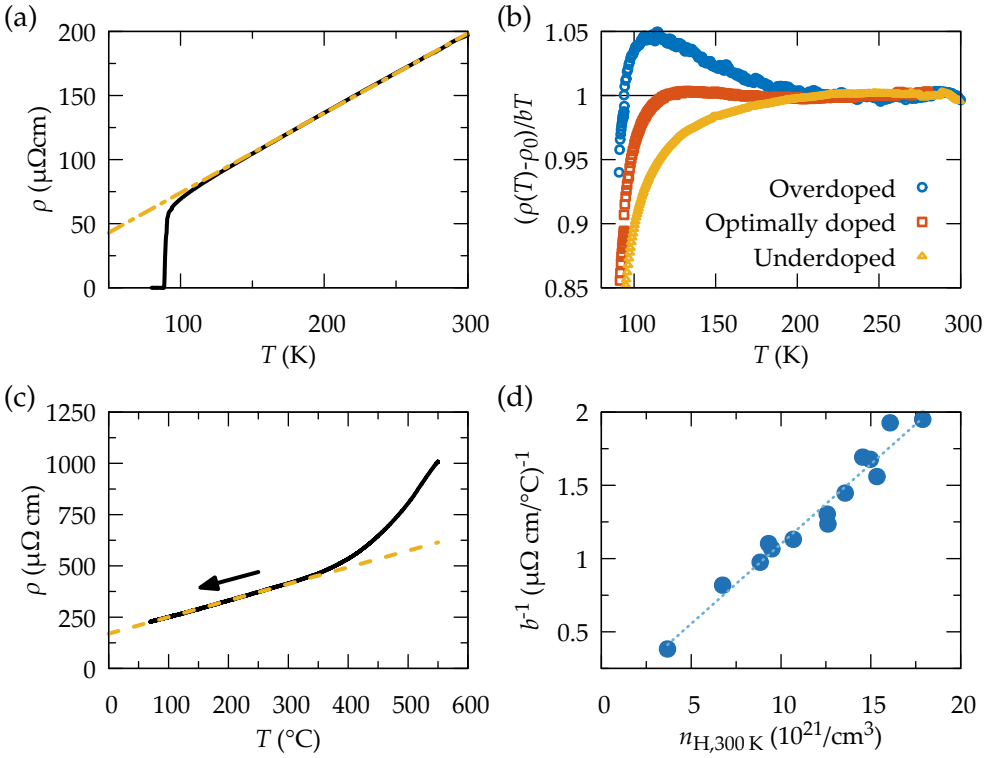

FIGURE 6.14: (a) Low T resistivity ρ of an oxygenated 200 nm PLD-YBCO film; linear fit $\rho(T) = bT + \rho_0$ for $T > 150$ K indicated by dashed line and (b) normalised resistivity to analyse doping state: downwards curvature indicates underdoping, deviation upwards overdoping. (c) High T *in situ* resistivity during cooling after oxygenation and (d) correlation between RT charge carrier density and slope of ρ extracted between 100 and 350 °C (fit indicated with dashed line in (c)).

into pseudogap states and does not any longer participate in the normal electrical transport [199]. On the other hand, the deviation upwards indicates that the film is in the overdoped state [227].

In *in situ* measurements we have found a linear slope, b, of the resistivity during cooling below 350 °C, as shown in Fig. 6.14(c). The slope, b, found at high temperatures seamlessly expands into the low temperature regime and Eq. (6.3) holds between 150 K and about 625 K (-125 °C to +350 °C). In Fig. 6.14(d) we present the inverse slope b^{-1}, obtained from *in situ* measurements, *vs.* the charge carrier density at RT, $n_{\mathrm{H,300\,K}}$, obtained by Hall effect measurements. We find a linear correlation between b^{-1} and $n_{\mathrm{H,300\,K}}$, which

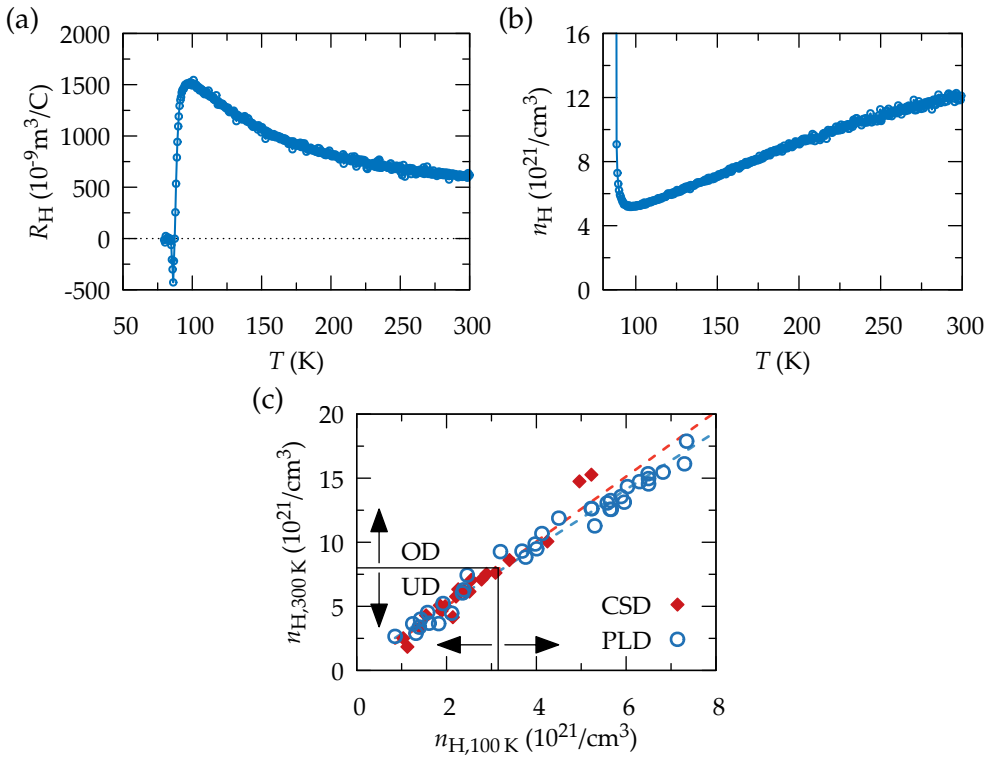

FIGURE 6.15: (a) Temperature dependence of the Hall coefficient R_H and (b) the apparent charge carrier density n_H of a 200 nm PLD-YBCO thin film. (c) Charge carrier density at 300 K *vs.* 100 K for YBCO thin films obtained by PLD and CSD, defining the under- (UD) and overdoped (OD) regime.

approximately follows:

$$b^{-1} = 0.109 n_{H,300\,K} + 0.01, \tag{6.4}$$

as obtained by fitting. This empirical relation enables us to estimate the charge carrier density already by *in situ* measurements during the oxygenation.

Temperature dependent Hall effect measurements

The Hall coefficient R_H of YBCO exhibits a strong temperature dependence, as shown in Fig. 6.15(a). This behaviour is experimentally well established in cuprate materials [228–230], however, it is anomalous compared to conventional metals. Within the Anderson theory [231] an explanation for this observation is given based on the process of spin-charge separation of electrons in

a Luttinger liquid. Other theoretical approaches describing the temperature dependence of the Hall coefficient R_H, are based on a marginal Fermi liquid phenomenology [227, 232] or comprise anisotropic scattering at different regions of the Fermi surface [233], variations of mobility in a single band model [234] and two carrier bands for electron and hole charge carriers [235, 236].
At temperatures $\leq$ 100 K the Hall coefficient R_H exhibits a sudden, strong drop. This particular feature was observed previously in optimally and slightly underdoped YBCO [237, 238] and was recently related to a reconstruction of the Fermi surface of the material [214, 215]. Below T_c we observe a transition through zero. This sign reversal of the Hall coefficient was reported to be doping dependent and due to the movement of magnetic vortices in the mixed state of the superconductor [239, 240], influenced by flux-flow pinning and superconducting fluctuations [241].

From measurements of the Hall coefficient one can obtain the apparent[2] charge carrier density from the **Drude relation** $n_H(T) = 1/eR_H(T)$, as shown in 6.15(b). We typically find a power law dependence $n_H(T) = aT^\beta + n_H(0)$ [243] for $T > 100$ K. At temperatures in proximity to room temperature we find a deviation from the exponent $\beta = 1$ to lower values. Typically in literature the charge carrier density at 300 K (RT) is used for comparison among different samples/parameters. As a and β slightly vary for each sample, the chosen temperature can be of significant relevance for the interpretation of the data in specific cases, as we will see in section 6.2.2.
However, in general we observe an approximately constant ratio of the n_H at 300 K and 100 K. This is shown in Fig. 6.15(c) for a broad selection of PLD and CSD YBCO films, equilibrated at different oxygen concentrations[3]. We observe a linear dependence, as indicated by dashed lines. The average ratio $n_{H,300\,K}/n_{H,100\,K}$ accounts to about 2.3 and 2.5 for PLD and CSD, respectively. Optimal doping in YBCO corresponds to $n_{H,300\,K} \approx 8 \times 10^{21}$charges/cm^3 [227]. Thus we can obtain from Fig. 6.15(c) that optimal doping in terms of n_H at 100 K is reached at about 3.2×10^{21}/cm^3, as we will confirm by T_c measurements in section 6.2.3.

As mentioned above, we find $R_H = 1/(n_H e) \propto 1/T$ and $\sigma = 1/\rho \propto 1/T$, and thus we can write for the mobility $\mu = R_H\sigma \propto 1/T^2$, which is unexpected within the framework of the Fermi liquid theory for conventional metals. As we will see in section 6.2.2, the observed temperature dependence of μ is similar as in the case of semiconductors (*e.g.* $\mu_p \propto T^{-2.3}$ for germanium [244]

[2]High resolution ARPES measurements revealed a temperature dependent Fermi surface, indicating that the change of R_H with T is actually caused by a depletion of available charges [242]

[3]Equilibration of the oxygen content and oxygen ordering is necessary to obtain a constant n_H ratio, as will be shown in section 6.2.2.

and $\propto T^{-2.2}$ for silicon [245]), where both, electrons and holes simultaneously contribute to the total conduction:

$$\sigma = \sigma_{\mathrm{p}} + \sigma_{\mathrm{n}} = \frac{1}{\rho} = \frac{1}{\rho_{\mathrm{p}}} + \frac{1}{\rho_{\mathrm{n}}}. \tag{6.5}$$

Such a model, assuming the simultaneous presence of two independent types of charge carriers, *e.g.* electrons and holes, is called **two-band model**. As we will see in the following it can account for the observed temperature dependence of the apparent charge carrier density $n_{\mathrm{H}}(T)$. The Hall effect for ambipolar conduction can be written as [246]:

$$R_{\mathrm{H}} = \frac{1}{e} \frac{n_{\mathrm{p}}\mu_{\mathrm{p}}^2 - n_{\mathrm{n}}\mu_{\mathrm{n}}^2}{\left(n_{\mathrm{p}}\mu_{\mathrm{p}} - n_{\mathrm{n}}\mu_{\mathrm{n}}\right)^2}, \tag{6.6}$$

with the charge carrier densities n_i for holes (p) and electrons (n). Using Eq. (6.5), the relation $\mu_i = 1/(\rho n_i e)$ and assuming that the charge carrier densities are temperature independent and equal for electrons and holes $n_{\mathrm{H,2band}} = n_{\mathrm{p}} = n_{\mathrm{n}}$, Equation (6.6) can be transformed into the equivalent forms:

$$R_{\mathrm{H}} = \frac{\mu_{\mathrm{p}} - \mu_{\mathrm{n}}}{\sigma} \tag{6.7a}$$

$$R_{\mathrm{H}} = \frac{1}{n_{\mathrm{H,2band}} e} \left(1 - 2\rho\rho_{\mathrm{n}}^{-1}\right) \tag{6.7b}$$

as a function of mobility or resistivity, respectively. If we assume that in YBCO also two types of charge carriers (two bands) participate to the conduction, experimental results of resistivity and Hall measurements can be satisfied by imposing a certain temperature dependence for μ_i or ρ_n, as *e.g.* the Taylor expansion $\mu_i = c_0/T(1 \pm c_1/T)$ (+/- for holes/electrons) [235] or $\rho_n = \rho_0 + bT + cT^2$ for the resistivity [247, 248].

We have followed the second approach, as outlined in [236], which consists of a residual resistance ρ_0 and a linear term in T, as observed in resistivity measurements. The quadratic term significantly increases the fit accuracy. Such a T^2 dependence of ρ was found for several high T_{c} materials at low temperatures [224, 249] and for the Cu-O chains in $YBa_2Cu_3O_{6.9}$ [250] and $YBa_2Cu_4O_8$ [251] up to 300 K. Nevertheless, the exact temperature dependence of the electronic contribution ρ_{n} is unknown within a two band model. This in combination with the better fit accuracy makes the approach followed reasonable.

An example is shown in Fig. 6.16(a), where the temperature dependence of R_{H} is sufficiently modelled by a single, temperature independent charge

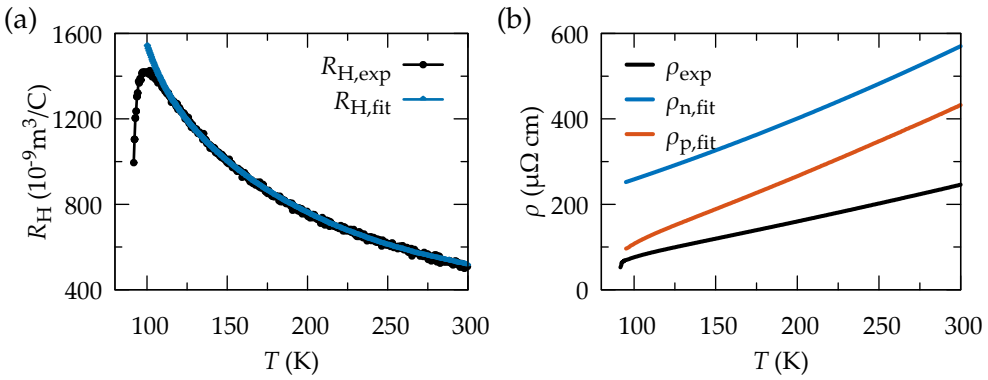

FIGURE 6.16: Contemplation of experimental results for simultaneous electron and hole conduction for 200 nm PLD-YBCO: (a) Temperature dependence of Hall coefficient $R_{H,exp}$ compared to the ambipolar $R_{H,fit}$ obtained by fitting Eq. (6.7b) between 110 and 300 K. (b) Measured total resistivity $\rho_{exp}(T)$ and separated electron ρ_n and hole ρ_p contributions via fitting in (a), with the imposed temperature dependence $\rho_n = \rho_0 + bT + cT^2$.

carrier density $n_{H,2band}$. We will see in section 6.2.4 that this is a very useful parameter for the comparison with the critical current density. The resistivity contributions of holes and electrons are shown in Fig. 6.16(b), where the experimental resistivity is consistently described by Eq. (6.5).

The correlation between the $n_{H,2band}$ parameter obtained by fitting and measured charge carrier densities at 300 K and 100 K are shown in Fig. 6.17(a & b). The statistical correlation coefficient r^2 between $n_H(T)$ and $n_{H,2band}$ is 0.55 at 300 K and 0.85 at 100 K. Thus a higher correlation is obtained for the temperature independent fit parameter $n_{H,2band}$ and $n_{H,100\,K}$. To establish a criteria for the optimally doped state in terms of $n_{H,2band}$, we perform a linear fit, as shown in Fig. 6.17(b). With $n_{H,100\,K} = 3.2 \times 10^{-21}/\text{cm}^3$ for optimal doping, we obtain the corresponding value $n_{H,2band} \approx 1.4 \times 10^{-21}/\text{cm}^3$.

The two-band model provides an explanation of the temperature dependence of the apparent charge carrier density by the coexistence of electrons and holes, both participating in the conduction process in the normal state above T_c. Below T_c, pairing is dominated by hole carriers localised in the CuO_2-planes, while it is suggested [236] that electrons may contribute to 3 dimensional mobility signatures observed for examples in *c*-axis Hall coefficient and *c*-axis transport.

The model can sufficiently describe experimental results of resistivity and

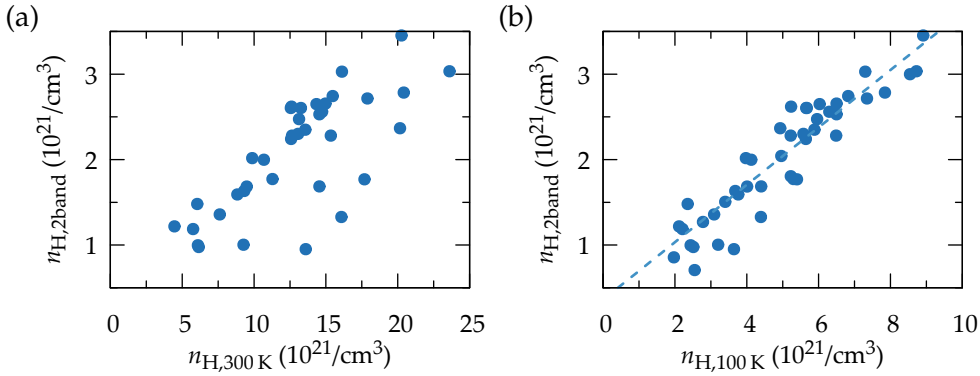

FIGURE 6.17: Correlation between $n_{H,2band}$ and apparent charge carrier density at (a) 300 K and (b) 100 K of 200 nm thick PLD YBCO film.

Hall measurements and additionally provides a single, temperature independent parameter, $n_{H,2band}$, containing information about the full temperature range of the charge carrier density. Further, as we will see in section 6.2.4, $n_{H,2band}$ scales very well with self-field and in-field critical current densities at low temperatures, making it a promising quantity for the analysis of the actual doping state of YBCO. However, some controversy remains as APRES measurements reveal a temperature dependent Fermi surface [242], indicating that n_H actually varies with temperature. This is in contradiction to expectations for *normal* metals and is a good indicator of the rich and complex physics of the normal state of cuprate superconductors.

Oxygen stoichiometry dependence of *c*-parameter

The unit cell of YBCO is highly sensitive to the oxygen content $(7-\delta)$. The c-parameter can be written as the sum of bond lengths, $c = 2d_{Cu(1)\text{-}O(4)} + 2d_{O(4)\text{-}Cu(2)} + d_{Cu(2)\text{-}Cu(2)}$, between the CuO-chain, the apical oxygen O(4) and the two CuO_2-planes (see YBCO unit cell structure in Fig. 2.3 for the nomenclature), and variations in c are mainly caused by changes in length of the $d_{O(4)\text{-}Cu(2)}$ bonding [22, 106]. The unit cell expands with decreasing oxygen content due to a lower overlap of the Cu(2) and O(4) orbitals.
In Fig. 6.18 we show the experimental correlation between the c-parameter and the charge carrier density at 300 K over a broad range of doping for films grown by CSD (red) and PLD (blue symbols). c varies from 11.85 Å down to 11.67 Å for poorly and highly oxygen loaded YBCO, respectively. Dashed lines indicate optimal doping in terms of n_H and c, respectively ($c_{opt} = 11.695$ Å

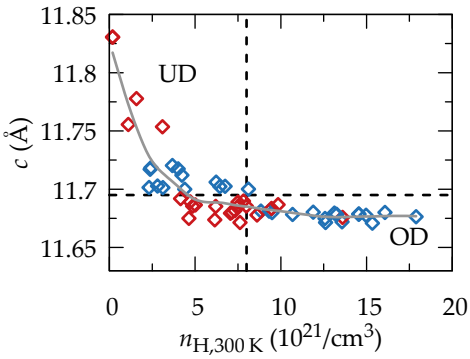

FIGURE 6.18: YBCO c-parameter as a function of the charge carrier density showing the broad range of possible c and $n_{H,300\,K}$ values, dashed lines indicate optimal doping confining the underdoped (UD) and overdoped (OD) regime. Blue and red symbols correspond to samples obtained by PLD and CSD technique, respectively.

[106]). In the overdoped region, c exhibits a much weaker dependence on the charge carrier density as compared to the underdoped regime.

6.2.2 Influence of dwell time on doping state of YBCO

The main parameters of the oxygenation process of YBCO are oxygen partial pressure, temperature and dwell time. In this section we will focus on the dwell (annealing) time, t, necessary to achieve the highest SC performance of our material, which can further contribute to the optimisation of the manufacturing process and its costs.

The analysis of the impact of different dwell times on the doping state was performed at 450 °C. However, in the following we briefly justify the chosen temperature. We look at three Ag coated PLD-YBCO films oxygenated at different temperatures. The resistivity of these 200 nm thick films during a temperature dwell at 300, 350 and 450 °C, respectively, is depicted in Fig. 6.19(a). At 300 °C equilibrium is reached slowly and ρ saturates after more than 120 minutes. Increasing the dwell temperature by 50 °C substantially shortens the saturation process to about 20 min. At even higher temperatures as 450 °C the mayor drop in ρ occurs already during the heating stage (not shown). During the dwell itself we observe only a minor decrease of the resistivity within the first 30 min, followed by a slight increase of ρ. This

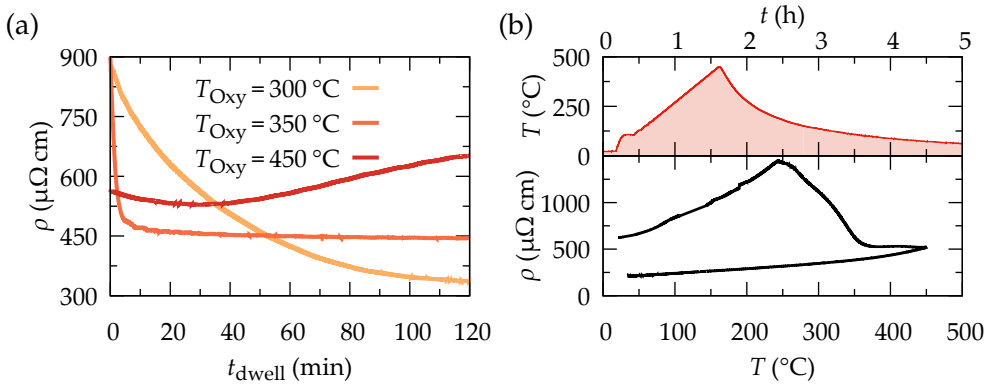

FIGURE 6.19: (a) *In situ* resistivity during oxygenation dwell at different temperatures of 200 nm PLD-YBCO (Ag), samples heated in high $P(O_2)$. (b) Oxygenation at 450 °C with a dwell of 0 min (temperature profile and $\rho(T)$).

suggests that at such high temperatures the sample is in quasi-equilibrium already during the heating stage and a major part of the oxygen incorporation takes place before the dwell temperature is reached.

Thus 450 °C is an interesting temperature to study the influence of the annealing time. The annealing time is varied between 0 and 240 minutes, while other parameters as heating rate (10 °C/min), oxygenation temperature (450 °C) and oxygen partial pressure (1 bar, flow of 0.6 l/min) are kept constant. The cooling rate is limited by the maximum cooling speed of the furnace.

An example for a 0 min dwell oxygenation (sample *S0*) is shown in Fig. 6.19(b). The temperature profile (T *vs.* t) is shown in the upper panel and the resistivity over T is drawn in the lower graph. We observe the typical characteristic features like a peak in $\rho(T)$ followed by a strong decrease. Between 350 and 450 °C the resistivity is temperature independent. We explain this behaviour by the compensation of the simultaneous increase of ρ due to the temperature increase and a decrease of ρ caused by the ongoing incorporation of oxygen into the structure, increasing the charge carrier density. During cooling ρ decreases linearly with decreasing temperature below 300 °C. The slope is determined to be 0.52 $\mu\Omega$ cm/°C, indicating a very high charge carrier density at room temperature ($\approx$ 17 $\times$ 10^{21} cm^{-3} using Eq. (6.4)), which is in agreement with Hall measurements at room temperature giving 16.1 $\times$ 10^{21} charge carriers/cm^3. A very low resistivity value of about 210 $\mu\Omega$ cm at room temperature suggests as well a high doping level.
This result is promising as it might allow to drastically shorten and facilitate a reel-to-reel production process, but discrepancies were found in the analysis

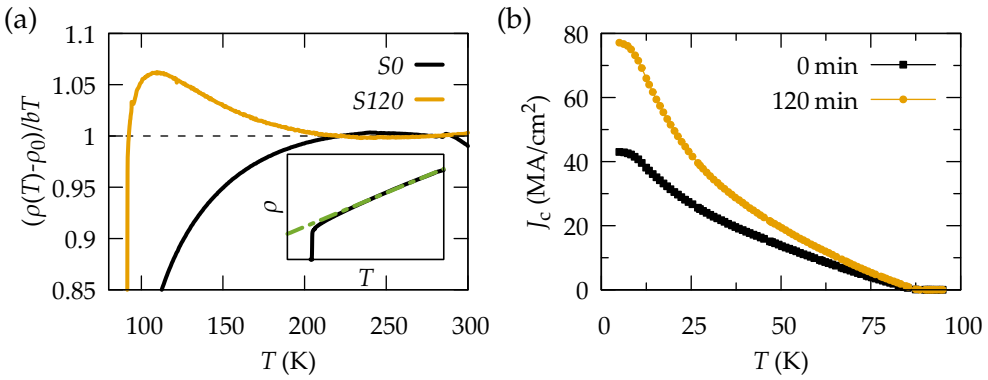

FIGURE 6.20: Influence of annealing time on low temperature physical properties for samples annealed for 0 and 120 min at 450 °C, respectively: (a) normalised resistivity: upward/downward deviation of ρ from 1 indicates high/low doping state; inset shows linear fit to extract ρ_0 and b. (b) $J_{c,sf}$ as a function of T.

of low temperature normal state and SC properties, as will be discussed in the following.

We have measured the resistivity of the film down to the critical temperature at 89 K. Typically for HTS materials one finds a linear dependence on T in a broad temperature range with $\rho(T) = bT + \rho_0$, as shown in the inset of Fig. 6.20(a) and discussed in the previous section. The normalised resistivity $(\rho(T) - \rho_0)/(bT)$ is shown in Fig. 6.20(a), where the parameters b and ρ_0 are obtained by a linear fit as shown in the inset for *S0*. The normalised resistivity deviates downwards from unity around 200 K for the case of a 0 min annealing process at 450 °C. This finding is in contradiction to room temperature electrical properties (high n_H, low ρ), as a downwards deviation indicates a low doping state [227]. Additionally, the derivative $d\rho/dT$ exhibits a small but constants slope pointing towards a non-neglectable quadratic contribution in the temperature dependence of the resistivity, which might be a hint to a different scattering mechanism in this sample.
In comparison we show a sample, which was oxygenated for 120 min (*S120*) at 450 °C. This sample has a lower, but still high charge carrier density at room temperature ($n_H(300\,K) = 10.7 \times 10^{21}\,cm^{-3}$) but exhibits a peak in the normalised temperature dependence of ρ, as expected for highly doped (overdoped) YBCO.

The self-field critical current densities of these two samples are shown in Fig. 6.20(b). The sample *S0* has a significantly lower critical current over the

full temperature range. At low temperatures J_c can be doubled by extending the annealing time from 0 min to 120 min.

The differences in the temperature dependence might be correlated with changes within the microstructure during longer annealing times and therefore modified pinning landscapes. Regarding the strength of different pinning sites, one can distinguish between strong and weak pinning centres. The total critical current can be written in a first approximation as the sum of the individual contributions:

$$J_c(T) = \underbrace{J_c^{weak}(0)\exp\left[-\frac{T}{T_0}\right]}_{J_c^{weak}(T)} + \underbrace{J_c^{strong}(0)\exp\left[-3\left(\frac{T}{T^*}\right)^2\right]}_{J_c^{strong}(T)}, \qquad (6.8)$$

with the characteristic temperatures T_0 and T^* and the J_c contributions at 0 K $J_c^{weak}(0)$ and $J_c^{strong}(0)$ of weak and strong pinning sites, respectively.
The first term was established within the weak collective pinning model [252], derived from the time dependence of J_c due to thermally activated flux motion (creep) first introduced in [253]. Its contribution rapidly decreases with increasing T. A source of weak pinning defects in YBCO are 0-D point defects with dimensions smaller than the material and temperature dependent coherence length $\xi(T)$. $k_B T_0$ is proportional to the collective pinning energy $U_c \propto H_c^2$ and of the order of 10 K in cuprates [254].
The second term in Eq. (6.8) for strong pinning was first described in [255] for vortex pinning in HTS by correlated defects as grain and twin boundaries, columnar defects and generally dislocations parallel to the *c*-axis. Its $J_c(T)$ contribution decays exponentially with T^2 and therefore it is slower than in the case of weak pinning. Thus, strong defects are relatively more effective at high temperatures to pin vortices.

To analyse the different pinning contributions, remanent magnetization measurements are performed under an applied external magnetic field of 7 T and the temperature dependence of J_c is fit to Eq. (6.8), as shown in Fig. 6.21(a). As in the case of self-field measurements presented above, the current densities $J_c(\mu_0 H \neq 0)$ of the two samples notably differ over the full temperature range. *S120* presents an about 50 % higher J_c compared to *S0* over the full temperature range. The data is well described by the model consisting of two different temperature dependent contributions, as can be seen with the continuous lines. A cross over of $J_c^{weak}(T)$ and $J_c^{strong}(T)$ can be observed at about 10 and 6 K for *S0* and *S120*, respectively. The extracted $J_c(0)$ values for weak and strong pinning are presented in Fig. 6.21(b). The sample annealed for 0 min exhibits lower $J_c(0)$ values for both, weak and strong pinning. The

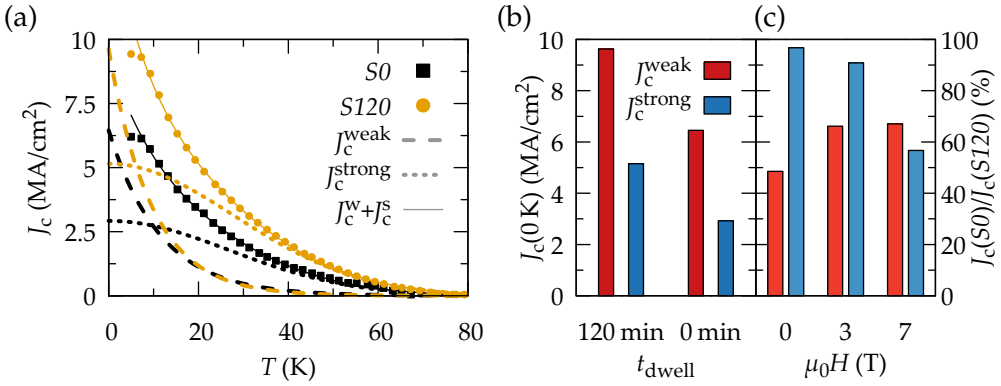

FIGURE 6.21: (a) $J_c(T)$ dependence in applied field of 7 T used to separate different pinning contributions via fitting: dashed lines indicate $J_c^{weak}(T)$, dotted lines $J_c^{strong}(T)$, respectively; continuous lines represent the sum $J_c^{weak}(T) + J_c^{strong}(T)$. (b) Resulting fit parameters for weak and strong J_c contributions from (a) using a least-squares method. (c) J_c of *S0* normalised to J_c of *S120* for each contribution at self-field, 3 T and 7 T, respectively.

contributions are reduced by about 30 and 40 %, respectively. For the characteristic temperatures T_0 and T^* we do not observe significant differences between the two samples.

In Fig. 6.21(c) we compare the J_c contributions of sample *S0* normalised to the values obtained for *S120* for measurements at 0, 3 and 7 T. At self-field the weak contribution of *S0* is decreased by about 50 %, while J_c^{strong} is the same for both films. With increasing field the contribution of strong pinning sites decreases from almost 100 % to less than 60 %. Upon applying a magnetic field J_c^{weak} remains at about 70 %.

These measurements show clear differences in the pinning contributions of the two different thin films. However, the exact origin of the different $J_c(T)$ dependencies can not be identified. At low fields, we find a lack of weak contribution in *S0*, while at high fields, weak and strong J_c are decreased to a similar extent. At 7 T we find only about 60 % of the weak and strong defects contributing to pinning.

The dependence of the self-field critical current density at 5 K on the oxygenation dwell time is depicted in Fig. 6.22. The critical current sharply increases with increasing annealing time from 0 to 30 min and saturates for longer dwell times. We address the increase of J_c to the development of beneficial defects for pinning with ongoing oxygenation, oxygen ordering effects during annealing and corresponding charge transfer from the CuO-chains to

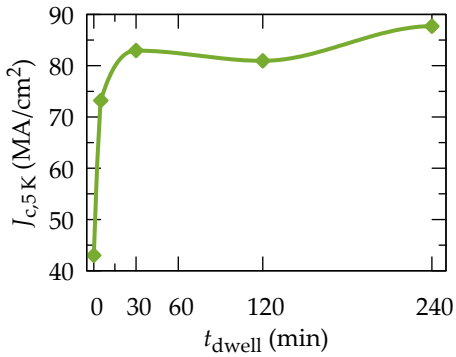

FIGURE 6.22: Self-field critical current J_c at 5 K *vs* dwell time for PLD YBCO films of 200 nm oxygenated at 450 °C in 1 bar of oxygen.

the superconducting CuO_2-planes. Therefore we will further study the doping state by means of electrical measurements in the following.

The temperature dependence of the charge carrier density is obtained by Hall effect measurements at a constant field of 3 T (see section 3.4.2). The apparent charge carrier density $n_H(T) = 1/eR_H(T)$ is depicted in Fig. 6.23(a) for *S0* and *S120*. We observe a strong temperature dependence for both films above 100 K.

In our films we typically find a power law dependence $n_H(T) = aT^\beta + n_H(0)$ [243] for $T > 100$ K, with $\beta < 1$ describing the negative curvature of n_H, as can be seen for sample *S120*. On the other hand sample *S0* exhibits a stronger dependence on temperature with $\beta > 1$. While at 100 K both films exhibit the same charge carrier density, at 300 K n_H of *S0* is increased by more than 50 %.

While it is not certain, that the strong temperature dependence of n_H is actually caused by a depletion of free charges with decreasing temperature, the rate of change can provide further insight into differences caused by annealing time. Therefore we compare the ratio of n_H at 300 and 100 K in Fig. 6.23(b) for different annealing times. For samples grown by PLD the ratio rapidly drops from 3.7 for the shortest annealing (0 min) to about 2.2, where it saturates for annealing times longer than 120 min. Analysed films grown by CSD seem to follow the same trend.

A complementary analysis is performed regarding the mobility of available charges in highly oxygen doped YBCO thin films. We have measured the hole mobility of *S0* and *S120* as a function of temperature, as shown in Fig. 6.24(a) in a log-log plot. The mobility of *S0* decreases slightly faster with increasing temperature than *S120*. The hole mobility at 300 K is about

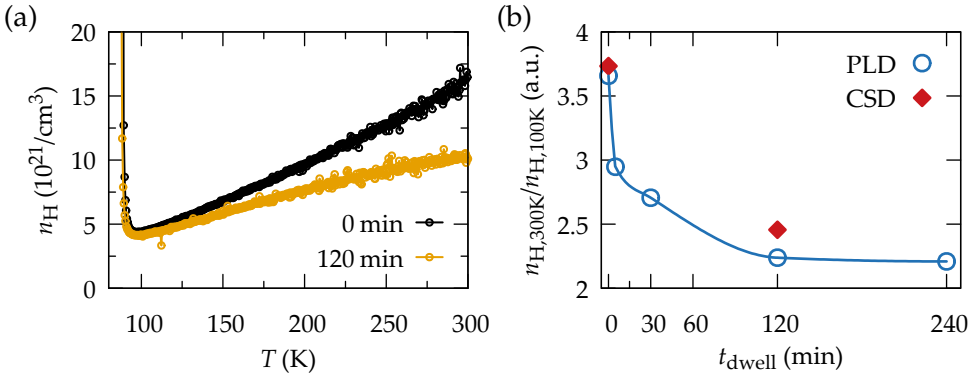

FIGURE 6.23: (a) Temperature dependence of the charge carrier density measured at 3 T for 200 nm PLD-YBCO sample *S0* and *S120*. (b) Influence of annealing time on ratio of n_H at 300 and 100 K for YBCO obtained by PLD and CSD.

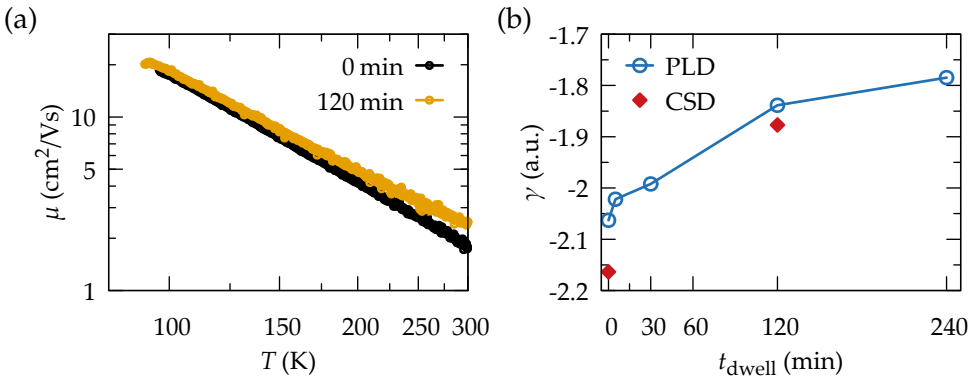

FIGURE 6.24: (a) Variation with temperature of the hole mobility $\mu_p(T) = \sigma(T)/n_H(T)e$ for *S0* and *S120* in a log-log plot. (b) Dependence of power law exponent γ in $\mu \propto T^\gamma$ on annealing time for PLD and CSD-YBCO films annealed at 450 °C.

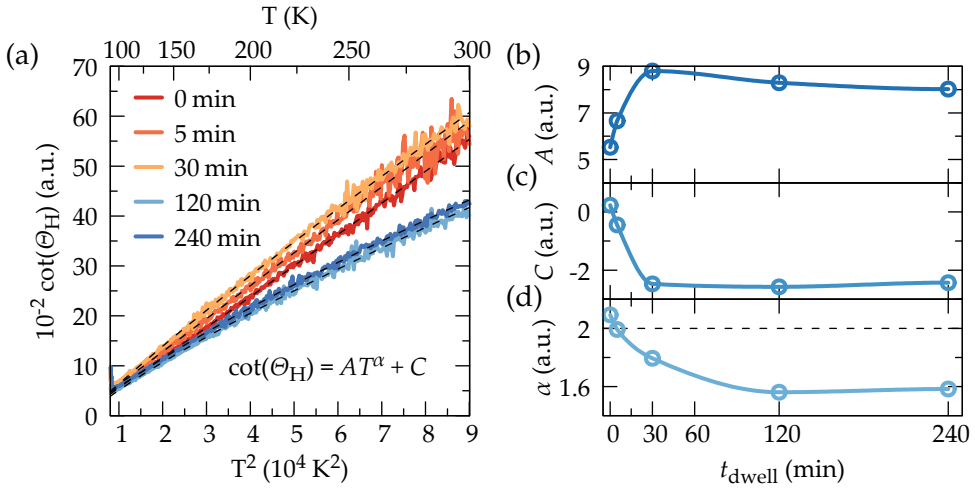

FIGURE 6.25: (a) Cotangent of Hall angle over T^2 for different annealing times. Experimental data is fit to $\cot(\Theta_H) = A(T/1\,\mathrm{K})^\alpha + C$ (dashed lines). The obtained fit parameter A, C and α are shown in the panels (b),(c) and (d), respectively as a function of the sample dwell time.

$2\,\mathrm{cm}^2/\mathrm{Vs}$, which is close to reported mobilities of conventional metals (*e.g.* iron: $4\,\mathrm{cm}^2/\mathrm{Vs}$ [256]). Similar mobilities were reported for the cuprate SC $La_{2-x}Sr_xCuO_4$ in [228]. The temperature dependence of the hole mobility, where phonon interaction is the predominant scattering mechanism, was found to follow a power law [257]. Also in our material $\mu(T)$ can be well expressed by:

$$\mu_p(T) = \frac{\sigma(T)}{n_H(T)e} = AT^\gamma, \tag{6.9}$$

with the elementary charge e and the fit parameters A and γ. We find a dependence of the power law exponent γ on the dwell time, as shown for several thin YBCO films in Fig. 6.24(b). γ increases from below -2 to about -1.8. In well doped PLD films, which consistently show all signs of overdoped YBCO such as high n_H, high J_c at all temperatures and an upwards curvature of the normalised resistivity, we typically find γ to be around -1.8. This result indicates, that oxygen annealings at 450 °C for less than 30 minutes are not sufficient to achieve overdoped YBCO.

Finally, a characteristic feature of high temperature superconductors is the universal, quadratic like temperature dependence of the cotangent of the Hall

angle, $\cot(\Theta_H)$ [222]:

$$\cot(\Theta_H) = \frac{\rho}{R_H \mu_0 H} \propto T^{\alpha}, \tag{6.10}$$

with $\alpha \approx 2$. Figure 6.25(a) shows $\cot(\Theta_H)$ vs. T^2 for several samples annealed at 450 °C for different times. At 300 K we find significantly lower absolute values of $\cot(\Theta_H)$ for films annealed for ≥ 120 min compared to films oxygenated only for short times. However, the dependence of $\cot(\Theta_H)$ on temperature reveals more information. The Hall angle can be accurately fit to $\cot(\Theta_H) = A(T/1\,\mathrm{K})^{\alpha} + C$, as indicated by dashed lines in Fig. 6.25(a). By allowing $\alpha \neq 2$ the measured data can be described within the full temperature range.
The subfigures 6.25(b), (c) and (d) depict the obtained fit parameters A, C and α, respectively, as a function of the dwell time. For all three parameters we observe a saturation with increasing annealing time. Similar trends are reported in [238], where fit parameters are evaluated in respect to the oxygen stoichiometry, thus closely related to the doping state of the material and resembling our case. This indicates that during longer annealing times, oxygen ordering effects within the structure take place, accompanied by charge transfer from CuO-chains to the superconducting CuO_2-planes increasing the doping state of the thin films.

In summary, even though we have observed very fast saturation of the *in situ* resistivity during the oxygenation process at 450 °C, we have found that physical properties improve with longer annealing times. YBCO thin films annealed for short times only (< 30 min) exhibit an unusual temperature dependence of the resistivity and charge carrier density inducing an inconsistent interpretation of the doping state. The critical current density at 5 K was found to reveal a dependence on the annealing time too. The analysis of the temperature dependence of the mobility and the Hall angle on the dwell time further clarifies the situation. The fit parameters describing the temperature dependence of μ and Θ_H saturate for oxygenation times above 120 min. We interpret this by ongoing oxygen ordering within the matrix with annealing time and enhanced charge transfer within the unit cell from the CuO-chain sites to CuO_2-planes, resulting in a higher doping state of the YBCO thin film.

6.2.3 Doping dependence of electronic and physical properties of YBCO thin films on $P(O_2)$

To undertake a deeper study on the influence of $P(O_2)$, we have obtained PLD films at different doping states by tuning the $P(O_2)$ during oxygen annealings of 2 h at 450 °C. The critical temperature obtained by resistivity measurements and defined as the midpoint of the transition, $T_{c,MP}$, as a function of the oxygen partial pressure during annealing is shown in Fig. 6.26(a). Upon decreasing $P(O_2)$ from 1 bar $T_{c,MP}$ remains initially unchanged. Below 0.1 bar the critical temperature rapidly drops.
In cuprate superconductors a parabolic dependence of T_c on doping was found [212, 258]:

$$1 - \frac{T_c}{T_{c,max}} = 82.6(p - 0.16)^2, \tag{6.11}$$

centred around a doping value of 0.16 holes/Cu, where T_c reaches its maximum, $T_{c,max}$ (compare with schematic representation in Fig. 2.2). The constant T_c in a broad $P(O_2)$ range is related to the plateau of T_c around optimal doping [259], as it was previously reported for thin YBCO films [105]. This plateau prevents an accurate evaluation of the doping state p using Equation (6.11) for optimally and slightly overdoped YBCO films.

The charge carrier density $n_{H,100\,K}$ *vs.* the $P(O_2)$ during annealing is shown in Fig. 6.26(b) for PLD-YBCO films. As expected, $n_{H,100\,K}$ decreases with decreasing partial pressure of oxygen. We observe a higher sensitivity of $n_{H,100\,K}$ on the $P(O_2)$ as compared to T_c for $P(O_2) > 0.1$ bar. Thus, close to optimal doping $n_{H,100\,K}$ is a better measure of the doping state than the critical temperature. The doping state is indicated as well by the deviation from unity of the normalised resistivity, as shown in Fig. 6.26(c). The shown three different cases correspond to the overdoped, optimally doped and underdoped regime and were oxygenated in a $P(O_2)$ of 1000 mbar, 100 mbar and 10 mbar, respectively.

In Fig. 6.27(a) we plot the critical temperature obtained by resistivity measurements as a function of the charge carrier density at 100 K. Initially, $T_{c,MP}$ rapidly increases with increasing $n_{H,100\,K}$, upon reaching its maximum around 90 K and *quasi* saturates at higher n_H. A similar trend was observed previously in different cuprate SC [227, 260]. We identify the onset of the plateau as the optimal doping state, with $n_{H,100\,K} = 3.2 \times 10^{21}/cm^3$, with the overdoped (OD) and underdoped (UD) regime at higher and lower charge carrier densities, respectively. As mentioned above, this is consisted with a definition of $n_{H,300\,K} = 8 \times 10^{21}/cm^3$ for the optimally doped state [227]. While $n_{H,100\,K}$

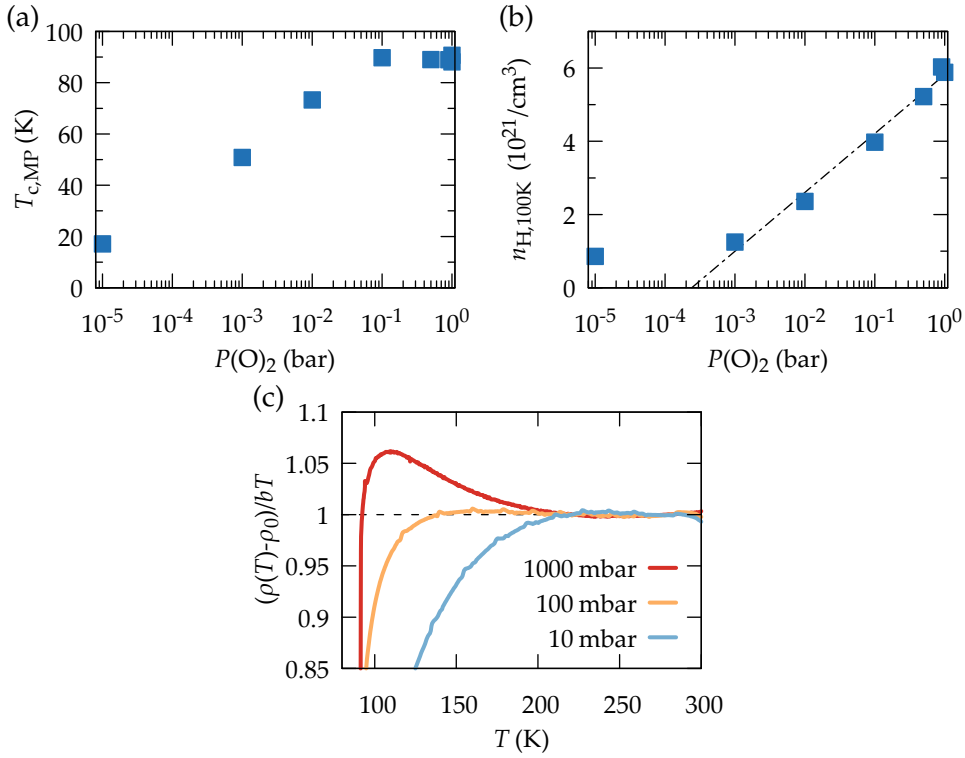

FIGURE 6.26: 200 nm YBCO films grown by PLD and annealed in different oxygen atmospheres at 450 °C for 2 h: (a) Critical temperature obtained by electrical measurements and (b) charge carrier density at 100 K as a function of $P(O_2)$. (c) Normalised resistivities of samples annealed in different $P(O_2)$ show transition from overdoped (1 bar) via optimally doped (100 mbar) to underdoped (10 mbar) regime.

varies between 3×10^{-21}/cm^3 and 9×10^{-21}/cm^3, the critical temperature remains almost constant. This confirms that $n_{H,100\,K}$ is a more precise measure of the doping state than the critical temperature $T_{c,MP}$.

As T_c is strongly reduced in the low doped films, we restrict our analysis to low temperature critical current densities to avoid the influence of a low T_c. Additionally, at low temperatures as 5 K the weak pinning contribution to the overall J_c becomes more important and thus the influence of the condensation energy is more significant. The dependence of the self-field J_c values at 5 K on the charge carrier density at 100 K, $n_{H,100\,K}$, is shown in Fig. 6.27(b). We observe a linear dependence of J_c on the charge carrier density. Very low critical current densities (< 0.1 MA/cm^2) are observed for $n_{H,100\,K} < 2\times10^{21}$/cm^3.

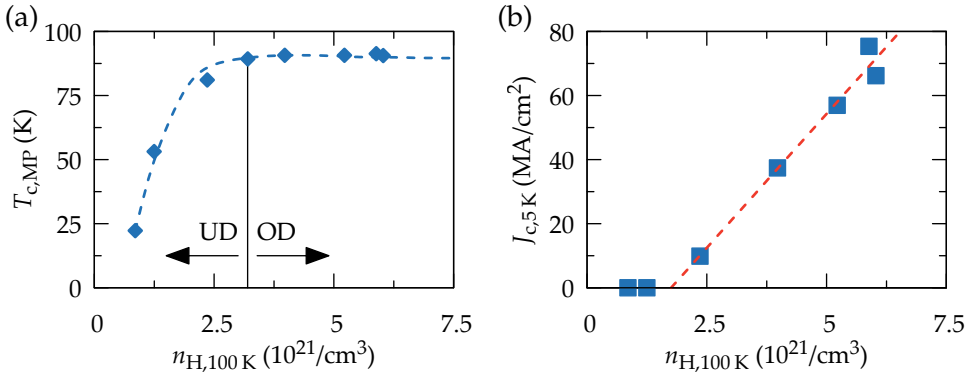

FIGURE 6.27: (a) $T_{c,MP}$ dependence on charge carrier density at 100 K, where the onset of the plateau in T_c, the optimal doping state is indicated by a black vertical line with the underdoped (UD) and overdoped (OD) regime below and above, respectively. (b) Self-field critical current at 5 K as a function of $n_{H,100\,K}$.

However, J_c can be strongly increased if the overall charge carrier density and thus available charges in the superconducting CuO_2-planes, is increased. This finding confirms our initial assumption that overdoping is a very promising route to enhance superconducting properties of YBCO thin films.

6.2.4 Oxygenation conditions for high performance superconducting films

We found a strong dependence of J_c on $P(O_2)$ and annealing time in section 6.2.3 and 6.2.2, respectively. Hence, we limit our comparison to samples annealed in 1 bar of oxygen for 120 min at different temperatures.

The charge carrier density n_H at 100 K of 200 nm PLD films as a function of the oxygenation temperature is shown in Fig. 6.28(a). We observe a nonmonotonic, dome shaped dependence with a maximum around $T_{oxy} = 375\,°C$.
For all oxygenation temperatures $\geq$300 °C we obtain highly doped YBCO, with charge carrier densities above the reference value of 3.2×10^{21} /cm^3 for optimally doped YBCO. Hence all films oxygenated at and above 300 °C are overdoped. As stated previously in Chapter 6.1.4 an oxygenation at 200 °C does not yield a sufficient oxygen doping of the structure. It is interesting that around 375 °C very high n_H values in the overdoped regime are reached and that only above 450 °C a slight decrease of n_H can be observed. The dependence of the n_H at 300 K on the oxygenation temperature is very similar (not shown).

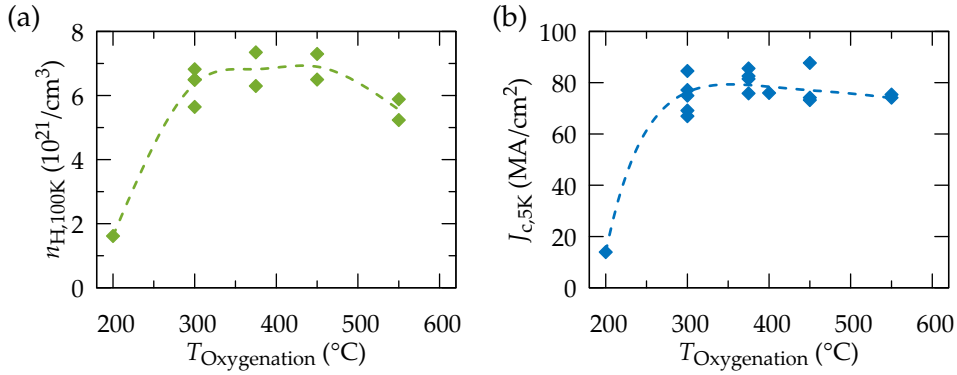

FIGURE 6.28: Influence of oxygenation temperature on (a) charge carrier density $n_{H,100\,K}$ at 100 K and (b) J_c at 5 K and self-field of 200 nm thick PLD YBCO films. Dashed lines are guide to the eye.

In Figure 6.28(b) J_c at 5 K is plotted *vs* T_{oxy}. Firstly, we have obtained tremendously high critical current densities exceeding 85 MA/cm^2 at low oxygenation temperatures. J_c is effectively limited by various mechanism, as the motion of magnetic vortices, grain boundary misorientation, phase fluctuations, *etc.* However, we can compare the critical current densities obtained in this study to the thermodynamic limit, the depairing current, as defined in Eq. (2.6) of the material. We can estimate the depairing current at 5 K using $\xi(0) = 1.2$ nm and $\lambda(0) = 168$ nm to $J_{d,5K}^{GL} = 297$ MA/cm^2 [261]. With a maximum J_c at 5 K of 89.4 MA/cm^2 we are close (factor 3) to the fundamental limit. For comparison, the highest J_c values reported for high temperatures (77 K) are one order of magnitude below the depairing current density (*e.g.* $J_{c,77\,K} \approx 7$ MA/cm^2 reported in [262] while $J_{d,77\,K}^{GL} = 65$ MA/cm^2).

Secondly, between 300 °C and 450 °C the critical current is independent of the actual oxygenation temperature, similar to the $n_H(T_{oxy})$ dependence. The observed variations in J_c for $T_{oxy} \geq 300$ °C are within the fluctuations of different sample batches. However, at higher temperatures (≥ 550 °C) J_c starts to decrease, which is expected to continue upon further increasing T_{oxy} due to an increased oxygen vacancy concentration at higher temperatures and therefore reduced charged doping into the superconducting CuO_2-planes.

To consummate this chapter we compare and recapitulate in the following on the results of various oxygenation treatments obtained in the different parts of the previous sections. We compare a large number of samples grown by PLD and CSD in the aspect of their doping state.

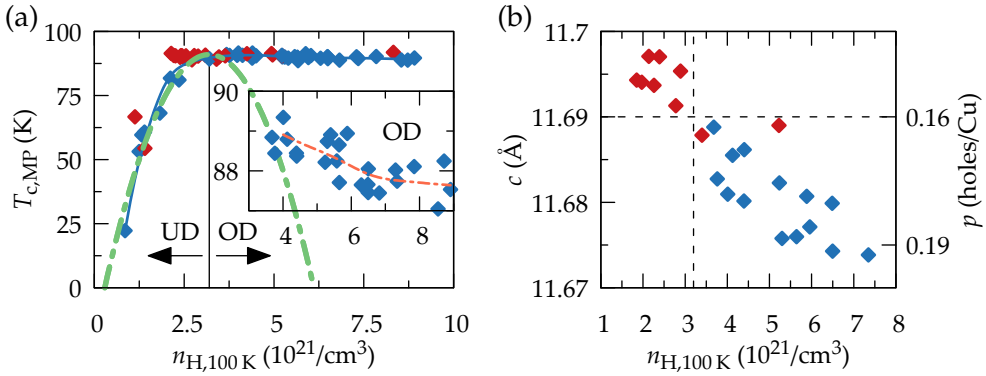

FIGURE 6.29: (a) $T_{c,MP}$ dependence on charge carrier density at 100 K of 200 nm PLD (blue) and CSD (red symbols) YBCO. The onset of the plateau in T_c for PLD films, the optimal doping state, is indicated by a black vertical line with the underdoped (UD) and overdoped (OD) regime below and above, respectively. Green dashed line indicates parabolic behaviour expected for cuprates as a function of doping. The inset magnifies the overdoped region. (b) c-parameter as a function of $n_{H,100\,K}$ in the overdoped regime for CSD (red symbols) and PLD (blue symbols). Right scale indicates actual doping level as reported in literature [106].

Our success of reaching the overdoped regime is emphasised in Fig 6.29(a), where the $T_{c,MP}$ is shown as a function of the n_H at 100 K for YBCO grown by CSD (red) and PLD (blue). A large number of samples exceeds the optimal doping state of $n_{H,100\,K} = 3.2 \times 10^{-21}/\text{cm}^3$. We notice that CSD-YBCO reaches the maximum T_c already at lower charge carrier densities, as compared to PLD-YBCO. A parabolic tendency is indicated with the green dashed lined centred around optimal doping. This parabola draws a comparison to the empirical law, stated in Eq. (6.11) observed in many cuprates. In the underdoped regime T_c follows this trend as a function of the charge carrier density. However, in the overdoped regime a much weaker dependence on $n_{H,100\,K}$ and a deviation from a parabolic behaviour is observed, as previously reported for the analysis of T_c *vs.* n_H in [227]. This discrepancy indicates that $n_{H,100\,K}$ is not exactly equivalent to the hole doping p in the superconducting CuO_2-planes.

The inset of Fig 6.29(a) focuses on the overdoped regime, where a starting decrease of T_c can be observed. This decrease in the overdoped regime might be explained by a depletion of particles participating in the superconducting state (the superfluid density) in spite of the increasing normal state charge carrier density [263, 264], combined with a decrease of the superconducting

energy gap in the strongly overdoped side of the phase diagram [202, 265, 266].

In Fig. 6.29(b) we present the *c*-parameter as a function of the charge carrier density at 100 K for overdoped CSD and PLD films. We observe a small shrinkage of the lattice parameter with increasing $n_{\mathrm{H,100\,K}}$, even in the overdoped region. On the right scale the corresponding doping level is indicated using a previously reported correlation between p and c (see Eq. (4.9) on page 71)[4] [106]. While a doping of 0.16 holes/Cu in the CuO_2-planes corresponds to optimal doping and a maximum in T_c, $p = 0.19$ is already far in the overdoped regime, where the condensation energy is expected to peak [203, 267] due to the closing of the pseudogap [201, 268].

Most interestingly, we want to correlate superconducting properties, especially J_c, with the directly measurable charge carrier densities of the YBCO thin films. In section 6.2.1 we have shown the correlation between the charge carrier densities at 300 K and 100 K (Fig. 6.15(c)) and the correlation between $n_{\mathrm{H,100\,K}}$ and $n_{\mathrm{H,2band}}$ (see Fig. 6.17(b)). However, some scattering remained and, generally, charge carrier densities are not exactly equivalent to the actual doping state of YBCO. Therefore we analyse the J_c as a function of the different parameters in the following.

As we are interested in the condensation energy we analyse the self-field critical current at low temperatures. J_c at 5 K is shown as a function of $n_{\mathrm{H,300\,K}}$, $n_{\mathrm{H,100\,K}}$ and $n_{\mathrm{H,2band}}$ in Fig. 6.30(a), (b) and (c), respectively. Optimal doping is indicated in all graphs with a vertical green line. In all three cases we observe the general trend of increasing J_c with increasing charge carrier density. This result is highly interesting as it confirms the importance of doping on the critical current density and extends its validity into the overdoped regime. Theoretically the increase of J_c with doping is understood due to an increase of the condensation energy in the near overdoped range [199]. However, we observe broad scattering of J_c over $n_{\mathrm{H,300\,K}}$ in Fig. 6.30(a) and J_c over $n_{\mathrm{H,100\,K}}$ in Fig. 6.30(b). The better correlation of $n_{\mathrm{H,100\,K}}$ with J_c may be due to its proximity to the superconducting state, as *i.e.* not all charge carriers participate in the superconducting state [269].

As introduced in section 6.2.1, we have further analysed the charge carrier density $n_{\mathrm{H}}(T)$ in aspect of a two band model, with the aim to obtain a temperature independent parameter $n_{\mathrm{H,2band}}$. The self-field J_c at 5 K *vs.* $n_{\mathrm{H,2band}}$ is shown in Fig. 6.30(c). The dependence of J_c becomes reasonable well monotonic, essentially linear with $n_{\mathrm{H,2band}}$. The dependence of the condensation energy on oxygen doping was shown in [199], where E_c is calculated from

[4] We have observed a systematic shift to lower *c*-parameters than described in [106]. To account for this shift we have corrected the *p*-*c* relation by a constant offset of 0.05 Å in *c* leading to equivalent criteria regarding the optimal doping in *c* and n_{H}

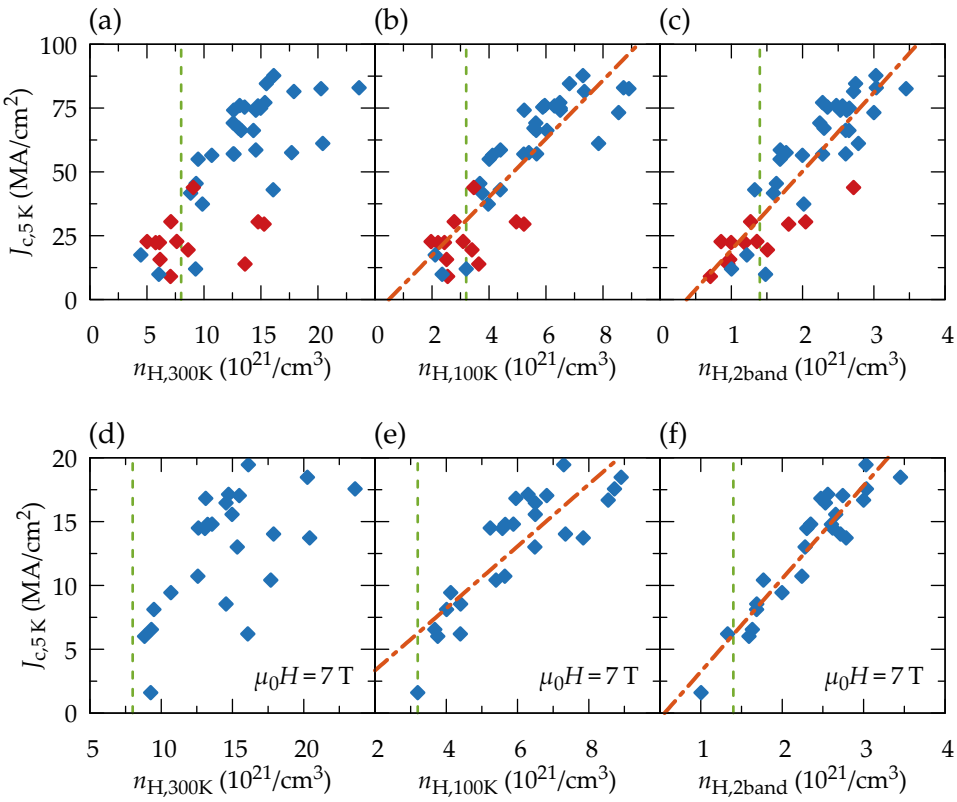

FIGURE 6.30: (a) - (c) Self-field critical current densities and (d) - (f) J_c at $\mu_0 H = 7\,\mathrm{T} \perp ab$-planes as a function of the charge carrier densities at 300 K and 100 K, and $n_{H,2band}$, respectively, for 200 nm thick YBCO films grown by PLD (blue symbols) and 250 nm CSD-YBCO (red symbols). Vertical bars indicate optimal doping, to the right is the overdoped regime. Dashed red lines in (b), (c), (e) and (f) are guides to the eye to show the trend of J_c.

heat capacity data reported in [270]. Therein a linear dependence of E_c on doping is reported in proximity to the optimal doped state. This supports our attempt to find a linear relation between J_c and the parameter closest related to the doping level of the CuO_2-planes. Hence, Figure 6.30(a) - (c) suggest that $n_{H,2band}$ is the most precise measure of the available charges in the superconducting CuO_2-planes. Going deeply into the overdoped regime (to the right of the green line), we find that J_c in PLD films can be increased up to 90 MA/cm^2, which represents a huge increase of 150%.

We can conclude that we have achieved highly overdoped YBCO thin films, both by PLD and CSD. The maximum critical current densities obtained

in self-field are 44.5 MA/cm^2 and 89.4 MA/cm^2 at 5 K for CSD and PLD films with a $n_{H,2band}$ of 2.7×10^{-21}/cm^3 and 3×10^{-21}/cm^3, respectively.

Additionally we have performed a similar comparison for the critical current at 5 K in an external magnetic field of 7 T. J_c is plotted as a function of $n_{H,300\,K}$, $n_{H,100\,K}$ and $n_{H,2Band}$ in Figure 6.30(d), (e) and (f), respectively. Qualitatively, we observe the same trends for the in-field J_c as for $J_{c,sf}$, as broad scattering in Fig. 6.30(d & e), especially in the high charge carrier density range. On the other hand J_c obeys a rather clear linear dependence when plotted as a function of $n_{H,2band}$ (Fig. 6.30(f)). Thus, the correlation between J_c and n_H increases going from the n_H value at 300 K via 100 K to the T independent value $n_{H,2band}$.

We can conclude that $n_{H,2band}$ is the most accurately and representative parameter related to the doping state of YBCO, accessible by electrical measurements. We have aimed to confirm this result by Seebeck effect measurements [200, 259]. However, limitations of the available setups in resolution and precision prevented a deep analysis. Another complementary approach to verify our conclusions could be the measurements of the doping level via the superfluid density by the mutual inductance technique [271], muon spin rotation [263] or nuclear magnetic resonance [272]. However, this remains future work.

As mentioned above, the increase in condensation energy with doping is expected to more significantly affect low temperature critical current densities, as thermal creep is strongly reduced and the irreversibility line is far away. Additionally, at low temperatures weak pinning sites are strongly contributing to the overall pinning and due to their small dimensionality (small pinning volume) condensation energy might have more influence in 0D pinning sites than in 1D, 2D or even 3D defects, which are active at high T. But also at high temperatures an increase in doping is expected to enhance J_c. This is confirmed in Fig. 6.31(a), where we compare the J_c at 77 K as a function of the temperature independent charge carrier density $n_{H,2band}$ for films grown by CSD and PLD. The red line indicates the trend for CSD films, where we find a strong increase of J_c with increasing n_H. For PLD films the situation is somewhat more complicated. Above $n_{H,2band} = 1.5 \times 10^{-21}$/cm^3, the increase of J_c with n_H is significantly weaker (compare with the approximately linear increase of J_c at 5 K within a broad $n_{H,2band}$ range in Fig. 6.30(c)).

The fact that the increase of $J_{c,77\,K}$ starts to saturate is emphasised in the lower panel of Fig. 6.31(b), which shows the self-field critical current at 77 K vs. J_c at 5 K for PLD and CSD films. Up to about 50 MA/cm^2 we find a linear trend between J_c at 77 K and 5 K for PLD-YBCO. However at higher $J_{c,5\,K}$ values a deviation from the initial trend can be observed, resulting in a

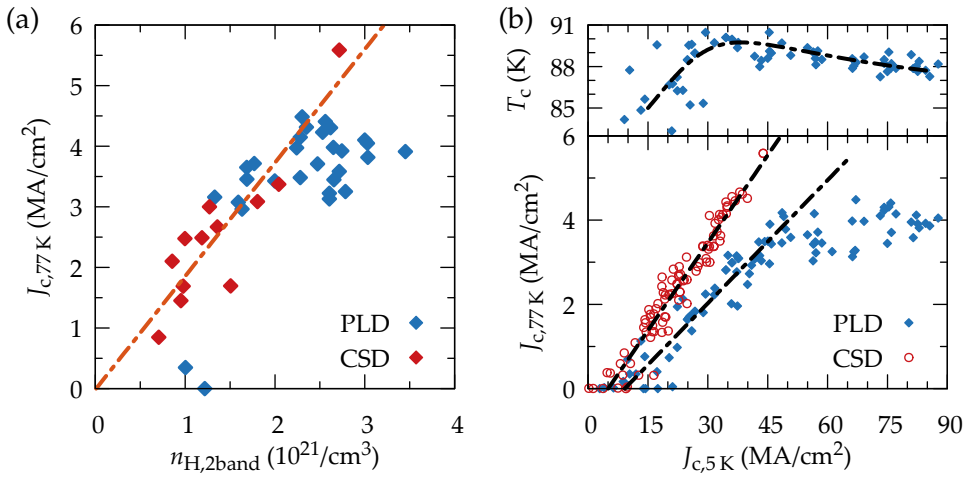

FIGURE 6.31: (a) J_c at 77 K as a function of $n_{H,2band}$ for 250 nm CSD (red) and 200 nm PLD (blue symbols) YBCO films. Dashed line indicates the trend for CSD films. (b) Lower panel shows J_c at 77 K *vs.* J_c at 5 K for YBCO obtained by PLD and CSD. Different trends for CSD and PLD are observed and marked by black dashed lines. A second, significantly weaker dependence is found for PLD films at high $J_{c,5\,K}$. The upper panel shows the critical temperature of PLD films as a function of $J_{c,5\,K}$.

second, much weaker dependence. J_c at 77 K only slightly increases from 3-4 MA/cm^2, while $J_{c,5\,K}$ tremendously increases from 50 MA/cm^2 to 90 MA/cm^2. Note, that the overdoped regime is linked to J_c values approximately above 40 MA/cm^2 at 5 K (compare with Fig. 6.30(c)). This is highlighted in the upper panel of Fig. 6.31(b), where T_c is shown over the same x-axis. The black lines mark the trend of T_c, which peaks around $J_{c,5\,K} \approx 35$ MA/cm^2. We conclude that the decrease of T_c in the overdoped regime and the proximity to the critical temperature already affects J_c at 77 K and causes the reduced influence of doping on $J_{c,77\,K}$. A saturation of J_c at 77 K with increasing doping was also reported previously in overdoped MOD-TFA films [200, 273].

A second interesting observation can be made by looking at the different trends of CSD and PLD films in Fig. 6.31(b). $J_{c,77\,K}$ is higher in CSD-YBCO as compared to PLD at the same $J_{c,5\,K}$ values. This can be understood due to different defect landscapes obtained by different growth techniques. CSD films typically preserve a much stronger distorted matrix (compare with Fig. 4.34(a & b)) giving raise to strong pinning in strained regions. Additionally at 77 K

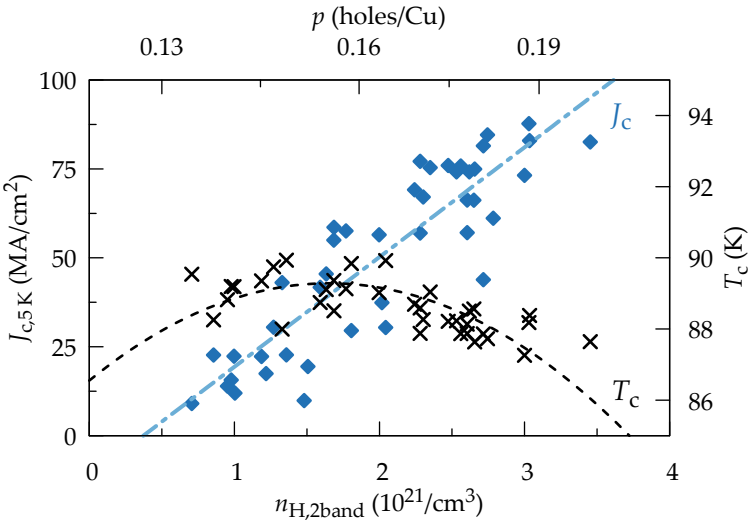

FIGURE 6.32: J_c and T_c as a function of charge carrier density and estimated hole doping p of holes per Cu in superconducting CuO_2-planes for CSD and PLD YBCO films. Dashed lines are guide to the eyes to show the trend, especially in the overdoped regime.

CSD films exhibit a strong contribution of twin boundary pinning [158], enhancing the performance as compared to PLD-YBCO. As stated in the beginning of this chapter and expressed in Eq. (6.1), the total pinning force can be improved by increasing the defect site density and by increasing the condensation energy. For the maximisation of J_c both contributions need to be optimised for the desired temperature range of operation of the final conductor.

Our efforts on reaching the overdoped regime are summarised in Figure 6.32, where we show the critical temperature, T_c, and J_c together as a function of the charge carrier density and the estimated hole doping p. Dashed lines are drawn to guide the eye and emphasise the trends, *e.g.* the increase of J_c with doping and the decrease of T_c in the under- and overdoped site of the diagram. The actual doping state p is estimated using the empirical relations between p linked via the c-parameter with $n_{H,100\,K}$ (see Fig. 6.29(b)) and the $n_{H,100\,K}$-$n_{H,2band}$ correlation, as shown in Figure 6.17(b). In conclusion, we have successfully reached the overdoped regime within this work. While an increase of J_c with doping up to $p = 0.19$ is expected from thermodynamic considerations and measurements of the superfluid density [201] and a linear increase of the condensation energy with increasing p was shown by measurements of the heat capacity [199], this is the first study actually showing

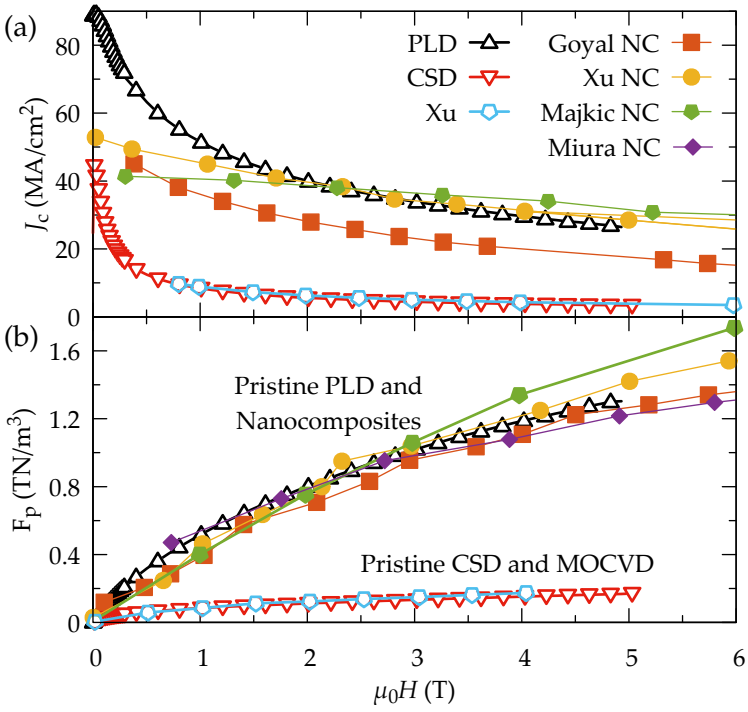

FIGURE 6.33: (a) Critical current density and (b) pinning force density, F_p as a function of applied magnetic field $H \parallel c$ for different nanocomposites (NC, full symbols) and pristine films (empty symbols). We compare the best 200 nm PLD and 250 nm CSD films obtained in this work to several nanocomposites reported in literature, which currently hold the record of high J_c at low temperatures: 15 % Zr doped (Gd,Y)BCO (Xu, MOCVD at 4.2 K) [193], nanoscale defected REBCO with 4 % BZO (Goyal, PLD at 5 K) [274] and REBCO with 15 % Zr addition (Majkic, MOCVD at 4.2 K) [275] and $SmBa_2Cu_3O_y$ with 3.8 %$BaHfO_3$ nanorods (Miura, PLD at 4.2 K) [276]. Additionally we have added a pristine MOCVD (Xu, MOCVD at 4.2 K) as reported in [277].

by direct measurements of the J_c a linear increase of critical current density with oxygen doping in the overdoped regime in thin YBCO films.

The importance of this result becomes clear when we compare our best CSD and PLD samples with the current records in literature for high critical current densities at low temperatures. The critical current density as

a function of magnetic field $\mu_0 H \parallel c$ is shown in Fig. 6.33(a) for the following nanocomposites: 15 % Zr doped (Gd,Y)BCO (Xu at 4.2 K, MOCVD) [193], nanoscale defected REBCO with 4 % BZO (Goyal at 5 K, PLD) [274] and REBCO with 15 % Zr addition (Majkic at 4.2 K, MOCVD) [275]; additionally shown are three pristine samples: a 200 nm PLD film and a 250 nm CSD layer (at 5 K) obtained in this work ($n_{\mathrm{H,2band}} = 3.0 \times 10^{-21}/\mathrm{cm}^3$ and $2.7 \times 10^{-21}/\mathrm{cm}^3$, respectively) and a pristine MOCVD film (Xu Pristine at 4.2 K) [277]. For all samples we observe a decreasing J_c with increasing magnetic field.

The most striking feature of the pristine PLD film is the strongly enhanced self-field J_c. By highly overdoping we have increased $J_c(H = 0)$ by 70 % as compared to J_c values reported by Xu et al. Up to a field of 2 T, our PLD sample exhibits the highest $J_c(H)$. We address this strong improvement of J_c to the increase of the condensation energy in the overdoped regime and therefore enhanced pinning in the pristine film, probably ascribed to weak pinning being the most relevant contribution at 5 K. This weak pinning contribution rapidly decreases at low fields, resulting in a strong $J_c(H)$ dependence at small magnetic fields. At higher fields the enhanced 1D and 3D vortex pinning in nanocomposites through nanorods and strain induced by nanoparticles, results in higher depinning critical current densities. This different pinning landscape also accounts for the weaker decay of J_c at low fields in nanocomposites. However, up to 5 T our pristine PLD film is among the highest reported samples.

The best pristine CSD film prepared in this work exhibits a very similar $J_c(H)$ behaviour as the Xu Pristine sample. Note that J_c for our films was measured by SQUID magnetometry, while in the reported samples by electrical transport measurements. J_c values obtained by SQUID are typically slightly smaller than by transport measurements due to flux creep., which makes our results even more remarkable.

The scalar pinning force density, F_p, defined as the product of the critical current density and the magnet field, $F_p = J_c \mu_0 H$, is shown as a function of $\mu_0 H$ in Fig. 6.33(b) for the same pristine and nanocomposite samples as discussed above. Additionally shown is a $SmBa_2Cu_3O_y$ film with 3.8 % $BaHfO_3$ nanorods (Miura at 4.2 K, PLD) [276]. Our pristine PLD film can compete with the best existing nanocomposite samples up to the measured field of 5 T, where a flux pinning force density of $1.3\,\mathrm{TN/m}^3$ was realised. This value is among the highest reported for nanostructured REBCO films and by far the highest for pristine YBCO. Pristine CSD films follow a different tendency with significantly lower pinning force densities at 5 T. However, also in this case the properties of pristine CSD-YBCO obtained in this work are very similar to the best pristine films reported in literature.

In summary, we have shown that doping is an extremely useful way to enhance the critical current density at low and intermediate magnetic fields (0-5 T). If we compare among pristine films, we see that J_c is increased in all magnetic fields due to overdoping. If we compare with nanocomposites, doped-pristine beat current J_c records up to 2 T and can compete at medium fields. The approach of oxygen doping could pave the way for the potential further improvement of the physical properties of nanocomposites at ultra high magnetic fields, which might have significant impact on future applications of coated conductors.

6.3 Conclusions

The main parameter of interest of superconductors is the critical current density[5]. As dissipation-free current transport in SCs is limited by magnetic vortices with their normal-state core moving through the material, a major aim of the R&D of SC is the maximisation of pinning forces, preventing the movement of these flux lines. This pinning force can be enhanced by an enriched defect landscape tailored to requirements of vortex pinning, or by increasing the superconducting condensation energy via increasing the doping state of YBCO. We have followed the latter approach by studying different thermal treatments influencing the oxygen content of YBCO and therefore the doping level.

In the first part of this chapter we have studied by *in situ* resistivity measurements the initial oxygenation process of YBCO thin films. We have found that the onset temperature of oxygen incorporation into the structure is indicated by a peak in *in situ* resistivity measurements. The process of oxygen incorporation is thermally activated and therefore the temperature of the peak depends on the heating rate and can be shifted within a certain temperature range. However, below a minimum temperature (< 300 °C) oxygen cannot be sufficiently incorporated, resulting in a poorly doping state.
Further we have shown that the catalytic activity of silver significantly decreases this onset temperature, enabling low temperature oxygenations at 300 °C for films grown by CSD and PLD. The coating of YBCO with silver enhances oxygen exchange kinetics but does not affect final normal-state and superconducting properties, in agreement with results presented in Chapter 4.

[5] or related properties as the engineering J_c relative to the total thickness of the conductor

The possible advantages of the use of low ozone concentrations during oxygenation have been briefly introduced. Essentially the lower onset temperature of oxygen incorporation due to ozone might enable oxygenation procedures below 300 °C, which in turn might open the possibility to further increase the doping level of YBCO.

We have used several techniques to gain information about the electronic state of our samples, as electrical resistivity, Hall, T_c and J_c measurements. We have shown a strong dependence of the physical properties of YBCO on $P(O_2)$ conditions during annealing. The electrical resistivity can be tuned over several orders of magnitude from good metallic to semiconducting behaviour. This is linked to a change of the charge carrier density, which is significantly lowered by a reduced oxygen partial pressure during the annealing process. The critical temperature T_c was found to be constant at pressures close to 1 bar and only drops after reducing $P(O_2)$ below 0.1 bar, while J_c immediately is affected by reduced $P(O_2)$ conditions.

Further we have found a strong dependence of the doping state of YBCO thin films on the annealing time. Physical quantities as critical current densities and the temperature dependencies of the mobility and the Hall angle saturate for annealing times $t \geq 120$ min. These extrinsic parameters are affected by disorder. Thus, we conclude that oxygen ordering effects during annealing are crucial to improve critical current densities, as we assume that these restructuring mechanisms lead to increased charge transfer of holes to the superconducting CuO_2-planes. For the case of silver coated PLD layers at an oxygenation temperature of 450 °C dwell times of ≥ 120 min were found to be essential to maximise J_c.

Finally, the charge carrier density was found to exhibit a dome shaped dependence on the oxygenation temperature with a maximum around 375 °C. High values of n_H and the beginning decrease of T_c confirm that we were able to overdope YBCO thin films grown by PLD. In these 200 nm thick films we have obtained ultra high critical current densities after oxygenation in a broad temperature range between 300 °C and 450 °C. J_c values can reach almost 90 MA/cm^2 at 5 K self-field. This is a highly remarkable achievement as we are approaching the depairing current: the obtained J_c values are only a factor 3 below this intrinsic limitation of superconductivity. These high values were enabled by the knowledge reached on oxygen kinetics of cuprates and the doping state of YBCO within this thesis. Using a two band model for electric conduction we found a monotonic correlation of self-field and in-field critical current densities on the temperature independent charge carrier density $n_{H,2band}$. This better correlation in comparison to the charge carrier density at 300 K and 100 K indicates that $n_{H,2band}$ might be a more precise measure of the actual doping level of the superconducting CuO_2-planes. This fact might

contribute another piece of the puzzle to the understanding of the complex physics in the normal state of cuprate high temperature superconductors, as still nowadays some controversy on the origin of the temperature dependence of the apparent charge carrier density exists.

The films prepared in this thesis exhibit record high critical current densities at low fields. Up to 2 T highly doped pristine PLD samples show enhanced J_c as compared to the best reported nanocomposites in literature. Highly overdoped pristine PLD compared with pristine films obtained by CSD and MOCVD have increased J_c values at all fields. This clearly demonstrates the relevant role of tuning the doping state to magnify the condensation energy and opens the possibility to essentially increase J_c in nanocomposites by overdoping.

Chapter 7

General conclusions

High temperature superconductors, especially cuprates, in form of coated conductors have the potential to be part of the next technological revolution due to unchallenged, extraordinary superconducting properties. Oxygen plays an essential role in these materials, where superconductivity is governed by hole doping.

In this thesis we have intensively studied all oxygen involved processes, from the initial incorporation of oxygen into the $YBa_2Cu_3O_{7-\delta}$ structure and related mechanisms, up to the influence of oxygen doping on the superconducting properties. We have advanced the understanding of each particular step, a necessary prerequisite for the optimisation and improvement for any commercial production line of REBCO coated conductors.

We have used electrical conductivity relaxation measurements to study the oxygen exchange kinetics of YBCO thin films. The full integral sensitivity of this technique was proven by simultaneous *in situ* XRD measurements. The time evolution of the relaxation process could be accurately described by Fick's second law with a first order reaction (mass-action law) boundary condition at the surface. The solution consists of two exponential terms, corresponding to two parallel processes.

Oxygen exchange kinetics of YBCO were found to be thermally activated with comparable high activation energies in pristine films. The introduction of a catalytic effect via the coating with a silver layer (typically 100 nm in this work) strongly reduced oxidation and reduction activation energies.

We have developed a model for the incorporation of oxygen into YBCO consisting of several elementary steps, as the adsorption, ionisation and dissociation of oxygen on the surface, ion surface diffusion and recombination with a surface oxygen vacancy and subsequent diffusion along the bulk.

By carefully analysing the electrical conductivity relaxation process between two, three and various oxygen partial pressure levels we could elucidate the role of the surface coverage and individual reaction mechanisms. The surface coverage was found to significantly vary upon changes in the $P(O_2)$ and it

mainly governs surface exchange coefficients. Additionally, we have found an asymmetry for the processes of oxygen in- and excorporation linked to different chemical barriers for the forward and backward reaction.
The analysis of reaction rates close and far from equilibrium in Ag coated YBCO thin films revealed that the recombination of oxygen ions with oxygen vacancies in the outermost layer of YBCO determines the overall reaction rate (RDS). These results are based on a defect chemical model for YBCO, which was adopted from previously reported defect models of well understood oxide materials as STO.

A broad variety of samples and microstructures, obtained by different growth methods, cation substitution, nanoparticles embedded precursor solutions and variations in thickness and/or substrate, has been studied. We have shown that modifications of the microstructure have strong influence on the oxygen exchange kinetics of the thin films. Nanostrain was identified to be the controlling parameter for the enhancement of oxygen kinetics, *e.g.* via the modification of the vacancy volume and thus the vacancy formation enthalpy.

The influence of thickness and macroscopic strain was studied in thin PLD films with thicknesses between 25 nm and 200 nm. Macrostrain was introduced by mismatch with the substrate (STO and LAO) in reduced film thicknesses. Increasing macrostrain with decreasing film thickness was found to be linked with a reduced charge carrier density and a lower T_c. In agreement with literature, tensile strain was found to enhance oxygen exchange kinetics compared to compressive strain for the thinnest films. However, with increasing thickness and decreasing macrostrain, exchange rates were strongly enhanced. It is suggested that a strain relaxation mechanism leads to a defected surface with enhanced surface exchange rates, causing faster kinetics in thicker films. Independent of the film thickness and surface coating, it was concluded that a surface mechanism limits the exchange of oxygen with environment.

The thorough use of electrical in situ measurements in combination with ex situ analysis techniques as XRD, STEM, SEM, electrical resistivity, Hall and magnetisation measurements enabled us to study the effects of thermal treatment parameters on the surface chemistry and bulk microstructure of YBCO thin films. The thermal history was found to have great influence on the oxygen exchange kinetics of pristine YBCO. A deactivation of surface exchange kinetics was found, resulting in significantly slower oxygen incorporation with increasing annealing time. The capacity of the film to exchange oxygen with environment might be reduced by a surface modification due to phase instability, segregation and depletion or accumulation of cations and the formation of carbonate side products. However, the precise mechanism could

not be identified and remains unclear. Surface coating dependent degeneration rates point towards a modification of the RDS upon silver coating of YBCO thin films.
Further, we have identified the formation of stacking faults (SF) already during low temperature annealings in low and high oxygen partial pressure. However, the presence of SF does not affect the oxygen exchange capability of the material.

We have not only studied the incorporation of oxygen in great detail but also its effect on the doping state of YBCO. In the last part of this thesis the influence of oxygen partial pressure, oxygenation temperature and oxygenation time on the charge carrier density and normal and superconducting physical properties was intensively studied. The oxygen stoichiometry of YBCO is very sensitive to the $P(O_2)$ during annealing and strongly affects the charge carrier density. We have prepared highly overdoped YBCO thin films grown by PLD with record-high critical current densities reaching 90 MA/cm^2 at 5 K and self-field by performing oxygenations between 300 °C and 450 °C. These high J_c values correspond to a third of the depairing current density. Even though oxygen is rapidly incorporated into the structure, oxygen ordering effects with longer oxygenation times were found to be crucial for good charge transfer into the superconducting CuO_2-planes and high critical current densities. The doping state was analysed by the use of temperature dependent resistivity, Hall and mobility measurements, as well as XRD and critical temperature measurements. By using a two band model for the simultaneous contribution of electrons and holes to the electrical transport in the normal state, we have obtained a temperature independent charge carrier density. We have demonstrated a linear correlation between the charge carrier density and the critical current densities in the overdoped state, thus evidencing the powerfulness of these studies for the enhancement of superconducting properties of YBCO thin films. At low temperatures the positive influence of increased doping in enhancing J_c was well observed. On the other hand, at 77 K, the dependence of J_c on the charge carrier density is weakened in the highly overdoped regime, probably due to the decrease of T_c. By highly overdoping pristine PLD films we have obtained the highest J_c values at low temperatures and low and medium magnetic fields ever reported. In the analysed field range up to 5 T, these films can compete with nanocomposite PLD and MOCVD samples. This result demonstrates the importance and potential of doping to increase the condensation energy and to push the limits for superconducting applications and paves the way to explore the overdoping state in nanocomposites.

In conclusion, we have investigated many different aspects of oxygen related mechanism in YBCO. We have developed a broad understanding of the

oxygen incorporation process, including exchange mechanism and bulk modifications during heat treatments. Further we have studied the effect of oxygen doping on superconducting properties and demonstrated its governing influence on critical current densities, especially in the overdoped region.

Appendix A

Fitting procedures

A.1 Activation energies of *in situ* measurements

The activation energies of oxidation and reduction processes are obtained by a linear regression based on the minimisation of the sum of the squared residuals, which is the offset of the actual to the predicted value. The fit parameters are gained in a linear plot of the natural logarithm of the surface exchange coefficient k_{chem} over the inverse temperature T. This corresponds to a least square fit of the residuals measured in distances in a semi-log plot (*e.g.* an Arrhenius plot). Therefore we take the logarithm ln of Eq. (4.4) on page 53:

$$\ln k_{\text{chem}} = \ln k_0 - \frac{E_{\text{a}}}{k_{\text{B}} T} \tag{A.1}$$

and compare it to a linear equation $y = mx + b$, with $x = 1/T$. We obtain the intercept and the slope via equating coefficients:

$$b = \ln k_0 \rightarrow k_0 = \exp[b] \tag{A.2}$$

and

$$m = -\frac{E_{\text{a}}}{k_{\text{B}}} \rightarrow E_{\text{a}} = -m k_{\text{B}}. \tag{A.3}$$

The resulting straight line is drawn in an Arrhenius plot using $k_{\text{chem}} = \exp\left[a/T + b\right]$. Since the measured data doesn't obey perfect exponential behaviour, there will be a discrepancy in the results compared to a standard nonlinear regression using $y' = 10^{mx+b}$ in a log-lin plot. This is caused by a lower impact of smaller k_{chem} values in the latter approach, for which reason the used method was chosen for the analysis. A comparison of this two methods is shown in Fig. A.1. The obtained activation energies are $E_{\text{a}}(y) = 1.15\,\text{eV}$ and $E_{\text{a}}(y') = 1.24\,\text{eV}$.

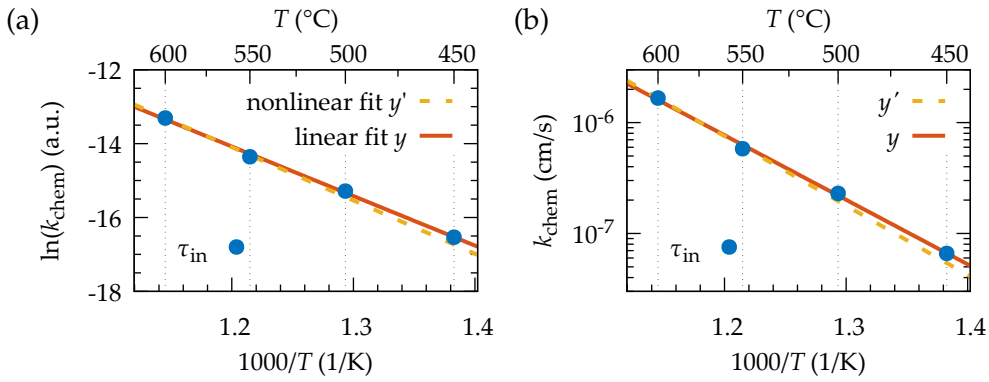

FIGURE A.1: Evaluation of E_a by (a) linear fit y in lin-lin plot ($\ln k_{chem}$ over $1/T$) and via (b) nonlinear fit y' in log-lin plot (k_{chem} over $1/T$, Arrhenius plot). For comparison the two fits are shown in both plots (a) and (b).

Bibliography

[1] Heike Kamerlingh Onnes. "The Resistance of Pure Mercury at Helium Temperatures". In: *Commun. Phys. Lab. Univ. Leiden. Suppl.* 29 (1911).

[2] W. Meissner and R. Ochsenfeld. "Ein neuer Effekt bei Eintritt der Supraleitfähigkeit". In: *Die Naturwissenschaften* 21.44 (Nov. 1933), pp. 787–788. ISSN: 0028-1042. DOI: 10.1007/BF01504252.

[3] J. Bardeen, L. N. Cooper, and J. R. Schrieffer. "Theory of Superconductivity". In: *Physical Review* 108.5 (Dec. 1957), pp. 1175–1204. DOI: 10.1103/PhysRev.108.1175.

[4] L. D. Landau. *Collected Papers of L.D. Landau*. Ed. by D. Ter Haar. Oxford: Pergamon Press, 1965, p. 546. ISBN: 9781483152707. DOI: 10.1016/C2013-0-01806-3.

[5] J. G. Bednorz and K. A. Müller. "Possible high T_c superconductivity in the Ba-La-Cu-O system". In: *Zeitschrift für Physik B Condensed Matter* 64.2 (June 1986), pp. 189–193. DOI: 10.1007/BF01303701.

[6] M. K. Wu et al. "Superconductivity at 93 K in a new mixed-phase Y-Ba-Cu-O compound system at ambient pressure". In: *Physical Review Letters* 58.9 (Mar. 1987), pp. 908–910. DOI: 10.1103/PhysRevLett.58.908.

[7] Hiroshi Maeda et al. "A New High-T_c Oxide Superconductor without a Rare Earth Element". In: *Japanese Journal of Applied Physics* 27.Part 2, No. 2 (Feb. 1988), pp. L209–L210. ISSN: 0021-4922. DOI: 10.1143/JJAP.27.L209.

[8] Yoichi Kamihara et al. "Iron-Based Layered Superconductor La[$O_{1-x}F_x$]FeAs (x = 0.05-0.12) with T_c = 26 K". In: *Journal of the American Chemical Society* 130.11 (Mar. 2008), pp. 3296–3297. ISSN: 0002-7863. DOI: 10.1021/ja800073m.

[9] A. P. Drozdov et al. "Conventional superconductivity at 203 kelvin at high pressures in the sulfur hydride system". In: *Nature* 525.7567 (2015), pp. 73–76. ISSN: 14764687. DOI: 10.1038/nature14964. arXiv: 1506.08190.

[10] B. Keimer et al. "From quantum matter to high-temperature superconductivity in copper oxides". In: *Nature* 518.7538 (2015), pp. 179–186. DOI: 10.1038/nature14165.

[11] Mark Buchanan. "Mind the pseudogap". In: *Nature* 409.6816 (Jan. 2001), pp. 8–11. ISSN: 0028-0836. DOI: 10.1038/35051238.

[12] G. R. Stewart. "Unconventional superconductivity". In: *Advances in Physics* 66.2 (Apr. 2017), pp. 75–196. DOI: 10.1080/00018732.2017.1331615. arXiv: 1302.3176.

[13] Patrick A. Lee, Naoto Nagaosa, and Xiao Gang Wen. "Doping a Mott insulator: Physics of high-temperature superconductivity". In: *Reviews of Modern Physics* 78.1 (2006). ISSN: 00346861. DOI: 10.1103/RevModPhys.78.17. arXiv: 0410445 [cond-mat].

[14] Y. J. Uemura et al. "Universal Correlations between T_c and n_s/m^* (Carrier Density over Effective Mass) in High-T_c Cuprate Superconductors". In: *Physical Review Letters* 62.19 (May 1989), pp. 2317–2320. DOI: 10.1103/PhysRevLett.62.2317.

[15] Guy Deutscher. "Coherence and single-particle excitations in the high-temperature superconductors". In: *Nature* 397.6718 (Feb. 1999), pp. 410–412. ISSN: 0028-0836. DOI: 10.1038/17075.

[16] John M. Tranquada. "Spins, stripes, and superconductivity in hole-doped cuprates". In: *AIP Conference Proceedings*. Vol. 1550. 2013, pp. 114–187. DOI: 10.1063/1.4818402. arXiv: 1305.4118.

[17] Sudip Chakravarty et al. "Hidden order in the cuprates". In: *Physical Review B* 63.9 (Jan. 2001), p. 094503. DOI: 10.1103/PhysRevB.63.094503.

[18] Debmalya Chakraborty, Corentin Morice, and Catherine Pépin. "Phase diagram of the underdoped cuprates at high magnetic field". In: *Physical Review B* 97.21 (2018), pp. 1–22. DOI: 10.1103/PhysRevB.97.214501. arXiv: 1802.10122.

[19] D.J. Scalapino. "The case for d_{x2-y2} pairing in the cuprate superconductors". In: *Physics Reports* 250.6 (Jan. 1995), pp. 329–365. DOI: 10.1016/0370-1573(94)00086-I.

[20] M. Magnuson et al. "Self-doping processes between planes and chains in the metal-to-superconductor transition of $YBa_2Cu_3O_{6.9}$". In: *Scientific Reports* 4 (2014), p. 7017. ISSN: 2045-2322. DOI: 10.1038/srep07017. arXiv: arXiv:1411.3301.

[21] Jun-ichi Shimoyama et al. “How to Optimize Critical Current Performance of RE123 Materials by Controlling Oxygen Content”. In: *MRS Proceedings* 689 (Jan. 2002), E8.18. DOI: 10.1557/PROC-689-E8.18.

[22] J. D. Jorgensen et al. “Structural properties of oxygen-deficient $YBa_2Cu_3O_{7-\delta}$”. In: *Physical Review B* 41.4 (1990), p. 1863. DOI: 10.1103/PhysRevB.41.1863.

[23] Joachim Maier. *Physical Chemistry of Ionic Materials*. Vol. 12. 8. Chichester, UK: John Wiley & Sons, Ltd, Apr. 2004. DOI: 10.1002/0470020229.

[24] S. Graser et al. “How grain boundaries limit supercurrents in high-temperature superconductors”. In: *Nature Physics* 6.8 (2010), pp. 609–614. ISSN: 17452473. DOI: 10.1038/nphys1687.

[25] H. Hilgenkamp and J. Mannhart. “Grain boundaries in high-T_c superconductors”. In: *Reviews of Modern Physics* 74.2 (2002), pp. 485–549. ISSN: 1539-0756. DOI: 10.1103/RevModPhys.74.485.

[26] Xavier Obradors et al. “Progress towards all-chemical superconducting $YBa_2Cu_3O_{7-\delta}$ coated conductors”. In: *Superconductor Science and Technology* 19.3 (2006). DOI: 10.1088/0953-2048/19/3/003.

[27] Michael Tinkham. *Introduction to Superconductivity*. 2nd ed. New York: McGraw-Hill, 1996.

[28] Charles P. Bean. “Magnetization of Hard Superconductors”. In: *Physical Review Letters* 8.6 (Mar. 1962), pp. 250–253. DOI: 10.1103/PhysRevLett.8.250.

[29] Charles P. Bean. “Magnetization of High-Field Superconductors”. In: *Reviews of Modern Physics* 36.1 (1964), pp. 31–39. DOI: 10.1103/RevModPhys.36.31.

[30] H. W. Weber and O. Hittmair. *Supraleitung*. München: Karl Thiemig Verlag, 1979. ISBN: 3-521-06113-2.

[31] Y. B. Kim, C. F. Hempstead, and A. R. Strnad. “Magnetization and Critical Supercurrents”. In: *Physical Review* 129.2 (Jan. 1963), pp. 528–535. ISSN: 0031-899X. DOI: 10.1103/PhysRev.129.528.

[32] Akihito Sawa. “Resistive switching in transition metal oxides”. In: *Materials Today* 11.6 (June 2008), pp. 28–36. ISSN: 13697021. DOI: 10.1016/S1369-7021(08)70119-6.

[33] Rainer Waser and Masakazu Aono. “Nanoionics-based resistive switching memories”. In: *Nature Materials* 6.11 (Nov. 2007), pp. 833–840. ISSN: 1476-1122. DOI: 10.1038/nmat2023.

[34] Rotraut Merkle and Joachim Maier. "How is oxygen incorporated into oxides? A comprehensive kinetic study of a simple solid-state reaction with $SrTiO_3$ as a model material". In: *Angewandte Chemie - International Edition* 47.21 (May 2008), pp. 3874–3894. ISSN: 14337851. DOI: 10.1002/anie.200700987.

[35] Peter Atkin and Julio Paula. *Physical chemistry*. 2006, p. 1072. ISBN: 978-0716787594. DOI: 10.1039/C1CS15191F. arXiv: arXiv:1011.1669v3.

[36] Rotraut Merkle and Joachim Maier. "Oxygen incorporation into Fe-doped $SrTiO_3$: Mechanistic interpretation of the surface reaction". In: *Physical Chemistry Chemical Physics* 4.17 (2002), pp. 4140–4148. DOI: 10.1039/b204032h.

[37] Stuart B. Adler. "Factors governing oxygen reduction in solid oxide fuel cell cathodes". In: *Chemical Reviews* 104.10 (2004), pp. 4791–4843. ISSN: 00092665. DOI: 10.1021/cr020724o.

[38] Joachim Maier. "On the correlation of macroscopic and microscopic rate constants in solid state chemistry". In: *Solid State Ionics* 112.3-4 (1998), pp. 197–228. ISSN: 01672738. DOI: 10.1016/S0167-2738(98)00152-0.

[39] Majid Mosleh, Martin Søgaard, and Peter Vang Hendriksen. "Kinetics and Mechanisms of Oxygen Surface Exchange on $La_{0.6}Sr_{0.4}FeO_{3-\delta}$ Thin Films". In: *Journal of The Electrochemical Society* 156.4 (2009), B441. DOI: 10.1149/1.3062941.

[40] Joachim Maier and Harry L. Tuller. "Defect chemistry and transport in $YBa_2Cu_3O_{6+x}$". In: *Phys. Rev. B* 47.13 (1993), p. 8105. DOI: 10.1103/PhysRevB.47.8105.

[41] M. Leonhardt et al. "Surface Kinetics of Oxygen Incorporation into $SrTiO_3$". In: *Journal of The Electrochemical Society* 149.2 (2002), J19. DOI: 10.1149/1.1430723.

[42] Rotraut Merkle and Joachim Maier. "The significance of defect chemistry for the rate of gas-solid reactions: Three examples". In: *Topics in Catalysis* 38.1-3 (2006), pp. 141–145. ISSN: 10225528. DOI: 10.1007/s11244-006-0079-5.

[43] W. Preis, M. Holzinger, and Werner Sitte. "Application of the van der Pauw method to conductivity relaxation experiments on $YBa_2Cu_3O_{6+\delta}$". In: *Monatshefte fur Chemie* 132.4 (2001), pp. 499–508. ISSN: 00269247. DOI: 10.1007/s007060170112.

[44] Joachim Maier and Gösta Pfundtner. "Defect chemistry of the high-T_c superconductors". In: *Advanced Materials* 3.6 (June 1991), pp. 292–297. DOI: 10.1002/adma.19910030605.

[45] G. M. Choi, Harry L. Tuller, and M-J. Tsai. "Defects and Transport in $YBa_2Cu_3O_{7-x}$". In: *Non-Stoichiometric Compounds*. Dordrecht: Springer Netherlands, 1989, pp. 451–470. DOI: 10.1007/978-94-009-0943-4_31.

[46] Hans Lüth. *Solid Surfaces, Interfaces and Thin Films*. Vol. 171. Graduate Texts in Physics 9. Cham: Springer International Publishing, 2015, p. 333. DOI: 10.1007/978-3-319-10756-1. arXiv: arXiv:1011.1669v3.

[47] M I Temkin. "Adsorption equilibrium and the kinetics of processes on nonhomogeneous surfaces and in the interaction between adsorbed molecules". In: *Zh. Fiz. Chim.* 15 (1941), pp. 296–332. URL: https://ci.nii.ac.jp/naid/10025397715/en/.

[48] M. Jaroniec. "Adsorption on heterogeneous surfaces: The exponential equation for the overall adsorption isotherm". In: *Surface Science* 50.2 (June 1975), pp. 553–564. DOI: 10.1016/0039-6028(75)90044-8.

[49] J O M Bockris, A K N Reddy, and M E Gamboa-Aldeco. *Modern Electrochemistry 2A: Fundamentals of Electrodics*. Modern electrochemistry. Springer US, 2001. ISBN: 9780306461675. URL: https://books.google.es/books?id=utDyTYpimkUC.

[50] Jürgen Fleig, Rotraut Merkle, and Joachim Maier. "The p(O2) dependence of oxygen surface coverage and exchange current density of mixed conducting oxide electrodes: model considerations". In: *Physical Chemistry Chemical Physics* 9.21 (2007), p. 2713. DOI: 10.1039/b618765j.

[51] H. Ibach et al. "The adsorption of oxygen on silicon (111) surfaces. I". In: *Surface Science* 38.2 (1973), pp. 433–454. ISSN: 00396028. DOI: 10.1016/0039-6028(73)90171-4.

[52] Wonyoung Lee et al. "Oxygen Surface Exchange at Grain Boundaries of Oxide Ion Conductors". In: *Advanced Functional Materials* 22.5 (2012), pp. 965–971. DOI: 10.1002/adfm.201101996. arXiv: 0706.1062v1.

[53] Albert Einstein. "Über die von der molekularkinetischen Theorie der Wärme geforderte Bewegung von in ruhenden Flüssigkeiten suspendierten Teilchen". In: *Annalen der Physik* 322.8 (1905), pp. 549–560. DOI: 10.1002/andp.19053220806.

[54] Helmut Mehrer. *Diffusion in Solids*. Vol. 155. Springer Series in Solid-State Sciences. Berlin, Heidelberg: Springer Berlin Heidelberg, 2007. ISBN: 978-3-540-71486-6. DOI: 10.1007/978-3-540-71488-0.

[55] J. C. Fisher. "Calculation of diffusion penetration curves for surface and grain boundary diffusion". In: *Journal of Applied Physics* 22.1 (1951), pp. 74–77. ISSN: 00218979. DOI: 10.1063/1.1699825.

[56] Y. Mishin and W. Gust. "Grain boundary diffusion metals versus non-stoichiometric compounds". In: *Ionics* 7.4-6 (July 2001), pp. 247–263. DOI: 10.1007/BF02373558.

[57] Edvinas Navickas et al. "Fast oxygen exchange and diffusion kinetics of grain boundaries in Sr-doped $LaMnO_3$ thin films". In: *Physical Chemistry Chemical Physics* 17.12 (2015), pp. 7659–7669. DOI: 10.1039/C4CP05421K.

[58] I.M. Ritchie and G.L. Hunt. "The kinetics and pressure dependence of surface controlled metal oxidation reactions". In: *Surface Science* 15.3 (July 1969), pp. 524–534. DOI: 10.1016/0039-6028(69)90139-3.

[59] John A. Kilner. "Isotopic exchange in mixed and ionically conducting oxides". In: *Ionic and Mixed Conducting Ceramics (Second International Symposium)*. Ed. by T. A. Ramanarayanan, W. L. Worrell, and Harry L. Tuller. The Electrochemical Society, 1994, p. 174.

[60] J C Jaeger and Martha Clarke. "LVI. Numerical results for some problems on conduction of heat in slabs with various surface conditions". In: *The London, Edinburgh, and Dublin Philosophical Magazine and Journal of Science* 38.282 (1947), pp. 504–515. ISSN: 1941-5982. DOI: 10.1080/14786444708521623.

[61] John Crank. *The Mathematics of Diffusion*. 2. Edition. Oxford: Clarendon Press, 1979. ISBN: 9780198534112.

[62] H.S. Carslaw and J C Jaeger. *Conduction of Heat in Solids*. 2. Edition. Oxford: Clarendon Press, 1959.

[63] Pablo Cayado et al. "Untangling surface oxygen exchange effects in $YBa_2Cu_3O_{6+x}$". In: *Physical Chemistry Chemical Physics* 3.19 (2017), pp. 14129–14140. DOI: 10.1039/C7CP01855J.

[64] John R. LaGraff and David A Payne. "Chemical diffusion of oxygen in single-crystal and polycrystalline $YBa_2Cu_3O_{6+x}$ determined by electrical-resistance measurements". In: *Physical Review B* 47.6 (Feb. 1993), pp. 3380–3390. DOI: 10.1103/PhysRevB.47.3380.

[65] D. Dimos, P. Chaudhari, and J. Mannhart. "Superconducting transport properties of grain boundaries in $YBa_2Cu_3O_7$ bicrystals". In: *Physical Review B* 41.7 (Mar. 1990), pp. 4038–4049. DOI: 10.1103/PhysRevB.41.4038.

[66] Xavier Obradors et al. "Growth, nanostructure and vortex pinning in superconducting $YBa_2Cu_3O_7$ thin films based on trifluoroacetate solutions". In: *Superconductor Science and Technology* 25.12 (2012), p. 123001. DOI: 10.1088/0953-2048/25/12/123001.

[67] R. Wördenweber. *High-Temperature Superconductors*. Woodhead Publishing Limited, 2011, 3–38e. ISBN: 9781845695781. DOI: 10.1533/9780857091031.1.3.

[68] L J van der Pauw. "A method of measuring the resistivity and hall coefficient on lamallae of arbitrary shape". In: *Philips Tech. Rev.* 20.8 (1958), p. 220.

[69] L J van der Pauw. "A method of measuring specific resistivity and Hall effect of discs of arbitrary shape". In: *Philips Res. Repts.* 13.1 (1958), p. 1.

[70] E. H. Hall. "On a New Action of the Magnet on Electric Currents". In: *American Journal of Mathematics* 2 (1879), p. 287.

[71] J B Nelson and D P Riley. "An experimental investigation of extrapolation methods in the derivation of accurate unit-cell dimensions of crystals". In: *Proceedings of the Physical Society* 57.3 (1945), pp. 160–177. ISSN: 09595309. DOI: 10.1088/0959-5309/57/3/302.

[72] G. K. Williamson and W. H. Hall. "X-ray Line Broadening from Filed Aluminium and Wolfram". In: *Acta Metallurgica* 1 (1953), pp. 22–31. DOI: 10.1016/0001-6160(53)90006-6.

[73] A. J. Jacobson et al. "Synthesis and properties of nonstoichiometric samples of $YBa_2Cu_3O_{7-x}$; $0.04 \leq x \leq 1.00$". In: *Physical Review B* 39.1 (Jan. 1989), pp. 254–258. DOI: 10.1103/PhysRevB.39.254.

[74] Kazimierz Conder. "Oxygen diffusion in the superconductors of the YBaCuO family: isotope exchange measurements and models". In: *Materials Science and Engineering: R: Reports* R32.2-3 (Feb. 2001), pp. 41–102. DOI: 10.1016/S0927-796X(00)00030-9.

[75] Brian C. H. Steele and Angelika Heinzel. "Materials for fuel-cell technologies". In: *Nature* 414 (Nov. 2001), pp. 345–352. DOI: 10.1038/35104620.

[76] Albert Tarancón et al. "Advances in layered oxide cathodes for intermediate temperature solid oxide fuel cells". In: *Journal of Materials Chemistry* 20.19 (2010), pp. 3799–3813. DOI: 10.1039/b922430k.

[77] Allan J. Jacobson. "Materials for Solid Oxide Fuel Cells". In: *Chemistry of Materials* 22.3 (2010), pp. 660–674. DOI: 10.1021/cm902640j.

[78] John A. Kilner and Mónica Burriel. "Materials for Intermediate-Temperature Solid-Oxide Fuel Cells". In: *Annual Review of Materials Research* 44.1 (2014), pp. 365–393. DOI: 10.1146/annurev-matsci-070813-113426. arXiv: arXiv:1011.1669v3.

[79] John M. Tranquada et al. "Mixed valency, hole concentration, and T_c in $YBa_2Cu_3O_{6+x}$". In: *Physical Review B* 38.13 (1988), pp. 8893–8899. ISSN: 0163-1829. DOI: 10.1103/PhysRevB.38.8893.

[80] Terrence B Lindemer et al. "Experimental and Thermodynamic Study of Nonstoichiometry in $YBa_2Cu_3O_{7-x}$". In: *Journal of the American Ceramic Society* 72.10 (Oct. 1989), pp. 1775–1788. DOI: 10.1111/j.1151-2916.1989.tb05978.x.

[81] D. de Fontaine, G. Ceder, and M. Asta. "Low-temperature long-range oxygen order in $YBa_2Cu_3O_z$". In: *Nature* 343.6258 (Feb. 1990), pp. 544–546. DOI: 10.1038/343544a0.

[82] Ling Chen, C. L. Chen, and A. J. Jacobson. "Electrical Conductivity Relaxation Studies of Oxygen Transport in Epitaxial $YBa_2Cu_3O_{7-\delta}$ Thin Films". In: *IEEE Transactions on Appiled Superconductivity* 13.2 (June 2003), pp. 2882–2885. ISSN: 1051-8223. DOI: 10.1109/TASC.2003.812032.

[83] G. Kim et al. "Measurement of oxygen transport kinetics in epitaxial $La_2NiO_{4+\delta}$ thin films by electrical conductivity relaxation". In: *Solid State Ionics* 177.17-18 (July 2006), pp. 1461–1467. DOI: 10.1016/j.ssi.2006.07.013.

[84] Pablo Cayado et al. "Large critical current densities and pinning forces in CSD-grown superconducting". In: (2017).

[85] S. Kittelberger, O. M. Stoll, and R P Huebener. "Oxygen diffusion in thin $YBa_2Cu_3O_{7-\delta}$ films studied from isothermal electric resistivity measurements". In: *Superconductor Science and Technology* 11.8 (Aug. 1998), pp. 744–750. DOI: 10.1088/0953-2048/11/8/006.

[86] H. Zhang, X. Yao, and X. H. Zeng. "Oxygen in-diffusion in LPE thick films of YBCO by electrical resistance relaxation". In: *Physica Status Solidi (A) Applied Research* 201.10 (2004), pp. 2305–2311. ISSN: 00318965. DOI: 10.1002/pssa.200306838.

[87] Christian Krauns and Hans-ulrich Krebs. "Comparison of the oxygen diffusion in $Y_1Ba_2Cu_3O_y$ bulk materials and thin films". In: *Zeitschrift für Physik B Condensed Matter* 92.1 (Mar. 1993), pp. 43–46. DOI: 10.1007/BF01309165.

[88] Chung-Liang Chang, Tai-Cheng Lee, and Ta-Jen Huang. "Oxygen reduction mechanism and performance of $Y_1Ba_2Cu_3O_{7-\delta}$ as a cathode material in a high-temperature solid-oxide fuel cell". In: *Journal of Solid State Electrochemistry* 2.5 (Aug. 1998), pp. 291–298. DOI: 10.1007/s100080050103.

[89] Alexander K. Opitz et al. "Investigation of the oxygen exchange mechanism on Ptyttria stabilized zirconia at intermediate temperatures: Surface path versus bulk path". In: *Electrochimica Acta* 56.27 (2011), pp. 9727–9740. DOI: 10.1016/j.electacta.2011.07.112.

[90] G.I. Golodets. "Chapter VII: The Dissociation of Molecular Oxygen, The Recombination of Oxygen Atoms and Isotopic Exchange with Molecular Oxygen". In: *Studies in Surface Science and Catalysis*. Ed. by G I Golodets. Vol. 15. Studies in Surface Science and Catalysis C. Elsevier, 1983, pp. 180–199. DOI: 10.1016/S0167-2991(08)64832-6.

[91] L. Chen et al. "CO adsorption and hydrogenation on crystalline $YBa_2Cu_3O_x$ thin films". In: *Berichte der Bunsengesellschaft für physikalische Chemie* 102.1 (Jan. 1998), pp. 103–110. DOI: 10.1002/bbpc.19981020113.

[92] Raghu N. Bhattacharya, Yunfei Qiao, and Venkat Selvamanickam. "Electrodeposited Cu-Stabilization Layer for High-Temperature Superconducting Coated Conductors". In: *Journal of Superconductivity and Novel Magnetism* 24.1-2 (Jan. 2011), pp. 1021–1026. DOI: 10.1007/s10948-010-0883-9.

[93] M D Vázquez-Navarro, A Kursumovic, and J E Evetts. "Study and modelling of oxygen diffusion in $YBa_2Cu_3O_{7-\delta}$ under isothermal conditions". In: *Superconductor Science and Technology* 12.12 (Dec. 1999), pp. 1117–1122. DOI: 10.1088/0953-2048/12/12/320.

[94] Robert J. Scheuplein. "Analysis of Permeability Data for the Case of Parallel Diffusion Pathways". In: *Biophysical Journal* 6.1 (Jan. 1966), pp. 1–17. DOI: 10.1016/S0006-3495(66)86636-5.

[95] R. A. Outlaw et al. "Oxygen transport through high-purity, large-grain Ag". In: *Journal of Materials Research* 3.06 (Dec. 1988), pp. 1378–1384. ISSN: 0884-2914. DOI: 10.1557/JMR.1988.1378.

[96] J.K K. Baird, T.R R. King, and C. Stein. "Diffusion of oxygen in silver". In: *Journal of Physics and Chemistry of Solids* 60.7 (July 1999), pp. 891–894. DOI: 10.1016/S0022-3697(99)00019-0.

[97] Stephan Steinhauer. "Gas Sensing Properties of Metal Oxide Nanowires and their CMOS Integration". PhD thesis. Technische Universität Wien, 2014.

[98] N. Barsan et al. "Modeling of sensing and transduction for p-type semiconducting metal oxide based gas sensors". In: *Journal of Electroceramics* 25.1 (2010), pp. 11–19. ISSN: 13853449. DOI: 10.1007/s10832-009-9583-x.

[99] Roberto Moreno et al. "Chemical Strain Kinetics Induced by Oxygen Surface Exchange in Epitaxial Films Explored by Time-Resolved X-ray Diffraction". In: *Chemistry of Materials* 25.18 (Sept. 2013), pp. 3640–3647. ISSN: 0897-4756. DOI: 10.1021/cm401714d.

[100] B. C. Chakoumakos et al. "Thermal expansion of $LaAlO_3$ and (La,Sr)(Al,Ta)O_3, substrate materials for superconducting thin-film device applications". In: *Journal of Applied Physics* 83.4 (1998), pp. 1979–1982. DOI: 10.1063/1.366925.

[101] Junichi Kawashima, Yasuji Yamada, and Izumi Hirabayashi. "Critical thickness and effective thermal expansion coefficient of YBCO crystalline film". In: *Physica C: Superconductivity* 306.1-2 (Sept. 1998), pp. 114–118. DOI: 10.1016/S0921-4534(98)00350-5.

[102] Yasuji Yamada et al. "Evaluation of Thermal Expansion Coefficient of Twinned $YBa_2Cu_3O_{7-\delta}$ Film for Prediction of Crack Formation on Various Substrates". In: *Japanese Journal of Applied Physics* 39.Part 1, No. 3A (Mar. 2000), pp. 1111–1115. DOI: 10.1143/JJAP.39.1111.

[103] M Zeisberger et al. "Measurement of the thermal expansion of melt-textured YBCO using optical fibre grating sensors". In: *Superconductor Science and Technology* 18.2 (Feb. 2005), S202–S205. DOI: 10.1088/0953-2048/18/2/041.

[104] L. Li et al. "Diffusion model of oxygen in *c*-axis oriented $YBa_2Cu_3O_{7-\delta}$ films". In: *Physica C: Superconductivity and its Applications* 544 (2018), pp. 1–5. ISSN: 09214534. DOI: 10.1016/j.physc.2017.10.016.

[105] Riccardo Arpaia et al. "Probing the phase diagram of cuprates with $YBa_2Cu_3O_{7-\delta}$ thin films and nanowires". In: *Physical Review Materials* 2.2 (Feb. 2018), p. 024804. DOI: 10.1103/PhysRevMaterials.2.024804. arXiv: 1712.02008.

[106] Ruixing Liang, D. A. Bonn, and W. N. Hardy. "Evaluation of CuO_2 plane hole doping in $YBa_2Cu_3O_{6+x}$ single crystals". In: *Physical Review B - Condensed Matter and Materials Physics* 73.18 (2006), pp. 1–4. ISSN: 10980121. DOI: 10.1103/PhysRevB.73.180505. arXiv: 0510674 [cond-mat].

[107] Mónica Burriel et al. "Enhancing Total Conductivity of $La_2NiO_{4+\delta}$ Epitaxial Thin Films by Reducing Thickness". In: *The Journal of Physical Chemistry C* 112.29 (July 2008), pp. 10982–10987. DOI: 10.1021/jp7101622.

[108] Wen-jye Jang et al. "Change in Crystal Structure and Electron Density by Introducing Oxygen in $YBa_2Cu_3O_y$ Single Crystal". In: *Journal of Solid State Chemistry* 130.1 (Apr. 1997), pp. 42–47. DOI: 10.1006/jssc.1997.7270.

[109] Fausto Cargnoni and Marco Scavini. "Direct-space analysis of the electronic structure of the $YBa_2Cu_3O_6$ and $YBa_2Cu_3O_7$ crystals". In: *Canadian Journal of Chemistry* 80.3 (Mar. 2002), pp. 235–244. DOI: 10.1139/v02-014.

[110] M. M. Kuklja et al. "Combined theoretical and experimental analysis of processes determining cathode performance in solid oxide fuel cells". In: *Physical Chemistry Chemical Physics* 15.15 (2013), pp. 5443–5471. DOI: 10.1039/c3cp44363a.

[111] I Riess. "Mixed ionic-electronic conductors-material properties and applications". In: *Solid State Ionics* 157.1-4 (Feb. 2003), pp. 1–17. DOI: 10.1016/S0167-2738(02)00182-0.

[112] S. H. Lee et al. "Oxygen diffusion in epitaxial $YBa_2Cu_3O_{7-x}$ thin films". In: *Physical Review B* 46.14 (Oct. 1992), pp. 9142–9146. DOI: 10.1103/PhysRevB.46.9142.

[113] K N Tu et al. "Diffusion of oxygen in superconducting $YBa_2Cu_3O_{7-\delta}$ ceramic oxides". In: *Physical Review B* 39.1 (Jan. 1989), pp. 304–314. ISSN: 0163-1829. DOI: 10.1103/PhysRevB.39.304.

[114] Marcel Ausloos and Andrzej Pękalski. "Oxygen diffusion in 123-YBCO". In: *Diffusion Processes: Experiment, Theory, Simulations*. Berlin/Heidelberg: Springer-Verlag, 1994, pp. 221–233. DOI: 10.1007/BFb0031129.

[115] Adolph Fick. "On liquid diffusion". In: *Journal of Membrane Science* 100.1 (Mar. 1995), pp. 33–38. ISSN: 03767388. DOI: 10.1016/0376-7388(94)00230-V.

[116] Kenneth A. Connors. *Chemical Kinetics: The Study of Reaction Rates in Solution*. 1st Editio. Wiley-VCH, 1990, p. 496. ISBN: 978-0-471-72020-1.

[117] David J.G. Ives. *Chemical Thermodynamics*. London: Macdonald and Co., Ltd, 1971. ISBN: 978-0356037363.

[118] Joachim Maier et al. "Defect-chemical Investigations of Defined $YBa_2Cu_3O_x$-Superconductors". In: *Berichte der Bunsengesellschaft für physikalische Chemie* 93.11 (1989), pp. 1350–1356. DOI: 10.1002/bbpc.19890931143.

[119] S. J. Rothman, J. L. Routbort, and J E Baker. "Tracer diffusion of oxygen in $YBa_2Cu_3O_{7-\delta}$". In: *Physical Review B* 40.13 (1989), pp. 8852–8861.

[120] Ayako Tokiwa et al. "Crystal Structure and Superconductivity Controlled by Cation Substitution and Oxygen Annealing in $Y_{1-x}Ca_xBa_2Cu_3O_y$ and $YBa_{2-x}La_xCu_3O_y$". In: *Japanese Journal of Applied Physics* 27.Part 2, No. 6 (June 1988), pp. L1009–L1012. DOI: 10.1143/JJAP.27.L1009.

[121] Dong Han Ha, Sunye Byon, and Kyu Won Lee. "On the role of apical oxygen in the charge transfer of YBCO superconductors". In: *Physica C: Superconductivity* 340.2-3 (Dec. 2000), pp. 243–250. DOI: 10.1016/S0921-4534(00)01502-1.

[122] N. P. Liyanawaduge et al. "The Role of Ca in Superconducting and Magnetic Properties of $Y_{1-x}Ca_xBa_2Cu_3O_{7-\delta}$ (x=0.0-0.30)". In: *Journal of Superconductivity and Novel Magnetism* 25.1 (Jan. 2012), pp. 31–37. DOI: 10.1007/s10948-011-1203-8.

[123] R. G. Buckley et al. "Ca- and La-substitution in $YBa_2Cu_3O_{7-\delta}$, $Y_2Ba_4Cu_7O_{15-\delta}$ and $YBa_2Cu_4O_8$". In: *Physica C: Superconductivity and its applications* 174.4-6 (1991), pp. 383–393. DOI: 10.1016/0921-4534(91)91574-N.

[124] Paolo Mele et al. "High pinning performance of $YBa_2Cu_3O_{7-x}$ films added with Y2O3nanoparticulate defects". In: *Superconductor Science and Technology* 28.2 (2015). DOI: 10.1088/0953-2048/28/2/024002.

[125] A. Llordés et al. "Nanoscale strain-induced pair suppression as a vortex-pinning mechanism in high-temperature superconductors". In: *Nature Materials* 11.4 (Apr. 2012), pp. 329–336. DOI: 10.1038/nmat3247.

[126] S.K. Bandyopadhyay et al. "A study of superconducting $(Y_{1-x}Ca_x)Ba_2Cu_3O_y$". In: *Physics Letters A* 226.February (1997), pp. 237–243.

[127] B. Fisher et al. "Effects of substituting calcium for yttrium on the properties of $YBa_2Cu_3O_{7-\delta}$". In: *Physical Review B* 47.10 (Mar. 1993), pp. 6054–6059. DOI: 10.1103/PhysRevB.47.6054. arXiv: 0401584 [cond-mat].

[128] Kaname Matsumoto and Paolo Mele. "Artificial pinning center technology to enhance vortex pinning in YBCO coated conductors". In: *Superconductor Science and Technology* 23.1 (2010). ISSN: 09532048. DOI: 10.1088/0953-2048/23/1/014001.

[129] Paolo Mele et al. "Ultra-high flux pinning properties of $BaMO_3$-doped $YBa_2Cu_3O_{7-x}$ thin films (M = Zr, Sn)". In: *Superconductor Science and Technology* 21.3 (2008). ISSN: 09532048. DOI: 10.1088/0953-2048/21/3/032002.

[130] M Coll et al. "Solution-derived $YBa_2Cu_3O_7$ nanocomposite films with a Ba_2YTaO_6 secondary phase for improved superconducting properties". In: *Superconductor Science and Technology* 26 (2013), p. 015001. DOI: 10.1088/0953-2048/26/1/015001.

[131] Xavier Obradors and Teresa Puig. "Coated conductors for power applications: materials challenges". In: *Superconductor Science and Technology* 27.27 (2014), p. 044003. DOI: 10.1088/0953-2048/27/4/044003.

[132] M Coll et al. "Size-controlled spontaneously segregated Ba_2YTaO_6 nanoparticles in $YBa_2Cu_3O_7$ nanocomposites obtained by chemical solution deposition". In: *Superconductor Science and Technology* 27 (2014), p. 044008. DOI: 10.1088/0953-2048/27/4/044008.

[133] Aixia Xu et al. "Role of weak uncorrelated pinning introduced by $BaZrO_3$ nanorods at low-temperature in (Y,Gd)$Ba_2Cu_3O_x$ thin films". In: *Physical Review B* 86.11 (Sept. 2012), p. 115416. DOI: 10.1103/PhysRevB.86.115416.

[134] Pablo Cayado. "Multifunctional nanostructured superconductors by chemical routes: towards high current conductors". PhD thesis. Universitat Autònoma de Barcelona, 2016.

[135] Ziliang Li. "Growth and Characterisation of Nanocomposite $YBa_2Cu_3O_{7-\delta}$ - $BaMO_3$ (M=Zr, Hf) Thin Films from Collodial Solutions". PhD thesis. Universitat Autònoma de Barcelona, 2018, p. 176.

[136] Pablo Cayado et al. "Epitaxial $YBa_2Cu_3O_{7-x}$ nanocomposite thin films from colloidal solutions". In: *Superconductor Science and Technology* 28.12 (Dec. 2015), p. 124007. DOI: 10.1088/0953-2048/28/12/124007. arXiv: arXiv:1206.2053v1.

[137] Xavier Obradors et al. "Epitaxial $YBa_2Cu_3O_{7-x}$ nanocomposite films and coated conductors from $BaMO_3$ (M = Zr, Hf) colloidal solutions". In: *Superconductor Science and Technology* 31.4 (Apr. 2018), p. 044001. DOI: 10.1088/1361-6668/aaaad7.

[138] S. J. Rothman et al. "Anisotropy of oxygen tracer diffusion in single-crystal $YBa_2Cu_3O_{7-\delta}$". In: *Phys. Rev. B* 44.5 (1991), pp. 2326–2333.

[139] J. B. Goodenough. "Electronic and ionic transport properties and other physical aspects of perovskites". In: *Reports on Progress in Physics* 67.11 (Nov. 2004), pp. 1915–1993. DOI: 10.1088/0034-4885/67/11/R01.

[140] J.-P. Locquet et al. "Doubling the critical temperature of $La_{1.9}Sr_{0.1}CuO_4$ using epitaxial strain". In: *Nature* 394.6692 (July 1998), pp. 453–456. DOI: 10.1038/28810.

[141] H. Sato et al. "$La_{2-x}Sr_xCuO_y$ epitaxial thin films (x=0 to 2): Structure, strain, and superconductivity". In: *Physical Review B* 61.18 (2000), pp. 12447–12456. DOI: 10.1103/PhysRevB.61.12447.

[142] I. Božović et al. "Epitaxial Strain and Superconductivity in $La_{2-x}Sr_xCuO_4$ Thin Films". In: *Physical Review Letters* 89.10 (Aug. 2002), p. 107001. DOI: 10.1103/PhysRevLett.89.107001.

[143] Alexander Chroneos et al. "Oxygen diffusion in solid oxide fuel cell cathode and electrolyte materials: mechanistic insights from atomistic simulations". In: *Energy & Environmental Science* 4.8 (2011), p. 2774. DOI: 10.1039/c0ee00717j.

[144] Bilge Yildiz. "Stretching the energy landscape of oxides - Effects on electrocatalysis and diffusion". In: *MRS Bulletin* 39.2 (2014), pp. 147–156. ISSN: 08837694. DOI: 10.1557/mrs.2014.8.

[145] Tricia L. Meyer et al. "Strain control of oxygen kinetics in the Ruddlesden-Popper oxide $La_{1.85}Sr_{0.15}CuO_4$". In: *Nature Communications* 9.1 (2018), pp. 1–7. DOI: 10.1038/s41467-017-02568-z.

[146] Ulrich Aschauer et al. "Strain-controlled oxygen vacancy formation and ordering in $CaMnO_3$". In: *Physical Review B - Condensed Matter and Materials Physics* 88.5 (2013), pp. 1–7. ISSN: 10980121. DOI: 10.1103/PhysRevB.88.054111. arXiv: 1303.4749.

[147] Jonathan R. Petrie et al. "Enhancing Perovskite Electrocatalysis through Strain Tuning of the Oxygen Deficiency". In: *Journal of the American Chemical Society* 138.23 (June 2016), pp. 7252–7255. DOI: 10.1021/jacs.6b03520.

[148] Tam Mayeshiba and Dane Morgan. "Strain effects on oxygen vacancy formation energy in perovskites". In: *Solid State Ionics* 311.October (Nov. 2017), pp. 105–117. DOI: 10.1016/j.ssi.2017.09.021.

[149] Q. Yang et al. "Strain effects on formation and migration energies of oxygen vacancy in perovskite ferroelectrics: A first-principles study". In: *Journal of Applied Physics* 113.18 (May 2013), p. 184110. DOI: 10.1063/1.4804941.

[150] Hans J Scheel, M Berkowski, and B Chabot. "Substrates for high - temperature superconductors". In: *Physica C: Superconductivity and its applications* 185-189 (1991), pp. 2095–2096. ISSN: 09214534. DOI: 10.1016/0921-4534(91)91172-Z.

[151] J. J. Roa et al. "Nanohardness and Young's modulus of YBCO samples textured by the Bridgman technique". In: 18.38 (2007), p. 385701. DOI: 10.1088/0957-4484/18/38/385701.

[152] L. D. Landau et al. *Theory of Elasticity*. 3. ed., re. Boston, MA: Oxford, Pergamon Press, Butterworth-Heinemann, 2012, p. 195. ISBN: 9780750626330. URL: https://www.sciencedirect.com/book/9780080570693/theory-of-elasticity.

[153] H. Y. Zhai and W. K. Chu. "Effect of interfacial strain on critical temperature of $YBa_2Cu_3O_{7-\delta}$ thin films". In: *Applied Physics Letters* 76.23 (June 2000), pp. 3469–3471. DOI: 10.1063/1.126680.

[154] K Hauser et al. "Oxygen mobility and charge transport in $YBa_2Cu_3O_{7-\delta}$". In: *Journal of Low Temperature Physics* 105.5-6 (Dec. 1996), pp. 1409–1414. DOI: 10.1007/BF00753897.

[155] O.B. Anikeeva, A.I. Romanenko, and L.P. Kozeeva. "Effect of Oxygen Redistribution on the Normal and Superconducting Properties of Yttrium High Temperature Superconductors". In: *Journal of Structural Chemistry* 44.2 (2003), pp. 227–230. DOI: 10.1023/A:1025546707371.

[156] Lu Yan and Paul A. Salvador. "Substrate and Thickness Effects on the Oxygen Surface Exchange of $La_{0.7}Sr_{0.3}MnO_3$ Thin Films". In: *ACS Applied Materials and Interfaces* 4.5 (2012), pp. 2541–2550. DOI: 10.1021/am300194n.

[157] César Fidel Sánchez Valdés. "Crecimiento epitaxial de películas delgadas de $YBa_2Cu_3O_{7-\delta}$ mediante soluciones químicas: análisis in-situ de la nucleación, el crecimiento y la oxigenación". PhD thesis. Universitat Autònoma de Barcelona, 2013.

[158] Victor Rouco et al. "Role of twin boundaries on vortex pinning of CSD YBCO nanocomposites". In: *Superconductor Science and Technology* 27.12 (2014). DOI: 10.1088/0953-2048/27/12/125009.

[159] Sung Hun Wee et al. "Formation of stacking faults and their correlation with flux pinning and critical current density in Sm-doped $YBa_2Cu_3O_{7-\delta}$ films". In: *Physical Review B - Condensed Matter and Materials Physics* 83.22 (2011), pp. 1–6. DOI: 10.1103/PhysRevB.83.224520.

[160] J. Gutiérrez et al. "The role of stacking faults in the critical current density of MOD films through a thickness dependence study". In: *Superconductor Science and Technology* 22.1 (Jan. 2009), p. 015022. DOI: 10.1088/0953-2048/22/1/015022.

[161] P. Marsh et al. "Crystal structure of the 80 K superconductor $YBa_2Cu_4O_8$". In: *Nature* 334.6178 (July 1988), pp. 141–143. DOI: 10.1038/334141a0.

[162] H. A. Ludwig, W. H. Fietz, and H. Wühl. "Calculation of the structural parameters of $YBa_2Cu_3O_{7-\delta}$ and $YBa_2Cu_4O_8$ under pressure". In: *Physica C: Superconductivity and its applications* 197.1-2 (July 1992), pp. 113–122. DOI: 10.1016/0921-4534(92)90244-7.

[163] Eliot D. Specht et al. "Stacking faults in $YBa_2Cu_3O_{7-x}$: Measurement using x-ray diffraction and effects on critical current". In: *Applied Physics Letters* 89.16 (2006), pp. 87–90. DOI: 10.1063/1.2364185.

[164] A. H. Puichaud, S. C. Wimbush, and R. Knibbe. "Enhanced low-temperature critical current by reduction of stacking faults in REBCO coated conductors". In: *Superconductor Science and Technology* 30.7 (2017). DOI: 10.1088/1361-6668/aa6ce8.

[165] Sterling Hendricks and Edward Teller. "X-ray interference in partially ordered layer lattices". In: *The Journal of Chemical Physics* 10.3 (1942), pp. 147–167. DOI: 10.1063/1.1723678.

[166] Jaume Gazquez et al. "Emerging diluted ferromagnetism in high-T_c superconductors driven by point defect clusters". In: *Advanced Science* 3.6 (2015), pp. 1–8. DOI: 10.1002/advs.201500295.

[167] Bernat Mundet. "Atomic-scale characterization of structural distortions in perovskite oxide thin films". PhD thesis. Universitat Autònoma de Barcelona, 2018.

[168] Yimei Zhu et al. "Variable nature of twin boundaries in $YBa_2Cu_3O_{7-\delta}$ and its alloys". In: *Physical Review B* 44.6 (1991), pp. 2871–2874. ISSN: 01631829. DOI: 10.1103/PhysRevB.44.2871.

[169] Jeanne Ayache. "Grain boundaries in high temperature superconducting ceramics". In: *Philosophical Magazine* 86.15 (May 2006), pp. 2193–2239. DOI: 10.1080/14786430600640494.

[170] Yu I Boiko et al. "Some peculiarities of labile oxygen kinetics in underdoped single crystals of $YBa_2Cu_3O_{7-x}$". In: *Low Temperature Physics* 346.4 (Apr. 2018), pp. 2–5. DOI: 10.1063/1.5030463.

[171] Ruslan V. Vovk, Nikolaj R. Vovk, and Oleksandr V. Dobrovolskiy. "Effect of Structural Relaxation on the In-Plane Electrical Resistance of Oxygen-Underdoped $ReBa_2Cu_3O_{7-\delta}$ (Re = Y, Ho) Single Crystals". In: *Journal of Low Temperature Physics* 175.3-4 (2014), pp. 614–630. DOI: 10.1007/s10909-014-1121-9.

[172] A. Egger et al. "Long-Term Oxygen Exchange Kinetics of $Nd_2NiO_{4+\delta}$ in H_2O- and CO_2-Containing Atmospheres". In: *Journal of The Electrochemical Society* 157.11 (2010), B1537. DOI: 10.1149/1.3481420.

[173] Yan Chen et al. "Segregated Chemistry and Structure on (001) and (100) Surfaces of $(La_{1-x}Sr_x)_2CoO_4$ Override the Crystal Anisotropy in Oxygen Exchange Kinetics". In: *Chemistry of Materials* 27.15 (Aug. 2015), pp. 5436–5450. DOI: 10.1021/acs.chemmater.5b02292.

[174] Andreas Egger et al. "Oxygen Exchange Kinetics and Chemical Stability of the IT-SOFC Cathode Material $Nd_2NiO_{4+\delta}$". In: *ECS Transactions* 25.2 (2009), pp. 2547–2556. DOI: 10.1149/1.3205811.

[175] J. Druce et al. "Surface termination and subsurface restructuring of perovskite-based solid oxide electrode materials". In: *Energy and Environmental Science* 7.11 (2014), pp. 3593–3599. DOI: 10.1039/c4ee01497a. arXiv: 1102.0581v1.

[176] Woochul Jung and Harry L. Tuller. "Investigation of surface Sr segregation in model thin film solid oxide fuel cell perovskite electrodes". In: *Energy and Environmental Science* 5.1 (2012), pp. 5370–5378. ISSN: 17545692. DOI: 10.1039/c1ee02762j.

[177] Ethan J. Crumlin et al. "Surface strontium enrichment on highly active perovskites for oxygen electrocatalysis in solid oxide fuel cells". In: *Energy & Environmental Science* 5.3 (2012), p. 6081. DOI: 10.1039/c2ee03397f.

[178] Markus Kubicek et al. "Relationship between Cation Segregation and the Electrochemical Oxygen Reduction Kinetics of $La_{0.6}Sr_{0.4}CoO_{3-\delta}$ Thin Film Electrodes". In: *Journal of The Electrochemical Society* 158.6 (2011), B727. DOI: 10.1149/1.3581114.

[179] K. Szot et al. "Restructuring of the surface region in $SrTiO_3$". In: *Applied Physics A: Materials Science & Processing* 64.1 (1997), pp. 55–59. ISSN: 09505849. DOI: 10.1016/j.infsof.2008.09.005. arXiv: 0402594v3 [arXiv:cond-mat].

[180] H.H. Brongersma et al. "Surface composition analysis by low-energy ion scattering". In: *Surface Science Reports* 62.3 (Mar. 2007), pp. 63–109. DOI: 10.1016/j.surfrep.2006.12.002.

[181] Jacques Choisnet et al. "X-ray photoelectron spectroscopy, temperature-programmed desorption and temperature-programmed reduction study of $LaNiO_3$ and $La_2NiO_{4+\delta}$ catalysts for methanol oxidation". In: *Journal of the Chemical Society, Faraday Transactions* 90.13 (1994), p. 1987. DOI: 10.1039/ft9949001987.

[182] San Ping Jiang. "Sintering behavior of Ni/Y_2O_3-ZrO_2 cermet electrodes of solid oxide fuel cells". In: *Journal of Materials Science* 38.18 (2003), pp. 3775–3782. ISSN: 00222461. DOI: 10.1023/A:1025936317472.

[183] M. Mogensen et al. "Factors controlling the oxide ion conductivity of fluorite and perovskite structured oxides". In: *Solid State Ionics* 174.1-4 (2004), pp. 279–286. ISSN: 01672738. DOI: 10.1016/j.ssi.2004.07.036.

[184] Mónica Burriel et al. "Influence of Crystal Orientation and Annealing on the Oxygen Diffusion and Surface Exchange of $La_2NiO_{4+\delta}$". In: *Journal of Physical Chemistry C* 120.32 (2016), pp. 17927–17938. DOI: 10.1021/acs.jpcc.6b05666.

[185] Yan Chen et al. "Impact of Sr segregation on the electronic structure and oxygen reduction activity of $SrTi_{1-x}Fe_xO_3$ surfaces". In: *Energy and Environmental Science* 5.7 (2012), pp. 7979–7988. DOI: 10.1039/c2ee21463f.

[186] Na Ni et al. "Degradation of $(La_{0.6}Sr_{0.4})_{0.95}(Co_{0.2}Fe_{0.8})O_{3-\delta}$ Solid Oxide Fuel Cell Cathodes at the Nanometer Scale and below". In: *ACS Applied Materials & Interfaces* 8.27 (July 2016), pp. 17360–17370. DOI: 10.1021/acsami.6b05290.

[187] Yuri A. Mastrikov et al. "Surface termination effects on the oxygen reduction reaction rate at fuel cell cathodes". In: *Journal of Materials Chemistry A* 6.25 (2018), pp. 11929–11940. DOI: 10.1039/c8ta02058b.

[188] Michele Riva et al. "Influence of surface atomic structure demonstrated on oxygen incorporation mechanism at a model perovskite oxide". In: *Nature Communications* 9.1 (Dec. 2018), p. 3710. DOI: 10.1038/s41467-018-05685-5.

[189] Jong Hoon Joo, Rotraut Merkle, and Joachim Maier. "Effects of water on oxygen surface exchange and degradation of mixed conducting perovskites". In: *Journal of Power Sources* 196.18 (2011), pp. 7495–7499. DOI: 10.1016/j.jpowsour.2011.04.032.

[190] Teruo Matsushita. *Flux Pinning in Superconductors*. Vol. 178. Springer Series in Solid-State Sciences. Berlin, Heidelberg: Springer Berlin Heidelberg, 2014, pp. 198–200. ISBN: 978-3-642-45311-3. DOI: 10.1007/978-3-642-45312-0.

[191] J. L. Macmanus-Driscoll et al. "Strongly enhanced current densities in superconducting coated conductors of $YBa_2Cu_3O_{7-x}$ + $BaZrO_3$". In: *Nature Materials* 3.7 (2004), pp. 439–443. ISSN: 14761122. DOI: 10.1038/nmat1156. arXiv: 0406087 [cond-mat].

[192] David C. Larbalestier et al. "High-T_c superconducting materials for electric power applications." In: *Nature* 414.6861 (2001), pp. 368–377. DOI: 10.1038/35104654.

[193] Aixia Xu et al. "Strongly enhanced vortex pinning from 4 to 77 K in magnetic fields up to 31 T in 15 mol.% Zr-added (Gd, Y)-Ba-Cu-O superconducting tapes". In: *APL Materials* 2.4 (2014), p. 046111. DOI: 10.1063/1.4872060.

[194] J. Gutiérrez et al. "Strong isotropic flux pinning in solution-derived $YBa_2Cu_3O_{7-x}$ nanocomposite superconductor films". In: *Nature Materials* 6.5 (2007), pp. 367–373. DOI: 10.1038/nmat1893.

[195] M. LeRoux et al. "Rapid doubling of the critical current of $YBa_2Cu_3O_{7-\delta}$ coated conductors for viable high-speed industrial processing". In: *Applied Physics Letters* 107.19 (2015), pp. 0–5. ISSN: 00036951. DOI: 10.1063/1.4935335.

[196] N. Haberkorn et al. "Influence of random point defects introduced by proton irradiation on critical current density and vortex dynamics of $Ba(Fe_{0.925}Co_{0.075})_2As_2$ single crystals". In: *Physical Review B* 85.1 (Jan. 2012), p. 014522. ISSN: 1098-0121. DOI: 10.1103/PhysRevB.85.014522.

[197] L. Civale et al. "Vortex confinement by columnar defects in $YBa_2Cu_3O_7$ crystals: Enhanced pinning at high fields and temperatures". In: *Physical Review Letters* 67.5 (1991), pp. 648–651. ISSN: 00319007. DOI: 10.1103/PhysRevLett.67.648.

[198] Jeffery L. Tallon et al. "Critical Doping in Overdoped High-T_c Superconductors: a Quantum Critical Point?" In: *physica status solidi (b)* 215.1 (Sept. 1999), pp. 531–540. DOI: 10.1002/(SICI)1521-3951(199909)215:1<531::AID-PSSB531>3.0.CO;2-W.

[199] Guy Deutscher. "Impact of pseudo-gap states on the pinning energy and irreversibility field of high temperature superconductors". In: *APL Materials* 2.9 (Sept. 2014), p. 096108. DOI: 10.1063/1.4894781.

[200] E. F. Talantsev et al. "Oxygen deficiency, stacking faults and calcium substitution in MOD YBCO coated conductors". In: *IEEE Transactions on Applied Superconductivity* 23.3 (2013), pp. 0–4. DOI: 10.1109/TASC.2012.2233843.

[201] Jeffery L. Tallon. "Thermodynamics and Critical Current Density in High-T_c Superconductors". In: *IEEE Transactions on Applied Superconductivity* 25.3 (June 2015), pp. 1–6. ISSN: 1051-8223. DOI: 10.1109/TASC.2014.2379660.

[202] P. J. White et al. "Rapid suppression of the superconducting gap in overdoped $Bi_2Sr_2CaCuO_{8+\delta}$". In: *Physical Review B* 54.22 (Dec. 1996), R15669–R15672. ISSN: 0163-1829. DOI: 10.1103/PhysRevB.54.R15669.

[203] Jeffery L. Tallon and J W Loram. "Doping dependence of T^* - what is the real high-T_c phase diagram?" In: *Physica C: Superconductivity and its Applications* 349 (2001), pp. 53–68. DOI: 10.1016/S0921-4534(00)01524-0.

[204] S A Hayward et al. "Transformation processes in $LaAlO_3$: Neutron diffraction, dielectric, thermal, optical, and Raman studies". In: (2005), pp. 1–17. DOI: 10.1103/PhysRevB.72.054110.

[205] Qingyun Mao et al. "Phase Transitions, Domains Walls and Defects Dynamics of $LaAlO_3$ via In Situ Heating in the Transmission Electron Microscope". In: *Microscopy and Microanalysis* 20.S3 (Aug. 2014), pp. 1556–1557. ISSN: 1431-9276. DOI: 10.1017/S1431927614009519.

[206] Akihito Sawa, Haruhiko Obara, and Shin Kosaka. "Effect of using pure ozone on in situ molecular beam epitaxy of $YBa_2Cu_3O_{7-x}$ thin films at low pressure". In: *Applied Physics Letters* 64.5 (Jan. 1994), pp. 649–651. ISSN: 0003-6951. DOI: 10.1063/1.111077.

[207] J.P. Sydow and R.A. Buhrman. "Effect of Ozone Anneals on $YBa_2Cu_{3-x}Co_xO_z$ Thin Films". In: *IEEE Transactions on Appiled Superconductivity* 9.2 (June 1999), pp. 1994–1997. ISSN: 10518223. DOI: 10.1109/77.784854.

[208] David Muñoz-Rojas et al. "Electronic Structure of $Ag_2Cu_2O_4$. Evidence of Oxidized Silver and Copper and Internal Charge Delocalization". In: *The Journal of Physical Chemistry B* 109.13 (Apr. 2005), pp. 6193–6203. DOI: 10.1021/jp044493w.

[209] H. Claus et al. "Reversible oxidation and critical current of $YBa_2Cu_3O_x$ coated conductors". In: *Physica C: Superconductivity* 416.1-2 (2004), pp. 1–10. ISSN: 09214534. DOI: 10.1016/j.physc.2004.08.008.

[210] M. Hücker et al. "Competing charge, spin, and superconducting orders in underdoped $YBa_2Cu_3O_y$". In: *Physical Review B* 90.5 (Aug. 2014), p. 054514. DOI: 10.1103/PhysRevB.90.054514.

[211] Shin-ichi Uchida. *High Temperature Superconductivity*. Vol. 213. Springer Series in Materials Science. Tokyo: Springer Japan, 2015. ISBN: 978-4-431-55299-4. DOI: 10.1007/978-4-431-55300-7.

[212] H Takagi et al. "Superconductor-to-nonsuperconductor transition in $(La_{1-x}Sr_x)_2CuO_4$ as investigated by transport and magnetic measurements". In: *Physical Review B* 40.4 (Aug. 1989), pp. 2254–2261. ISSN: 0163-1829. DOI: 10.1103/PhysRevB.40.2254.

[213] R. McCormack, D. de Fontaine, and G. Ceder. "Oxygen configurations and their effect on charge transfer in off-stoichiometric $YBa_2Cu_3O_z$". In: *Physical Review B* 45.22 (June 1992), pp. 12976–12987. DOI: 10.1103/PhysRevB.45.12976.

[214] S. Badoux et al. "Change of carrier density at the pseudogap critical point of a cuprate superconductor". In: *Nature* 531.7593 (Mar. 2016), pp. 210–214. DOI: 10.1038/nature16983.

[215] C. Collignon et al. "Fermi-surface transformation across the pseudogap critical point of the cuprate superconductor $La_{1.6-x}Nd_{0.4}Sr_xCuO_4$". In: *Physical Review B* 95.22 (2017), p. 224517. DOI: 10.1103/PhysRevB.95.224517.

[216] Subir Sachdev and Debanjan Chowdhury. "The novel metallic states of the cuprates: Topological Fermi liquids and strange metals". In: *Progress of Theoretical and Experimental Physics* 2016.12 (2016), pp. 1–26. ISSN: 20503911. DOI: 10.1093/ptep/ptw110. arXiv: arXiv:1605.03579v1.

[217] Daniel C. Harris and Terrell A. Hewston. "Determination of Cu3+ Cu2+ ratio in the superconductor $YBa_2Cu_3O_{8-x}$". In: *Journal of Solid State Chemistry* 69.1 (1987), pp. 182–185. ISSN: 1095726X. DOI: 10.1016/0022-4596(87)90025-9.

[218] W. M. Chen et al. "An accurate method of iodometric titration to measure copper valence of high-T_c superconductors". In: *Journal of Superconductivity* 10.1 (1997), pp. 41–44. ISSN: 08961107. DOI: 10.1007/BF02763949.

[219] M. A. Hossain et al. "In situ doping control of the surface of higherature superconductors". In: *Nature Physics* 4.7 (2008), pp. 527–531. DOI: 10.1038/nphys998.

[220] J. Valo and M. Leskelä. "Thermal Analysis in Studies Of High-T_c Superconductors". In: *Handbook of Thermal Analysis and Calorimetry*. Ed. by M E Brown and P K Gallagher. Vol. 2. Elsevier B. V., 2003, pp. 817–879. DOI: 10.1016/S1573-4374(03)80019-5.

[221] Paola Benzi, Elena Bottizzo, and Nicoletta Rizzi. "Oxygen determination from cell dimensions in YBCO superconductors". In: *Journal of Crystal Growth* 269.2-4 (Sept. 2004), pp. 625–629. DOI: 10.1016/j.jcrysgro.2004.05.082.

[222] B. Wuyts et al. "Influence of the oxygen content on the normal-state Hall angle in $YBa_2Cu_3O_{xn}$ films". In: *Physical Review B* 47.9 (1993), pp. 5512–5515. ISSN: 01631829. DOI: 10.1103/PhysRevB.47.5512.

[223] Yoichi Ando et al. "Electronic Phase Diagram of High-T_c Cuprate Superconductors from a Mapping of the In-Plane Resistivity Curvature". In: *Physical Review Letters* 93.26 (Dec. 2004), p. 267001. DOI: 10.1103/PhysRevLett.93.267001.

[224] S.H Naqib et al. "Temperature dependence of electrical resistivity of high-T_c cuprates - from pseudogap to overdoped regions". In: *Physica C: Superconductivity* 387.3-4 (May 2003), pp. 365–372. DOI: 10.1016/S0921-4534(02)02330-4.

[225] J.W. Cochrane, G.J Russell, and D.N. Matthews. "Seebeck coefficient as an indicator of oxygen content in YBCO". In: *Physica C: Superconductivity* 232 (1994), pp. 89–92.

[226] C Bernhard and Jeffery L. Tallon. "Thermoelectric power of $Y_{1-x}Ca_xBa_2Cu_3O_{7-\delta}$: Contributions from CuO_2 planes and CuO chains". In: *Physical Review B* 54.14 (1996), pp. 10201–10209. DOI: 10.1103/PhysRevB.54.10201.

[227] Hector Castro and Guy Deutscher. "Anomalous Fermi liquid behavior of overdoped high-T_c superconductors". In: *Physical Review B - Condensed Matter and Materials Physics* 70.17 (2004), pp. 1–8. DOI: 10.1103/PhysRevB.70.174511.

[228] Yoichi Ando et al. "Mobility of the doped holes and the antiferromagnetic correlations in underdoped high-T_c cuprates". In: *Physical Review Letters* 87.1 (2001), pp. 1–4. DOI: 10.1103/PhysRevLett.87.017001.

[229] B. Wuyts, V V Moshchalkov, and Y Bruynseraede. "Resistivity and Hall effect of metallic oxygen-deficient $YBa_2Cu_3O_x$ films in the normal state". In: *Physical Review B* 53.14 (Apr. 1996), pp. 9418–9432. ISSN: 0163-1829. DOI: 10.1103/PhysRevB.53.9418.

[230] Anthony T. Fiory and G. S. Grader. "Extraordinary Hall effect in $YBa_2Cu_3O_{7-\delta}$ superconductors". In: *Physical Review B* 38.13 (Nov. 1988), pp. 9198–9200. ISSN: 0163-1829. DOI: 10.1103/PhysRevB.38.9198.

[231] Philip W. Anderson. "Hall effect in the two-dimensional Luttinger liquid". In: *Physical Review Letters* 67.15 (Oct. 1991), pp. 2092–2094. ISSN: 0031-9007. DOI: 10.1103/PhysRevLett.67.2092.

[232] Elihu Abrahams and C. M. Varma. "Hall effect in the marginal Fermi liquid regime of high-T_c superconductors". In: *Physical Review B* 68.9 (Sept. 2003), p. 094502. DOI: 10.1103/PhysRevB.68.094502.

[233] Branko P. Stojković and David Pines. "Anomalous Hall Effect in $YBa_2Cu_3O_7$". In: *Physical Review Letters* 76.5 (Jan. 1996), pp. 811–814. ISSN: 0031-9007. DOI: 10.1103/PhysRevLett.76.811.

[234] D. Y. Xing and M. Liu. "Single-band model of normal-state transport properties of high-T_c copper oxides". In: *Physical Review B* 43.4 (Feb. 1991), pp. 3744–3747. DOI: 10.1103/PhysRevB.49.4209.

[235] A. Davidson et al. "Conduction and Hall measurements of $Ba_2YCu_3O_{6+\delta}$ films at high temperatures: The role of oxygen". In: *Physical Review B* 38.4 (Aug. 1988), pp. 2828–2831. DOI: 10.1103/PhysRevB.38.2828.

[236] Dale R. Harshman, John D. Dow, and Anthony T. Fiory. "Coexisting holes and electrons in high-T_c materials: Implications from normal state transport". In: *Philosophical Magazine* 91.5 (2011), pp. 818–840. DOI: 10.1080/14786435.2010.527864.

[237] T. Ito, K. Takenaka, and Shin-ichi Uchida. "Systematic deviation from T-linear behavior in the in-plane resistivity of $YBa_2Cu_3O_{7-y}$: Evidence for dominant spin scattering". In: *Physical Review Letters* 70.25 (1993), pp. 3995–3998. ISSN: 00319007. DOI: 10.1103/PhysRevLett.70.3995.

[238] Kouji Segawa and Yoichi Ando. "Intrinsic Hall response of the CuO_2-planes in a chain-plane composite system of $YBa_2Cu_3O_y$". In: *Physical Review B - Condensed Matter and Materials Physics* 69.10 (2004), p. 104521. DOI: 10.1103/PhysRevB.69.104521.

[239] Edwin C Jones, David K Christen, and Brian C Sales. "Sign reversals in the vortex-state Hall effect in Y-Ba-Cu-O: Correlations with the normal-state Seebeck coefficient". In: *Phys. Rev. B* 50.10 (1994), pp. 7234–7237.

[240] Jan Kolácek and Petr Vasek. "Hall voltage sign reversal in type II superconductors". In: *Physica C: Superconductivity and its Applications* 336.3 (2000), pp. 199–204. ISSN: 09214534. DOI: 10.1016/S0921-4534(00)00286-0. arXiv: 9811222 [cond-mat].

[241] W Lang et al. "Paraconductivity and excess Hall effect in epitaxial $YBa_2Cu_3O_7$ films induced by superconducting fluctuations". In: *Physical Review B* 49.6 (Feb. 1994), pp. 4209–4217. DOI: 10.1103/PhysRevB.49.4209.

[242] Andrea Damascelli, Zahid Hussain, and Zhi Xun Shen. "Angle-resolved photoemission studies of the cuprate superconductors". In: *Reviews of Modern Physics* 75.2 (2003), pp. 473–541. DOI: 10.1103/RevModPhys.75.473.

[243] T. R. Chien et al. "Unusual $1/T^3$ temperature dependence of the Hall conductivity in $YBa_2Cu_3O_{7-\delta}$". In: *Physical Review B* 43.7 (Mar. 1991), pp. 6242–6245. DOI: 10.1103/PhysRevB.43.6242.

[244] R Lawrance. "The Temperature Dependence of the Drift Mobility of Injected Holes in Germanium". In: *Proceedings of the Physical Society. Section B* 67.1 (Jan. 1954), pp. 18–27. DOI: 10.1088/0370-1301/67/1/304.

[245] F. J. Morin and J. P. Maita. "Electrical properties of silicon containing arsenic and boron". In: *Physical Review* 96.1 (1954), pp. 28–35. ISSN: 0031899X. DOI: 10.1103/PhysRev.96.28.

[246] Safa O. Kasap. *Hall Effect in Semiconductors*. Saskatoon: University of Saskatchewan, Canada, 2001. URL: https://www.webcitation.org/5c0UeBBsZ.

[247] Nigel E. Hussey. "Phenomenology of the normal state in-plane transport properties of high-T_c cuprates". In: *Journal of Physics: Condensed Matter* 20.12 (Mar. 2008), p. 123201. ISSN: 0953-8984. DOI: 10.1088/0953-8984/20/12/123201.

[248] Cyril Proust et al. "Fermi liquid behavior of the in-plane resistivity in the pseudogap state of $YBa_2Cu_4O_8$". In: *Proceedings of the National Academy of Sciences* 113.48 (2016), pp. 13654–13659. DOI: 10.1073/pnas.1602709113.

[249] Takashi Manako, Yoshimi Kubo, and Yuichi Shimakawa. "Transport and structural study of $Tl_2Ba_2CuO_{6+\delta}$ single crystals prepared by the KCl flux method". In: *Physical Review B* 46.17 (Nov. 1992), pp. 11019–11024. ISSN: 0163-1829. DOI: 10.1103/PhysRevB.46.11019.

[250] Robert Gagnon, Christian Lupien, and Louis Taillefer. "T^2 dependence of the resistivity in the Cu-O chains of $YBa_2Cu_3O_{6.9}$". In: *Physical Review B* 50.5 (Aug. 1994), pp. 3458–3461. DOI: 10.1103/PhysRevB.50.3458.

[251] Nigel E. Hussey et al. "Anisotropic resistivity of: Incoherent-to-metallic crossover in the out-of-plane transport". In: *Physical Review B - Condensed Matter and Materials Physics* 56.18 (1997), R11423–R11426. DOI: 10.1103/PhysRevB.56.R11423.

[252] G Blatter et al. "Vortices in high-temperature superconductors". In: *Reviews of Modern Physics* 66.4 (1994), pp. 1125–1388. ISSN: 00346861. DOI: 10.1103/RevModPhys.66.1125.

[253] Philip W. Anderson. "Theory of Flux Creep in Hard Superconductors". In: *Physical Review Letters* 9.7 (Oct. 1962), pp. 309–311. ISSN: 0031-9007. DOI: 10.1103/PhysRevLett.9.309.

[254] S Senoussi et al. "Exponential H and T decay of the critical current density in $YBa_2Cu_3O_{7-\delta}$ single crystals". In: *Physical Review B* 37.16 (June 1988), pp. 9792–9795. ISSN: 0163-1829. DOI: 10.1103/PhysRevB.37.9792.

[255] David R. Nelson and V. M. Vinokur. "Boson localization and correlated pinning of superconducting vortex arrays". In: *Physical Review B* 48.17 (1993), pp. 13060–13097. ISSN: 01631829. DOI: 10.1103/PhysRevB.48.13060.

[256] N.W. Ashcroft and N.D. Mermin. *Solid State Physics*. Philadelphia: Holt-Sounders College, 1988.

[257] Antonella Parisini and Roberto Fornari. "Analysis of the scattering mechanisms controlling electron mobility in β-Ga_2O_3 crystals". In: *Semiconductor Science and Technology* 31.3 (Mar. 2016), p. 035023. ISSN: 0268-1242. DOI: 10.1088/0268-1242/31/3/035023.

[258] M.R. Presland et al. "General trends in oxygen stoichiometry effects on T_c in Bi and Tl superconductors". In: *Physica C: Superconductivity* 176.1-3 (May 1991), pp. 95–105. DOI: 10.1016/0921-4534(91)90700-9.

[259] Jeffery L. Tallon et al. "Generic superconducting phase behavior in high-T_c cuprates: T, variation with hole concentration in $YBa_2Cu_3O_{7-\delta}$". In: *Physical Review B* 51.18 (1995), pp. 911–914. DOI: 10.1103/PhysRevB.51.12911.

[260] Huanbo Zhang and Hiroshi Sato. "Universal relationship between T_c and the hole content in p-type cuprate superconductors". In: *Physical Review Letters* 70.11 (1993), pp. 1697–1699. DOI: 10.1103/PhysRevLett.70.1697.

[261] W Lang et al. "Depairing current and superconducting transition of YBCO at". In: 1624.5 (2005), pp. 1615–1624. DOI: 10.1002/pssc.200460801.

[262] Pablo Cayado et al. "Chemical solution deposition of $Y_{1-x}Gd_xBa_2Cu_3O_{7-\delta}$-$BaHfO_3$ nanocomposite films: combined influence of nanoparticles and rare-earth mixing on growth conditions and transport propert". In: *RSC Advances* 8.74 (2018), pp. 42398–42404. DOI: 10.1039/C8RA09188A.

[263] Ch Niedermayer et al. "Muon spin rotation study of the correlation between T_c and n_s/m^* in overdoped $Tl_2Ba_2CuO_{6+\delta}$". In: *Physical Review Letters* 71.11 (1993), pp. 1764–1767. DOI: 10.1103/PhysRevLett.71.1764.

[264] I. Božović et al. "Dependence of the critical temperature in overdoped copper oxides on superfluid density". In: *Nature* 536.7616 (2016), pp. 309–311. DOI: 10.1038/nature19061.

[265] K. Nishikawa et al. "Superconducting gap of overdoped $Tl_2Ba_2CuO_{6+\delta}$ observed by Raman scattering". In: *Journal of Physics and Chemistry of Solids* 69.12 (Dec. 2008), pp. 3074–3077. ISSN: 00223697. DOI: 10.1016/j.jpcs.2008.06.022.

[266] J. K. Ren et al. "Energy gaps in $Bi_2Sr_2CaCu_2O_{8+\delta}$ cuprate superconductors". In: *Scientific Reports* 2 (2012), pp. 1–7. DOI: 10.1038/srep00248.

[267] Jeffery L. Tallon, J. G. Storey, and J. W. Loram. "Fluctuations and critical temperature reduction in cuprate superconductors". In: *Physical Review B - Condensed Matter and Materials Physics* 83.9 (2011), pp. 2–5. ISSN: 10980121. DOI: 10.1103/PhysRevB.83.092502. arXiv: 0908.4428v1.

[268] O. Cyr-Choinière et al. "Pseudogap temperature T^* of cuprate superconductors from the Nernst effect". In: *Physical Review B* 97.6 (2018), pp. 1–24. DOI: 10.1103/PhysRevB.97.064502.

[269] C. W. Chu, L. Z. Deng, and B. Lv. "Hole-doped cuprate high temperature superconductors". In: *Physica C: Superconductivity and its Applications* 514 (2015), pp. 290–313. DOI: 10.1016/j.physc.2015.02.047. arXiv: 1502.04686.

[270] Alain Junod et al. "Experimental survey of critical fluctuations in the specific heat of high-temperature superconductors". In: *Physica B: Condensed Matter* 280.1-4 (2000), pp. 214–219. ISSN: 09214526. DOI: 10.1016/S0921-4526(99)01581-1.

[271] J. Locquet et al. "Variation of the in-plane penetration depth as a function of doping thin films on: Implications for the overdoped state". In: *Physical Review B - Condensed Matter and Materials Physics* 54.10 (1996), pp. 7481–7488. ISSN: 1550235X. DOI: 10.1103/PhysRevB.54.7481.

[272] Damian Rybicki et al. "Perspective on the phase diagram of cuprate high-temperature superconductors". In: *Nature Communications* 7.4 (May 2016), p. 11413. ISSN: 2041-1723. DOI: 10.1038/ncomms11413.

[273] E. F. Talantsev et al. "Hole doping dependence of critical current density in $YBa_2Cu_3O_{7-\delta}$ conductors". In: *Applied Physics Letters* 104.24 (2014), p. 242601. DOI: 10.1063/1.4883483.

[274] A. Goyal and S. H. Wee. "Optimal, Nanodefect Configurations via Strain-Mediated Assembly for Optimized Vortex-Pinning in Superconducting Wires from 5K-77K". In: *Journal of Physics: Conference Series* 871.1 (July 2017), p. 012039. DOI: 10.1088/1742-6596/871/1/012039.

[275] Goran Majkic et al. "Engineering current density over 5 kA mm^{-2} at 4.2 K, 14 T in thick film REBCO tapes". In: *Superconductor Science and Technology* 31.10 (Oct. 2018), 10LT01. DOI: 10.1088/1361-6668/aad844.

[276] Shun Miura et al. "Strong flux pinning at 4.2 K in $SmBa_2Cu_3O_y$ coated conductors with $BaHfO_3$ nanorods controlled by low growth temperature". In: *Superconductor Science and Technology* 30.8 (Aug. 2017), p. 084009. ISSN: 0953-2048. DOI: 10.1088/1361-6668/aa76a1.

[277] Aixia Xu et al. "Broad temperature range study of J_c and H_{irr} anisotropy in $YBa_2Cu_3O_x$ thin films containing either Y_2O_3 nanoparticles or stacking faults". In: *Applied Physics Letters* 106.5 (Feb. 2015), p. 052603. DOI: 10.1063/1.4907891.